



HAL
open science

Investigations of the Tube Support Plate (TSP) clogging phenomenon in PWR steam generators - understanding and prioritization of its formation mechanisms

Guangze Yang

► **To cite this version:**

Guangze Yang. Investigations of the Tube Support Plate (TSP) clogging phenomenon in PWR steam generators - understanding and prioritization of its formation mechanisms. Chemical Physics [physics.chem-ph]. Université Pierre et Marie Curie - Paris VI, 2017. English. NNT : 2017PA066441 . tel-01925862

HAL Id: tel-01925862

<https://theses.hal.science/tel-01925862>

Submitted on 18 Nov 2018

HAL is a multi-disciplinary open access archive for the deposit and dissemination of scientific research documents, whether they are published or not. The documents may come from teaching and research institutions in France or abroad, or from public or private research centers.

L'archive ouverte pluridisciplinaire **HAL**, est destinée au dépôt et à la diffusion de documents scientifiques de niveau recherche, publiés ou non, émanant des établissements d'enseignement et de recherche français ou étrangers, des laboratoires publics ou privés.

Université Pierre et Marie Curie

ED388 / IRCP Chimie ParisTech

Investigations of the Tube Support Plate (TSP) clogging phenomenon in PWR steam generators – understanding and prioritization of its formation mechanisms

Par **Guangze YANG**

Thèse de doctorat de chimie physique et chimie analytique

Dirigée par Alexandre CHAGNES

Présentée et soutenue publiquement le 16 Novembre 2017

Devant un jury composé de :

Didier Devilliers, Université Pierre et Marie Curie, Paris, Président

Gilles Berger, Université de Toulouse III, Toulouse, Rapporteur

Nicolas Marmier, Université Nice Sophia Antipolis, Nice, Rapporteur

Isabelle Mabile, Université Pierre et Marie Curie, Paris, Examineur

Etienne Tevissen, CEA, Cadarache, Invité

Sophie Delaunay, EDF, Renardières, Invité

Veronique Pointeau, CEA, Cadarache, Encadrante (co-direction)

Alexandre Chagnes, Université de Lorraine, Nancy, Directeur de thèse

Acknowledgements

It gives me immense pleasure to write this note of acknowledgement for everyone who has been involved with this project in one way or the other.

First and foremost I want to thank my CEA supervisor Véronique. Pointeau. It has been an honour to be your first PhD student. I appreciate all your contributions of time and ideas to make my PhD experience productive and stimulating. The joy and enthusiasm you have for the research was contagious and motivational for me. I wholeheartedly thank you for the constant support and encouragement, both personally and professionally, during the entire duration of my PhD.

I take this opportunity to thank Alexandre. Chagnes (Université de Lorraine) for agreeing to be my thesis director and your constant guidance throughout. Your time and effort in helping me well adapt the thesis approaches and improving my scientific redaction have been invaluable. I am also thankful for your precious implications in the obtainment of my future researcher position in the IFCEN.

I would like to thank Etienne. Tevissen (CEA), for welcoming me on April, 2014 in Cadarache for the thesis interview and accepting me as a PhD student. Your guidance on the development of my thesis was constant and useful during all these three years.

I would like to thank all the jury members for your presence, your suggestions to improve the manuscript and your pertinent questions and comments on the day of my defence.

I want to thank, Huber Catelette (EDF), Gérard Côte (Chimie ParisTech), Philippe Moisy (CEA) and François Paquet (IRSN), for recommending me for this PhD position.

I want to thank my laboratory (LHC) chief in CEA, Isabelle Tkatchenko, for supporting me to present my PhD work in various French and international conferences. Thank you, Isabelle Mounet and Gaëlle Pestel, for solving administrative issues to facilitate my participation in these conferences. Thank you Alexandre, Véronique and Etienne once again for encouraging me to participate to conferences and reviewing my proceedings, as well as journal articles.

Thanks to members of COLENTEC team in LHC, Patricia. Schindler, Yves. Philibert, Isabelle. Holveck, Stéphane. Bantiche, Pascal. Marand, Jean-Philippe. Descamps and Véronique. Pointeau, for successfully performing this highly complicated experiment. Particular thanks go to Yves and Isabelle. H, for helping me establish the security file for autoclave tests and launch each campaign. It was an immense pleasure to work in this enthusiast team.

I take this opportunity to thank the team in *the University of Manchester*, particularly Fabio. Scenini and Stefano. Cassineri, for your agreement of establishing our collaboration in electrokinetic investigations. I am also thankful for your welcome during my stay in Manchester. Your insight on electrokinetic phenomenon has been highly appreciated.

Thank you, Frédéric Rey and Serge Delafontaine (CEA), for providing me the modelling of the fluid for the interpretation of electrokinetic results. I appreciate your precious contributions of time and ideas.

I would like to thank Martiane. Cabié (Université Aix-Marseille), for your contributed time and efforts during my TEM characterizations. Your suggestions and advice were useful for the analysis of results. My sincere thanks to Brigitte. Thormos of LIPC (CEA) for your helps in SEM sample preparation and observation. Thank you Véronique for sharing with me your insight on SEM/TEM characterizations.

I want to thank Phillipe Barboux, Domitille Giaume, Phillipe Marcus and Cédric Guyon (Chimie ParisTech) for the initial intention of collaboration.

Thanks to everyone in my laboratory LHC for making my stay pleasurable and memorable! I would like to make a special mention of my “young” lab-mates, Antoine. Dupré, Roberto. Capanna, Saptarshi. Bhattacharjee, Brice. Bourdeaux and Corentin. Bouzet for the wonderful time spent together.

My sincere thanks go to Alexandre, Véronique and Etienne for correcting and improving the present manuscript. This work would not have been possible without your dynamic and efficient corrections.

I would like to thank my parents for your support at every stage of my life. I am also thankful for my friends in Aix en Provence for the amazing three years spent together.

This thesis has been the combined effort of so many people, Véronique, Alexandre, Etienne, my family and friends...

Thank you all!

Abstract

The steam generator is an essential component in PWR which allows the heat exchange between the primary and secondary circuits. After 15-20 years of functioning, an obstruction by deposits of flow holes between Tube Support Plate (TSP) and primary tubes is observed, called TSP clogging. This phenomenon may lead to dramatic consequences for nuclear power plant operation and may be responsible for safety issues. The aim of this thesis is to deepen, experimentally and numerically, the understanding of the mechanisms responsible for TSP clogging by identifying and prioritizing the preponderant processes.

COLENTEC is an experimental facility designed to reproduce TSP clogging deposits under representative conditions of the upper part of steam generators. Microscopic characterizations (SEM and TEM) allowed revealing the deposit formation by precipitation and the initiation role of material passivation in deposit formation. Lipping and ripple forms, specifying TSP clogging, were not observed in COLENTEC tests. This is suggested to be caused by insufficient concentration of suitable particles at the test section. Particle deposition is supposed to be essential for the formation of lipping deposits at the inlet of TSP.

Electrokinetic and flashing phenomena are supposed to contribute to TSP clogging formation, having cementing effects on the deposits initially formed by particle deposition. An experimental collaboration program with *the University of Manchester* was established to better understand the clogging formation by investigating the role of electrokinetic phenomenon. This study allowed reforming deposits with lipping and ripple forms as observed in EDF steam generators. Electrokinetic involvement, strongly affected by flow velocity, was considerably suggested in TSP clogging formation.

Numerical quantification of deposit formation by particle deposition, flashing and electrokinetic phenomenon was performed and compared to EDF feedbacks on TSP clogging formation. Electrokinetic phenomenon was found to play a predominant role, whereas particle deposition was suggested to have a minor contribution to clogging formation.

Key words: clogging, magnetite, precipitation, particle deposition, electrokinetic, mechanism prioritization, experimental deposit rebuild-up, calculation.

Contents

Contents	vi
List of Figures	ix
List of Tables	xv
Nomenclature.....	1
Introduction.....	6
Chapter 1 State of the art	8
1.1 Introduction.....	8
1.2 PWR secondary circuit.....	8
1.2.1 General description	8
1.2.2 Recirculating steam generator.....	9
1.2.3 Thermohydraulics in PWR steam generator	11
1.2.3.1 Two-phase flow fundamentals.....	11
1.2.3.1.1 Two-phase flow system basic notions.....	11
1.2.3.1.2 Two-phase flow patterns	13
1.2.3.2 Thermohydraulics of 51B type steam generators.....	14
1.2.4 Materials used in the secondary circuit.....	14
1.2.5 PWR secondary flow chemistry.....	15
1.2.6 Corrosion phenomena in PWR secondary circuit	16
1.2.6.1 Stress corrosion cracking (SCC).....	16
1.2.6.2 General corrosion and Flow accelerated corrosion (FAC).....	17
1.2.6.3 Parameters affecting flow accelerated corrosion – TSP clogging source	18
1.2.6.3.1 Effects of pH and temperature – magnetite solubility.....	18
1.2.6.3.2 Effect of oxygen concentration	19
1.2.6.3.3 Effect of material composition.....	20
1.2.6.3.4 Effect of thermohydraulics.....	22
1.3 Properties of magnetite particle	23
1.3.1 Structural property	24
1.3.2 Magnetite surface charge	25
1.3.2.1 Electrical double layer (EDL)	25
1.3.2.2 Zeta potential	26
1.3.2.3 Surface characterizations of magnetite	27
1.4 Steam generator degradation phenomena	27
1.4.1 Tube fouling.....	28
1.4.2 Tube Support Plate clogging.....	29
1.4.2.1 TSP clogging consequences.....	29

1.4.2.2	TSP clogging diagnosis.....	30
1.4.2.2.1	Televsual inspections	30
1.4.2.2.2	Wide Range Level (WRL) monitoring in stationary regime.....	30
1.4.2.2.3	Eddy current inspection.....	30
1.4.2.3	NPP feedbacks of TSP clogging	30
1.4.2.4	Current countermeasures.....	32
1.5	Phenomenology of TSP clogging formation.....	32
1.5.1	Magnetite particle deposition.....	33
1.5.1.1	Previous experimental studies.....	33
1.5.1.2	Magnetite particle deposition models	34
1.5.1.2.1	Transport step.....	35
1.5.1.2.2	Attachment step.....	38
1.5.2	Surface precipitation	39
1.5.2.1	Attainment of solubility	39
1.5.2.2	Formation of nuclei.....	39
1.5.2.3	Growth of crystals.....	40
1.5.3	Specific TSP clogging formation mechanisms at the inlet of TSP	41
1.5.3.1	Vena contracta mechanism	42
1.5.3.2	Flashing.....	44
1.5.3.3	Results of modelling study comprising vena contracta and flashing.....	45
1.5.3.4	Electrokinetics.....	45
1.6	Conclusions of Chapter 1	48
Chapter 2	Experimental investigation of TSP clogging phenomenon.....	49
2.1	Introduction.....	49
2.2	Representative experiments	49
2.2.1	Global deposit build-up tool under representative conditions: COLENTEC facility ...	50
2.2.2	COLENTEC – 2015 experimental conditions	52
2.2.3	Materials used for COLENTEC test	54
2.2.4	Characterization results of COLENTEC-2015 samples.....	55
2.2.4.1	Optical and SEM observations.....	56
2.2.4.2	TEM investigations	59
2.2.4.2.1	Characterization of titanium thin section	59
2.2.4.2.2	Characterization of stainless steel thin section.....	64
2.3	Simulated experiments.....	70
2.3.1	Description of autoclave tests	70
2.3.2	Iron incorporation into stainless steel corrosion layer	72
2.3.3	Ti/SS galvanic corrosion effects	74
2.4	Conclusions of Chapter 2.....	75
Chapter 3	Specific experimental investigation of deposit build-up by electrokinetic phenomenon	

3.1	Introduction and basic notions of electrokinetically induced deposit	76
3.2	Literature review relative to the effects of water chemistry and thermohydraulics on electrokinetic deposit build-up	78
3.3	Experimental system	79
3.4	Experimental conditions	81
3.5	Results	83
3.5.1	Morphology and characterization of the deposits	83
3.5.2	Deposit build-up rates	92
3.6	Discussions	93
3.6.1	Effect of flow velocity	93
3.6.2	Comparisons with COLENTEC results and EDF observations	98
3.7	Conclusions of Chapter 3	100
Chapter 4	Numerical investigation of TSP clogging phenomenon	102
4.1	Introduction	102
4.2	Hypotheses and input data	103
4.2.1	Hypotheses	103
4.2.2	Input data	104
4.3	Results	105
4.3.1	Phenomenon prioritization with different particle sizes	105
4.3.2	Phenomenon prioritization with different total iron concentrations	107
4.4	Discussions	108
4.5	Conclusions of Chapter 4	109
Chapter 5	Overall conclusions and perspectives	110
References	115
Appendix A	Scanning Electronic Microscope	130
Appendix B	Transmission Electronic Microscope	131
Appendix C	Synthesis of CeO ₂ -Fe ₃ O ₄ core-shell particles	133

List of Figures

Figure 1.1: Scheme of PWR secondary circuit (Pressurized Water Reactor Systems, n.d.).....	9
Figure 1.2: Scheme of 51B-type PWR recirculating steam generator (Bodineau and Sollier, 2013; Girard et al., 2013). TSP clogging phenomenon is observed after several decades of operation and is represented at the top right.....	10
Figure 1.3: Two-phase flow patterns' sequence as a function of steam quality x (K. Popov, 2015). "G" and "L" represents the vapour phase and the liquid phase, respectively.	13
Figure 1.4: Pourbaix diagram of iron calculated with PHREEPLOT, using the Lawrence Livermore National Laboratory (llnl) database ("llnl.dat", n.d.). Temperature = 200 °C corresponding to the temperature of the secondary circuit before entering into the SG; $\text{pH}_{25\text{ }^\circ\text{C}} > 9$ corresponds to $\text{pH}_{200\text{ }^\circ\text{C}} > 6$ (Yang et al., 2017a); Potential Eh in Volt given vs. the Standard Hydrogen Electrode (SHE). Red point indicates that the stable form of iron is magnetite under the above-mentioned conditions.	17
Figure 1.5: Magnetite solubility as a function of temperature and pH at 25 °C. pH was conditioned by adding ammonia at 0.1 ppm to 2.0 ppm. A maximum of magnetite solubility is observed at about 150 °C whatever the pH values. Detailed data cannot be provided. (Unpublished EPRI results)	19
Figure 1.6: SEM images of the oxide film after immersion in simulated PWR primary water at 320 °C for 380 h, observed by Terachi's investigation (Terachi et al., 2008).	20
Figure 1.7: Schematic image of cross-sectional oxide film on stainless steel, proposed by Terachi's work (Terachi et al., 2008).....	21
Figure 1.8: Electron diffraction patterns of the inner layer in 5% Cr, 10% Cr and 16% Cr after immersion in simulated PWR primary water at 320 °C for 380 h, obtained by Terachi's investigation (Terachi et al., 2008).	21
Figure 1.9: Observed double-layer structure for HCM12A sample exposed for eight weeks in supercritical water conditions. Iron and chromium evolutions are shown, which highlight chromium enrichment in the inner corrosion layer (Bischoff et al., 2012).	22
Figure 1.10: Photo of a magnetite mineral from Bolivia (Wikipedia source). Bipyrmaid crystals are observed.	23
Figure 1.11: Structure of magnetite. Red spheres represent O^{2-} ; marron spheres represent the ferrous and ferric ions. FeA (ferric ions) occupy tetrahedral sites and FeB (ferric and ferrous ions) occupy octahedral sites.....	24
Figure 1.12: Potential variation across the EDL. The potential between the surface and IHP, as well as the IHP and the OHP varies linearly and then exponentially in the diffuse layer. Ψ^0 , Ψ^i and Ψ^d represent the wall potential, IHP potential and OHP potential respectively. A shear plane is placed with a distance of d^{ek} from the wall. ζ represents the corresponding potential at this plane, named zeta potential.....	26
Figure 1.13: Photo of SG tube fouling (Prusek, 2012).	28
Figure 1.14: Photo of TSP clogging: top view of a "clean" quatrefoil flow hole (a); almost fully clogged quatrefoil flow hole (b) (Prusek et al., 2013; adapted by Yang et al., 2017a). Lipping form and ripple form are observed for clogged flow hole.	29

Figure 1.15: Schematic of TSP clogging lipping form and ripples (J. Morrison, 2014).....	31
Figure 1.16: Main phenomena involved in SG deposits.	33
Figure 1.17: Pattern of vena contracta region (Prusek, 2012; Prusek et al., 2013).....	43
Figure 1.18: Top view of a pattern of a TSP (secondary flow hole in white colour).....	44
Figure 1.19: Illustration of magnetite formation due to electrokinetic phenomena onto TSP. i_w represents the wall current; i_s represents the streaming current.	46
Figure 1.20: The proposed electrokinetic mechanism of deposit propagation along the annulus of a flow-restriction (Guillodo et al., 2012).....	47
Figure 2.1: Flowsheet of the COLENTEC test loop.....	50
Figure 2.2: Photo of COLENTEC primary loop (a), COLENTEC air cooler (b), and COLENTEC CVCS system (c).....	51
Figure 2.3: Photo of COLENTEC secondary loop (a), COLENTEC test section (b) with four primary SG tubes maintained by a titanium TSP (the COLENTEC secondary fluid circulates in the quatrefoils between the tubes and TSP) and COLENTEC titanium TSP with removable test coupons inserted in the dedicated sites (c).....	51
Figure 2.4: Evolution of the temperature in the test section (1), at the inlet (2) and the outlet of the condenser (3) and at the inlet of the secondary boiler (4) in COLENTEC-2015-1 test from the 24 th February to the 4 th March 2015.....	52
Figure 2.5: Evolution of the temperature during the COLENTEC-2015-2 test. (1): temperature in the test section; (2): temperature at the inlet; (3): temperature at the outlet of the condenser; (4): temperature at the inlet of the secondary boiler.....	53
Figure 2.6: Photo of COLENTEC test coupons made of titanium (Ti), stainless steel (SS) and mirror-polished titanium (M-Ti) (a); Scheme of COLENTEC test coupons (b). A specific ergot is implemented for the TSP fixation and the coupon surface is curved to satisfy the real geometric configuration of TSP flow hole; Scheme of COLENTEC test coupons (c). Both titanium and stainless steel test coupons have a length of 30 mm, a maximal width of 7.19 mm and an equally-curved surface; Photo of the titanium TSP with 16 test coupons inserted for COLENTEC-2015-1 (d).	55
Figure 2.7: Surface morphology observed by secondary electron mode SEM of titanium test coupon after 11 days under experimental conditions of COLENTEC-2015-1. A depleted-deposit region is observed at the inlet of TSP.	56
Figure 2.8: Comparison between a titanium (Ti) test coupon and a mirror-polished titanium (M-Ti) coupon after 11 days under experimental conditions of COLENTEC-2015-1. Ti sample after 11 days appears to be covered by a homogenous black layer, which contains majorly iron and oxygen (measured by EDS); M-Ti coupon appears unchanged.	57
Figure 2.9: Surface morphology observed by secondary electron mode SEM of titanium test coupon after 11 days under experimental conditions of COLENTEC-2015-1 (a) and after 63 days under experimental conditions of COLENTEC-2015-2 (b). Iron oxide crystal twinning is observed in both cases. Crystal size is estimated to be around 1 μm after 11 days (a), and 5 μm after 63 days (b).....	57
Figure 2.10: SEM picture in Back-scattered electron mode of stainless steel cut coupon obtained during the COLENTEC-2015-2 test (a) and titanium cut coupon obtained during the COLENTEC-2015-2 test (b).....	58
Figure 2.11: Thin section of titanium sample (a). Three principal areas are observed: (1): area close to titanium substrate; (2): porous layer; (3): compact layer; Zoom close to titanium substrate (b). White lines delimit a porous layer of around 100 nm, which is supposed to be the corrosion layer mainly composed of titanium and oxygen.	59
Figure 2.12: Seven different EDS analyses of titanium sample obtained during COLENTEC 2015 test in the area close to Ti substrate (a); High resolution (HR) TEM image (b) of a particle from #2 region in Figure 2.12a (white dash line represents the border of a particle present in this layer).....	60

Figure 2.13: EDS analyses showing atomic percent of element was performed along the white line, crossing titanium sample, TiO ₂ corrosion layer, two potential (Mn _{1-x} Fe _x)TiO ₃ solid solution layers separated by the yellow dash line and iron particles. Only the evolution of each element is intended to be shown along the white line, comparisons between different elements are not significant.....	61
Figure 2.14: EDS mapping of the closed titanium area, containing titanium substrate, TiO ₂ corrosion layer, potential solid solution layer and deposited iron particles, showing the TEM image and mapping zone (a); and element distribution of iron (b), titanium (c), oxygen (d) and manganese (e).	62
Figure 2.15: EDS mapping of a zoomed close titanium area, containing TiO ₂ corrosion layer, the two potential solid solution layers and deposited iron particles, showing the TEM image and mapping zone and element distribution of iron, titanium, oxygen and manganese.....	62
Figure 2.16: Surface TEM and EDS analysis of porous and external compact layer in the titanium sample obtained during the COLENTEC 2015 test (a). The EDS analyses were performed under the same conditions in the four red areas shown in the TEM image; Diffraction patterns (b) of a area in Figure 2.16a.	63
Figure 2.17: EDS mapping of a selected area of the compact layer of the titanium thin section.	64
Figure 2.18: Pictures by TEM in the bright field (BF) mode of the thin section of stainless steel sample obtained during the COLENTEC 2015 test (a). Three different layers are observed: (1) Compact inner corrosion layer delimited by an outer-inner layer interface (white dash line), (2) Compact outer corrosion layer and (3) Particle aggregation; Specific TEM BF observation of particle aggregation (b) (Particles size is of about several hundreds of nm).....	65
Figure 2.19: Surface TEM and EDS analysis of stainless steel sample obtained during the COLENTEC-2015 test. (a) stainless steel material; (b) inner corrosion layer; (c) and (d) outer corrosion layer; (e) particle aggregation. The EDS analysis was performed under same conditions in the five red areas (see composition in Table 2.7).	66
Figure 2.20: Indicator of different regions where analyses are performed (a); Diffraction patterns of b area (b); Diffraction patterns of c area (c); Diffraction patterns of d area (d); High resolution (HR) TEM image of a particle from e area (white dash line represents the border of a particle present in this layer) (e).	67
Figure 2.21: EDS analyses performed along the white line in images (a), (b) and (c). Only the evolution of each element is intended to be shown along the white line. Comparisons between different elements are not significant.....	68
Figure 2.22: EDS mapping of the interface area between particle aggregation layer and outer corrosion layer, showing the TEM image and mapping zone (a); and element distribution of iron (b), chromium (c) and oxygen (d). A thin chromium (around 100 nm) enriched layer is observed at the outermost corrosion layer and delimited by white line in (c).	69
Figure 2.23: Photo of autoclave system.	71
Figure 2.24: Scheme of the test coupon designed especially for autoclave to investigate galvanic corrosion. Green coupon is made of stainless steel inserted into the pre-machined titanium coupon coloured in grey.	71
Figure 2.25: SEM observation of the SS coupon in the Autoclave-A (Ti-SS-Ti sample) after an immersion during one month at 250 °C and 30 bars without iron in the autoclave (a). A corrosion layer of 2 µm containing iron, oxygen, silicon, aluminium and chromium is observed; SEM observation of the SS coupon in the Autoclave-B (Ti-SS-Ti sample) after an immersion during one month in an autoclave containing 5 ppb of iron (b). A corrosion layer of 6 µm containing iron, oxygen, silicon, aluminium and chromium is observed.	73
Figure 2.26: SEM observation of the surface of SS coupon in the Autoclave-C (Ti-SS-Ti sample) after ten days of immersion at 250 °C and 30 bars in autoclave without iron (a). No corrosion layer is observed; SEM observation of the surface of SS coupon in the Autoclave-D (Ti-SS-Ti sample) after ten days of immersion in the presence of 5 ppb of iron in the autoclave (b). A corrosion layer of 5 µm containing iron, oxygen, silicon, aluminium and chromium is observed.	73

Figure 3.1: Scheme showing the deposits on the disc (gray color) that are quantified and converted to Build-Up Rates (B_R : radial BUR; B_S : surface BUR; B_I : inner orifice BUR) (McGrady et al., 2017).	77
Figure 3.2: Scheme of the recirculating stainless steel autoclave at the University of Manchester fitted with a flow cell (2) which could be activated by opening the flow cell valve (3) (McGrady et al., 2017).	80
Figure 3.3: Photos of the recirculating autoclave containing the flow cell (a) and feed tanks (b); Geometry of the flow cell inside the autoclave vessel (c).	81
Figure 3.4: Scheme of titanium discs used for studying the deposit build-up during test at the University of Manchester.	81
Figure 3.5: Secondary electron mode SEM pictures (left column) and 3D visualisations obtained by laser confocal microscopy measurements (right column) of front face of disc 1 (4 m/s (a)), disc 2 (8 m/s (b)) and disc 3 (18 m/s (c)) after electrokinetic tests. Yellow dash circles show the location where deposit formation starts onto the surface of discs 2 and 3.	85
Figure 3.6: Magnified secondary electron mode SEM images of the surface deposits on (left) disc 1 (4 m/s) and (right) disc 2 (8 m/s). Deposits containing iron and oxygen follow the flow direction.	86
Figure 3.7: Magnified secondary electron mode SEM images of the surface deposits of disc 3 (18 m/s). Deposits containing iron and oxygen seem to be less porous than that formed on discs 1 and 2. No preferred direction is observed for the deposit formation.	86
Figure 3.8: Magnified secondary electron mode SEM images of the inlet of disc 1 (4 m/s (a)), disc 2 (8 m/s (b)) and disc 3 (18 m/s (c)); EDS profile analysis of a line crossing the orifice of disc 3, indicating the formation of iron oxide on the edge of the orifice (d).	87
Figure 3.9: SEM images of the inner surface of disc 1 (4 m/s (a)) and disc 2 (8 m/s (b)). Negligible deposits are present onto the inner surface at the entrance region. For disc 1, hydrodynamically controlled deposits appear to be formed on the inner surface at about 150 μm from the orifice edge.	87
Figure 3.10: Secondary electron mode SEM image of disc 3 (a) showing the formation of deposits on the edge of orifice (radial BUR) and a general view of the inner surface near the orifice inlet; magnified visualisation of the inner surface of disc 3 (b), indicating the formation of ripples containing iron oxide.	88
Figure 3.11: Secondary electron mode SEM pictures (left column) and 3D visualisations obtained by laser confocal microscopy measurements (right column) of front face of disc 4 (a) and disc 5 (b) after electrokinetic tests. Red dash circle represents the initial orifice edge, overlapped by deposits for disc 4.	89
Figure 3.12: SEM image (secondary electron mode) of the outer deposit layer onto disc 4 in which deposits appear to follow the flow (a); SEM image of the intermediate deposit layer which is less porous than the outer layer (flow-perpendicular ripples containing iron and oxygen are observed) (b).	89
Figure 3.13: Observation of two important circular ripples containing iron and oxygen on the initial edge of the orifice of disc 4.	90
Figure 3.14: SEM image (secondary electron mode) of the inner deposit layer observed within the orifice of the disc 4 where faceted particles can be observed (a); SEM image of particles present in this layer (b), which contain iron, chromium and oxygen (size of these particles can reach 15 μm).	90
Figure 3.15: EDS mapping of a part of the disc 4 showing chromium and iron distribution throughout the orifice as well as the inner and intermediate deposit layers. Particles containing chromium are preferentially present within the orifice at the inlet.	91
Figure 3.16: SEM image (secondary electron mode) of the front surface of disc 5 showing the presence of iron oxide on the edge (a); SEM image of disc 5 (b), showing a depleted-deposit region within the orifice throat at the entrance. Deposits can be observed on the inner surface at about 100 μm from the orifice.	92

Figure 3.17: 2D CFD modelling streamlines of pure water flow crossing through the orifice of disc 1 (flow velocity of 4 m/s at the inner orifice). Modelling was performed by taking half of the flow cell (shown in Figure 3.3c) with a restriction radius of 0.15 mm and a pre-restriction radius of 3.35 mm.	95
Figure 3.18: 2D CFD modelling streamlines of pure water flow crossing through the orifice of disc 2 (left) and disc 3 (right).	95
Figure 3.19: Top view of CFD modelling streamlines of disc 1-3, showing that the flow converges towards the disc orifice on the front surface.	96
Figure 3.20: Magnitude of flow velocity at the inlet region of the disc 1 (4 m/s, top), disc 2 (8 m/s, middle) and disc 3 (18 m/s, bottom). 6 m/s corresponds to the magnitude of flow velocity at a certain distance from the orifice edge, respectively 0, 20 and 40 μm for the disc1, disc 2 and disc 3.	97
Figure 3.21: An example of the iron oxide deposits formed onto titanium test coupons after COLENTEC-2015 test, showing that the deposits are hydrodynamically affected by flow.	100
Figure 4.1: Schematic representation of the calculated contribution percentage of particle deposition by vena contracta (blue), flashing (red) and electrokinetics (green) to global deposit formation under nominal EDF conditions, with particle size equal to 100 nm (a), 1 μm (b) and 10 μm (c).	106
Figure 4.2: Schematic representation of the calculated contribution percentage of particle deposition by vena contracta (blue), flashing (red) and electrokinetics (green) to global deposit formation under nominal EDF conditions, with total iron concentration of 6 ppb (a), 30 ppb (b), 100 ppb (c), 1 ppm (d) and 3 ppm (e).	108
Figure 5.1: Schematic illustration of TSP clogging formation by particle deposition and precipitation phenomena.	111
Figure 5.2: Suggested formation processes of TSP clogging phenomenon.	112

List of Tables

Table 1.1: Main characteristics of tube bundles used in 51B-type steam generators (Girard, 2014). ..	11
Table 1.2: Chemical composition (in % _{wt}) of alloys usually used in PWR secondary circuit.	15
Table 1.3: Principal EDF Chemical specification of PWR secondary feedwater.	16
Table 1.4: Main physical properties of magnetite (Blaney, 2007; Fu, 2012).	24
Table 2.1: COLENTEC-2015 operating conditions.	54
Table 2.2: Chemical composition of the stainless steel test coupons used in COLENTEC tests (wt%).	54
Table 2.3: Chemical composition of the titanium test coupons used in COLENTEC tests (wt%).	54
Table 2.4: Chemical composition of the carbon steel boiler used in COLENTEC tests (wt%).	55
Table 2.5: Chemical composition (in at%) obtained by comparative EDS analyses at the different regions localized in Figure 2.12a. Percentages of each element are normalized to have a total of 100%. Relative uncertainties are estimated to be 1% for major elements (at% > 10%), and 5% for other elements. The numbers correspond to the numerated regions in the figure on the right.	60
Table 2.6: Chemical composition (in at%) deduced from EDS analyses of points a, b, c and d in Figure 2.16a. Percentages of each element are normalized to have a total of 100%. Relative uncertainties are estimated to be 0.5% for iron and oxygen, and 5% for other elements.	63
Table 2.7: Chemical composition (in at%) obtained by comparative EDS of the different regions defined in Figure 2.19. Percentages of each element are normalized to have a total of 100%. Relative uncertainties are estimated to be 0.5% for iron and oxygen, and 5% for other elements.	66
Table 2.8: Experimental conditions for tests in autoclaves.	72
Table 2.9: Average thicknesses of the corrosion layer on SS samples and SS coupons from the Ti-SS-Ti samples.	74
Table 3.1: General test conditions during electrokinetic tests. *: Conditioned by ammonia and morpholine.	82
Table 3.2: Flow velocity inside the hole of the disc, soluble dihydrogen concentration and duration of each test. Discs 4 and 5 underwent 4 and 3 steps, respectively, with dihydrogen injection or flow velocity change. Characterization was not performed after each step.	82
Table 3.3: Calculated radial BUR deduced from Eq. 3-1 and 3-2) and surface BUR deduced from Eq. 3-3 of deposits formed onto discs 1-5.	92
Table 3.4: Comparison of operating conditions used during COLENTEC-2015 campaign test, electrokinetic investigation for disc 3 and EDF feedback under nominal conditions. *: The flow velocity within TSP flow holes under EDF or COLENTEC two-phase flow conditions is estimated by mass flow rate, supposing that liquid phase velocity is equal to that of the vapour phase.	99
Table 4.1: Values of input parameters for quantification of particle deposition and flashing, under nominal EDF operating and COLENTEC-2015 conditions.	105

Table 4.2: Quantification of particle deposition, flashing and electrokinetics phenomena under nominal EDF operating conditions and COLENTEC-2015 operating conditions after 15 years (Particle size is equal to 0.1, 1 and 10 μm ; total iron concentration is equal to 30 ppb)..... 106

Table 4.3: Quantification of particle deposition, flashing and electrokinetics phenomena under nominal EDF operating conditions and COLENTEC-2015 operating conditions after 15 years (Particle size is equal to 1 μm ; total iron concentration is equal to magnetite solubility, 30 ppb, 100 ppb, 1 ppm and 3 ppm). 107

Nomenclature

Abbreviations

EDF: Electricité de France

CEA: Commissariat à l'Énergie Atomique et aux énergies alternatives

EPRI: Electric Power Research Institute

AECL: Atomic Energy Canada Limited

PWR: Pressurized Water Reactor

CVCS: Chemical and Volume Control System

NPP: Nuclear Power Plant

MWe: MegaWatt Electrical

TSP: Tube Support Plate

SG: Steam Generator

SEM: Scanning Electronic Microscope

TEM: Transmission Electronic Microscope

EDS: Energy Dispersive X-ray Spectroscopy

SE: Secondary Electron

BSE: Back-Scattered Electron

HR: High Resolution

FIB: Focused Ion Beam

ICP-MS: Inductively Coupled Plasma Mass Spectrometry

HP: High Pressure

MSR: Moisture Separator/Reheaters

AVT: All Volatile Treatment

SCC: Stress Corrosion Cracking

IGSCC: InterGranular Stress Corrosion Cracking

IGA: InterGranular Attack

FAC: Flow Accelerated Corrosion

SHE: Standard Hydrogen Electrode

WRL: Wide Range Level

SGOG: Steam Generator Owners' Group

HTCC: High Temperature Chemical Cleaning

ASCA: Advanced Scale Conditioning Agents

DMT: Deposit Minimization Treatment

PACCO: Preventive Acid Chemical Cleaning Operation

IHP: Inner Helmholtz Plane

OHP: Outer Helmholtz Plane

PZC: Point of Zero Charge

IEP: IsoElectric Point

ppb: Parts Per Billion ($\mu\text{g}/\text{kg}$)

ppm: Parts Per Million (mg/kg)

EDL: Electrical Double Layer

XRD: X-Ray Diffraction

GDOES: Glow Discharge Optical Emission

AFM: Atomic Force Microscopy

BUR: Build-Up Rate

SIMS: Secondary Ion Mass Spectrometry

Roman symbols

a = modelling coefficient

A = area (m^2)

g = standard gravity constant (9.8 m/s^2)

x = steam quality

C_p = particle concentration (kg/kg)

C_l = mass fraction of liquid phase

C_g = mass fraction of vapour phase

C_b = ion concentration in the bulk (kg/m^3)

C_i = ion concentration at the solid-liquid interface (kg/m^3)

C_s = saturation concentration (kg/m^3)

E = activation energy (J/mol)

E_r = re-entrainment rate (s^{-1})

H_{lg} = heat of vaporization (J/kg)

ΔH_l = enthalpy variation of liquid phase (J/kg)

S_s = solubility of soluble species (kg/kg)

$S_{v/l}$ = slip ratio

T_l = fluid temperature (K)

T_s = surface temperature (K)

Sc = Schmidt number of particles

Re_l = Reynolds number of liquid phase

D_p = diffusion coefficient of particles (m^2/s)

U = friction velocity (m/s)

U_l = average velocity of liquid phase (m/s)

U_z = vertical mixture velocity (m/s)

R = universal gas constant (8.314 J/mole/K)

N = function of the nucleation sites provided by particles

M_f = mass of deposit at time t (kg)

M_{fg} = mass of deposit at the start of crystal growth (kg)

K_0 = constant (m/s)

K_d = particle deposition rate (m/s)

$K_d(1\phi)$ = particle deposition rate for one-phase flow (m/s)

$K_d(2\phi)$ = particle deposition rate for two-phase flow (m/s)

K_t = particle transport rate (m/s)

K_a = particle attachment rate (m/s)

K_b = deposition rate due to boiling process (m/s)

K_{diff} = diffusion rate (m/s)

K_s = sedimentation rate (m/s)

K_i = inertial rate (m/s)

K_{th} = thermophoresis rate (m/s)

$K_{t,s}$ = soluble iron transport rate (m/s)

$K_{b,s}$ = soluble iron precipitation rate (m/s)

$K_{v,p}$ = particle deposition rate in "vena contracta" mechanism (m/s)

K_r = reaction rate constant ($\text{m}^4/\text{kg s}$, if $n = 2$)

W = mass flow (kg/s)

Q = volumetric flow (m^3/s)

m_d = deposit mass (kg/m^2)

m' = deposit mass by crystallization fouling (kg/m^2)

t = time (s)

n = order of reaction

n' = exponent

k_b = Boltzmann constant ($1.38 \times 10^{-23} \text{ J.K}^{-1}$)

k_v = variable blockage rate (m^{-1})

t_p^+ = relaxation time

d_p = particle diameter (m)

L = half the distance between two consecutive SG tubes (m)

R = equivalent radius of a TSP flow hole (m)

S = section of a TSP flow hole (m^2)

e_d = deposit thickness (m)

B_R = the radial BUR ($\mu\text{m/hr}$)

B_S = the surface BUR ($\mu\text{m}^3/\text{hr}$)

B_T = the inner orifice BUR ($\mu\text{m/hr}$ or $\mu\text{m}^3/\text{hr}$)

Greek letters

α = void fraction

β = mass transfer coefficient (m/s)

$\rho_{p/l}$ = particle/fluid density (kg/m^3)

ρ_m = average density of liquid/gas mixture (kg/m^3)

ρ_d = deposit density (kg/m^3)

μ_l = dynamic viscosity of fluid (kg/m/s)

ν_l = kinematic viscosity of fluid (m^2/s)

ϕ_w = heat flux (W/m^2)

ϕ_l = mass flux per unit of surface of liquid (kg/s/m^2)

ϕ_s = mass flux per unit of surface of soluble specie precipitation (kg/s/m^2)

λ = dimensionless parameter used for flashing modelling, depending on TSP clogging rate

λ_p = particle thermal conductivity (W/m/K)

λ_f = fluid thermal conductivity (W/m/K)

τ_c = TSP clogging rate (dimensionless)

Introduction

Since the first commercial nuclear power station operation in the 1950s, over 440 commercial nuclear power reactors provide electricity in 31 countries nowadays, with over 390,000 MWe of total capacity. They provide over 11% of the world's electricity as continuous, reliable base-load power, without carbon dioxide emissions ("World Energy Outlook 2016", 2016). Pressurized Water Reactors (PWR) are majorly used in the Nuclear Power Plants (NPP) worldwide: 65% according to the number and 70% according to the output. The steam generator (SG) is a crucial component of PWR, where the heat exchange between the primary and secondary circuit occurs. The reactor production efficiency relies thus largely on the proper functioning of SG. SG is equally one of the PWR three safety barriers between the radioactive and non-radioactive sides of the NPP. In particular the SG tube's rupture, inducing primary-to-secondary leaks, may lead to dramatic consequences on NPP functioning and workers' safety.

The corrosion of secondary upstream SG materials leads to the formation of soluble and particle species, which are then conveyed into SG, inducing the formation of deposits onto the inner surfaces of SG. These deposits are composed of metallic oxides, majorly of magnetite. Following the deposit nature and localization, various degradation phenomena caused by secondary-side corrosion products are observed since the beginning of PWR exploitations:

- SG tube fouling, referring to the deposit formation alongside the extern surfaces of SG tubes, decreases the heat transfer efficiency between the primary and secondary circuit.
- SG tube sludge, referring to the hard deposit formation at the bottom of SG between SG tubes and tube sheet, induces tube denting and decreases SG lifetime.
- Tube Support Plate (TSP) clogging or blockage, referring to the partial or total secondary flow hole obstruction between SG tubes and TSP by deposits.

The present work focuses on TSP clogging phenomenon, which is relatively new in France and has been identified as the major cause of the three primary-to-secondary leaks observed between 2004 and 2006 in the EDF Cruas NPP. This phenomenon decreases the secondary flow section, and then induces high velocity zones and transverse velocities in the secondary flow, which can imply flow induced vibrations, SG tube cracks and leaks in the worse cases. Chemical cleaning is currently the main effective cure against TSP clogging. Nevertheless, it remains extremely costly and difficult to perform. Therefore, it appears of great interest to investigate alternative solutions to avoid TSP clogging. For this aim, it is necessary to understand firstly the phenomena responsible for TSP clogging. In this context, an extensive research project "COLMATage des générateurs de vapeur" was engaged in 2008 by EDF and CEA.

The present work is a part of this research project with two main objectives:

- Better understand TSP clogging formation by characterizing experimentally reformed deposits under close representative conditions;
- Prioritize numerically and experimentally the supposed implicated mechanisms in TSP clogging formation.

For this purpose, the mechanistic investigation of TSP clogging formation has been undertaken with two general approaches:

- Experimentally

- Representative investigation of TSP clogging formation under similar PWR SG secondary conditions with COLENTEC (*COLmatage des ENTretroises – Etude Cinétique*) two-phase flow test loop. This geometrically representative test loop has been co-financed by CEA and EDF, and designed and constructed to reproduce the

most encouraging conditions for representative deposit formation. This investigation has provided reformed deposits for characterization and quantitative data of global TSP clogging formation in laboratory scale.

- Simulated investigation in monophasic static solutions by autoclaves. This study provided majorly complementary supports for the interpretation of COLENTEC test characterization results.

- Specific investigation of electrokinetically induced deposits by microfluidic flow cell in recirculating autoclave system. This investigation was performed in collaboration with *the University of Manchester (UK)* under comparable COLENTEC-2015 conditions, in order to better understand the electrokinetic behaviours and suggest its contribution to the global deposit formation.

- Numerically

Calculation of the contribution percentage of each supposed formation mechanism with identified numerical models in the literature. This study allowed predicting the predominant role of electrokinetics in TSP clogging formation.

These approaches are presented in the present work throughout four chapters:

- Chapter 1 introduces the state of the art of TSP clogging phenomenon through NPP feedbacks and previous experimental or numerical investigations. Supposed implicated mechanisms will be studied, with associated phenomenological and numerical models reported in the literature.
- Chapter 2 presents the representative deposit formation tests by means of the COLENTEC facility. Such studies provide the first experimental data of the deposit formation. Microscopic characterizations of the formed deposit by COLENTEC and complementary autoclave tests bring first elements of phenomenon understanding.
- Chapter 3 presents the specific experimental investigation of electrokinetics performed in *the University of Manchester*. This preparative study provides the first experimental data of electrokinetically induced deposit under comparable PWR secondary conditions.
- Chapter 4 presents the performed numerical calculations, estimating the contribution percentage of each supposed implicated mechanism.

Chapter 1 State of the art

1.1 Introduction

PWRs were designed in the Westinghouse Bettis Atomic Power Laboratory and are enormously complicated thermodynamic heat engines. Nuclear fission of uranium-235 fuel produces fast neutrons, which are moderated into thermal neutrons by the coolant water. Thermal neutrons are responsible for maintaining the criticality of the nuclear reaction, and for heating coolant water, that is held under high pressure to maintain a liquid state. The heat in the primary coolant (330 °C and 155 bars) is transferred to a secondary coolant loop where steam is raised to drive a conventional steam turbine. Steam generators (SG) play a crucial role as a heat exchanger from the primary to the secondary flow and as one of the three safety barriers of NPP. The steam leaving the turbine is converted back into water in the condenser. For this cooling process in the condenser, cooling water from an external source is used (*e.g.*, sea, river, lake) in a ternary circuit.

Ageing effects, especially material degradation by corrosion, have been experienced worldwide since the start of exploitation of PWRs and may consist of the major challenge of PWRs' safety and performance. TSP clogging, a relatively new PWR SG degradation phenomenon (Yang et al., 2017a), can induce severe operation consequences and its formation remains nowadays poorly understood.

This chapter aims at identifying the state of the art of TSP clogging phenomenon from a phenomenological and numerical point of view. It describes the PWR secondary circuit, particularly the steam generators, and discusses the corrosion phenomena occurring in the PWR secondary circuit such as TSP clogging of SG. A particular attention will be paid to give a complete overview of TSP clogging formation mechanisms. This review will support the next chapters focusing on experimental and numerical investigations of TSP clogging phenomenon.

1.2 PWR secondary circuit

After describing PWR secondary circuit, PWR recirculating steam generators (SG) and the different materials used, this section will be devoted to introduce the water chemistry management in PWR in order to better understand the different parameters involved in corrosion and TSP clogging phenomena.

1.2.1 General description

The two major secondary systems of a pressurized water reactor (PWR) are the main steam system and the condensate/feedwater system. The steam goes from the outlet of the steam generator into the high pressure (HP) main turbine firstly in order to resist to the steam high pressure (Figure 1.1#1). After passing through the high-

pressure turbine, the steam is piped to the moisture separator/reheaters (MSR) (Figure 1.1#2). In the MSRs, the steam is dried by means of moisture separators and reheated to avoid turbine blade corrosion. The stream moves then from the MSR to the low-pressure turbines (Figure 1.1#3) to generate electricity. After passing through the low-pressure turbines, the steam goes to the main condenser (Figure 1.1#4). The steam is condensed into water by the flow of circulating water through the condenser tubes. The condensate then passes through some low-pressure feedwater heaters (Figure 1.1#5). The temperature of the condensate is then increased from 40 to 75 °C in the heaters. The condensate flow then enters the suction of the main feedwater pumps (Figure 1.1#6), which permits to increase the water pressure from 11 to 65 bars so that the condensate can be sent into the steam generator. The feedwater is then heated by means of a set of high-pressure heaters (Figure 1.1#7), which are heated by the extraction steam from the high-pressure turbine (heating the feedwater helps to increase the efficiency of the plant).

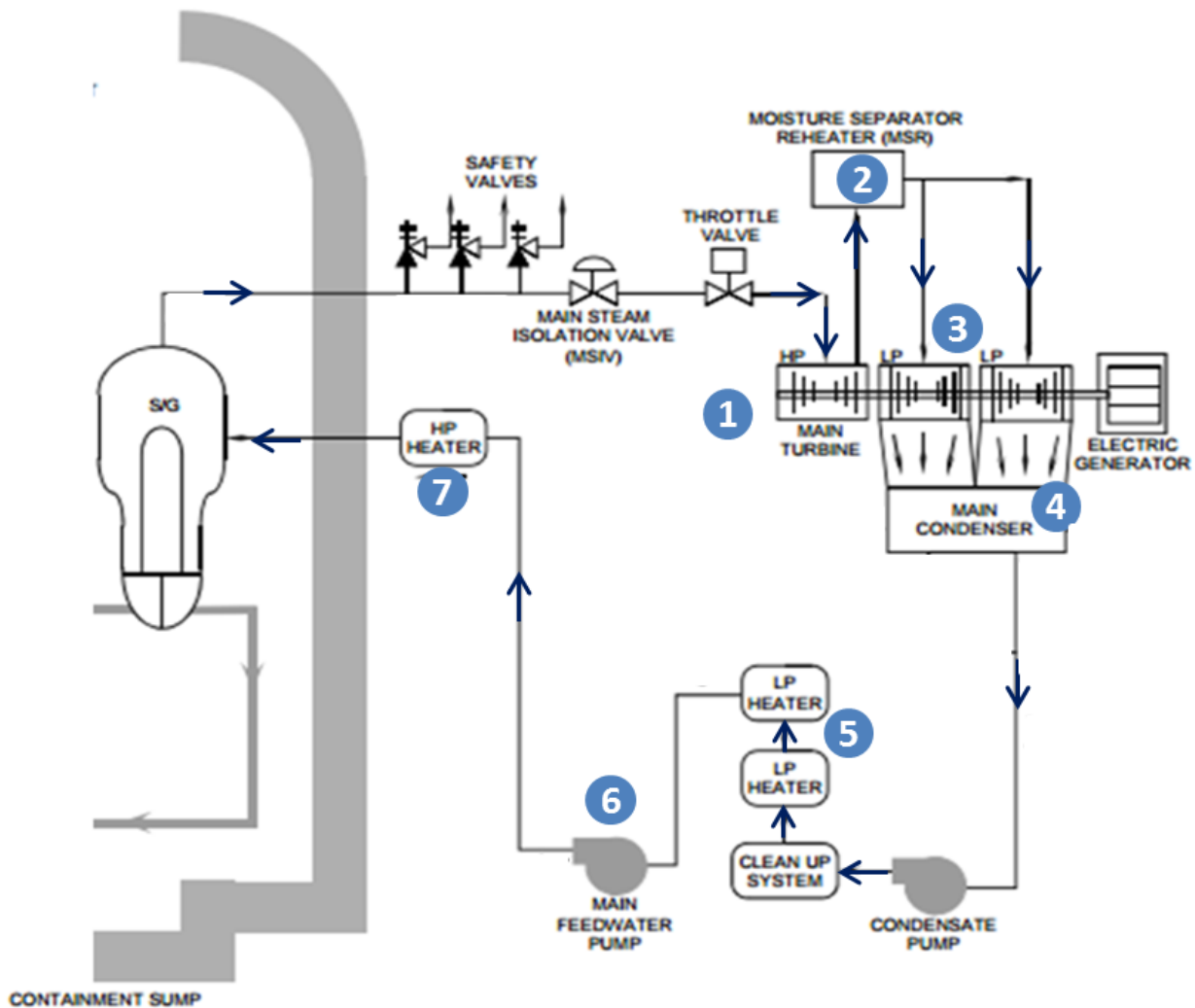


Figure 1.1: Scheme of PWR secondary circuit (*Pressurized Water Reactor Systems*, n.d.).

1.2.2 Recirculating steam generator

A recirculating steam generator (SG) is about 20 meters high, its diameter ranges from 3 to 5 meters and it weighs between 300 and 430 tonnes (Delaunay, 2010). In SG, the primary system coolant flows through several

thousands of U-tubes (Figure 1.2). Primary coolant enters the steam generator at 315-330 °C on the hot-leg side and leaves at about 288 °C on the cold-leg side. The secondary system flow (feedwater) is fed through a feedwater distribution ring into the downcomer, where it mixes with recirculating water draining from the moisture separators. This downcomer water, in contact with hot primary tubes, flows to the bottom of the steam generator, and is then transferred into steam up through the tube bundle. About 25% of the secondary coolant is converted into steam on each pass through the generator while the other 75% recirculates (Bonavigo and Salve, 2011).

The different types of SG are mainly characterized by two parameters: the total outer exchange area represented by the tube bundle and the external diameter of SG tubes (Prusek, 2012). For example, a 51B type SG (Figure 1.2, left) has a total outer exchange area of 4700 m² and a tube external diameter of 22.22 mm (Girard, 2014). Complete characteristics of the tube bundle of 51B type steam generators are listed in Table 1.1. As the tubes are long and thin, 8 circular plates called Tube Support Plates (TSP) are used for their mechanical maintain (Figure 1.2, left) in 51B type SG. The tubes fit in the circular holes drilled in the TSP. These holes are surrounded by additional quatrefoil holes to let the secondary steam-liquid mixture flow through (Figure 1.2, bottom right). After several decades of operation, deposit formation is observed in the quatrefoil holes between SG tubes and TSP (See TSP clogging phenomenon in Figure 1.2, top right).

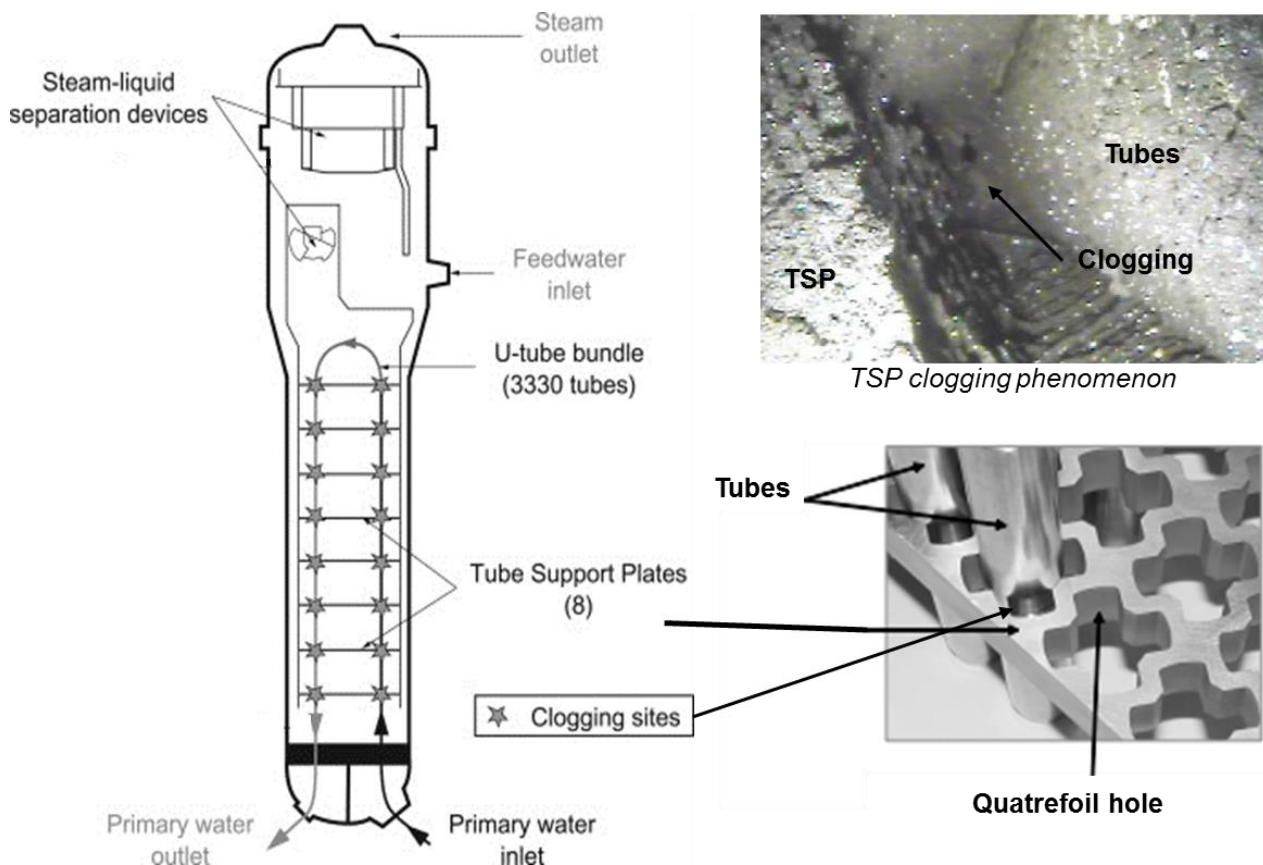


Figure 1.2: Scheme of 51B-type PWR recirculating steam generator (Bodineau and Sollier, 2013; Girard et al., 2013). TSP clogging phenomenon is observed after several decades of operation and is represented at the top right.

Table 1.1: Main characteristics of tube bundles used in 51B-type steam generators (Girard, 2014).

Characteristics	Value
Number of tubes	3330
Number of Tube Support Plates (TSP)	8
Tube external diameters (mm)	22.22
Tube thickness (mm)	1.27
Outer exchange area (m ²)	4700
Inter-tube distance (mm)	32.54
Total mass of tube bundle (t)	51.5

1.2.3 Thermohydraulics in PWR steam generator

TSP clogging phenomena are highly dependent on the thermohydraulics. A general knowledge of PWR SG thermohydraulics is necessary for the further discussions in the present work. In this section, basic notions of two-phase flow parameters, as void fraction, are introduced and defined and different two-flow patterns are presented. Most TSP clogging phenomenon has been observed on the 8th TSP in the EDF NPPs. After describing fundamentals of two-phase flow typical values of major thermohydraulic parameter on the 8th TSP of 51B type SG will be identified in section 1.2.3.2 since thermohydraulics will govern TSP clogging phenomena.

1.2.3.1 Two-phase flow fundamentals

Basic theory and definitions are introduced in this section. Given that there are many two-phase flow models in the literature and the objectives of this section is not to give a thorough description of two-phase flow models, only few of them are presented hereafter and the reader can find more information about these models elsewhere in the literature (Cong et al., 2013, 2015; Rummens, 1999; Vergnault et al., 2008; Zohuri and Fathi, 2015).

1.2.3.1.1 Two-phase flow system basic notions

The primary parameters used in two-phase flow modelling are (Royer, 2015):

- Thermal: thermal power, temperature, heat flux, *etc.*
- Hydraulic: pressure, mass flow rate, fluid temperature, pressure drop, *etc.*
- Geometric: flow and heated areas, hydraulic and heated equivalent diameters, *etc.*

Along with these primary parameters, in two-phase flow analysis, the following calculated parameters are commonly used:

- Mass flux
- Dynamic mass quality
- Void fraction

In addition, two-phase flow calculations require information about fluid properties such as density, viscosity, enthalpy, thermal conductivity, and heat capacity, which depends on the above-mentioned primary fluid parameters. Major basic two-phase flow notions will be briefly defined and presented as following:

Void fraction α (dimensionless) is defined as the volumetric fraction of vapour phase or the cross-sectional area occupied by vapour phase (A_v) to the total flow area of a pipe (A) in the limit case of a “thin” volume (Royer, 2015), as expressed in Eq. 1-1. The opposite of void fraction is the liquid fraction.

$$\alpha = \frac{A_v}{A}, \quad (1 - \alpha) = \frac{A_l}{A} \quad 1-1$$

where A_l represents the cross-sectional area occupied by liquid phase.

Dynamic mass quality x or steam quality (dimensionless) is defined as the ratio of vapour mass flow W_v (kg/s) to total mass flow W (Eq. 1-2). The opposite is the liquid quality.

$$x = \frac{W_v}{W}, \quad (1 - x) = \frac{W_l}{W} \quad 1-2$$

where W_l represents the liquid mass flow (kg/s).

Mass flux φ is the mass flow rate per unit flow area ($W_{v/l}/A$) (kg/s/m²). Vapour and liquid phase fluxes are defined using steam quality, as in Eq. 1-3.

$$\varphi_v = \varphi x, \quad \varphi_l = \varphi(1 - x) \quad 1-3$$

The vapour phase velocity v_v and the liquid phase velocity v_l (m/s) can be expressed in Eq. 1-4 and Eq. 1-5 , using the volumetric flow Q (m³/s).

$$v_v = \frac{Q_v}{A_v} = \frac{W_v}{\rho_v A_v} \quad 1-4$$

$$v_l = \frac{Q_l}{A_l} = \frac{W_l}{\rho_l A_l} \quad 1-5$$

Where ρ_v and ρ_l denote the density of vapour and liquid, respectively.

Using the previous relationships, the ratio between the vapour and liquid velocities in a two-phase flow system, called slip ratio $S_{v/l}$ (dimensionless), can be expressed as:

$$S_{v/l} = \left(\frac{x}{1-x}\right) \left(\frac{\rho_l}{\rho_v}\right) \left(\frac{1-\alpha}{\alpha}\right) \quad 1-6$$

The vapour in a moving two-phase flow system trends to move at a higher velocity than the liquid because of its buoyancy, density and different resistance characteristics. Experimental data or theoretical correlations for $S_{v/l}$ covering all possible operating and design variables do not exist. Experimental values of $S_{v/l}$ under conditions defined for a particular design are difficult to obtain experimentally. Such procedures are usually expensive and time-consuming. In calculations and modelling, the usual procedure is to neglect the difference between vapour phase and liquid phase velocities or to assume a constant value of $S_{v/l}$ throughout the fuel channel.

Other parameters, like static quality (vapour mass fraction C_g) or thermodynamic quality of the two phases are less used because they do not bring relevant information about the flows (velocities). The associated definitions can be found in (Royer, 2015).

1.2.3.1.2 Two-phase flow patterns

Multiphase flow is classified according to the internal phase distributions or "flow patterns" or "regimes". For instance, in the case of a two-phase mixture of a gas or vapour and a liquid flowing together in a channel, different internal flow geometries or structures can occur depending on the size or orientation of the flow channel, the magnitudes of the gas and liquid flow parameters, the relative magnitudes of these flow parameters, and on the fluid properties of the two phases. In particular, two-phase flow patterns are strongly influenced by phase mass flow rates or velocities (K. Popov, 2015). The sequence of flow patterns generally encountered in vertical two-phase flow as a function of the steam quality x is shown in Figure 1.3.

The bubbly pattern means that the vapour phase is distributed in discrete bubbles within a liquid continuum. When the concentration of bubbles becomes higher, bubble coalescence occurs and progressively, the bubble diameter approaches that of the tube. The slug flow (also named plug flow) regime is entered. As the vapour flow is increased with steam quality, the velocity of these bubbles increases and ultimately, a breakdown of these bubbles occurs leading to an unstable regime. In this regime, there is an oscillatory motion of the liquid upwards and downwards in the tube (churn flow). Annular flow represents the pattern where the liquid flows on the wall of the tube as a film and the gas phase flows in the centre. Finally, in the disperse droplet pattern, the liquid phase loses contact with the tube and forms concentrated individual liquid droplets more or less homogeneously in the flow.

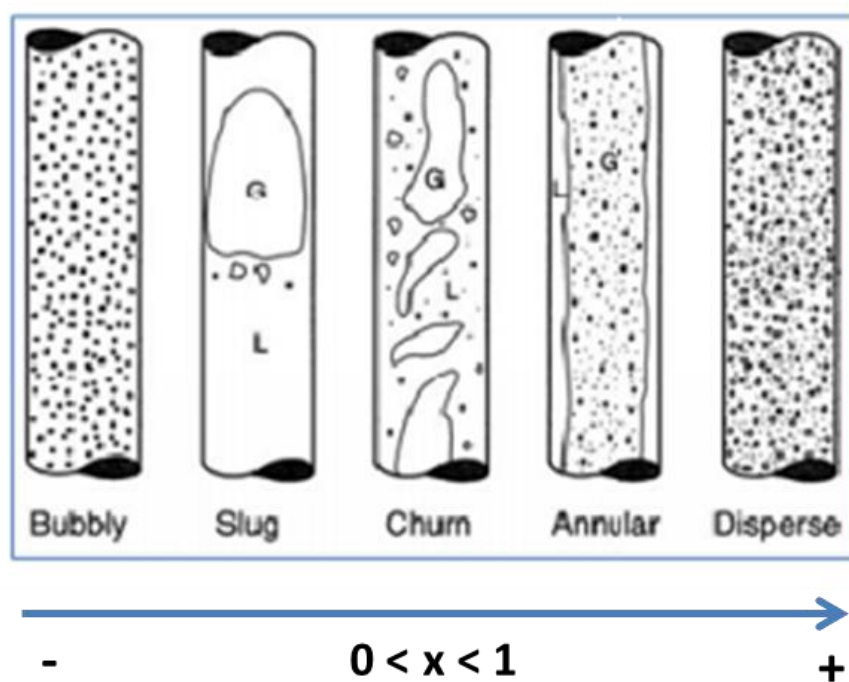


Figure 1.3: Two-phase flow patterns' sequence as a function of steam quality x (K. Popov, 2015). "G" and "L" represents the vapour phase and the liquid phase, respectively.

Two-phase flow parameters change significantly from one flow pattern to another one. In particular, the interfacial area between the two phases has a significant impact on the exchange of mass, momentum, and heat between phases. Various two-phase flow parameters are affected differently by flow patterns, and hence various correlations and models are needed to capture phenomena for each flow pattern. This implies the need for well-defined and predictable flow patterns in two-phase flow modelling. Many pattern maps are reported in the literature from experiments or calculations (Cheng et al., 2008). They give a good description of the two-phase flow pattern as a function of flow properties such as steam quality, mass flux, *etc.* However, most of these pattern maps are limited to relatively low temperature systems (from 20 to 80 °C) and they are not relevant for describing water/vapour flow systems like those reported in PWR SG. More experiments are then required under the same thermohydraulic conditions as those reported in SG. Nevertheless, plot of such map patterns is

particularly challenging because it needs to develop new sensors, which can operate at high temperature and pressure (Hogsett and Ishii, 1997). Efforts are currently made at CEA Cadarache (France) for the development of such two-phase flow measuring sensors (Dupré et al., 2016).

1.2.3.2 Thermohydraulics of 51B type steam generators

Numeric simulations based on porous media models and experimental single-phase and steam-water two-phase flow investigations were performed by several groups (Cong et al., 2013, 2015; Tian et al., 2016; Zhang et al., 2017) to investigate the thermohydraulic characteristics of PWR steam generators. Heat transfer from primary to secondary side, pressure drop for a vertical two-phase flow across a horizontal rod bundle and the effects of power level on thermohydraulic characteristics were discussed. However, only few data are available in the literature about basic parameters in a specific localization in SG like at the 8th TSP of 51B type SG (void fraction, secondary temperature, etc.).

An EDF modelling tool (THYC) was used for investigating thermohydraulic parameters at the 8th TSP of 51B type SG (Schindler, 2010, 2016). Schindler's works summarized the main results of this study and showed the dynamic steam quality varies from about 0.22 to 0.38 on the hot leg side of the 8th TSP. The maximal steam quality is located at the centre of the tube bundle while a steam quality of 0.30 is observed in the intermediate region between the centre and the wall (see definition of the steam quality x in Eq. 1-2). The void fraction (α , Eq. 1-1) reaches 0.85 on the hot leg of 8th TSP with a relatively homogeneous distribution. The pressure is equal to 61.5 bars in the whole 8th TSP section with a temperature of 277.2 °C in the secondary flow. A mean vertical velocity of the two-phase flow of about 3 m/s has been calculated at the intermediate region of the hot leg of the 8th TSP. From these calculated thermohydraulic parameters, the two-phase flow located in the 8th TSP is often supposed to have a disperse droplet regime because of the high void fraction and dynamic steam quality. However, neither experimental nor theoretical works have been performed to confirm such an expectation because of the difficulties mentioned previously.

Most TSP clogging phenomenon is observed on the 8th TSP of PWR 51B type steam generator's secondary side. A general description of PWR secondary circuit and steam generators has been done. Important thermohydraulic notions have been introduced and associated parameters have been identified specifically for the 8th TSP region in 51 B type SG in order to feed further discussion in the present work. Thereafter, the major source term of TSP clogging phenomenon will be identified, by firstly introducing the different materials used in the secondary circuit and the associated corrosion phenomena under the specific PWR secondary water chemistry. Magnetite is the stable form of iron species under PWR SG conditions and is the main composition of TSP clogging. Its structural and physio-chemical properties will be provided.

1.2.4 Materials used in the secondary circuit

In the secondary circuit, the fluid circulation piping is made of carbon steel. SG tube sheet, turbine rotors, high-pressure heater, condensate and feedwater piping are usually made of carbon steel or low alloy steels (Feron, 2012). The steam generator tubes are made of nickel-based alloys: alloys 600 MA (MillAnnealed: thermal treatment at 980 °C for 15 minutes), alloys 600 TT (Thermally Treated at 700 °C for 16 hours) or alloys 690 TT for the most recent steam generators (Le Calvar and De Curières, 2012). The SG Tube Support Plates (TSP) are nowadays made of stainless steel with about 13%_{wt} of chromium (Delaunay, 2010). Condenser tubes are

made of stainless steels, or copper alloys or titanium-based alloys. Chemical compositions (%_{wt}) of alloys usually used in PWR secondary circuit are gathered in Table 1.2.

Table 1.2: Chemical composition (in %_{wt}) of alloys usually used in PWR secondary circuit.

Type	C	Cr	Fe	Mn	Ni	Si	other
Stainless steel 13%_{wt} Cr	<0.12	12-14	balance	<1		<1	P,S<0.025 and Co<0.2
Carbon steel (A285 Gr C)	0.28		balance	0.9			P, S = 0.035
Alloys 600	<0.05	14-17	6-10	<1	>72	<0.5	Co<0.1
Alloys 690	<0.05	27-31	7-11	<0.5	>58	<0.5	Co<0.035
Copper alloys	<0.06		0.4-0.7	0.5-1.5	29-32		Cu balance/Cu 70 – Zn 30
Titanium alloys	<0.1		0.3	2			Ti balance – O<0.25

1.2.5 PWR secondary flow chemistry

Slightly alkaline solution in the secondary circuit is used to limit corrosion phenomena in the PWR secondary circuit (Nordmann and Fiquet, 1996). For this goal, most of the nuclear operators use volatile alkaline reagent (AVT, All Volatile Treatments). Two main reagents are used: morpholine (C₄H₉NO) and ammonia (NH₄OH). Other reagents are less frequently used like ethanolamine (C₂H₇NO). Hydrazine (N₂H₄) is used for reducing dissolved oxygen concentration for Stress Corrosion Cracking (SCC) prevention.

Ammonia was largely used thanks to its easy implementation, low cost and its relatively low decomposition. However, its use is limited in the presence of copper alloys in secondary circuit materials because ammonia corrosion leads to the formation copper ions that form stable copper-ammonia complexes (Cu(NO₃)₆²⁺) when pH is higher than 9.4 at 25 °C (Yang et al., 2017a), which participate actively in the corrosion of copper material and increase the risk of copper reprecipitation elsewhere in the secondary circuit. Therefore, pH_{25 °C} is fixed at between 9.1 and 9.3 in the presence of copper alloys in the secondary circuit. The use of hydrazine in the presence of copper alloys is also limited due to its decomposition inducing the formation of ammonia. Its concentration ranges generally from 5 to 10 µg/kg (ppb) (Delaunay, 2010; Nordmann and Fiquet, 1996; Suat and Francis, n.d.). In the absence of copper alloys, pH_{25 °C} is fixed by ammonia or morpholine around 9.6 to 9.7 to prevent corrosion.

In certain cases, hydrazine concentration can be increased up to 50-100 µg/kg in the absence of copper, especially for enhancing SCC prevention. Morpholine allows providing a homogeneous protection all over the steam-water system since its distribution coefficient (concentration in vapour/concentration in liquid phase) is close to 1. However, more and more operators work on the substitution of morpholine by another reactive because the high concentration of morpholine in secondary circuit and its low thermal stability increase the risk of formation of organic compounds by chemical decomposition such as ethenol and ethenamine (Altarawneh and Dlugogorski, 2012). Ethanolamine (ETA) is a good candidate to replace morpholine. This reactive is for instance largely used in US because it can be used at lower molar concentration than morpholine and thermal decomposition is limited (Suat and Francis, n.d.).

Most chemical elements remain in the liquid phase as their distribution coefficients are generally around 10⁻⁴. In order to limit the corrosion phenomena associated with the presence of these pollutants in the liquid phase, periodical purges of secondary water are performed. A purge rate of 1% of the feedwater flow is generally used in France (Suat and Francis, n.d.), which leads to an estimated super-concentration coefficient in SG water of 100 compared to the feedwater.

In restricted zones of SG as in clogged TSP flow holes, primary tubes' cooling is less efficient due to the reduced secondary water flow, which may induce local overheating, leading to an increase of pollutant concentrations. The super-concentration coefficient in these regions can reach as high as 10^6 compared to SG water (Nordmann and Fiquet, 1996). The current pollutant concentration is maintained below $0.01 \mu\text{g/kg}$ in the feedwater. Therefore, the concentration in the SG water can then be estimated to be around $1 \mu\text{g/kg}$ (1 ppb) with a super-concentration coefficient of 100 and the pollutant concentration can reach between 1 mg/kg (1 ppm) and 1 g/kg .

The total iron concentration in the feedwater is measured to be around 30 ppb by EDF (De Bouvier, 2015a). No data is available in the literature for estimating iron concentration in SG water or SG restricted regions by taking into account the super-concentration phenomenon in PWR SG.

The French EDF chemical specification of PWR secondary feedwater is summarized in Table 1.3.

Table 1.3: Principal EDF Chemical specification of PWR secondary feedwater.

Parameters	Value	
$\text{pH}_{25^\circ\text{C}}$	9.1 to 9.3 with copper alloys	9.6 to 9.7 without copper alloys
Hydrazine concentration (ppb)	5 to 10 with copper alloys	50 to 100 without copper alloys
Oxygen concentration (ppb)	< 3	
Redox potential (V/SHE)	-0.4	
Total iron concentration (ppb)	30	
Impurities (sodium, chlorine...) concentration(ppb)	< 1	

1.2.6 Corrosion phenomena in PWR secondary circuit

The PWR secondary water chemistry management, previously presented, aims at protecting the whole secondary circuit towards corrosion phenomena. Flow accelerated corrosion (FAC) of components in carbon steel is found to be the major term source of TSP clogging formation. Effects of different parameters, as material composition and flow thermohydraulics, will be discussed based on previous studies available in the literature. Stress corrosion cracking (SCC) majorly affects SG tubes in alloy 600 and will be briefly presented.

SCC will be firstly introduced, affecting majorly SG tube materials. FAC is believed to be the major source of TSP clogging phenomenon. Effects of major parameters, as pH and oxygen concentration, will be carefully discussed in paragraph 1.2.6.2.

1.2.6.1 Stress corrosion cracking (SCC)

SCC is responsible for material cracking under both environment and mechanical stresses. The propagation rate of SCC ranges generally from 10^{-5} to $1 \mu\text{m/s}$ and increases with stress (Arioka et al., 2006).

Steam generator tubes in the secondary circuit constituted of Alloy 600 MA suffered from SCC. Such SCC induced intergranular stress corrosion cracking (IGSCC) and intergranular attack (IGA). A generic designation for these secondary side degradations is IGA/IGSCC because they are often observed together.

SCC of Alloy 600 MA has been carefully discussed from a mechanistic point of view by Delaunay (Delaunay, 2010). A double-layer deposit composed of a compact inner layer enriched in chromium and a porous outer layer containing nickel oxides was observed onto Alloy 600 surface undergoing SCC.

IGA/IGSCC is mostly found in restricted regions as between the tubes and the TSP. In these locations, the flow of secondary fluid is restricted, which may be further impeded by the presence of corrosion product deposits, like TSP clogging, inducing even more restricted geometries. The restricted flow conditions enable a local super-concentration of any impurities, as previously mentioned in paragraph 1.2.5. Severe chemical conditions can thus be obtained, which are capable to induce IGA/IGSCC of Alloy 600 MA tubes. The main detrimental polluting elements are sodium, sulfur, copper and lead (De Bouvier, 2015b; Feron, 2015).

Alloy 600 TT, Alloy 690 TT and stainless steel suffer much less from IGA/IGSCC than Alloy 600 MA. The older carbon steel TSPs with drilled holes have been more subject to IGA/IGSCC since they undergo more easily concentrated crevice environment than those with current stainless steel quatrefoil tube holes.

1.2.6.2 General corrosion and Flow accelerated corrosion (FAC)

According to the International Standard ISO 8044, general corrosion of metallic materials is defined as a “general proceeding at almost the same rate over the whole considered surface” (Féron and Richet, 2010). In an aqueous environment, such as water-cooled reactors like PWR, metallic materials corrosion is of electrochemical nature (Feron, 2015), with the metal oxidation as anodic reaction and the reduction of dissolved oxygen or water as cathodic reaction. General corrosion is characterized by these basic electrochemical reactions that take place uniformly over the whole considered surface. If the corrosion products are soluble, general corrosion is evidenced by a decrease in metal mass or thickness over time; if the corrosion products are not soluble, the corrosion is evidenced by the formation of a uniform layer of corrosion products which may be more or less protective against further corrosion. Iron contained in carbon steel is oxidized into magnetite form under typical PWR SG conditions, predicted by various authors using Pourbaix diagrams (Chexal et al., 1998; Chivot, 2004; Delaunay, 2010; Mansour, 2009; Pourbaix, 1963). Figure 1.4 shows that the Pourbaix diagram of iron predicts magnetite as the stable form of iron in deionized and degassed reducing water ($E_h = -0.4$ V vs. SHE) at 200 °C and $pH_{200\text{ °C}} > 6$ ($pH_{25\text{ °C}} > 9$).

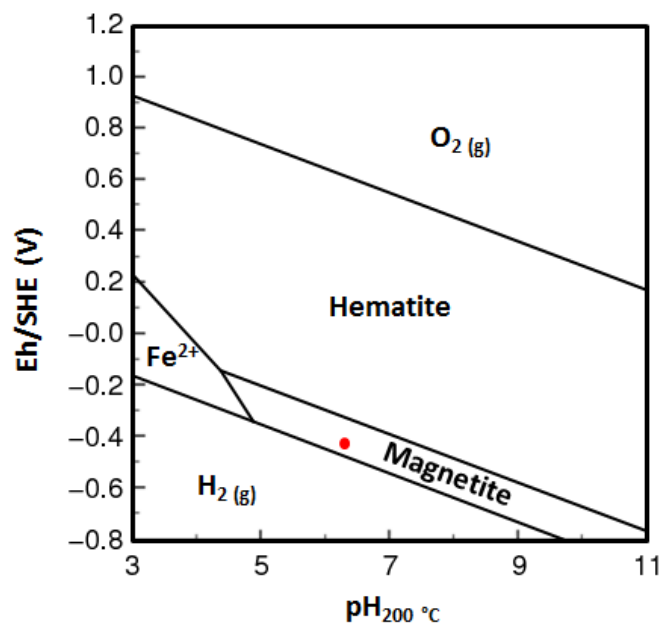
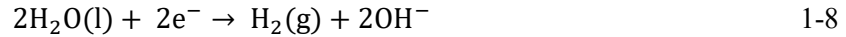


Figure 1.4: Pourbaix diagram of iron calculated with PHREEPLOT, using the Lawrence Livermore National Laboratory (llnl) database (“llnl.dat”, n.d.). Temperature = 200 °C corresponding to the temperature of the secondary circuit before entering into the SG; $pH_{25\text{ °C}} > 9$ corresponds to $pH_{200\text{ °C}} > 6$ (Yang et al., 2017a); Potential E_h in Volt given vs. the Standard Hydrogen Electrode (SHE). Red point indicates that the stable form of iron is magnetite under the above-mentioned conditions.

The magnetite formation can be explained by Eq. 1-7 to 1-10. Iron in carbon steel forms soluble ions at the iron-oxide interface through the following anodic reaction:



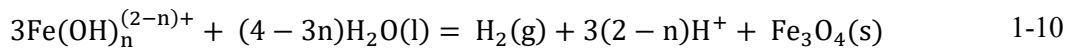
In the absence of oxygen in the PWR secondary circuit (see paragraph 1.2.5) or other oxidant species, the only possible reduction reaction is:



Depending on the pH, iron (II) forms several ferrous hydroxide species as expressed in Eq. 1-9 ($n = 0, 1, 2, 3$):



The magnetite (Fe_3O_4) is then formed from ferrous hydroxide ions following the Sweeton and Baes equilibrium (Yang et al., 2017a):



The formed magnetite is constituted of two layers: an inner compact and adherent layer characterized by the presence of small grains (0.05 to 0.2 μm) and an outer porous layer characterized by larger tetrahedral or octahedral particles of 0.5 to 5 μm (Delaunay, 2010). This magnetite layer may play the role of passivation which may limit reactions at the liquid-material interface including electrochemical reactions.

FAC can be considered as a particular case of general corrosion, which is accelerated by turbulent flow. FAC can occur if the flow rate is greater than 1.5 $\text{m}\cdot\text{s}^{-1}$ with Reynold number ranging from 10^5 to 10^8 (Chexal et al., 1998). FAC is a physico-chemical process that contributes to the increase of general corrosion rate up to a few millimetres per year (Le Calvar and De Curières, 2012). Morrison (J. Morrison, 2014) wrote a review of the magnitude of current corrosion issues affecting NPP primary and secondary coolant systems and stated that FAC represents the largest proportion of various corrosion problems (39.3%). FAC may lead to dramatic consequences in nuclear power plants. For instance severe accidents resulting from FAC were reported in various papers (De Bouvier, 2015a; Le Calvar and De Curières, 2012). The FAC phenomenon is well understood and believed to be largely present in NPP due to the enormous number of geometric singularities, *e.g.*, bends and contractions, inducing flow turbulences. De Bouvier (De Bouvier, 2015a) estimated the presence of more than 1200 geometric singularity elements in French 900 MWe NPPs.

1.2.6.3 Parameters affecting flow accelerated corrosion – TSP clogging source

FAC is the main source term of corrosion products in the secondary flow and then of TSP clogging phenomenon and other SG degradation phenomena, like the tube fouling. In this section, main parameters affecting FAC rate are identified and discussed. Current efforts for TSP clogging prevention are majorly based on minimization of the source term, without appropriate understanding of its formation mechanisms.

1.2.6.3.1 Effects of pH and temperature – magnetite solubility

The magnetite solubility is the key parameter regarding the quality of the passivation layer for limiting carbon steel corrosion. The FAC rate is controlled by reductive dissolution of the magnetite layer on carbon steels (reverse reaction in Eq. 1-10) and the transfer of dissolved iron from the surface to the bulk fluid. According to

Eq. 1-10, the proton concentration (and therefore the pH in diluted solution) plays a predominant role on magnetite solubilisation. An increase of proton concentration will promote the magnetite layer dissolution, and thus increase the FAC rate. Numerous studies showed that magnetite solubility decreases with an increase in pH up to 11 at 25 °C (Bignold et al., 1980; Fujiwara et al., 2011; Heitmann and Katsner, 1974; Machiels and Munson, 2005). Similar evolutions were found at higher temperatures up to 150 °C (Chivot, 2004). A recent EPRI report (unpublished results) stated that an increase of pH_{25 °C} from 9.0 to 9.6 induces a decrease of magnetite solubility from about 15 to 5 µg/kg at 250 °C when the solution is conditioned by ammonia. This pH effect explains why the PWR secondary water is maintained to alkaline pH values. More TSP clogging was observed in NPPs functioning with lower pH values (1.4.2.3), as reported by EDF feedbacks.

Temperature also influences the magnetite solubility. In previous studies, some authors investigated the variation of FAC for carbon steel under single-phase flow and found that the maximum FAC rate occurs at temperatures ranging from 130 °C and 150 °C in neutral and alkaline solutions ($7 < \text{pH}_{25\text{ °C}} < 9$) (Bignold et al., 1980; Heitmann and Schub, 1994; Rocchini, 1994), while the maximum FAC rate of carbon steel in two-phase flow was observed at about 180 °C (Keller, 1974). De Bouvier (De Bouvier, 2015a) recently reported that the maximum of FAC rate occurs between 150 °C and 180 °C. Therefore, the highest solubility of magnetite is expected to be between 150 °C and 180 °C as the greatest FAC rate temperature matches with the maximum of magnetite solubility (Corredera et al., 2008). It was observed in an unpublished EPRI study that the maximum of solubility is located at about 150 °C whatever the pH values ranging from 8.75 and 9.60 in the presence of ammonia at concentration between 0.1 and 2 ppm, respectively (Figure 1.5). Above 150 °C, magnetite solubility decreases with an increase of temperature (Figure 1.5).

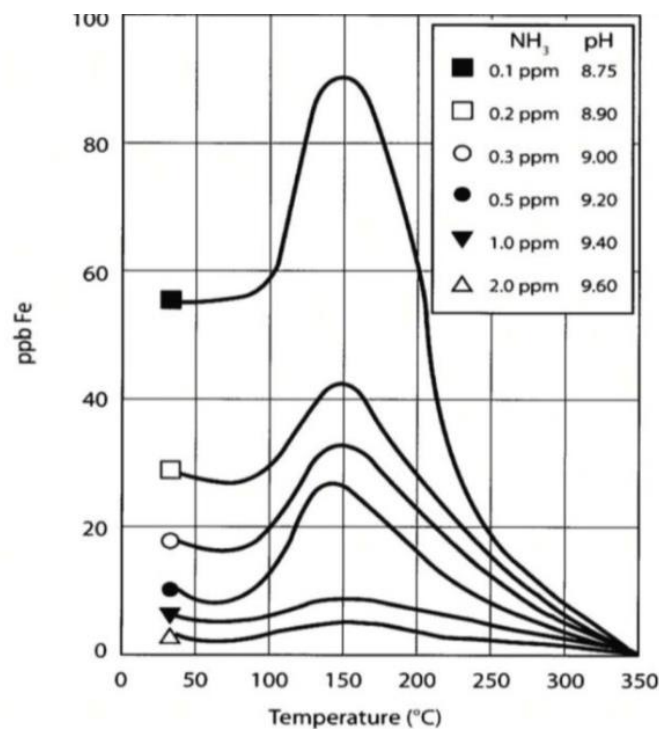


Figure 1.5: Magnetite solubility as a function of temperature and pH at 25 °C. pH was conditioned by adding ammonia at 0.1 ppm to 2.0 ppm. A maximum of magnetite solubility is observed at about 150 °C whatever the pH values. Detailed data cannot be provided. (Unpublished EPRI results)

1.2.6.3.2 Effect of oxygen concentration

FAC is also affected by the dissolved oxygen concentration. FAC of the feedtrain is inhibited when oxygen concentration is greater than 5 ppb in the secondary circuit (Dinov et al., 1993; Fujiwara et al., 2008; *Handbook of Water Chemistry of Nuclear Reactor System*, 2000; Izumiya et al., 1976). Indeed, oxygen can change the

nature of the oxide layer from magnetite to more protective hematite (Fe_2O_3), which has a considerably lower solubility and reduces dramatically the FAC rate (Eq. 1-11). However, dissolved oxygen should be maintained below 3 ppb in SG water for SCC prevention as previously mentioned. Maintaining simultaneously dissolved oxygen concentration up to 5 ppb in the feedwater and below 3 ppb in SG water can prevent both SCC and FAC in PWR secondary circuit.



1.2.6.3.3 Effect of material composition

Tsuruta et al. (Tsuruta et al., 2006) showed that the chemical composition of carbon steel also affects FAC rate. Indeed, the addition of 1 wt% chromium in carbon steel decreases the FAC rate by one order of magnitude. The increase of chromium content decreases oxide layer porosity, making oxide layer less soluble than neat magnetite (Fujiwara et al., 2011). For this reason, stainless steel used in PWR secondary components ($\text{Cr}\% = 12$ to 14, Table 1.2) is supposed to be less affected by FAC compared to carbon steels. Nevertheless, the corrosion of stainless steels remains an important degradation phenomenon in PWRs. Many studies have been conducted to investigate the influences of various parameters, such as water chemistry, material composition and stress, on the initial and growth of corrosion and to elucidate stainless steel corrosion mechanisms (Arioka et al., 2006; Bischoff et al., 2012; Liu et al., 2015; Tan et al., 2007; Terachi et al., 2008). Main experimental conditions were conducted under PWR primary conditions and supercritical water conditions. Stainless steel corrosion has been poorly investigated under exact two-phase flow SG conditions, undoubtedly due to the huge difficulties of experiments implementation. Several results will be presented hereafter in this section, which consist of the base for the further characterization of COLENTEC samples.

Corrosion of stainless steel

Terachi et al. (Terachi et al., 2008) investigated the formation processes of surface oxide films on different %Cr stainless steels (chromium: 5-20%_{wt}; nickel: 12-14%_{wt}; molybdenum: 2%_{wt}; manganese: 1%_{wt}; silicon: 0.5%_{wt}; sulfur/phosphate: trace; iron: Balance) in simulated PWR primary water (500 ppm boron, 2 ppm lithium) at 320 °C and with dissolved oxygen < 5 ppb. Figure 1.6 shows the surface appearance of specimens with different chromium contents observed by SEM. The specimen surface was covered with corrosion products. The particle size was larger for lower chromium content. The typical particle size was stated to be 4 μm in 5% chromium alloy and 1 μm in 20% chromium alloy. Each particle had a polyhedral morphology.

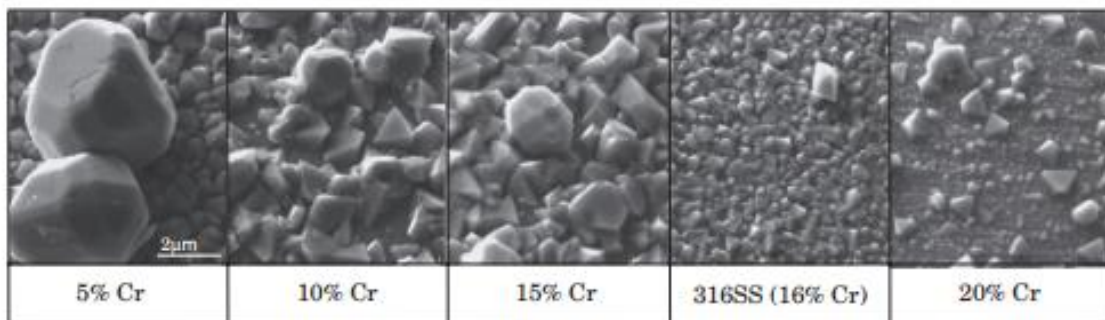


Figure 1.6: SEM images of the oxide film after immersion in simulated PWR primary water at 320 °C for 380 h, observed by Terachi's investigation (Terachi et al., 2008).

Further TEM observation of the cross section of the oxide film in stainless steel showed the formation of double-layer structure (Figure 1.7). The oxide film contains larger particles (up to several μm) of Fe_3O_4 and nickel substituted magnetite particles in the outer layer and fine particles of chromium substituted magnetite particles in the compact inner oxide layer (exact particle sizes were not given). Both layers were identified to have spinel structure. However, the inner layer contains higher chromium content than the outer layer, which contains

almost no chromium. Figure 1.8 shows electron diffraction patterns of the inner layer of different specimens. Ring patterns were observed in higher chromium alloy, whereas lower chromium alloys showed relatively clear spot patterns. The results indicate that the inner layer in lower chromium alloys contains larger particles than in higher chromium alloys. Nickel, initially presented at 10%_{wt} in the material, was found to be majorly localized at the interface of inner layer and material, and was slightly detected in both inner and outer corrosion layers (Figure 1.7).

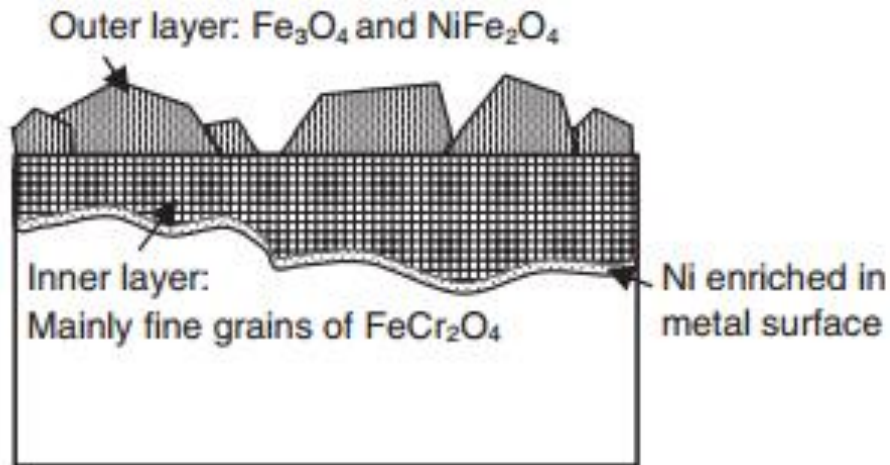


Figure 1.7: Schematic image of cross-sectional oxide film on stainless steel, proposed by Terachi's work (Terachi et al., 2008).

Bischoff et al. and Tan et al. (Bischoff et al., 2012; Tan et al., 2007) studied the corrosion of stainless steel (HCM12A with Cr: 10.83%_{wt}, C/N/Al/Si/P/S/V/Mn/Ni/Cu/Nb/Mo/W: trace; Fe: balance) in supercritical water conditions and steam conditions ($T = 500\text{ }^{\circ}\text{C} - 600\text{ }^{\circ}\text{C}$ and dissolved oxygen content of about 10 ppb). They obtained consistent results of oxide film formation. The double-layer structure has equally been observed in this environment (Figure 1.8), with the outer layer containing majorly Fe_3O_4 particles and the inner layer comprising of a mixture of Fe_3O_4 and FeCr_2O_4 . Chromium enrichment was observed in the inner corrosion layer by EDS profile analysis (Figure 1.9). Additionally, marker experiments using a novel photolithographic deposition process confirmed that the original water-metal interface corresponds with the outer-inner layer interface.

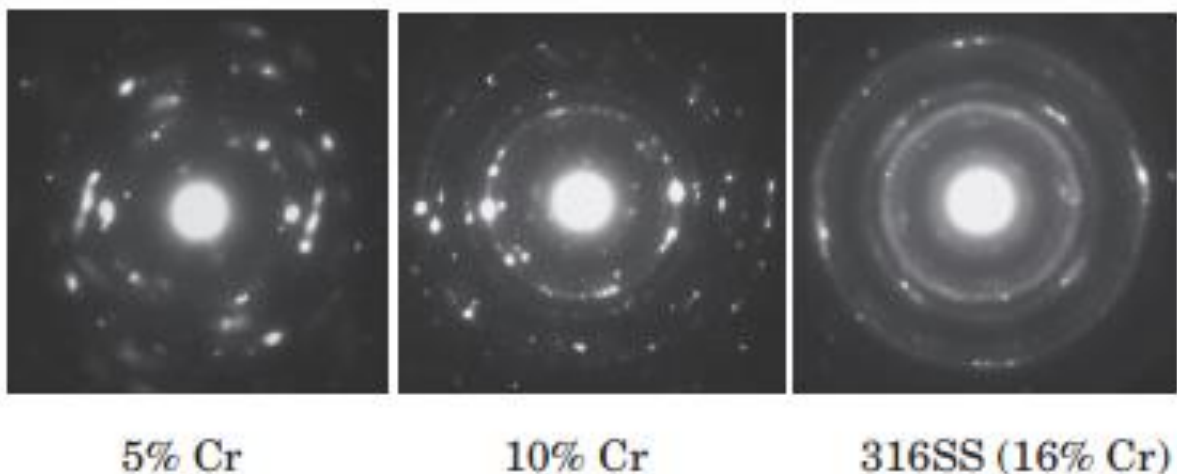


Figure 1.8: Electron diffraction patterns of the inner layer in 5% Cr, 10% Cr and 16% Cr after immersion in simulated PWR primary water at 320 °C for 380 h, obtained by Terachi's investigation (Terachi et al., 2008).

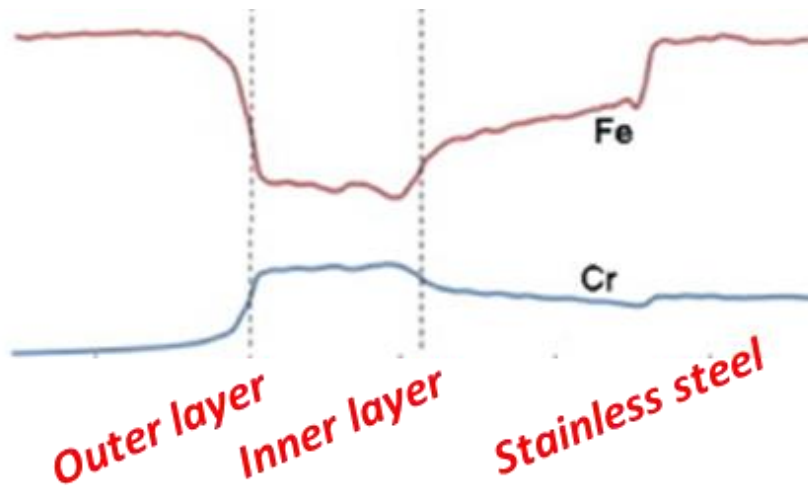


Figure 1.9: Observed double-layer structure for HCM12A sample exposed for eight weeks in supercritical water conditions. Iron and chromium evolutions are shown, which highlight chromium enrichment in the inner corrosion layer (Bischoff et al., 2012).

All previous investigations on stainless steel corrosion under different conditions highlighted the formation of the double-layer structure: compact fine-particle chromium-rich inner corrosion layer and porous large-particle iron-rich outer corrosion layer. The original water-metal interface corresponds to the interface between outer and inner corrosion layers. In general, the thickness of the oxide layers is between 0.1 and a few μm . The corrosion behaviour is expected to be the same as under steam generator secondary conditions. Above literature observations will thus bring essential support for interpreting the COLENTEC stainless steel samples characterized in Chapter 2.

1.2.6.3.4 Effect of thermohydraulics

Finally, thermohydraulic effects cannot be neglected since FAC is increased by strong turbulences. Regions with geometrical singularities, *e.g.*, bends and TSP, promote thus FAC. EDF progressively replaces carbon steel in these regions by stainless steel, which is less affected by FAC in nuclear power plants (Bischoff et al., 2012; Chen et al., 2006; Liu et al., 2015; Sinha et al., 2015; Tan et al., 2006, 2007). Surface roughness is considered to have similar effects because of the creation of local turbulences. Fluid velocity is also an encouraging factor, which accelerates formed ferrous iron transport into the fluid and shifts the equilibrium of Eq. 1-10 towards magnetite dissolution.

FAC induces thus the formation of soluble iron species from the magnetite layer dissolution. Its concentration has never been reported in the public literature. It has been estimated to be closed to the magnetite solubility by means of FAC modelling of SG secondary components (Delaunay, 2010). The magnetite layer on the carbon steel can also be entrained by the high-velocity of the secondary flow, especially in the presence of geometric singularities (Silbert, 2002), which induce magnetite particle circulation in the secondary flow. The size of these magnetite particles ranges from 1 to 3 μm in ammonia conditioning, and from 0.1 to 0.5 μm in morpholine conditioning (Delaunay, 2010). The presence of particles up to 100 μm has been also observed. The magnetite particle concentration has been estimated in SG water to be around 20 ppb, supposing that the magnetite concentration in the purge water is similar to that observed in the SG water (Pujet, 2002). The value of 30 ppb is thus considered as the approximate iron total concentration in the secondary flow in SG, without taking into account the super concentration phenomenon in restricted regions.

Flow accelerated corrosion (FAC) of carbon steel materials has been identified as the major source of steam generator degradation phenomena, like TSP clogging, which induces the formation of soluble iron species and magnetite particles in the PWR secondary fluid. Effects of different chemical and thermohydraulic parameters on FAC rate have been discussed. Minimizing magnetite solubility is essential for the source term reducing, mainly performed by high-pH secondary water management in nuclear power plants. Stainless steel is more resistant against FAC compared to carbon steel due to the higher content on chromium. Its corrosion behavior, double-layer structure, has been predicted by previous studies, which consists of the interpretation base of the further COLENTEC stainless steel samples' characterization.

TSP clogging is one of the major consequences of FAC, formed by FAC induced soluble iron species and magnetite particles. TSP clogging has been found to be mainly comprised of magnetite. In the next section, magnetite particle will be described, from a structural and physico-chemical point of view. Investigation of magnetite surface charge under secondary steam generator conditions will be specifically essential for the further mechanistic studying of TSP clogging.

1.3 Properties of magnetite particle

Magnetite is a black magnetic mineral. The molecular formula, Fe_3O_4 , can also be written as $\text{FeO} \cdot \text{Fe}_2\text{O}_3$, which consists of wüstite (FeO) and hematite (Fe_2O_3). It has the strongest magnetism of all the natural minerals existing on the earth (Zaitsev et al., 1999). An example of magnetite mineral is shown in Figure 1.10.



Figure 1.10: Photo of a magnetite mineral from Bolivia (Wikipedia source). Bipyramid crystals are observed.

Main physical properties of magnetite are listed in Table 1.4.

Table 1.4: Main physical properties of magnetite (Blaney, 2007; Fu, 2012).

Properties	Magnetite (Fe ₃ O ₄)
Density (g/cm ³)	5.18
Melting point (°C) (bulk scale)	1583 to 1597
Standard free energy of formation (kJ/mol)	-1012.6
Electric conductivity (Ω ⁻¹ cm ⁻¹)	100 to 1000, almost metallic

1.3.1 Structural property

Magnetite's crystal structure follows an inverse spinel pattern with alternating octahedral and tetrahedral-octahedral layers (Hill et al., 1979). The iron and oxygen ions form a face-centered cubic crystal system, and the oxygen ions are in the cubic close-packed arrangement (Figure 1.11, red spheres). Ferric (Fe³⁺) ions occupy all the tetrahedral sites and both ferric and ferrous (Fe²⁺) ions share equally all the octahedral sites. This preponderance allows for application of the chemical formula Y[XY]O₄, where brackets represent octahedral sites while the absence of brackets represents tetrahedral sites; consequently, X and Y symbolize ferrous and ferric ions, respectively. Magnetite unit cells adhere to the face-centered cubic pattern with crystal lattice parameter, $a = 0.84$ nm (Zaitsev et al., 1999).

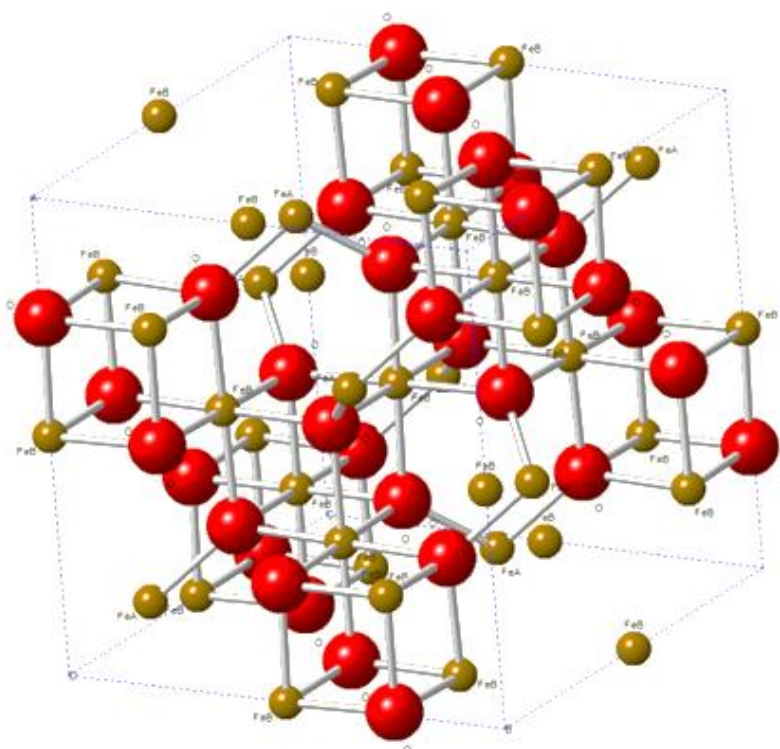


Figure 1.11: Structure of magnetite. Red spheres represent O²⁻; marron spheres represent the ferrous and ferric ions. FeA (ferric ions) occupy tetrahedral sites and FeB (ferric and ferrous ions) occupy octahedral sites.

1.3.2 Magnetite surface charge

Magnetite particles and TSP surface are found to be negatively charged under SG secondary conditions, by numerous previous experimental investigations presented below. This result is essential for the further discussion on TSP clogging formation mechanisms, involving magnetite particle deposition phenomenon. An understanding of interfacial electrochemistry is required. The notions of Electrical Double Layer (EDL) and zeta potential appear particularly important, and will be briefly reminded in the following of the present work.

1.3.2.1 Electrical double layer (EDL)

The EDL is a region existing at the boundary of two phases. In the present case, the EDL is an interfacial region formed in a fluid that is in contact with a solid. The layer forms to reach charge neutrality between the material and the fluid, as the solid surface is normally charged. In order to balance the charge of the wall with an equal and opposite charge in the fluid, a layer of charged ions forms (Bock et al., 1969; Morrison et al., 2013; Prigogine and Rice, 2009).

Several models for the structure of the double layer have been put forward, each building on the previous model's shortcomings. A general presentation of these different models will be done in this manuscript but readers can find more details and associated mathematical models in referenced publications (Bockris and Reddy, 1973; Grahame, 1947; Helmholtz, 1879).

The first model, suggested by Helmholtz in 1879 (Lyklema, 1995), simply consisted of a rigid double layer structure where the electrode's charge is countered by equal and opposite charges adsorbed directly upon the electrode wall. Such a structure is clearly analogous to a parallel plate capacitor and this model is generally described by capacitance approach. Helmholtz model is an over simplification of reality which does not take into account any effects of bulk electrolyte concentration, nor any interactions that occur beyond the first layer of adsorbed ions (J. Morrison, 2014).

In order to overcome these deficiencies, a model was suggested independently by both Gouy and Chapman which took into account the ability of dissolved ions to move freely through solution, as well as the tendency to accumulate in close proximity to an opposite charge (Gerischer, 1973). This model consisted entirely of a diffuse layer, where the concentration of ions was highest close to the metal surface and gradually diminishing with distance from wall, until the concentration was equal to that of the bulk solution.

A further model was suggested by Stern which combined both the Helmholtz and the Gouy-Chapman models into a single one. In the Helmholtz layer, a portion of the electrostatic potential drop is linear across the region of adsorbed ions; once past this layer, the potential falls as a smoother curve across the diffuse layer, eventually falling to the same value as the bulk solution potential.

Grahame added the concept of specifically adsorbed ions to the double layer model and developed a model with three distinct regions: inner Helmholtz plane (IHP), which is the plane passing through the centre of the specifically adsorbed ions, placed with a distance of β from the wall. Specifically adsorbed ions can have the same or opposite charge as the electrode and are bonded strongly to the surface; outer Helmholtz plane (OHP), which passes through the centre of the solvated and non-specifically adsorbed ions, placed with a distance of d from the wall (Morrison et al., 2013). The distance between the wall and OHP is several nanometres (Delaunay, 2010). Figure 1.12 shows the potential variation across the EDL, highlighting that the potential difference between the wall and the IHP, and the IHP and OHP vary in a linear way. The potential across the diffuse layer varies in an exponential manner and the potential drop across the diffuse layer is affected by ionic strength.

The most recent version of the EDL is that put forward by Bockris, Dacanthan and Müller (Erdemoglu and Sarikaya, 2006). This model is qualitatively the same as the Grahame model, with an addition of the notion of

shear plane, at which particles cease to be rigidly held by adsorption to the electrode wall. The corresponding potential is named zeta potential (ζ) and will be presented in the next section (1.3.2.2).

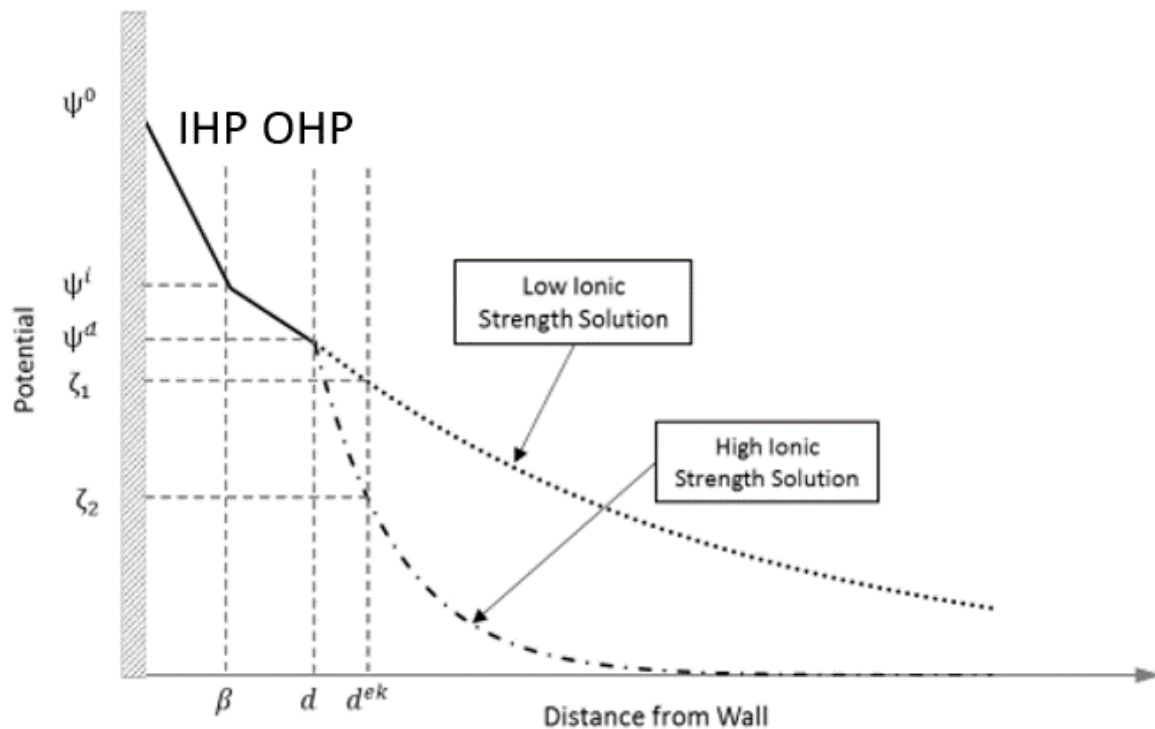


Figure 1.12: Potential variation across the EDL. The potential between the surface and IHP, as well as the IHP and the OHP varies linearly and then exponentially in the diffuse layer. ψ^0 , ψ^i and ψ^d represent the wall potential, IHP potential and OHP potential respectively. A shear plane is placed with a distance of d^{ek} from the wall. ζ represents the corresponding potential at this plane, named zeta potential.

1.3.2.2 Zeta potential

The zeta potential (ζ) of a particle is defined as the difference in potential between the shear plane and the bulk solution. The shear plane is the plane at which particles near the wall of an electrode cease to be held immobile, as previously mentioned. Indeed, when a solid particle and the liquid are in relative movement, part of liquid surrounding the particle and containing the counter ions is entrained by the particle. The plane separating the entrained liquid and immobile liquid is the so-called shear plane. Zeta potential is generally the only parameter which can be measured to characterize the charge of EDL. Zeta potential must be calculated from various electrokinetic phenomena, including basically: electrophoresis, electro-osmosis, sedimentation potential and streaming current and potential (J. Morrison, 2014). Zeta potential of any given system is dependent upon the pH of the electrolyte in which the EDL exists. The point at which the double layer exhibits a zero-zeta potential has been named the point of zero charge (PZC), often called the isoelectric point (IEP), which is the point at which zeta potential is zero. However PZC differs from IEP in that it only describes systems where the surface potential-determining ions are H^+ and OH^- (Friedlander and Johnstone, 1951). Therefore, PZC is effectively IEP in the absence of any other specifically absorbed ions, and this distinction is often ignored. The surface is negative when the pH is greater than the PZC and positive when the pH is lower than the PZC (*Surface Chemistry and Ion Exchange*, n.d., sec. UTexas).

1.3.2.3 Surface characterizations of magnetite

There are only very limited experimental data on the temperature dependence of the PZC of iron oxides, and almost all experimental data are restricted to temperatures below 95 °C. Tewari and Mclean (Tewari and Mclean, 1972) firstly estimated by Zetametry that the PZC of magnetite is equal to 6.5 at 25 °C. Sankaya (Erdemoglu and Sarikaya, 2006) proposed a PZC value of magnetite equal to 5 at 25 °C. Schoonen (Schoonen, 1994) predicted that the PZCs for magnetite and hematite at 270 °C are equal to 4.6 and 6.7, respectively. In a recent study, Barale et al. (Barale et al., 2008) measured between 5 and 320 °C the PZCs of typical oxides (magnetite (Fe_3O_4), nickel ferrite (NiFe_2O_4) and cobalt ferrite (CoFe_2O_4) recovered from PWR primary circuits. They gave PZC values of magnetite of 5.2 and 5.9 at 250 °C and 285 °C, respectively. PWR secondary water is conditioned at $\text{pH}_{25\text{ }^\circ\text{C}} > 9$, which corresponds to a pH value from 6 to 7 between 200 and 285 °C (De Bouvier, 2015a; Delaunay, 2010). At these pH values, magnetite particles are predicted to be negatively charged as well as the surface of Alloy 600 and stainless steel under SG conditions (Lu et al., 2015; Prusek, 2012; Turner et al., 2000). Exact PZC values of Alloy 600 and stainless steel under similar SG conditions are not provided in these works.

Delaunay (Delaunay, 2010) studied the effects of the presence of impurities on magnetite surface charge by sorption experiments. Suspension of magnetite particles containing impurities such as copper, zinc and aluminium were prepared in alkaline media for zeta potential measurements at 25 °C. Zetametry measurements showed that the addition of impurities induces changes in magnetite surface charge from negative to neutral values or even positive values. The presence of impurities may thus decrease repulsive effects between magnetite particles and TSP or SG tubes, and then encourage deposition phenomenon.

Magnetite mineral is a black nature mineral, usually under bipyramid crystal form. Magnetite has an inverse spinel structure, forming face-centered cubic crystal system. Magnetite structure can be identified by XRD based on its crystallographic properties.

Magnetite particles and stainless steel have been predicted to be negatively charged under similar PWR steam generator conditions. This result is essential for the further studies on TSP clogging formation mechanisms.

FAC are considered to be the major source of SG degradation phenomena. SG tube fouling and TSP clogging phenomena will be presented in the next section.

1.4 Steam generator degradation phenomena

FAC induces the formation of soluble iron in the secondary circuit by magnetite layer dissolution. Magnetite particles can also be formed by high-velocity flow entrainment. These soluble and particular corrosion products are then conveyed into PWR SG and contribute to further degradation phenomena (J. Morrison, 2014). SG tube fouling and TSP clogging are nowadays the two major SG degradation phenomena in the centre of nuclear industry concerns. The consequences of these phenomena on NPP are presented hereafter.

1.4.1 Tube fouling

Fouling is usually caused by iron oxides deposition upon the surface of the SG tubes. Figure 1.13 illustrates fouled SG tubes inserted into TSP.

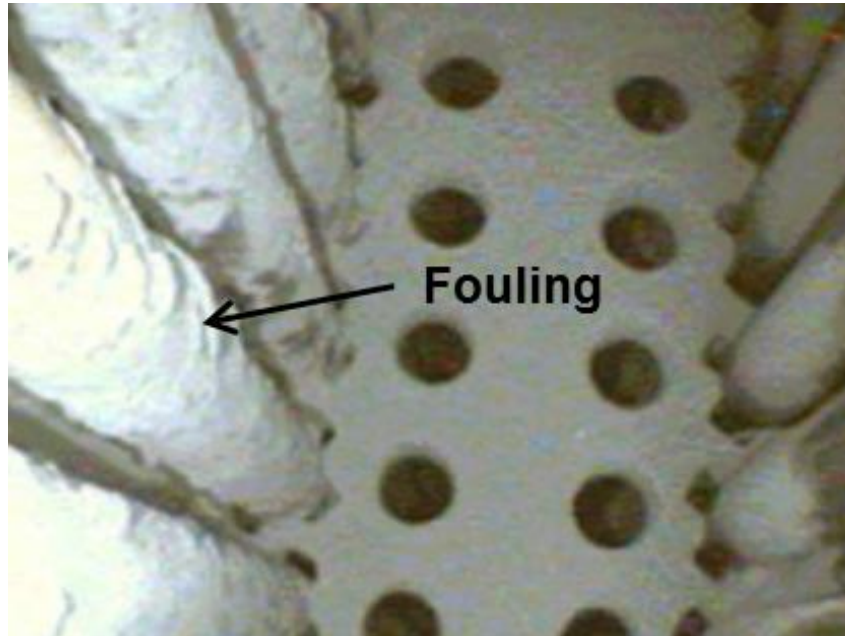


Figure 1.13: Photo of SG tube fouling (Prusek, 2012).

Fouling increases the thermal resistance of the tubes and, consequently, degrades the steam generator energetic performance. Plant operators need to gradually open the steam line valve at the steam generators outlets to compensate the pressure drop in the dome. Fouling phenomena cannot be observed directly in NPP but measurements of SG pressure evolution and oxide mass balance calculations are good indicators of such phenomena.

Pujet (Pujet, 2002) mentioned an accumulation of deposits of 200 kg per cycle per SG, which corresponds to a fouling rate of about 10 $\mu\text{m}/\text{year}$ assuming that the deposit is uniformly distributed onto the SG tubes. This estimation is in agreement with the fouling rate found by other NPP operators (from 1 to 100 $\mu\text{m}/\text{year}$ depending on the nuclear unit, the operating period and the location in the SG (Delaunay, 2010)). Pujet (Pujet, 2002) found that magnetite (Fe_3O_4) is the main chemical compound found in the fouling deposits of 12 NPPs operating in France between 1993 and 1997 as it was also reported by other operators in other countries (EPRI, 1984).

Corredera et al. (Corredera et al., 2008) evidenced secondary water conditioning influences fouling. In particular, they showed that low pH encourages fouling formation. For instance, higher pressure drop was observed when NPPs operate at $\text{pH}_{25\text{ }^\circ\text{C}} = 9.2$ instead of $\text{pH}_{25\text{ }^\circ\text{C}} = 9.6$ in the presence of morpholine or at $\text{pH}_{25\text{ }^\circ\text{C}} = 9.7$ in the presence of ammonia. Likewise, among the 22 plants operating at low pH, ten of them exhibited a significant fouling in 2007 (all of them were running for 22 to 28 years with original SG). A relationship between fouling and the amount of corrosion products were also established since high quantities of corrosion products and high fouling level were observed in NPPs operating at low pH. Except the straightforward observations mentioned above, fouling phenomena must still be thoroughly investigated since different fouling levels are observed in NPPs operating under similar conditions.

1.4.2 Tube Support Plate clogging

In the early 1990's, SG water oscillations were observed at Surry Power Units 1 and 2 in Virginia, at Kori Units 3 and 4 and Yongwang Units 1 and 2 in Korea (Rummens et al., 2004; Schindler et al., 2012). This phenomenon was caused by a severe deposit build-up in the TSP quatrefoil-shaped holes. EDF Nuclear Power Plants (NPPs) have been recently affected by the same phenomenon. Between 2004 and 2006, three primary-to-secondary leaks occurred in NPP located in Cruas (France). In-situ investigations showed that the flow holes of the uppermost TSP (8th TSP in SG 51B) were partially or completely clogged by corrosion products (Bodineau and Sollier, 2013; Corredera et al., 2008). This phenomenon, so-called TSP clogging or TSP blockage, was considered potentially generic for all EDF NPPs. Figure 1.14 shows a comparison between a “clean” quatrefoil flow hole and an almost fully clogged flow hole.

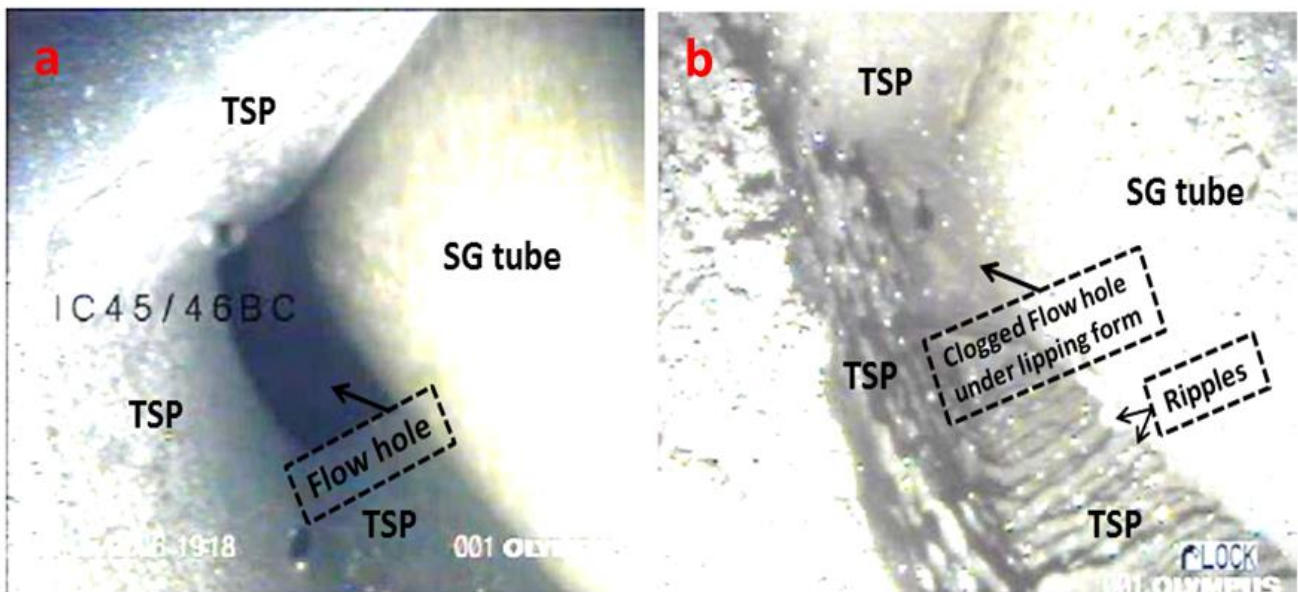


Figure 1.14: Photo of TSP clogging: top view of a “clean” quatrefoil flow hole (a); almost fully clogged quatrefoil flow hole (b) (Prusek et al., 2013; adapted by Yang et al., 2017a). Lipping form and ripple form are observed for clogged flow hole.

1.4.2.1 TSP clogging consequences

TSP blockage or clogging is defined as deposits formed by corrosion products in the secondary side of SG between TSP and SG tubes. This phenomenon can decrease the secondary flow section, and then induce high velocity zones and transverse velocities in the secondary flow, which can imply flow induced vibrations, tube cracks and leaks in some cases as it was observed in the NPP located in Cruas (France) as described above. TSP clogging phenomenon can also decrease the recirculation ratio of the steam generator. In other words, the secondary side effective flow of water available for cooling is decreased. The decrease of the available coolant water may then induce local overheats in restricted regions, encouraging local super concentration phenomenon and SCC with concentrated impurities. Thus, TSP clogging phenomena in nuclear steam generators may lead to dramatic consequences for NPP operation and may be responsible for safety issues (Bodineau and Sollier, 2013).

1.4.2.2 TSP clogging diagnosis

Face to this novel degradation phenomenon, EDF launched firstly a research program to develop methods for diagnosing TSP clogging in steam generators. The main obstacle to perform accurate diagnosis of TSP clogging lies in the difficulty to observe inside the SG during operation and the absence of internal sensors (Girard, 2014; Paillard et al., 2010). Three different methods have been implemented to diagnosis TSP clogging by EDF (Corredera et al., 2008; Girard, 2014; Moreau et al., 2013; Skarlatos et al., 2010):

1.4.2.2.1 Televsual inspections

Televsual inspections are conducted by introducing monitoring devices holding video cameras into steam generators through their upper openings. Televsual inspections are time-consuming and the sampling analysis is limited since only one hole per tube can be inspected at a time whereas the EDF maintenance objective is to inspect 90 holes by SG (Girard, 2014). For a sake of illustration, a 51B type SG has 3330 U-tubes, each surrounded by 4 quatrefoil holes which sums to a total of $3330 \times 2 \times 4 = 26640$ holes in the uppermost plate.

1.4.2.2.2 Wide Range Level (WRL) monitoring in stationary regime

This method is based on recording the pressure difference between the top and the bottom of SG, which is a global thermohydraulic parameter directly linked with the magnitude of TSP clogging. The main limitation of this method is that WRL can give neither a precise idea of TSP blockage distribution nor a quantitative assessment. Therefore, this method is only used by EDF as a supplementary assessment method to televsual inspections (Corredera et al., 2008).

1.4.2.2.3 Eddy current inspection

Eddy current inspection is a fast and effective non-destructive technique relying on the use of electromagnetic induction to detect and characterize the flows in the tube wall. It can give access to the vertical repartition of TSP clogging (Ida et al., 1985). However, this method is restricted to the observation of blockage levels greater than 50% (Corredera et al., 2008).

Girard (Girard, 2012; Girard et al., 2013) developed a new diagnostic method in 2012 based on the analysis of the WRL dynamic response to power transients in dynamic regimes. This new method gives access to additional sensitivity information that can be used to avoid bias and uncertainties in the vertical distribution of the SG deposit.

1.4.2.3 NPP feedbacks of TSP clogging

In 2008, EDF published a report on TSP clogging assessment results for 900 MW NPPs equipped with 51B or 51BI SG (Corredera et al., 2008). NPP located in Cruas (France) exhibited the greatest TSP clogging level likely due to the low pH value in the SG generator of Cruas NPP. Indeed, the $\text{pH}_{25\text{ }^\circ\text{C}}$ was equal to 9.14 in Cruas NPP while operating $\text{pH}_{25\text{ }^\circ\text{C}}$ was equal to 9.6 in other NPPs that were not affected by TSP clogging. From this feedback results, EDF concluded that low pH value of the fluid in SG may promote dramatically TSP blockage. The same effect of the low pH was highlighted for the tube fouling phenomenon (1.4.1). Oxidizing conditions were also considered as an aggravating factor. However, the impact of oxidizing conditions on TSP blockage

may be lower than the pH as oxidizing condition is responsible for the oxidation of magnetite into hematite which could be harder and less susceptible to be re-entrained (Corredera et al., 2008; Guillodo, 2004). Likewise, impurities such as silicon and calcium may have a negative impact since these elements can play a role in deposit consolidation (Turner, 1997).

Furthermore, examination of the morphology of the deposit at the inlet of the flow holes showed more clogging at the uppermost TSP and even more at the periphery than at the centre of the TSP as well as at the hot leg of SG (Prusek, 2012). In 51B type PWR SG, most TSP clogging is observed on the 8th TSP (highest), corresponding to a temperature of 277.2 °C, a pressure of 61.5 bars, a pH_{25 °C} of 9.2 and a void fraction of about 85%. Lipping form at the inlet of TSP and ripple form along the TSP are observed, like illustrated in Figure 1.14b and Figure 1.15. Lipping and ripple forms specify TSP clogging from the other deposits formed in SG, *e.g.*, tube fouling, which exhibits a relatively homogeneous thickness along the tube.

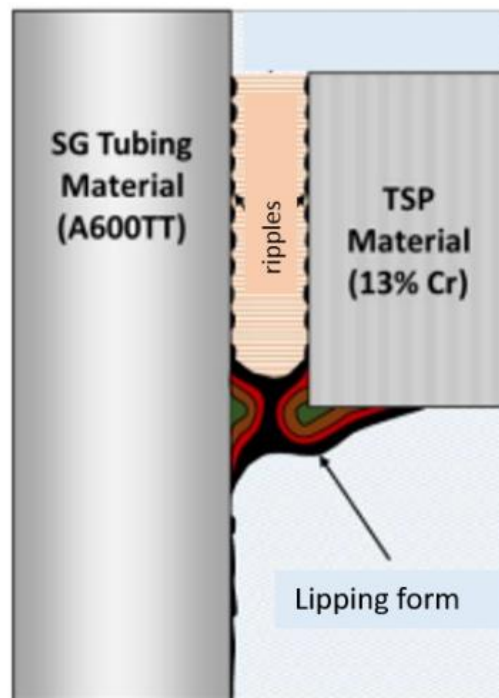


Figure 1.15: Schematic of TSP clogging lipping form and ripples (J. Morrison, 2014).

Chemical analyses of deposits onto TSP and SG tubes have been performed by EDF from 1993 to 1997 in France (Delaunay, 2010). Analysis data showed that magnetite is the major compound of the deposits collected from TSP with a mass percentage of 70.8%_{wt} in Dampierre NPP analysis in 1994. ZnO (6.4%_{wt}), SiO₂ (5.89%_{wt}) and MnO (2.76%_{wt}) were also present. All other analysis data in France showed a mean percentage of magnetite of about 60%, which was confirmed to be the major compound in either deposits collected from SG tubes or from TSP (EDF unpublished results). In the analyses in the USA, magnetite was equally found as the major compound with a mean mass percentage of 95% (Delaunay, 2010). Pujet and Corredera et al. stated more recently that the compounds found in materials responsible for TSP blockage were spinel ferrites AFe₂O₄ (A= Fe, Mn, Co, Ni, Cr...) with a majority of magnetite (Fe₃O₄) which has an inverse spinel structure as mentioned in paragraph 1.3.1 (Corredera et al., 2008; Pujet, 2002).

Morphological information of deposits onto TSP cannot be found in the public literature. Delaunay stated from limited EPRI analyses that the deposit may comprise a relatively porous outer layer of magnetite principally and an inner layer less porous (Delaunay, 2010). A deposit growth rate was estimated between 1 to 100 μm/year for tube fouling phenomenon as previously mentioned. The deposit growth rate of TSP clogging appears to be higher in low pH conditioning than the fouling growth rate and can be estimated knowing the deposit thickness, which is up to 5.8 mm (distance between SG tube and TSP, corresponding to 2R in Figure 1.18) at the inlet of TSP after 15 to 20 years, as in Cruas NPP, *e.g.*, up to 386 μm/year.

1.4.2.4 Current countermeasures

Various countermeasures, especially chemical or mechanical cleaning and high pH water treatment of the secondary circuit, are currently being implemented by EDF to face up SG degradation phenomena. Such countermeasures were found effective by foreign reactor operators who also detected these types of deposits in the 1980s and 1990s (Balakrishnan et al., 1981; Takamatsu et al., 2000; Tsubakizaki et al., 2013). Two main curative chemical cleaning processes are used by EDF in order to remove as much as 2000 kg of deposits per SG: EPRI-SGOG (Electric Power Research Institute – Steam Generator Owners’ Group) and HTCC (High Temperature Chemical Cleaning), developed by Westinghouse and Areva, respectively (Bodineau and Sollier, 2013). Three preventive chemical cleaning processes also exist. They allow removing between 200 to 1000 kg of deposits per SG: ASCA (Advanced Scale Conditioning Agents), DMT (Deposit Minimization Treatment) and PACCO (Preventive Acid Chemical Cleaning Operation) developed by Westinghouse, Areva and Comex-Lainsa, respectively (Carrette, 2015). The reader could find detailed information about these processes in ref. (Balakrishnan et al., 1981; Carrette, 2015; Puzzuoli et al., 1997; Rufus et al., 2001).

Chemical cleaning is currently the main effective method to remove most of the deposits in steam generators. Nevertheless, it remains costly, difficult to perform and may damage certain parts of the steam generators due to the corrosive properties of the chemical cleaning solution (Prusek, 2012).

TSP clogging damages NPP functioning. Four major results concerning TSP clogging formation have been obtained by NPP feedback analyses:

- *A low pH favors TSP clogging formation, which is also observed for tube fouling phenomenon.*
- *TSP clogging is majorly composed of magnetite.*
- ***Lipping** and **ripple** forms are observed for TSP clogging deposits.*
- *The deposit growth rate of TSP clogging appears to be higher than fouling growth rate.*
- *The kinetic of TSP clogging formation has been estimated to be up to **386 $\mu\text{m}/\text{year}$ at the inlet of TSP.***

Investigating alternative solutions to avoid TSP clogging is essential. In the next section, the phenomenology of TSP clogging formation will be presented. Magnetite particle deposition and soluble species precipitation will be studied. A unique specific TSP clogging formation model including particle deposition, flashing, and electrokinetic mechanisms will be proposed.

1.5 Phenomenology of TSP clogging formation

FAC induces soluble iron (II) species and magnetite particles in solution. The formed soluble and particle species are carried into SG and are considered to be the source terms of SG deposit phenomena, including SG tube fouling and TSP clogging. The fundamental origins of these phenomena have been proposed by various authors in the literature (Delaunay, 2010; Mansour, 2009; Pujet, 2002; Rummens et al., 2004; Turner, 2013): particle deposition, precipitation of soluble species and erosion of formed deposit (Figure 1.16).

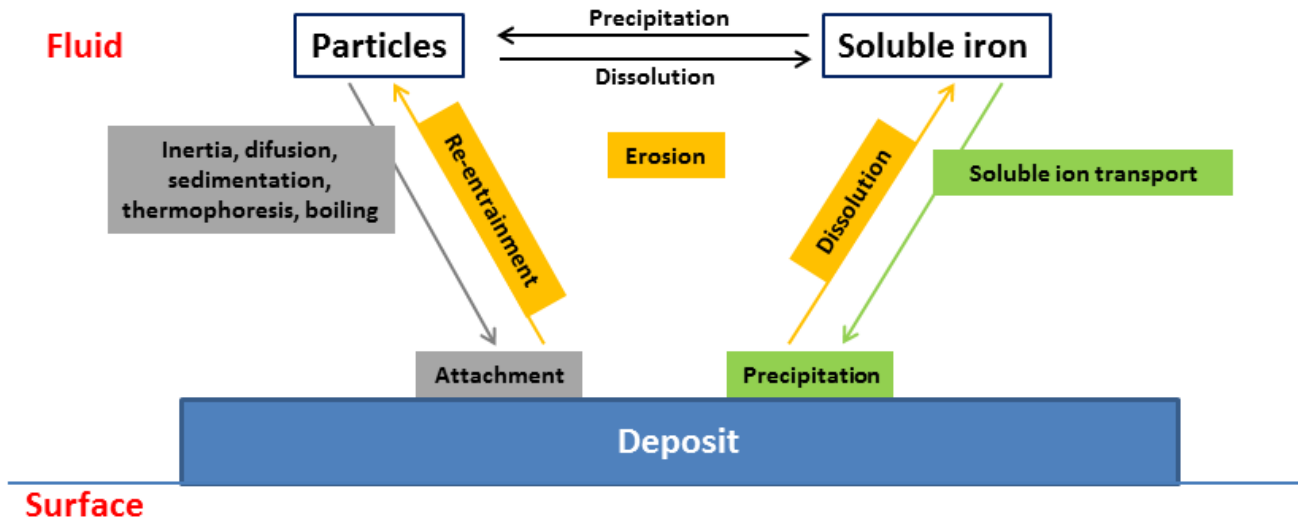


Figure 1.16: Main phenomena involved in SG deposits.

Particle deposition phenomenon comprises two steps (Figure 1.16): particle transport from the bulk circuit to the surface and particle attachment onto the surface. Particle deposition will be discussed in detail in paragraph 1.5.1. Soluble iron precipitation phenomenon will be described in the section 1.5.2. In the last section (1.5.3), specific formation mechanisms allowing explaining lipping and ripple forms of TSP clogging will be described, by considering the specific TSP geometry and the associated thermohydraulic conditions in SG.

1.5.1 Magnetite particle deposition

Studies conducted by AECL under high-temperature-high-pressure conditions will be mainly presented in paragraph 1.5.1.1. Models will be given to basic phenomena governing transport and attachment steps in 1.5.1.2.

1.5.1.1 Previous experimental studies

Burrill (Burrill, 1977) studied the effect of temperature on magnetite particle deposition onto Zircaloy-4 tubes from 28 °C to 80 °C at pH = 10 at magnetite concentration of 350 ppm. He stated that an increase of fluid temperature is responsible for an increase of the deposition rate. However, the electrostatic repulsion should tend to be more important and decrease the deposition rate as the magnitude of the zeta potential of magnetite increases with the temperature (Tewari and Mclean, 1972). Burrill attributed this strengthening effect of the temperature to the increase of the number of particles smashing onto the surface at high speed.

AECL investigated the effect of amines on the tube fouling rate by magnetite particle deposition (Turner et al., 1997, 2000) from 1994 to 2000. It was postulated that the amine, used for pH control, are absorbed onto the surface of magnetite and changes its surface potential. The presence of amine may increase the magnetite deposition rate onto Alloy 600 because protonated amine adsorbed onto magnetite particles diminishes the repulsion force between magnetite (negatively charged) and Alloy 600 (negatively charged) by increasing the surface charge of magnetite particles (Turner and Godin, 1994). The measurements were performed in a high-temperature recirculating loop, which allowed to produce nominal experimental conditions ($T = 270$ °C, $P = 5.6$ bars) and steam quality at test section varying from 25% to 51%. During each experiment, a suspension of radioactive magnetite particles was continuously injected into the loop, and the deposition of colloidal particles onto the test section was monitored by on-line γ -ray detector. The AECL experimental loop has been found to

be the most performant facility regarding the high-pressure and high-temperature capabilities by a review of existing experimental loops. Although the achieved conditions are still different from the characterized ones of most TSP blockage configuration ($T = 277.2\text{ }^{\circ}\text{C}$, $P = 61.5\text{ bars}$, void fraction = 85%), the results obtained with this loop seem to be the best ones for an extrapolation to TSP blockage. The reader can get more details about this experimental loop in the report written by Turner et al. (Turner et al., 1997).

Deposition rates of magnetite onto Alloy 600 surfaces were measured by means of this high-temperature loop. The effect on two parameters on the deposition rates was studied:

- Tube surface morphology
- Amines used for pH control (morpholine, ethanolamine, ammonia and dimethylamine)

The main conclusions drawn from this work are (Turner et al., 1997):

- The nature of the amine used for pH control affects the magnetite deposition rate;
- The deposition rate of magnetite increases with increasing concentration of amine at constant pH;
- The particle deposition rate can be affected by the tube surface morphology, *e.g.*, the rate is significantly higher on surfaces covered with porous deposits;
- The heat transfer mechanism and the steam quality strongly affect the deposition rate, *e.g.*, the deposition rate increases sharply at high steam qualities.

AECL undertook a follow-up program around 2000 to confirm that amine adsorption affects the particle deposition rate by altering the surface interaction potential between the particles and the surface of Alloy 600 (Turner et al., 2000). This program included investigation of amine adsorption onto magnetite surface by Laser Raman spectroscopy and determination of the effect of amine adsorption on the surface potential by means of electrophoretic mobility measurement and Atomic Force Microscopy (AFM). This study was finally completed by performing high-temperature loop tests.

The main conclusion is that amines exhibiting the highest base strength (to reduce the concentration of amine required to achieve the target pH) and the largest molecular size (to obtain a large footprint on the surface of magnetite and to reduce the amount of adsorption for a given amine concentration) lead to weak adsorption onto magnetite particles and low deposition rate. However, it seems difficult to identify an amine which fulfils all the criteria. For example, low amine adsorption is obtained with morpholine due to its large molecular size but this molecule is not perfect because of its relatively low base strength. Finally, loop tests highlighted in this study that morpholine is responsible for more deposition than ammonia at the same pH. The same study with ethanolamine was performed by the authors but data are not available in the literature.

AECL provided a large amount of interesting results for understanding the amine effect on magnetite deposition onto alloys surface in order to describe fouling phenomenon (Corredera et al., 2008). More NPP field data should be collected to thoroughly compare the morpholine and ammonia chemistry as no obvious difference has been observed when morpholine or ammonia are used at the same pH in plants (Corredera et al., 2008).

Parallel with the above experimental investigations, magnetite particle deposition has been studied from a modelling point of view and the developed models will be presented in the next section.

1.5.1.2 Magnetite particle deposition models

Large numbers of studies have been carried out from the 1980s on magnetite particle deposition following the detection of SG fouling and TSP clogging. It is fairly well established that deposition of colloidal particles onto a surface in forced convective regime is a two-step process occurring in series: the transport of particles from the bulk of the liquid to the vicinity of surface and their attachment (Beal and Chen, 1986; Burrill, 1977).

Burrill (Burrill et al., 1996) found that the deposition rate onto SG tubes increases linearly with magnetite concentration up to 300 ppm at 25 °C, pH = 7 and with Reynolds number of 1.2×10^5 . A number of studies of magnetite concentration effect under boiling water reactor conditions showed similar trend (Charlesworth, 1970; D. and Grigull, 1974; Mankina, 1960; Parkins, 1961; Stinchcombe, 1966; Zarembo et al., 1988). Based on this linear dependency with the concentration in the bulk C_p , the particle deposition quantity is generally expressed by (Basset et al., 2000; Turner and Godin, 1994):

$$m_d(t) = \rho_l C_p K_d t \quad 1-12$$

with,

$$1/K_d = 1/K_t + 1/K_a \quad 1-13$$

Turner and Godin (Turner and Godin, 1994) highlighted the potential influence of particle surface charge on deposition. If the particle and surface have the same sign of surface charge, then the particle deposition rate can be limited by the rate of attachment ($K_t \gg K_a$) (Eq. 1-13). Conversely, if the particle and surface have surface charges of opposite sign, then the rate of deposition can be limited by the particle transport rate to the surface ($K_t \ll K_a$) (Eq. 1-13).

Turner et al. (Turner et al., 1994) extended the previous deposition rate expression in two-phase flow situation (2ϕ), by introducing a deposition contribution from boiling process K_b (later described, Eq. 1-25).

$$K_d(2\phi) = K_d(1\phi) + K_b \quad 1-14$$

where the deposition rate for one-phase flow $K_d(1\phi)$ (m/s) is given by Eq. 1-13

They also developed the particle transport rate K_t accounting for diffusion (K_{diff}), inertial coasting (K_i) and thermophoresis (K_{th}):

$$K_t = K_{diff} + K_i + K_{th} \quad 1-15$$

1.5.1.2.1 Transport step

Basic phenomena affecting the transport step of particle deposition will be presented below. Electrokinetics is equally believed to enhance particle transport when electric fields are present (1.5.3.4). Nevertheless, no model exists describing this phenomenon.

Inertial coasting

Flow carrying magnetite particles in SG is highly turbulent (Burrill, 1977; Burrill et al., 1996), which can be separated into three layers: the centre region of flow, the buffer zone where the velocity fluctuations decrease as the distance to the wall decreases and the laminar boundary layer which is theoretically devoid of turbulence. The magnetite particles can reach the wall through the laminar layer providing that their initial momentum is high enough. Friedlander and Johnstone (Friedlander and Johnstone, 1951) were the first to introduce the notion of inertial coasting, considered as an important step in particle deposition. The inertial coasting, known also as particle impacting, is a hydrodynamical phenomenon induced by the fluid motions (McNab and Meisen, 1973).

The thickness of each layer depends on the physical parameters of the system. Burrill (Burrill, 1977) firstly stated that more magnetite particles are deposited when the velocity of the flow increases due to the decrease of the boundary layer thickness.

Thomas et al. (D. and Grigull, 1974) published the first experimental work on magnetite deposition from a turbulent liquid in SG tubes in 1974. They found that the deposition rate increases linearly with Reynolds number from 1700 to 1.85×10^5 , corresponding to a water velocity evolution from 0.03 to 3 m/s. Regarding deposit removal, they suggested that a particle, once deposited, would not be detached from the surface if the fluid Reynolds number remains unchanged (Weisbrod et al., 2002).

Hirano et al. (Hirano et al., 2010) presented a Japanese study of the effect of flow rate on TSP blockage in 2010. The work was carried out at 270 °C using a high-velocity test loop with quatrefoil flow hole TSP. Test solution in the feedwater tank and the spare tank were adjusted to $\text{pH}_{25\text{ }^\circ\text{C}} = 9.3$ using ammonia. The concentration of hydrazine in the both tanks was maintained at 200 ppb, and dissolved oxygen concentration was maintained below 5 ppb by bubbling with high purity nitrogen gas. 500 ppb of magnetite particles of 0.4 μm were injected into the test section. The numerical analyses around the flow hole were conducted after 500 hours. The obtained results lead to the following conclusion:

- The amount of scale deposition and the differential pressure caused by scale adhesion at the inlet of quatrefoil-type flow hole increases when the flow rate increases from 2.5 m/s to 5.9 m/s.
- Localized pressure drop and localized increase of turbulent energy are suggested to contribute to deposition formation.

The results are consistent with each other. The authors predicted that the mass transfer step dominates the attachment step at high Reynolds numbers ($>10^5$). The author acknowledges, however, that some studies have stated that an increase of fluid velocity does not affect magnetite deposition rate (Charlesworth, 1970; Mankina, 1960).

The following equation is used to calculate the inertial rate (K_i) that represents the increase of inertial coating rate due to SG deposit when the fluid velocity increases (Prusek, 2012):

$$K_i = a_i(t_p^+)U \quad 1-16$$

where the empirical parameters a_i vary as a function of the dimensionless relaxation time t_p^+ given by:

$$t_p^+ = \frac{\rho_p \rho_l d_p^2 U^2}{18 \mu_l^2} \quad 1-17$$

$$a_i = \min[A, 0.12] \quad 1-18$$

$$\text{with } A = \max\left(0.00038 \frac{\rho_l}{\rho_p} t_p^+ e^{0.48 t_p^+}, 0.0003 (t_p^+)^2\right)$$

This expression shows that the empirical parameter a_i depends on both fluid properties, *e.g.*, fluid density ρ_l (kg/m^3) and fluid viscosity μ_l ($\text{kg/m}\cdot\text{s}$), and particle properties, *e.g.*, particle density ρ_p (kg/m^3) and particle size d_p (m).

Diffusion

Diffusion explains the net flux of molecules from a region of higher concentration to one of lower concentration (Brogioli and Vailati, 2000). By assuming a homogeneous distribution of magnetite particles concentration in PWR secondary flow, diffusion or self-diffusion describes the random motion of the molecules.

Particle diffusion is generally given by the following expression:

$$K_{diff} = a_{diff} U S_c^{-\frac{2}{3}} \quad 1-19$$

with the empirical parameter $a_{diff} = 0.031$ as suggested by Turner (Turner et al., 1994).

The Schmidt number (S_c) of particles depends on the kinematic viscosity of the fluid (ν_l in m^2/s) and the diffusion coefficient of particles (D_p in m^2/s):

$$S_c = \nu_l / D_p \quad 1-20$$

The diffusion coefficient (D_p) is proportional to the liquid phase temperature (T_l) and inversely proportional to the particle diameter (d_p) and the dynamic viscosity of the fluid (μ_l) as expressed in the following equation:

$$D_p = \frac{k_b T_l}{3\pi\mu_l d_p} \quad 1-21$$

Basset et al. (Basset et al., 2000) gathered inertial coating and diffusion, including inertial effects into diffusion phenomenon and proposing the same expression as Eq. 1-19 with $a_{diff} = 0.084$. Inertial effects may be thus more important than particle diffusion (0.053 vs 0.031).

Thermophoresis

Thermophoresis described firstly the movement of small particles located in stagnant region of gas from hotter temperature towards colder temperatures. In the 1970s, equations were extended to describe thermophoresis effect in liquids (McNab and Meisen, 1973), which appears a predominant process in tube fouling formation in primary circuits of PWR (Yang et al., 2017a).

Based on the work of Epstein (Chen and Ahmadi, 1997), EDF included in their modelling tool the following relationship to calculate the thermophoresis rate K_{th} (m/s) (Prusek, 2012):

$$K_{th} = -a_{thermo} \nu_l \Phi_w / (\lambda_p + 2\lambda_l) T_l \quad 1-22$$

where $a_{thermo} = 0.042$.

This equation indicates that the thermophoresis rate depends on (i) the temperature gradient, induced by the applied heat flux Φ_w (W/m^2) (ii) the fluid viscosity and fluid density, represented by the kinematic viscosity of the fluid ν_l (m^2/s) (iii) the thermal conductivity of the fluid λ_l and particle λ_p as well as (iv) the absolute fluid temperature T_l .

Sedimentation

At first sight, sedimentation does not seem to occur in TSP blockage formation because the deposit occurs at a vertical surface of the TSP. On the other hand, Rummens (Rummens, 1999) has predicted a flow stagnant region by flow velocity analysis at the outlet of TSP where sedimentation can be the predominant phenomenon for the particle transportation onto the TSP upper surface.

Sedimentation corresponds to the tendency of particles to settle onto a surface due to forces like gravity, centrifugal acceleration or electromagnetism. In the model presented by Prusek, the sole gravity force is taken into account (Prusek, 2012).

Sedimentation phenomena depend on the angle between the surface direction and the vertical direction: if the surface direction is vertical, no particles can be deposited by gravity force; if the angle is 90° , sedimentation rate K_s (m/s) can be expressed as in Eq. 1-23 in the Stokes regime and as in Eq. 1-24 above this regime:

$$K_s = (\rho_p - \rho_l)d_p^2g / 18\mu_l \quad 1-23$$

$$K_s = 0.153 \left((\rho_p - \rho_l)d_p^{1.6}g / \mu_l^{0.6}\rho_l^{0.4} \right)^{0.714} \quad 1-24$$

Particular Reynolds number determines the regime and its expression can be found in the section A.1.3 of the Prusek thesis (Prusek, 2012).

Boiling

Thomas and Grigg (D. and Grigg, 1974) pointed out the importance of the "boiling factor". They performed a series of experiments on the deposition of magnetite in single- and two-phase flow (Basset et al., 2000). They suggested that, in the case of nucleate boiling, the rate of deposition increases linearly with the heat flux. The authors suggested a possible correlation between the increase of deposition rate and the number of bubbles formed per unit surface area and time. According to them, the formation of bubbles produces an increase in the turbulence in the boundary layer adjacent to the wall, combined with an increasing flow of water and magnetite in the direction of the wall to replace the space occupied by the leaving bubbles. Based on this suggestion, the following deposition rate K_b (m/s) describing the boiling process has been proposed by EDF:

$$K_b = \Phi_w a_b / \rho_m C_l H_{lg} \quad 1-25$$

where the deposition rate is proportional to heat flux ϕ_w (W/m²), the empirical parameter a_b is equal to 0.05 as suggested by Prusek (Prusek, 2012) and ρ_m is the average density of liquid/gas mixture (kg/m³).

1.5.1.2.2 Attachment step

Attachment was firstly accounted for by multiplying the mass transfer rate by a sticking probability, which is defined as the probability that a particle that reaches the wall will stick to it (Ruchenstein and Prieve, 1973). The sticking probability is usually given an Arrhenius dependence on the surface temperature. Attachment has since been put on a more fundamental basis by recognizing that when a particle arrives in the vicinity of the wall, its motion will be influenced by surface forces. The latter force is repulsive if the wall and the particle have the same sign of surface charge. When the repulsive force is sufficiently large, there will be an activation energy that the particle must overcome if it is to reach the wall. Hence, the rate of attachment is equal to the rate at which particles surmount this energy barrier (Ruchenstein and Prieve, 1973).

The attachment rate K_a (m/s) has thus been found to follow this Arrhenius law (Turner and Godin, 1994):

$$K_a = K_0 \exp(-E/RT_s) \quad 1-26$$

where E (J/mole) represents the activation energy for attachment which depends on the pH and the fluid temperature (Turner and Godin, 1994). Based on the AECL experimental results, the best fit of Eq. 1-26 to the experimental data gives the following expression for $\text{pH}_{25^\circ\text{C}}$ ranging from 8.8 to 9.2 and T_s ranging from 242 to 298 °C:

$$K_a = \exp(1.74) \exp(-9187/T_s) \quad 1-27$$

1.5.2 Surface precipitation

Iron ions produced by FAC mechanism can precipitate on SG surfaces, forming SG deposits. This phenomenon is also called “crystallization fouling” (Bansal et al., 2008; Bott, 1997; Lei et al., 2011). The precipitation reaction is actually the equilibrium of magnetite formation reported in Eq. 1-10.

Crystallization fouling describes the deposits formed on the surface itself, tenacious and difficult to remove. On the other hand, the term “sludge” is often used to describe crystals of softer deposits formed in the bulk liquid, which arrive at the surface as particles and accumulate in a loose agglomeration rather than in a more oriented matrix.

Crystallization fouling involves three basic steps: attainment of supersaturation, formation of nuclei and growth of crystals (Mwaba et al., 2006). The effects of temperature, pH, the presence of particles, surface conditions and electrokinetic mechanism are discussed in the following paragraphs.

1.5.2.1 Attainment of solubility

Supersaturation can be reached (Bansal et al., 2008) (i) by decreasing the fluid temperature in the presence of normal solubility salts, *e.g.*, salts exhibiting an increase of their solubility when temperature increases, (ii) by increasing the fluid temperature in the presence of inverse solubility salts, *e.g.*, salts exhibiting a decrease of their solubility when temperatures increases, (iii) by evaporating the fluid in order to reach the solubility limit, and (iv) by changing the pH.

The tube fouling phenomenon in the secondary circuit is particularly affected by supersaturation resulting from the heating effect of the primary flow circulating inside the SG tubes.

In SG, the temperature of secondary flow varies from 200 to 280 °C (Yang et al., 2017a). At these temperatures, boiling occurs in the secondary circuit besides the heating effect. Vapour formation will favour the attainment of supersaturation by concentrating the solution. Moreover, magnetite precipitation in Eq. 1-10 is increased by the boiling which encourages dihydrogen gassing. More TSP blockage is observed at the top of SG likely due to the boiling process in the uppermost regions and the “flashing” phenomenon (more details in 1.5.3.2).

1.5.2.2 Formation of nuclei

Formation of nuclei (also called nucleation) refers to the process by which the smallest stable aggregates of a crystalline phase are formed in a crystallization system. These aggregates act as building blocks for crystal

formation. Factors that can speed up nucleation include the presence of impurities and the surface conditions, such as roughness (Mwaba et al., 2006).

The effect of the presence of particles on fouling due to calcium sulphate or sodium aluminium silicate crystallization onto a plate heat exchanger has been reviewed by Bansal et al. (Bansal et al., 2008). The solution containing soluble species was conditioned between 40 and 55 °C. It appears that crystallization rate usually increases in the presence of particles likely because crystalline particles in solution play the role of nucleation sites (Vaessen et al., 2002). Depending on the turbulence phenomena, some of the particles are able to settle in the regions where the conditions are not conducive to crystallization such as high turbulent regions like in the inlet of TSP. Later in the present work, a specific TSP clogging model including particle effect will be presented and applied to the inlet of TSP.

An inverse effect of the presence of particles as seeds on crystallization rate has also been mentioned (Gainey and Thorp, 1963; Rautenbach and Habbe, 1991). Indeed, the introduction of seeds is usual in many industrial applications to achieve crystallization on these seeds in the bulk, decreasing available soluble species and preventing fouling on the heat transfer surfaces (Bansal et al., 2008). For instance, it has been reported that calcium sulphate deposits have been prevented in sodium chloride salt plants by maintaining about 20 grams per liter of calcium sulphate solids in suspension (Bansal et al., 2008).

These competing effects make it difficult to define the role of particles in soluble species precipitation mechanism. However, most of the recent studies showed a benefit effect of the presence of particles to fouling formation (Barnes et al., 1999; “Detachment of Spherical Microparticles Adhering on Flat Surfaces by Hydrodynamic Forces”, n.d.; Duffy et al., 2011; Hasson and Zahavi, 1970).

Surface morphology effect on calcium carbonate crystallization fouling was experimentally studied by Lei et al. (Lei et al., 2011). They highlighted that the fouling weight became five times more when the average surface roughness varied from 0.1 to 0.3 µm. From this study, the authors demonstrated that a mirror polished sample leads to the best antifouling surface.

1.5.2.3 Growth of crystals

Nucleation is followed by crystal growth. Minute crystal particles that are formed during nucleation subsequently grow into crystals. In general, two main mechanisms are considered (Bansal et al., 2008; Mwaba et al., 2006): transport of ions from the bulk to the liquid-crystal interface and surface integration of ions into the crystal lattice.

Electrokinetic mechanism affects the growth of crystals and is supposed to be a potential specific formation mechanism of TSP clogging (Paragraph 1.5.3.4). Mathematical models aiming to quantify the crystallization fouling are generally based on this crystal growth step. Accurate and detailed mathematical modelling of fouling processes is generally difficult, because of the difficulties involved in reproducible measurement of the fouling resistance and the complex nature of deposit formation (Mwaba et al., 2006). Classically, the deposition rate of fouling is taken as a function of concentration driving force and the impact of nucleation sites is ignored. In the classical approach, the precipitation rate can be transport controlled, surface reaction controlled, or a combination of both (Bansal et al., 2008).

Transport of ions is estimated by (Mwaba et al., 2006):

$$dm'/dt = \beta(C_b - C_i) \quad 1-28$$

Reaction-controlled rate is modelled by (Bansal et al., 2008; Mwaba et al., 2006):

$$\frac{dm'}{dt} = K_r (C_i - C_s)^n \quad 1-29$$

where m' is the mass deposited per unit area, C_b is the concentration of the ions in the bulk, C_i is the concentration of the ions at the solid-liquid interface, C_s is the saturation concentration, β is the mass transfer coefficient, K_r is the reaction rate constant and n is the order of reaction.

The rate constant K_r depends on the surface temperature T_s and is given by the Arrhenius equation (Reitzer, 1964):

$$K_r = K_0 \exp(-E/RT_s) \quad 1-30$$

where K_0 , E and R stand for the Arrhenius constant, activation energy and gas constant, respectively.

The “classical” deposition rate law approach discussed above is driven by concentration differences and does not consider the effect of nucleation even though such an effect is known to have a major impact on crystallization. The presence of particles in the process solution and the increasing amount of crystalline deposits onto the surface have been identified as the sources of nucleation sites and modelled in a modified deposition rate law by Bansal et al. (Bansal et al., 2008) in the case of calcium sulphate precipitation. Considering the precipitation is reaction controlled, the modified deposition rate is expressed as:

$$\frac{dm'}{dt} = K_r (C_i - C_s)^n N \left(\frac{M_f}{M_{fg}} \right)^{n'} \quad 1-31$$

where N is a dimensionless function of the nucleation sites provided by particles present in the process solution, M_{fg} denotes the total deposited mass when the crystal growth starts and M_f represents the total deposit mass at time t .

No clear explanation is given regarding the value of N in the work of Bansal et al. (Bansal et al., 2008). $N = 1$ was chosen when the particles present in the process solution were filtered out by the 1 μm in-line filter. Thus, particle size seems to be related to this value. The value of n' depends on the fouling conditions. For cases where new deposits keep on growing on the top of the existing ones, the increase in the deposit mass may have a little impact, *e.g.*, low value of n' are used in Eq. 1-31. In contrast, when the deposits spread along the surface, the increase in the deposit mass may have a stronger effect on the deposition rate and high values of n' are used in Eq. 1-31. No value of n' is proposed by Bansal et al. (Bansal et al., 2008) whereas Smith and Sweett (Smith and Sweett, 1971) proposed a value of 2/3 in a similar model for calcium sulphate precipitation.

This modified model seems to be the most developed model for crystallization fouling in the literature as it includes the effect of the presence of particles and the effect of deposit build up. However, many other processes or parameters, like supersaturation attainment, boiling, electrokinetic mechanism, deposit dissolution and initial surface roughness, are not taken into account, which add further complications to the basic concepts already discussed (Bott, 1997). Moreover, no models are available in the literature describing specifically iron precipitation. Uncertainties thus exist if using these models for quantifying iron precipitation issues.

1.5.3 Specific TSP clogging formation mechanisms at the inlet of TSP

Based on the two basic mechanisms involved in TSP blockage, *e.g.*, particle deposition and soluble iron precipitation, specific models have been recently proposed in France for SG deposits. Pujet (Pujet and Dijoux, n.d.) firstly described a specific model to predict fouling thickness and thermal performance degradation of SG in PWR. This model is based on the following assumptions of fouling formation mechanisms:

- Iron oxide particle deposition forms a porous layer onto the surface;
- Soluble iron precipitation inside the porous layer generates a dense inner layer near the tube surface;
- The dense inner layer is detrimental to heat transfer from primary to secondary water and plays a major role in the loss of thermal performance of SG.

Governing equations for porous layer and dense layer build-up can be found in Pujet's work (Pujet and Dijoux, n.d.). This model has been tested on laboratory experiments and applied to three PWR units, providing reasonably satisfactory results. The main conclusion of these calculations is that iron solubility in the SG should be kept as low as possible during normal plant operation to minimize SG fouling.

In 2013, Prusek (Prusek et al., 2013) developed a deposit process for modelling the TSP blockage in order to include it in the EDF reference code for modelling two-phase thermal-hydraulic phenomena at the sub-channel scale. A consecutive two-step mechanism was proposed in this model for TSP blockage, similar to the fouling formation mechanisms discussed above: Particle deposition followed by a strengthening process called "flashing" occurring due to precipitation phenomena in the porosity of the particle deposit.

According to Prusek, two special mechanisms, *e.g.*, "*vena contracta*" and "flashing" are used to describe particle transport and soluble species precipitation for TSP blockage, respectively, at the inlet of TSP. Another phenomenon: "electrokinetics", is supposed to enhance the soluble iron precipitation and particle deposition (De Bouvier, 2015b; Guillodo, 2004; Prusek et al., 2013; Yang et al., 2017a). However, it was not included in the Prusek's model, which appears to be the only specific model aiming to describe TSP clogging in the public literature (Yang et al., 2017a). These three mechanisms will be described in this section with the associated models, if existing. The results obtained by Prusek's modeling work, including *vena contracta* and flashing phenomena, will be presented.

1.5.3.1 *Vena contracta mechanism*

Rummens (Rummens, 1999) was the first to propose a particle deposition mechanism where a sudden contraction in the flow circulation occurs. A conceptual figure of the *vena contracta* is shown in Figure 1.17. It is important to notice that this figure does not represent exactly the real geometry of a TSP flow hole, which is vertical in the SG. It just allows describing the main hydraulic phenomena when a flow passes through the contraction.

The "lipping" phenomenon observed in the field can be attributed to this "*vena contracta*" region. Indeed, at the inlet of this region, the mainstream flow separates from the wall following the sharp contraction. A low-velocity recirculation zone is created. The particles with a given kinetic energy are deviated from their initial trajectory and start to follow the recirculation flow pattern. In this recirculation zone, the particles continue to lose kinetic energy, thus encouraging particle deposition; a tiny deposit can begin to grow. As the deposit grows, the flow contraction becomes more and more important, and consequently, the particle deposition is more and more favoured.

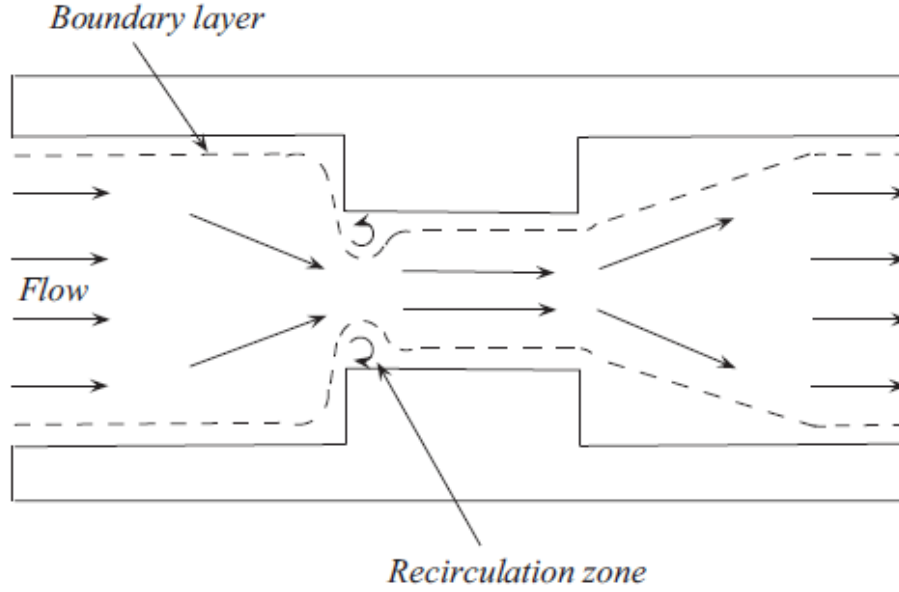


Figure 1.17: Pattern of vena contracta region (Prusek, 2012; Prusek et al., 2013).

Considering that the particle deposition exclusively results from this “vena contracta” mechanism at the inlet of TSP, the deposition rate $K_{v,p}$ (m/s) proposed in Prusek’s work (Prusek et al., 2013) takes into account the main parameters that influence the TSP clogging and the self-sustained phenomenon represented by k_v (m^{-1}) (expressed in Eq. 1-33), which represents the TSP variable blockage rate:

$$K_{v,p}(t) = a_v k_v (\rho_p - \rho_l) C_g d_p^2 U_z^2 / \mu_l \quad 1-32$$

This equation shows that:

- The deposition rate increases with the density of particles (ρ_p), the vapour mass fraction (C_g) and the particle size (d_p);
- The deposition rate increases with the fluid kinetic energy (U_z^2);
- The deposition rate decreases with the value of fluid viscosity (μ_l).

The empirical dimensionless parameter a_v , should *a priori* be experimentally determined by representative TSP clogging formation experiments at the SG scale. This parameter is supposed to be constant all over the SG and it allows one to calibrate the deposition rate. However, its value was calculated by means of a mathematical method by Prusek in well-defined simulation conditions. An optimized value was proposed: 0.00087 (Prusek et al., 2013).

k_v (1/m) allows taking into account the specific TSP flow hole geometry, which indicates that this *vena contracta* mechanism is a self-sustained phenomenon. Indeed, the flow contraction becomes more and more important as the deposit grows and consequently, the particle deposition is more and more favoured. This parameter is modelled by the following expression:

$$k_v(t) = \frac{L - [R(1 - \tau_c)]}{S} \quad 1-33$$

where L , R and S are characteristic values of the specific geometry of flow holes’ entrance. They respectively represent half the distance between two consecutive tubes (32.54 mm), the equivalent radius of a flow hole (2.895 mm) and its section (72.14 mm²), as shown in Figure 1.18. Parameter τ_c represents the TSP clogging rate

which is a ratio between the flow blockage section to the total hole section. It is a dimensionless number and its value ranges between 0 and 1.

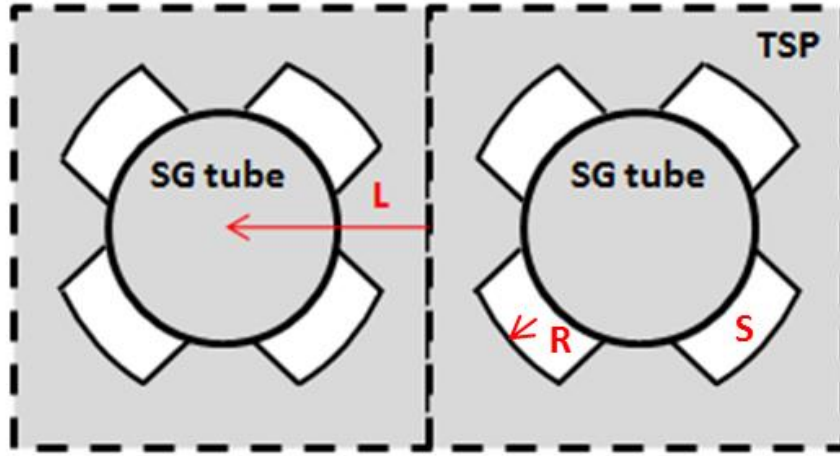


Figure 1.18: Top view of a pattern of a TSP (secondary flow hole in white colour).

The deposit thickness e_d (m) formed by *vena contracta* mechanism can then be expressed as following (Yang et al., 2017b):

$$e_d(t) = \frac{\rho_l C_p K_{v,p}}{\rho_d} t \quad 1-34$$

where ρ_d (kg/m³) represents the formed deposit density; C_p is the particle concentration (kg/kg).

1.5.3.2 Flashing

This phenomenon is attributed to a sudden decrease in pressure which is created at the inlet of flow holes due to the presence of the sharp contraction. This pressure reduction can be related to a liquid enthalpy reduction ΔH_l (J/kg) which induces a local change from liquid to steam. Due to the vaporization, the concentration of soluble species in liquid tends to increase and reach the solubility. A local precipitation occurs. This so called “flashing” precipitation may act as a deposit cementing agent and strengthens a preliminary particle deposit.

The mass flux of soluble species precipitation ϕ_s per unit area (kg/s/m²) can be expressed using Eq. 1-35 proposed by Prusek (Prusek, 2012) when all the soluble species are supposed to participate to precipitation:

$$\phi_s = \frac{\phi_l \Delta H_l S_s}{H_{lg}} \quad 1-35$$

where ϕ_l represents the mass flux of liquid per unit area (kg/s/m²), which can be obtained by multiplying liquid density ρ_l (kg/m³) by liquid phase velocity $U_{z,l}$ (m/s); S_s represents the solubility (kg/kg); and H_{lg} is the heat of vaporisation of liquid (J/kg).

The liquid enthalpy reduction depends on the TSP clogging rate (τ_c) and the liquid phase velocity (m/s) at the inlet of TSP ($U_{z,l}$):

$$\Delta H_1 = \lambda(\tau_c)U_{z,1}^2 \quad 1-36$$

where the dimensionless parameter λ is supposed to be 9.97 when $\tau_c = 0$ (Prusek et al., 2013). Two other λ values of about 18 and 76 were proposed respectively with $\tau_c = 0.44$ and 0.72 by Prusek et al. (Prusek et al., 2013). The flashing mechanism shows thus a strong dependence onto TSP clogging rate and especially the secondary fluid velocity, which determine the magnitude of the pressure drop, so the liquid enthalpy reduction.

1.5.3.3 Results of modelling study comprising vena contracta and flashing

The deposit simulations based on these two mechanisms have been performed over a period of 22 years, which corresponds to the working period of SG before televisual inspections. Two simulations have been performed:

- Simulation 1: only the flux of particle deposition is taken into account, calculated by Eq. 1-32;
- Simulation 2: the strengthening process “flashing” is taken into account.

The main conclusions are (Prusek et al., 2013):

- Flashing seems to be a governing factor for deposition;
- The mean blockage rate is more important in hot leg than in cold leg;
- The mean blockage rate is more important at the top than at the bottom of SG;
- Simulation 2, taking into account “flashing” process allows to have a better representation of asymmetry between hot leg and cold leg;
- TSP blockage has the distinctive feature to be more important at the periphery than at the centre;
- A reduction of magnetite solubility before entering into SG seems to be an interesting remedy for reducing TSP blockage.

These conclusions deduced from modelling are in accordance with the observations in the NPPs (1.4.2.3). The proposed two-step mechanism seems to predict that TSP blockage localization is controlled by particle deposition and deposit morphology (density, porosity etc.) is controlled by strengthening process, which has a cementation effect. Reducing magnetite solubility allows decreasing the term source production (1.2.6.3.1), which is consistent with results of the simulations. However, the main limitations in this model may be (Prusek et al., 2013):

- Non-implementation of electrokinetics phenomenon
- Neglected erosion mechanism

In the next section, the neglected electrokinetic phenomenon in this model will be presented.

1.5.3.4 Electrokinetics

Electrokinetic phenomena occur in the presence of a charged fluid or a charged surface as well as when the fluid velocity changes. Strong interactions occurring between the ions in fluid and charged surface gives rise to the Electrical Double Layer (EDL) (El-Adawy et al., 2011), as previously mentioned in paragraph 1.3.2.1. In order for the interface to remain neutral the charge held onto the solid is balanced by the redistribution of ions of opposite charge in solution close to the solid. When a differential pressure applies to the ionic fluid, inducing a velocity in the fluid, a current named streaming current (i_s) is generated by the motion of the excess charge in the EDL. Any changes in streaming current in the direction of flow result in a current vector normal to the wall, named wall current (i_w) to satisfy electroneutrality. In the case of TSP blockage, both non clogged and magnetite clogged TSP are charged negatively under SG conditions (Barale et al., 2008). Anodic reactions driven by wall

currents, such as precipitation of magnetite, can then occur at the inlet of TSP, where the flow is accelerated. The streaming current is partially accommodated by back conduction of ions through the bulk solution, which generates a potential between the bulk and the metal surface. The generated electric field can drive the electrophoretic deposition of particles from the solution onto the metal surface (McGrady et al., 2017).

Figure 1.19 illustrates the formation of magnetite deposits due to electrokinetic effects onto TSP. When a fluid is accelerated, *e.g.*, SG secondary water at the inlet of TSP, initially neutral EDL is disturbed with the entrainment of positive charges into the fluid in the case of the TSP surface (negatively charged under SG conditions). Anodic activities, *e.g.*, magnetite formation from soluble ferrous species (Eq. 1-10), are encouraged, inducing electron migration (wall current in the reverse direction) via metallic material to a cathodic zone at a different localization. The electron migration allows re-establishing the electroneutrality of the EDL. In the cathodic region, reduction reactions take place under SG reducing and degassed conditions (water reduction to H_2) as expressed in Eq. 1-8. Ion back conduction can be equally supposed to occur through the bulk solution, accommodating the increasing streaming current (Figure 1.19, black dash arrow). A potential is thus created between the bulk and the metal surface, encouraging deposition of negatively charged particles, like magnetite (Figure 1.19, red dash arrow).

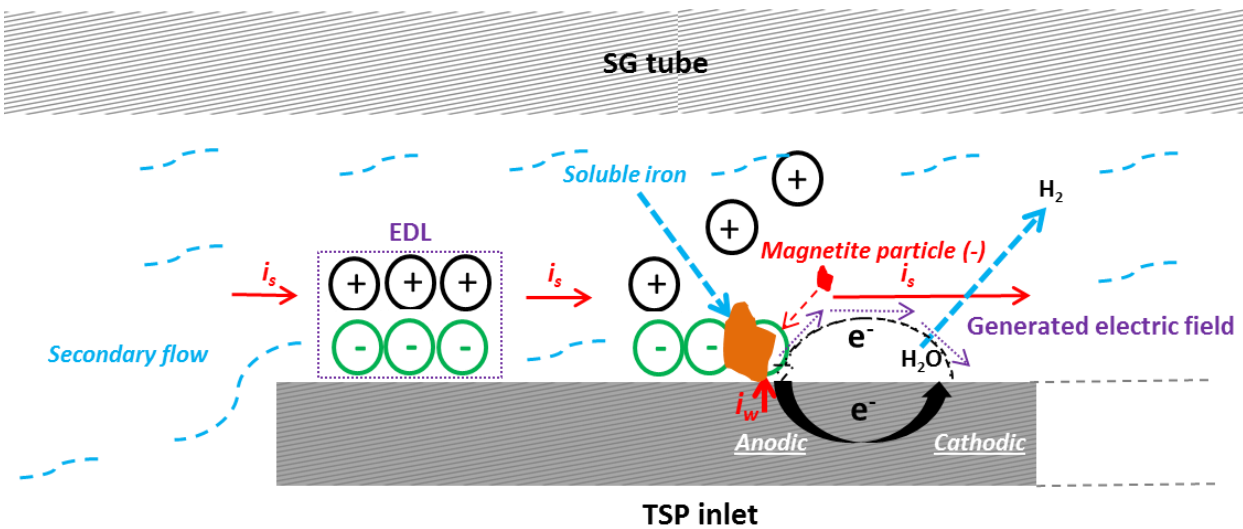


Figure 1.19: Illustration of magnetite formation due to electrokinetic phenomena onto TSP. i_w represents the wall current; i_s represents the streaming current.

In 1986, Robertson stated possible mechanisms to describe this phenomena and developed theoretical approach (Morrison et al., 2012). Recently, Guillodo et al. (Guillodo et al., 2012) suggested deposition is initiated at the inlet of TSP by electrokinetic effects (Figure 1.20). In particular, they proposed that the formation of the initial deposit disturbs sufficiently the flow to form other flow singularities, resulting in a propagation of annular deposits along the length of the TSP.

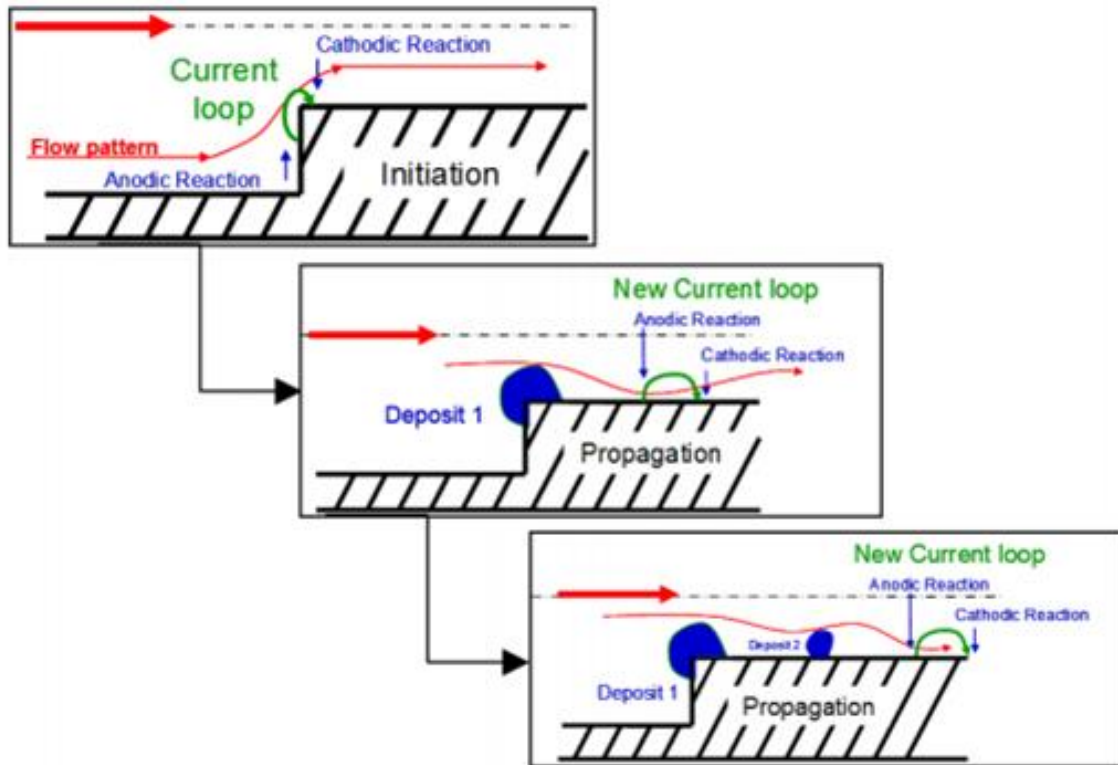


Figure 1.20: The proposed electrokinetic mechanism of deposit propagation along the annulus of a flow-restriction (Guillodo et al., 2012).

This mechanism allows explaining the lipping form at the inlet of TSP and the annular rippled deposits along the length of TSP observed in NPPs (Figure 1.14b and Figure 1.15).

More recently, Scenini et al. (Scenini et al., 2014) investigated the role of electrokinetic effects in corrosion deposit formation in primary circuit. A miniature flow cell was designed to accelerate fluid flow and produce negatively charged regions onto electrodes leading to polarization. X-Ray Diffraction (XRD) and Glow Discharge Optical Emission GDOES analyses of the polarized electrodes showed that anodic processes resulting from electrokinetic phenomena can increase oxide deposition by a factor of 12.

Electrokinetics allows thus explaining perfectly the localization and the form of TSP clogging. It seems that the electrokinetic phenomenon may be strongly involved in TSP clogging formation. However, this phenomenon remains poorly understood due to the lack of experimental or modelling investigations under typical SG conditions. Compared to *vena contracta* and flashing, no model describing electrokinetics under similar SG conditions has been reported in the literature. Therefore, its contribution in global TSP clogging formation cannot be directly estimated (Yang et al., 2017b).

A collaboration program has been created during the present work with the team of Scenini et al. in *the University of Manchester*, for investigating experimentally under simulated PWR secondary water conditions the deposit build-up by electrokinetic phenomenon (Chapter 3). More details will be given in paragraph 3.2 regarding the effects of water thermohydraulics and chemistry on deposit build-up by electrokinetics.

1.6 Conclusions of Chapter 1

In this chapter, flow accelerated corrosion of carbon steel materials, inducing magnetite particles and soluble iron species, has been identified as the major source term of PWR steam generator degradation phenomena. Different thermohydraulic and chemical parameters affecting FAC rate have been discussed. Among these parameters, pH is found to have a primary role by affecting magnetite solubility.

Magnetite particle deposition and soluble iron precipitation are the two main formation mechanisms of TSP clogging and SG tube fouling phenomena. Magnetite particle is predicted to be negatively charged under PWR SG conditions by previous experimental studies, as well as TSP composed of stainless steel. This prediction is essential for studying magnetite particle deposition phenomenon onto TSP surface. The basic particle deposition process comprises the particle transfer from bulk solution to the wall and the particle attachment. The specific model, *vena contracta*, considering the specific TSP geometric and thermohydraulics configuration, has also been proposed. Flashing is supposed to enhance soluble iron precipitation. Electrokinetics, allowing to explain the TSP clogging form and localization, remains poorly studied and no numeric model has ever been proposed regarding this phenomenon.

From this literature review on TSP clogging formation, a specific equation has been proposed at the inlet of TSP:

$$TSP \text{ clogging} = \text{magnetite particle deposition by vena contracta} + \text{flashing} + \text{electrokinetics}$$

This equation helps to understand the higher deposit growth rate of TSP clogging compared to tube fouling and is the starting point and a guideline for developing the experimental and numeric approaches for investigating TSP clogging phenomena in the next chapters of the present manuscript. The main objective of this work is to assay the magnitude of the different phenomena presented in the right side of this equation.

The sole existing data about the global TSP clogging formation has been reported from the EDF NPP feedback: up to 386 $\mu\text{m}/\text{year}$ of deposit is formed at the inlet of TSP. Laboratory-scale experimental deposit build-up tests under representative conditions appear of great interest to carry out parametric studies for improving the comprehension of TSP clogging phenomenon.

In the following chapter of the present manuscript, global TSP clogging deposit build-up tests in COLENTEC facilities and complementary tests in autoclave will be presented.

Chapter 2 Experimental investigation of TSP clogging phenomenon

2.1 Introduction

Global deposit build-up tests will be performed at the laboratory scale in order to characterize deposits, improve the knowledge about the phenomena responsible for TSP clogging and identify the influence of various parameters including test duration, materials, surface roughness *etc.*

The “COLMATage des générateurs de vapeur” project co-funded by EDF and CEA started in 2008 in order to provide data on deposit formation at the 8th TSP of steam generators under specific thermohydraulic and chemical conditions. For this goal, experiments were carried out by means of the two-phase flow test loop COLENTEC located at CEA Cadarache (France).

In 2015, two deposit build-up tests of 11 and 63 days were performed under experimental conditions close to nominal conditions. Stainless steel and titanium removable test coupons were majorly used onto a TSP made of titanium in order to characterize the deposits by means of visual observation, Scanning Electronic Microscopy (SEM) and Transmission Electronic Microscopy (TEM).

Representative tests using COLENTEC facility are very costly and time consuming. Simulated monophasic and static tests using autoclaves have been developed in parallel during this work for performing complementary studies, particularly for material corrosion investigations. Autoclave tests allow equally investigating galvanic corrosion's effects between stainless steel test coupons and contacted titanium TSP in COLENTEC tests, by using specifically designed titanium and stainless steel coupon combination.

2.2 Representative experiments

TSP clogging phenomena are predominant at the 8th TSP of 51B type steam generators where the temperature is equal to 277.2 °C, the pressure reaches 61.5 bars, $\text{pH}_{25\text{ °C}}$ and void fraction are equal to 9.2 and 85%, respectively (paragraph 1.4.2). In this section, a description of the representative test loop and experimental conditions applied during the tests will be presented.

2.2.1 Global deposit build-up tool under representative conditions: COLENTEC facility

The COLENTEC facility is composed of three loops that generate the two-phase flow configuration at the 8th TSP under representative conditions in the secondary circuit of the steam generators (Figure 2.1). The primary loop (Figure 2.2a) includes a boiler which is designed to provide pressurized water at 350 °C and 155 bars. The primary fluid velocity inside the tubes can reach near 6.5 m/s like in EDF NPP (Schindler et al., 2012). In order to respect and maintain these thermohydraulic conditions, primary thermal power must reach around 500 kW. This loop is connected to the secondary loop by another boiler and a four-tube steam generator mock-up, which is the test section of the COLENTEC loop. The flow is then condensed through the condenser connected to an air cooler (Figure 2.2b), which has the same maximal power as in the primary loop (500 kW). The condensate container plays the role of buffer volume. Measurements of chemical parameters (pH, redox, conductivity, oxygen concentration) and injection of chemical additives are performed by the chemical and volume control system (CVCS) (Figure 2.2c).

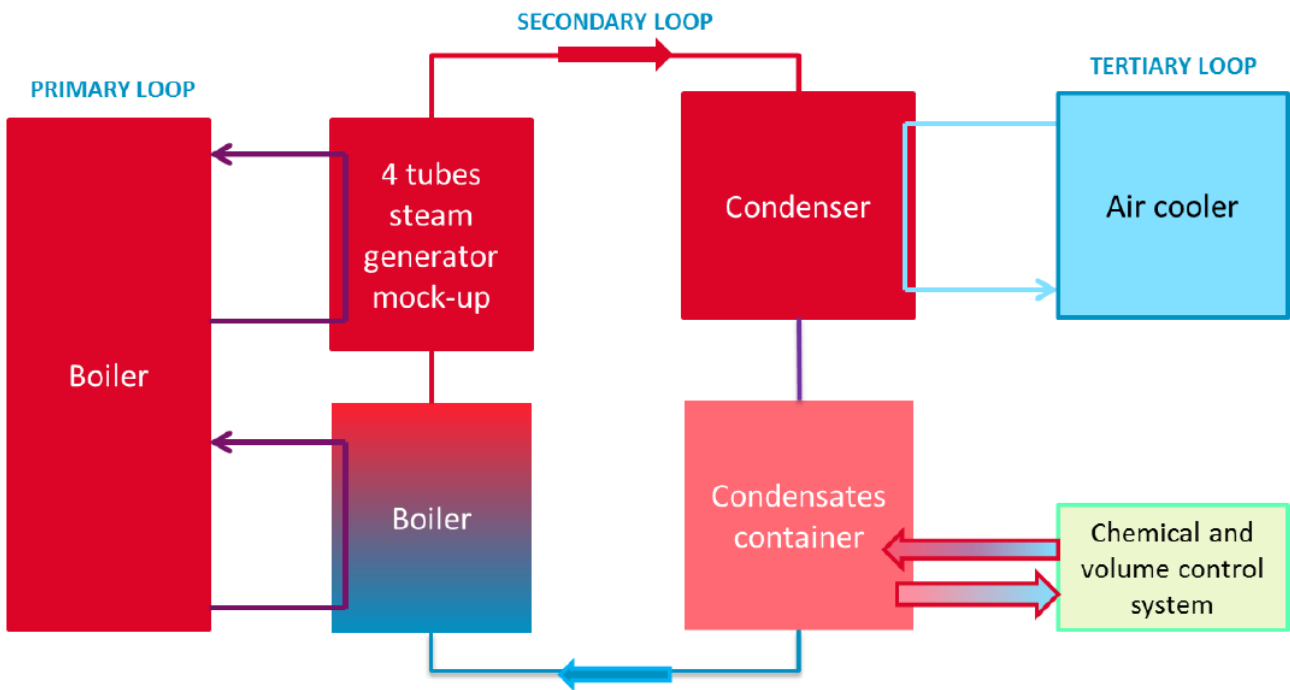


Figure 2.1: Flowsheet of the COLENTEC test loop.



Figure 2.2: Photo of COLENTEC primary loop (a), COLENTEC air cooler (b), and COLENTEC CVCS system (c).

The test section of the COLENTEC secondary loop (Figure 2.3a) contains a mock-up which is geometrically representative of the TSP (Figure 2.3b). Primary tubes are made of Inconel 600 TT like in real NPP and they are supplied by the same manufacturer as the SG tubes used in EDF NPP. The COLENTEC TSP is made of titanium and has been designed with removable test coupons in the four quatrefoils to allow deposit characterization (Figure 2.3c). The TSP in COLENTEC has a representative thickness of 3 cm like in TSP used in EDF NPPs.

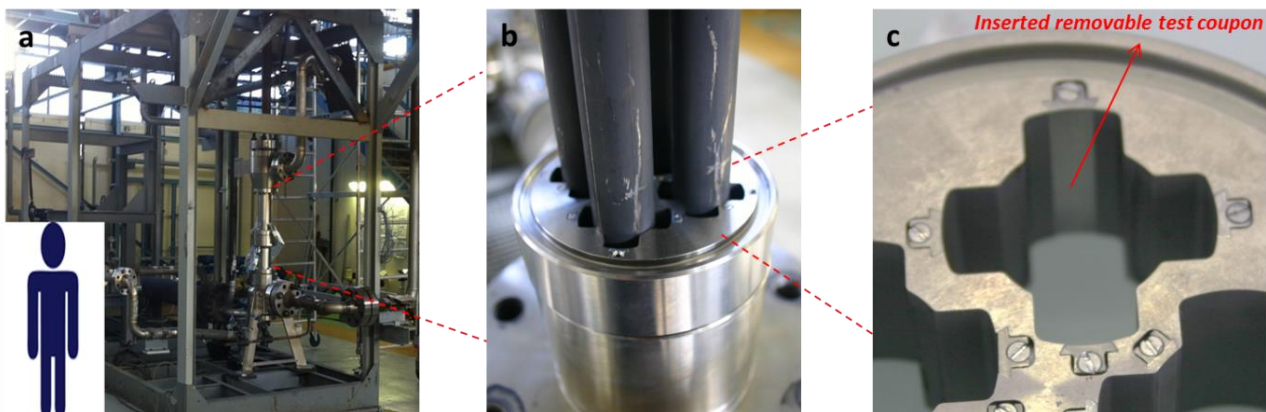


Figure 2.3: Photo of COLENTEC secondary loop (a), COLENTEC test section (b) with four primary SG tubes maintained by a titanium TSP (the COLENTEC secondary fluid circulates in the quatrefoils between the tubes and TSP) and COLENTEC titanium TSP with removable test coupons inserted in the dedicated sites (c).

Removable test coupons enable to perform various investigations such as the influence of the nature of the material and its roughness or the influence of surface pre-treatments on deposit formation.

COLENTEC tests require precise monitoring and control of the thermohydraulic and chemical operating conditions. A dedicated team of seven on-call workers ensures a proper functioning of COLENTEC during tests.

2.2.2 COLENTEC – 2015 experimental conditions

COLENTEC test loop has been designed to reproduce representative thermohydraulic and chemical conditions at the 8th TSP of 51B type PWR steam generators ($T = 277.2\text{ }^{\circ}\text{C}$, $P = 61.5\text{ bars}$, $\text{pH}_{25\text{ }^{\circ}\text{C}} = 9.2$ and void fraction = 85%). In 2015, a first test was conducted for 11 days (COLENTECT-2015-1) and a second test was performed for 63 days (COLENTECT-2015-1) to investigate the deposit formation kinetics. Unfortunately, thermohydraulic conditions were not exactly representative of SG during these tests because the condenser was too powerful. However, such conditions allow reaching a void fraction of 90% very close to those encountered in SG. This part of the manuscript will be dedicated to present the test conditions before characterizing deposits onto coupon surface.

COLENTEC-2015-1 was performed between the 13th of February and the 4th of March 2015. The test was resumed on the 24th of February after a shutdown during 20 days due to monitoring anomalies. Figure 2.4 shows the evolution of the temperature in the test section (red line), at the inlet and the outlet of the condenser (purple line and orange line, respectively) and at the inlet of the secondary boiler (blue line). Two-phase flow configuration in the test section (Figure 2.4, red line) was obtained during 6 days with a void fraction of about **90%**, a mass flow of about **0.9 kg/s** and a maximal temperature of **256 °C**. Before resuming the test, the similar two-flow configuration was achieved during 5 days (not represented in the Figure). Figure 2.4 shows the same profile of temperature was observed in each component of COLENTEC.

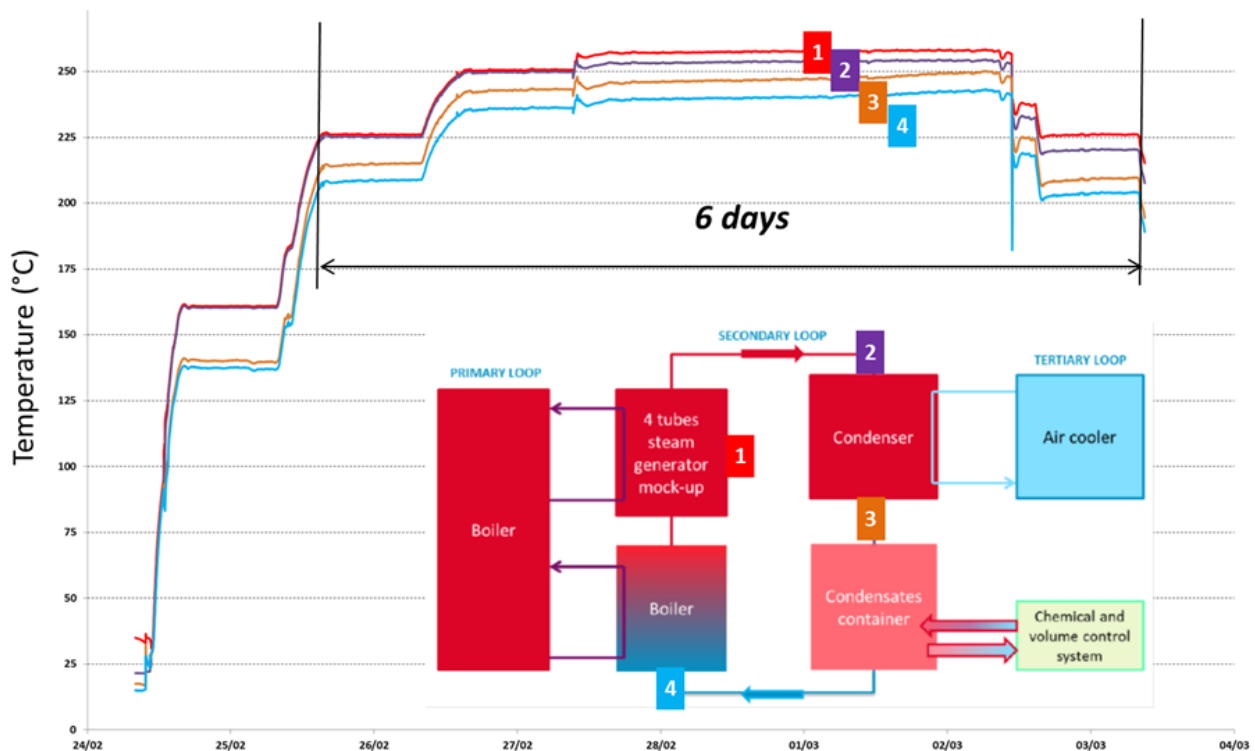


Figure 2.4: Evolution of the temperature in the test section (1), at the inlet (2) and the outlet of the condenser (3) and at the inlet of the secondary boiler (4) in COLENTEC-2015-1 test from the 24th February to the 4th March 2015.

During COLENTEC-2015-2, it was possible to achieve a two-phase flow configuration in the test section during 63 days with a void fraction of about **90%**, a secondary mass flow of about **0.9 kg/s** and a maximal temperature of **243 °C** (Figure 2.5, red line). Like in the COLENTEC-2015-1 test, the same profile of temperature was observed in each component of COLENTEC (Figure 2.5).

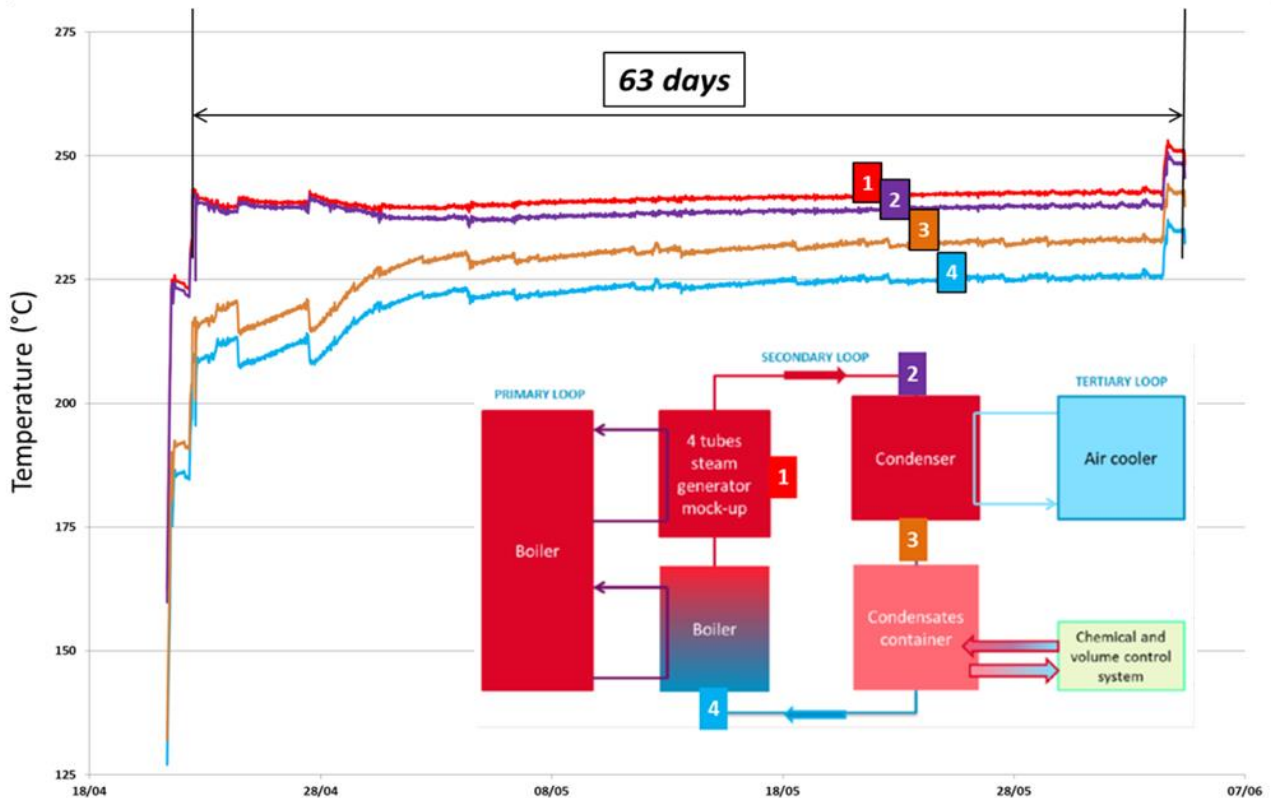


Figure 2.5: Evolution of the temperature during the COLENTEC-2015-2 test. (1): temperature in the test section; (2): temperature at the inlet; (3): temperature at the outlet of the condenser; (4): temperature at the inlet of the secondary boiler.

Chemical conditions were achieved during both COLENTEC-2015-1 and COLENTEC-2015-2 tests as the targeted values of pH and oxygen concentration were reached. A $\text{pH}_{25\text{ }^\circ\text{C}}$ of 9.2 was fixed during the tests to form the maximum of deposits during the tests (low pH values favour deposit formation). This pH was reached by using morpholine and ammonia. A flushing of pipes was performed by using a mixture of N_2 and H_2 (97.5% $_{\text{vol}}$ /2.5% $_{\text{vol}}$) before start-up in order to remove soluble oxygen from the secondary fluid (reducing environment). The soluble oxygen concentration was measured to be nil during both COLENTEC-2015-1 and COLENTEC-2015-2 tests.

A total iron concentration of around **30 ppb** was monitored and maintained for the two COLENTEC-2015 tests, by measuring CVCS samples by UV spectrophotometer and ICP-MS. The secondary boiler, made of carbon steel, is believed to be the major source term of iron. Magnetite in a degassed supersaturated solution was prepared and added to the secondary fluid when UV spectrophotometer measurements indicated a decrease of iron concentration in the fluid. One should remind that this total iron concentration of 30 ppb, measured via CVCS system, may not be the real concentration in the test section due to the changes in void fraction and temperature. Moreover, magnetite particle transport may be affected by the components between CVCS and test section as the secondary boiler and pipes.

Main experimental thermohydraulic and chemical conditions of COLENTEC-2015 are summarised in Table 2.1. Slight deviations in temperature between the two steps are not significant and the temperature in the test section is supposed to be **250 °C** for both COLENTEC-2015 tests.

Table 2.1: COLENTEC-2015 operating conditions.

Temperature (°C)	250
Void fraction	90%
Secondary fluid mass flow (kg/s)	0.9
pH_{25 °C}	9.2
Soluble oxygen concentration (ppb)	0
Targeted iron concentration in CVCS (ppb)	30

2.2.3 Materials used for COLENTEC test

For COLENTEC-2015 tests, titanium and stainless steel removable coupons were placed at the 8th TSP made of titanium in the secondary loop as previously illustrated in Figure 2.3c. The chemical composition of the used stainless steel samples is shown in Table 2.2. Such a composition is representative of real TSPs used in 51B type PWR steam generators. In addition of representative stainless steel coupons, titanium samples were used to facilitate the deposit detection and thickness measurement. Indeed, titanium has a similar zeta potential under SG conditions with that of stainless steel. Furthermore, iron detection onto titanium test coupons resulting from deposit formation would be indubitably related to a supply of iron species in the secondary fluid and not by the material corrosion. The chemical composition of used titanium test coupons is shown in Table 2.3.

Table 2.2: Chemical composition of the stainless steel test coupons used in COLENTEC tests (wt%).

Cr	Mn	Si	C	Ni	P	S	Fe
12.600	0.580	0.530	0.102	0.110	0.015	<0.003	Balance

Table 2.3: Chemical composition of the titanium test coupons used in COLENTEC tests (wt%).

O	Fe	N	C	H	Ti
0.150 – 0.170	0.040	0.012-0.016	0.010	0.001	Balance

Removable test coupons have a length of 30 mm, a maximal width of 7.19 mm and curved surface (Figure 2.6c), which allows satisfying the real geometric TSP flow hole configuration when inserted. A specific ergot is designed onto each coupon, for facilitating the fixation with TSP (Figure 2.6b). Figure 2.6d shows the initial TSP top view photo for COLENTEC-2015-1 test, with 16 test coupons fixed by means of the ergots. TSP flow hole surface is perfectly continuous and smooth (Figure 2.6d).

Surface pre-treatments, such as mirror-polishing, were performed for several coupons to investigate the effect of the surface roughness on deposit formation. Figure 2.6a shows an initial removable test coupons of titanium (Ti), stainless steel (SS) and mirror-polished titanium (M-Ti).

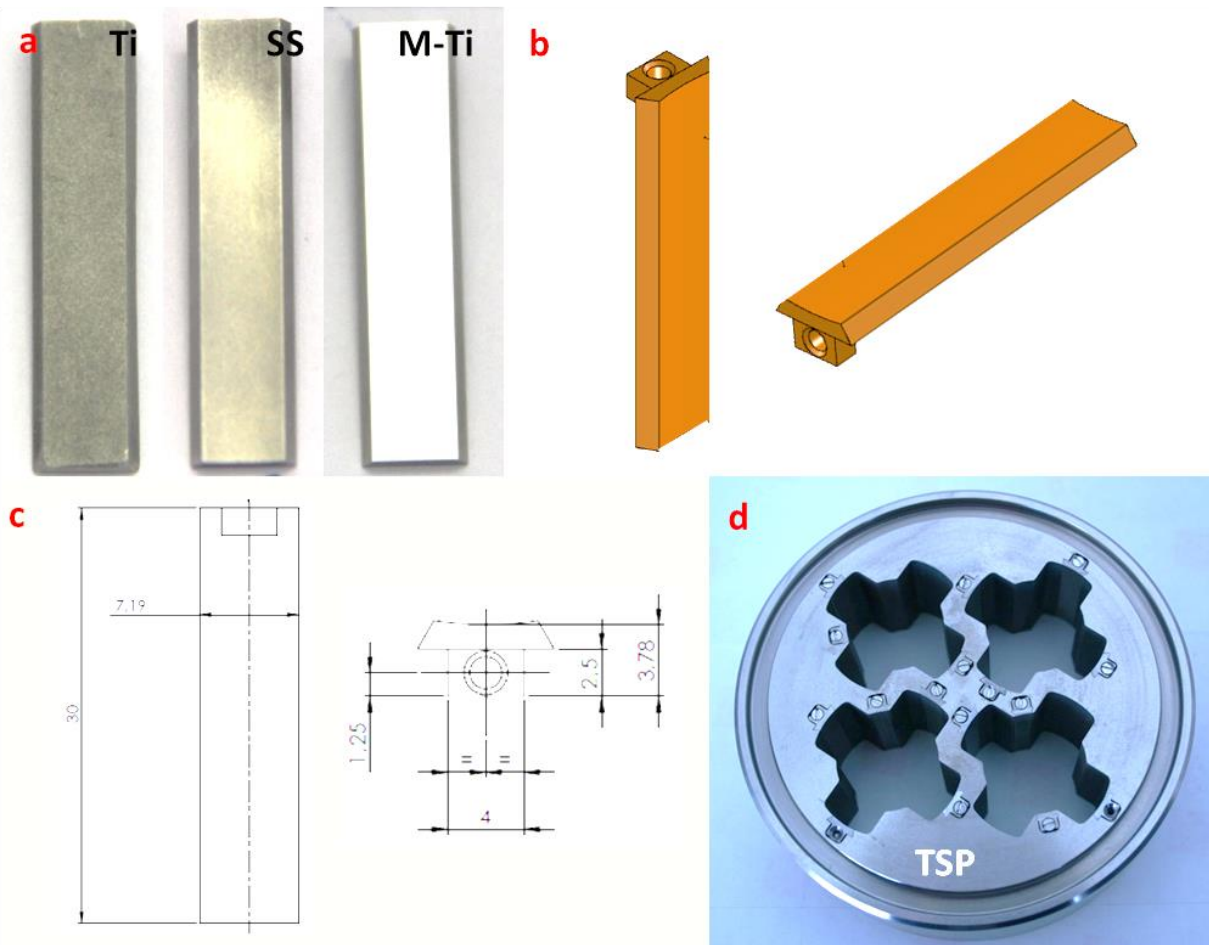


Figure 2.6: Photo of COLENTEC test coupons made of titanium (Ti), stainless steel (SS) and mirror-polished titanium (M-Ti) (a); Scheme of COLENTEC test coupons (b). A specific ergot is implemented for the TSP fixation and the coupon surface is curved to satisfy the real geometric configuration of TSP flow hole; Scheme of COLENTEC test coupons (c). Both titanium and stainless steel test coupons have a length of 30 mm, a maximal width of 7.19 mm and an equally-curved surface; Photo of the titanium TSP with 16 test coupons inserted for COLENTEC-2015-1 (d).

COLENTEC-2015-1 and COLENTEC-2015-2 were designed to study the kinetic of deposit formation. For this purpose, few test coupons were removed after 11 days for characterization, and afterward replaced by novel coupons. Test coupons were initially weighted, visualized and surface-characterized by roughness measurements.

All the pipes and components of the secondary loop are made of stainless steel (Type 316), except the boiler in the secondary loop, which is in carbon steel (Table 2.4) for ensuring the source term of deposit formation.

Table 2.4: Chemical composition of the carbon steel boiler used in COLENTEC tests (wt%).

Si	Mn	P	C	S	Fe
0.40	0.85	0.045	0.20	0.045	Balance

2.2.4 Characterization results of COLENTEC-2015 samples

Complete optical and SEM observations of coupons from COLENTEC-2015 test was performed (Pointeau, 2015). The main results and conclusions of these observations are summarized in this section. Such observations

demonstrate that SEM technique does not bring enough information about stainless steel samples because the corrosion layer and the outer layer of the deposits exhibit the same chemistry and crystallography. Therefore, additional characterizations by TEM have been performed within the framework of this PhD thesis on titanium and stainless steel thin section after 63 days under COLENTEC-2015 conditions to have more information about the nature of the deposits. This part of the manuscript is therefore mainly focused on the analyses of TEM characterization (Paragraph 2.2.4.2).

The functioning principle of SEM and TEM is described in Appendix A and B, respectively.

2.2.4.1 *Optical and SEM observations*

This deposit covers homogeneously the titanium surface. No lipping form and no ripple was observed onto the sample surface while EDF reported the presence of lipping form at the inlet and annular ripples along the TSP. A depleted-deposit region was observed on most of the titanium test coupons, which corresponds to the inlet of TSP (Figure 2.7).

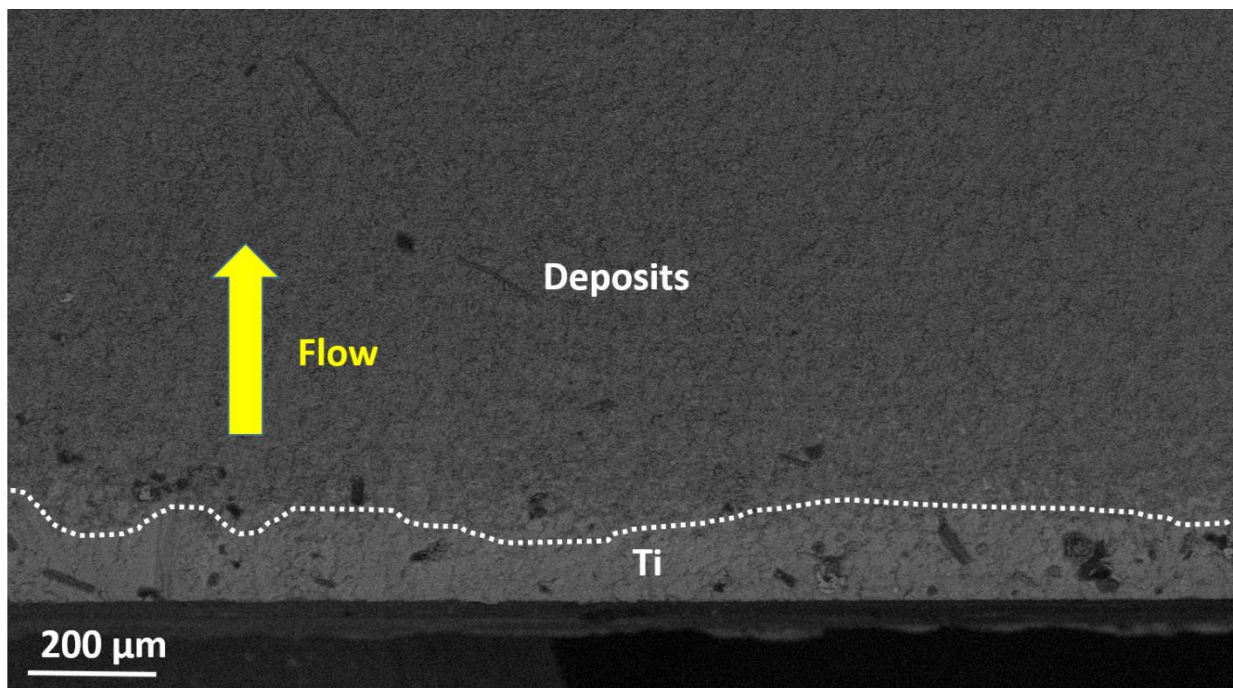


Figure 2.7: Surface morphology observed by secondary electron mode SEM of titanium test coupon after 11 days under experimental conditions of COLENTEC-2015-1. A depleted-deposit region is observed at the inlet of TSP.

Figure 2.8 shows a visual comparison of a titanium coupon and a mirror-polished titanium coupon after 11 days under the experimental conditions of the COLENTEC-2015-1 test. A comparison of the appearance of the sample surface after 11 days with the pristine surface shows the presence of a homogenous black deposit layer onto the sample surface, which is mainly composed of iron and oxygen. Conversely, no significant deposit can be observed on the mirror-polished titanium coupon after test under the same conditions. Therefore, there is obviously an effect of surface roughness on deposit formation. This effect was confirmed by correlating the estimated amount of deposit onto titanium coupons and its initial surface roughness. Indeed, it has been found that the deposit thickness increases with the initial surface roughness (Pointeau, 2015).

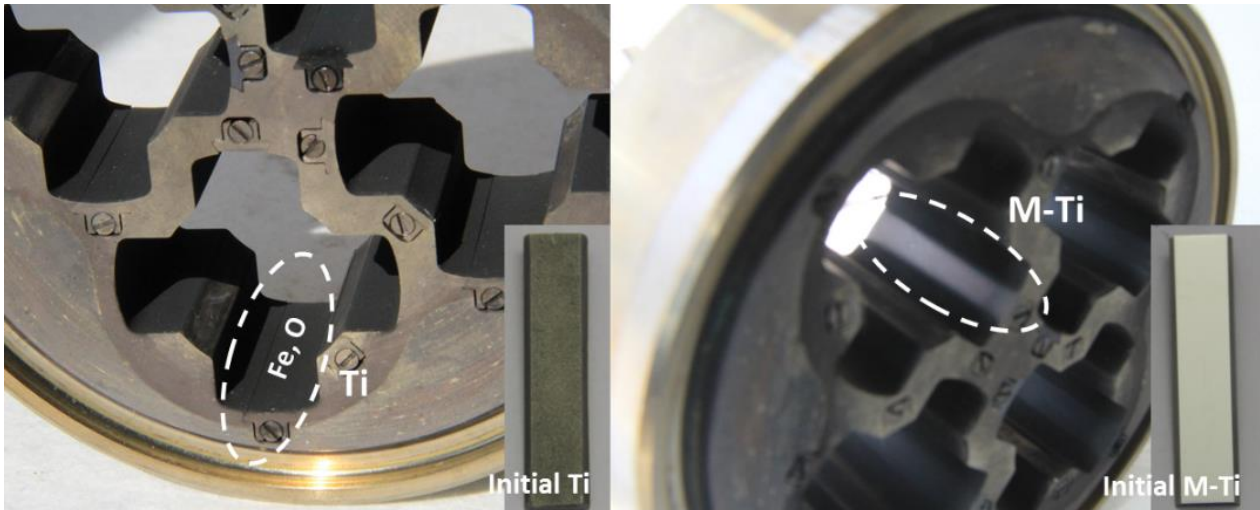


Figure 2.8: Comparison between a titanium (Ti) test coupon and a mirror-polished titanium (M-Ti) coupon after 11 days under experimental conditions of COLENTEC-2015-1. Ti sample after 11 days appears to be covered by a homogenous black layer, which contains majorly iron and oxygen (measured by EDS); M-Ti coupon appears unchanged.

SEM analyses of the coupons morphology showed in-situ precipitation (Pointeau, 2015). Figure 2.9a and b show the surface morphology of titanium test coupon after 11 days under COLENTEC-2015-1 conditions and 63 days under COLENTEC-2015-2 conditions, respectively. Cristal twinning is observed (surrounded by dash white line in Figure 2.9) in both surfaces, which results of intergrowth of two separate crystals following specific orientations. This result appears to highlight the deposit formation by in-situ crystal growth and not by simple particle deposition. Magnetite crystal twinning has been previously stated in the literature (Devouard et al., 1998). Moreover, larger particles of about $5\ \mu\text{m}$ are observed after 63 days compared to particles of about $1\ \mu\text{m}$ after 11 days, and the proportion of small particles appears to decrease with longer test duration. These results bring complementary supports for a deposit formation by in-situ precipitation and not by particle deposition. Particles with suitable size for deposition phenomenon may be insufficient in the test section.

Thicknesses of around $5\ \mu\text{m}$ and $30\ \mu\text{m}$ are generally measured on COLENTEC titanium test coupons after 11 days and 63 days, respectively. Deposit growth appears thus to follow a linear increase with time within 63 days.

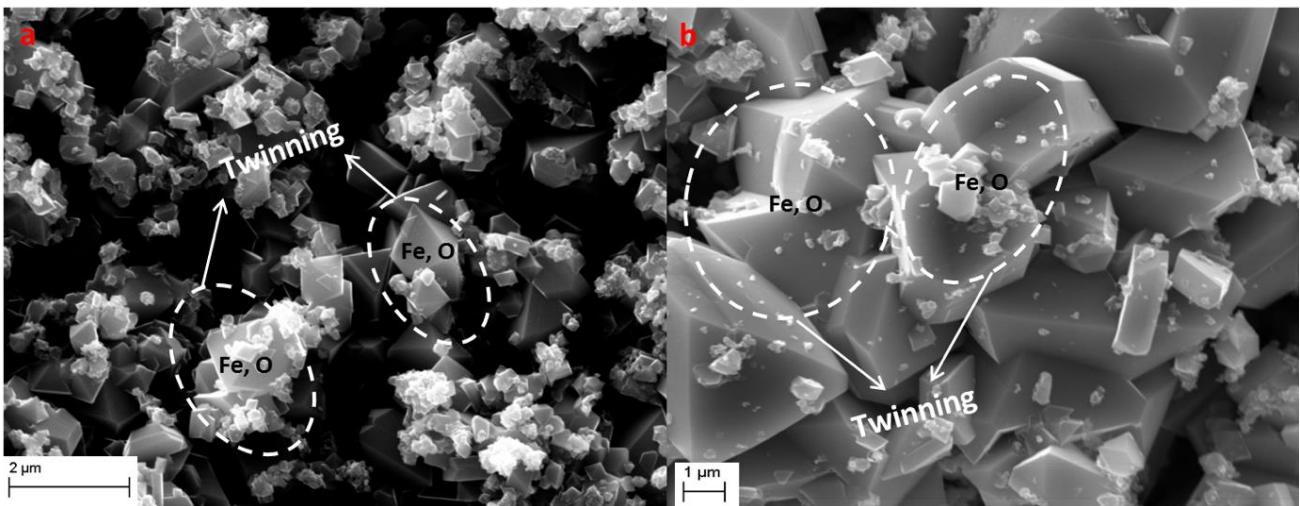


Figure 2.9: Surface morphology observed by secondary electron mode SEM of titanium test coupon after 11 days under experimental conditions of COLENTEC-2015-1 (a) and after 63 days under experimental conditions of COLENTEC-

2015-2 (b). Iron oxide crystal twinning is observed in both cases. Crystal size is estimated to be around 1 μm after 11 days (a), and 5 μm after 63 days (b).

Figure 2.10a shows SEM observation of a stainless steel cut coupon after the COLENTEC-2015-2 test. A compact alteration layer containing majorly iron and oxygen is observed. The initial metal-water interface seems to be observed (dash white line in Figure 2.10a). Therefore, the observed alteration layer contains likely the outer and inner corrosion layers of stainless steel, as previously stated in the literature (paragraph 1.2.6.3.3). Deposit layer formed on titanium test coupon also contains iron and oxygen but the morphology is different (Figure 2.10b), which appears more porous and discontinuous from the initial titanium-water interface (white line in Figure 2.10b). Therefore, the nature of the materials on which the deposit occurs influences deposit formation. The contribution of external iron brought by fluid is difficult to observe by SEM because the material corrosion layer exhibits the same composition and the same crystallography.

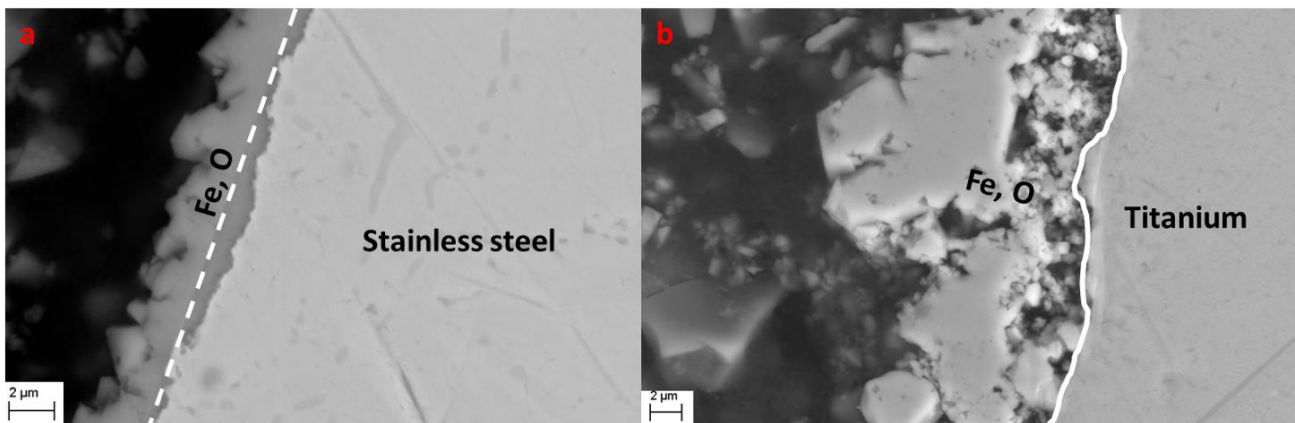


Figure 2.10: SEM picture in Back-scattered electron mode of stainless steel cut coupon obtained during the COLENTEC-2015-2 test (a) and titanium cut coupon obtained during the COLENTEC-2015-2 test (b).

*In summary, optical and SEM observations of coupons obtained during the COLENTEC-2015 test evidences that the nature of material and the initial surface roughness influence the amount of deposit. A rough surface favours deposit formation. The role of particle deposition cannot be clearly highlighted under COLENTEC conditions. Average thickness of the deposit after 11 and 63 days reaches 5 μm and 30 μm . **No ripple and no lipping form** has been observed at the inlet of TSP in COLENTEC 2015 tests unlike in EDF report.*

In the next section, TEM investigations will be performed in order to have additional and complementary information about deposit formation. A particular attention will be paid on the role of material corrosion on deposit formation.

2.2.4.2 TEM investigations

TEM observations were performed on a titanium and stainless steel test coupon obtained during COLENTEC-2015-2 test. Thin sections were prepared for each coupon for fine investigations by Focused Ion Beam (FIB).

2.2.4.2.1 Characterization of titanium thin section

Titanium alloys have excellent corrosion resistance, which results from the formation of very stable, continuous, highly adherent, and protective oxide films on metal surfaces. Because titanium metal is highly reactive and has an extremely high affinity for oxygen, these beneficial surface oxide films form spontaneously and instantly when fresh metal surfaces are exposed to air and/or moisture. The nature, composition, and thickness of the protective surface oxides that form on titanium alloys depend on environmental conditions. In most aqueous environments, the oxide is typically TiO_2 .

Three different areas of the COLENTEC-2015-2 titanium thin section are observed in Figure 2.11a: a close titanium substrate area (1), a porous layer (2) and an external compact layer (3). More attentions were paid to the close titanium layer, where different types of investigations have been performed in order to understand corrosion and deposition phenomena in this interface zone.

Close titanium layer (Figure 2.11a (1))

This thin area close to titanium is about 100 nm (Figure 2.11b, delimited by white lines), onto which particles of few hundreds of nanometres are deposited. This thin layer corresponds to the TiO_2 corrosion layer (Figure 2.11b) and the deposited particles are provided by secondary fluid, containing iron and oxygen, confined by EDS analyses (Table 2.5).

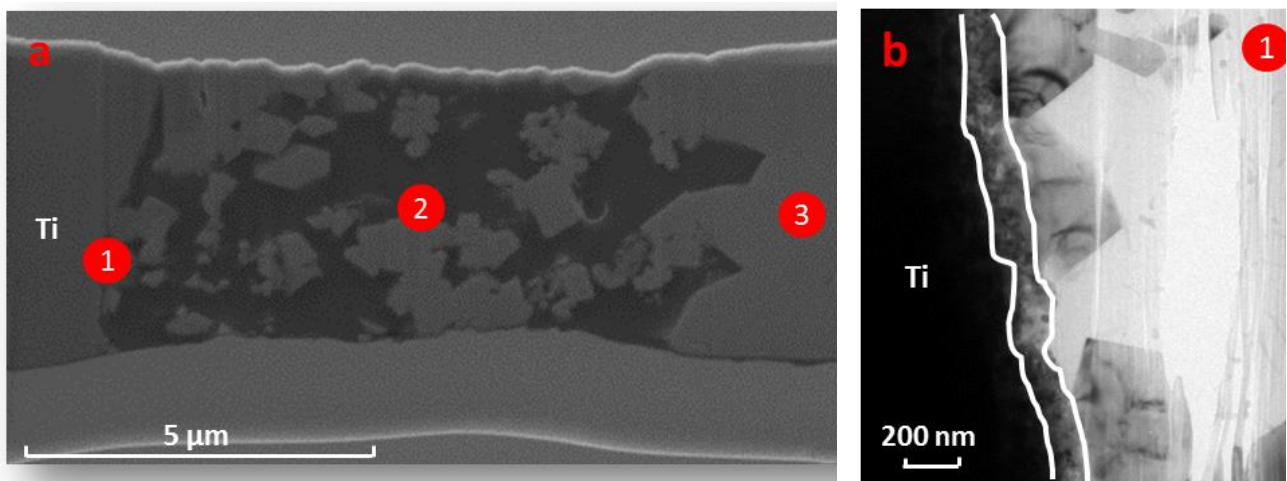


Figure 2.11: Thin section of titanium sample (a). Three principal areas are observed: (1): area close to titanium substrate; (2): porous layer; (3): compact layer; Zoom close to titanium substrate (b). White lines delimit a porous layer of around 100 nm, which is supposed to be the corrosion layer mainly composed of titanium and oxygen.

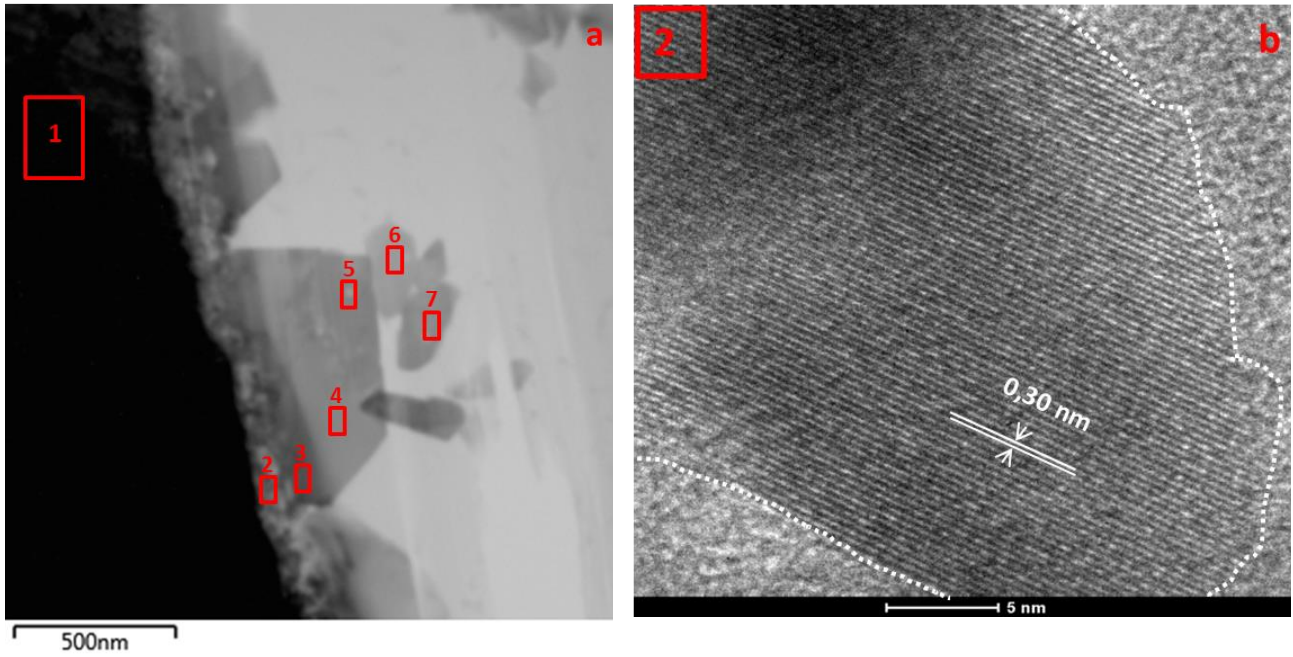
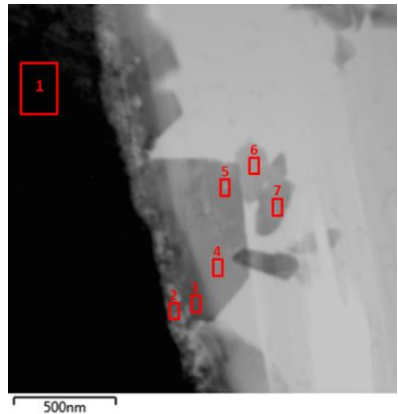


Figure 2.12: Seven different EDS analyses of titanium sample obtained during COLENTEC 2015 test in the area close to Ti substrate (a); High resolution (HR) TEM image (b) of a particle from #2 region in Figure 2.12a (white dash line represents the border of a particle present in this layer).

Table 2.5: Chemical composition (in at%) obtained by comparative EDS analyses at the different regions localized in Figure 2.12a. Percentages of each element are normalized to have a total of 100%. Relative uncertainties are estimated to be 1% for major elements (at% > 10%), and 5% for other elements. The numbers correspond to the numerated regions in the figure on the right.

	O(K)	Ti(K)	Al(K)	S(K)	P(K)	Mn(K)	Fe(K)	Zn(K)
1	13.12	84.33	0.04		0.02	0.02	0.11	2.37
2	62.75	34.05	0.23		0.23	0.58	2.15	
3	67.30	16.96				6.70	9.04	
4	63.47	19.03				8.04	9.46	
5	74.99	0.73	0.40	0.10	0.16	0.12	23.50	
6	71.25	0.54	0.49	0.16	0.13	0.09	27.34	
7	71.10	0.58	0.52	0.06	0.17	0.06	27.52	



The presence of zinc in the titanium sample may be attributed to its fabrication. The nanometric porous layer corresponding to EDS analysis #2 in Figure 2.12a is supposed to be the TiO_2 corrosion layer. Indeed, the atomic percentage of oxygen and titanium, measured by EDS, matches TiO_2 stoichiometry. Iron, which can only be provided by COLENTEC secondary fluid, is slightly presented in this corrosion layer (2.15%). HRTEM (Figure 2.12b) shows the presence of a crystallized particle in the TiO_2 layer with an interatomic distance of 3.0 Å, which corresponds to the 220 plane of the synthesised magnetite particles. This observation highlights the inclusion of external iron species into titanium corrosion layer forming magnetite particles.

An intermediary compact layer with manganese enrichment, corresponding to EDS analyses #3 and #4 in Figure 2.12a, is observed next to the TiO_2 corrosion layer. Impurities like aluminium, sulfur and phosphate are not detected in this layer. This compact layer may be composed of a solid solution comprising manganese, iron,

titanium and oxygen, with an approximated atomic proportion of 1, 1, 2 and 6, respectively. Similar stoichiometric hexagonal solid solutions $(\text{Mn}_{1-x}\text{Fe}_x)\text{TiO}_3$ ($x = 0.5$ and $x = 0.6$) have been reported in the literature (Wu et al., 2010). However, they were synthesised by mixing MnCO_3 , Fe_2O_3 and TiO_2 particles under $1200\text{ }^\circ\text{C}$ and CO-CO_2 gas mixtures, which are highly different from COLENTEC conditions. Diffraction patterns of this layer should be acquired to verify the formation of the corresponding solid solutions.

Particles corresponding to EDS analyses #5, 6 and 7 in Figure 2.12a contain mainly iron and oxygen. The presence of aluminium, sulfur and phosphate is also detected. The size of these particles is of about several hundreds of nm.

EDS profile analyses (Figure 2.13) confirm that the porous thin layer close to titanium substrate comprises majorly titanium and oxygen. A slight increase of iron and manganese is observed in this corrosion layer, consistent with previous EDS analyses (Table 2.5, EDS analysis #2). Two intermediate layers are then observed with the presence of titanium, oxygen, iron and manganese, with a relatively stable atomic proportion respectively. Iron particle layer is detected next to the intermediate layer, comprising majorly iron and oxygen. The formation of this layer is indubitably linked with external secondary fluid.

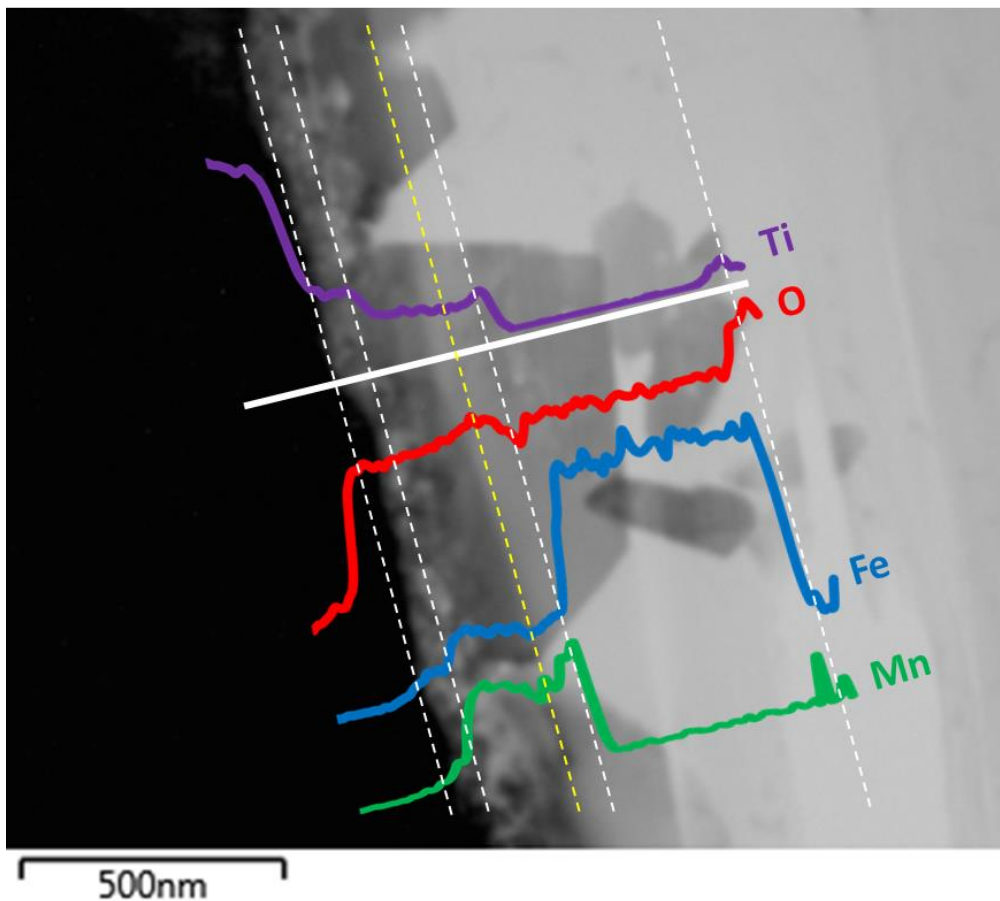


Figure 2.13: EDS analyses showing atomic percent of element was performed along the white line, crossing titanium sample, TiO_2 corrosion layer, two potential $(\text{Mn}_{1-x}\text{Fe}_x)\text{TiO}_3$ solid solution layers separated by the yellow dash line and iron particles. Only the evolution of each element is intended to be shown along the white line, comparisons between different elements are not significant.

EDS mapping in Figure 2.14 and Figure 2.15 confirm the above observations throughout the titanium thin section and in a selected zoomed area, respectively. The mapping indicates generally minor iron inclusion into titanium corrosion layer, enrichment of manganese in the intermediate layer and formation of particles comprising iron and oxygen on the external side of mapping zone. The same multi-layer structure is observed in the EDS zoomed mapping presented in Figure 2.15, as previously indicated in Figure 2.13.

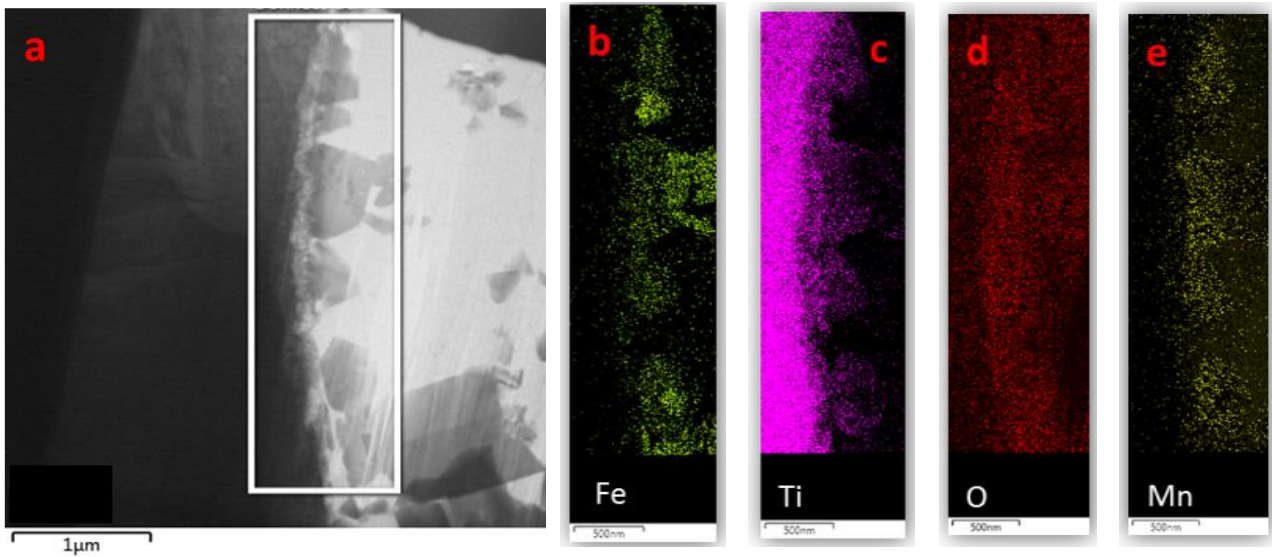


Figure 2.14: EDS mapping of the closed titanium area, containing titanium substrate, TiO_2 corrosion layer, potential solid solution layer and deposited iron particles, showing the TEM image and mapping zone (a); and element distribution of iron (b), titanium (c), oxygen (d) and manganese (e).

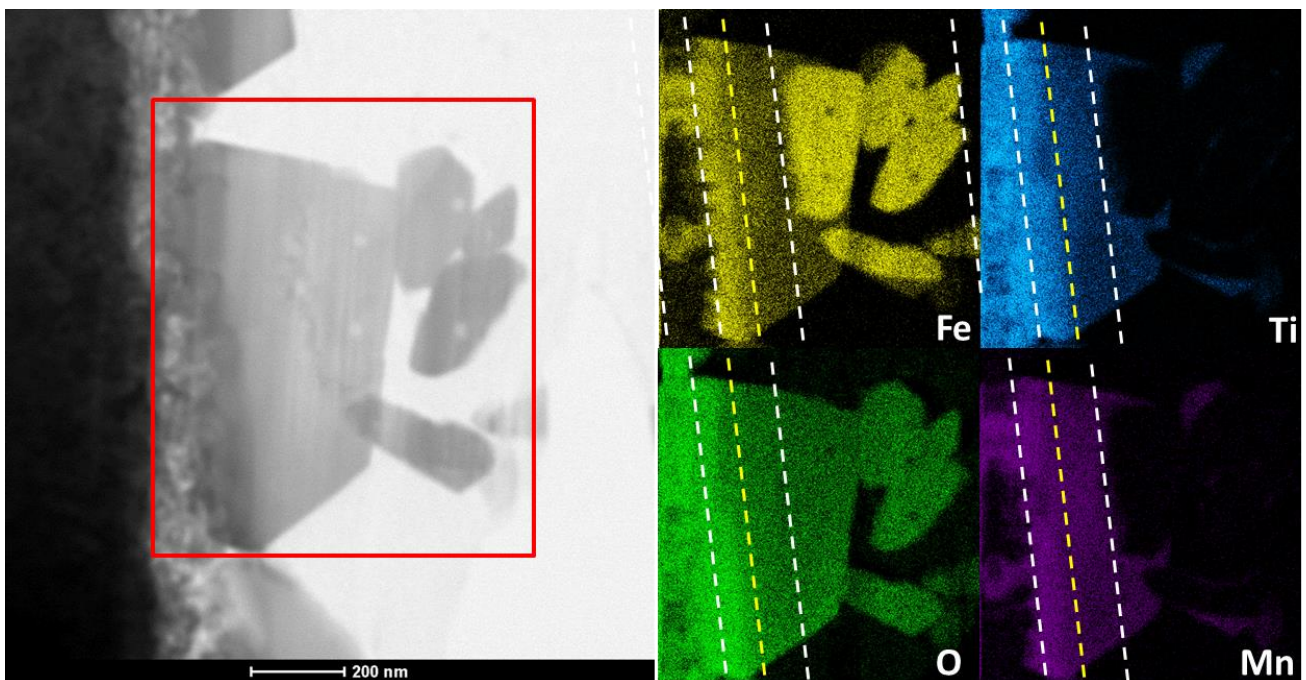


Figure 2.15: EDS mapping of a zoomed close titanium area, containing TiO_2 corrosion layer, the two potential solid solution layers and deposited iron particles, showing the TEM image and mapping zone and element distribution of iron, titanium, oxygen and manganese.

Porous and compact layers (Figure 2.11a (2), (3))

EDS measurements and the electron diffraction patterns were then performed for particles located in the porous and external compact layers of titanium thin section in order to determine their chemical composition resulting from the fluid without titanium substrate effects.

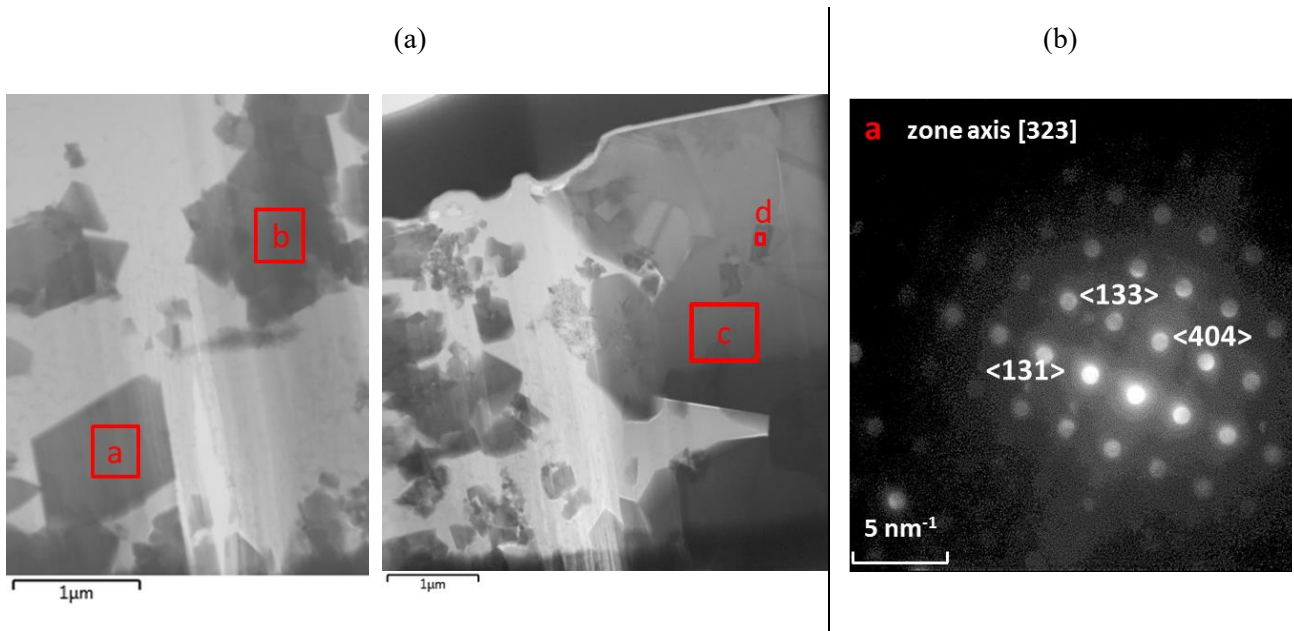


Figure 2.16: Surface TEM and EDS analysis of porous and external compact layer in the titanium sample obtained during the COLENTec 2015 test (a). The EDS analyses were performed under the same conditions in the four red areas shown in the TEM image; Diffraction patterns (b) of *a* area in Figure 2.16a.

Table 2.6: Chemical composition (in at%) deduced from EDS analyses of points *a*, *b*, *c* and *d* in Figure 2.16a. Percentages of each element are normalized to have a total of 100%. Relative uncertainties are estimated to be 0.5% for iron and oxygen, and 5% for other elements.

	O(K)	Ti(K)	Al(K)	Cr(K)	P(K)	Mn(K)	Fe(K)	Ni(K)
a	62.71	0.11				0.84	36.33	
b	61.11	0.07	0.40	0.04	0.28	0.43	37.24	0.43
c	54.65		0.44		0.57	0.51	43.61	0.22
d	42.85		0.35		0.60	0.61	55.36	0.24

Oxygen and iron are the two major elements for both EDS analyses *a*, *b*, *c* and *d* in Figure 2.16a. Iron/oxygen ratio increases when analyses are performed from the porous layer to the external compact layer. Diffraction patterns confirm the presence of the magnetite structure composite by identifying <131>, <133> and <404> planes of magnetite. Chromium is not detected in the micrometric well crystallized particles (EDS analysis *a*) and compact layer (EDS analyses *c* and *d*) whereas its presence is observed in the zone exhibiting smaller particles (several hundreds of nm) (region *b* in Figure 2.16a). Impurities like aluminium, phosphate and silicon are detected in the compact external layer and their presence is confirmed by EDS mapping (Figure 2.17). An enrichment of chromium and manganese is detected in a local zone of the selected area, corresponding to an impoverishment of iron (Figure 2.17). This result indicates the possible iron substitution by chromium or manganese in the magnetite structure composites when chromium and manganese are present.

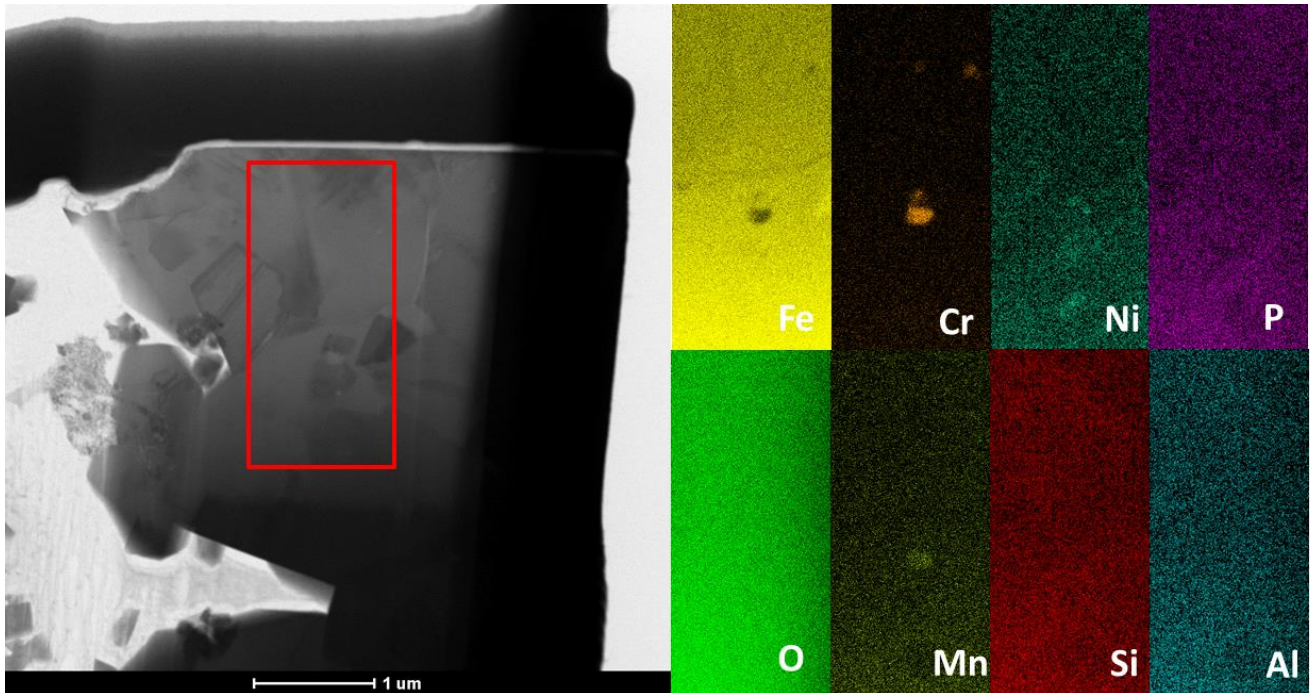


Figure 2.17: EDS mapping of a selected area of the compact layer of the titanium thin section.

2.2.4.2.2 Characterization of stainless steel thin section

Three different layers for the thin section of stainless steel sample obtained during the COLENTEC 2015 test were identified by TEM (Figure 2.18a). This Figure shows an inner corrosion layer of about 1 μm (1), an outer corrosion layer of about 5 μm (2) and a local particle aggregation (3) deposited onto the outer corrosion layer.

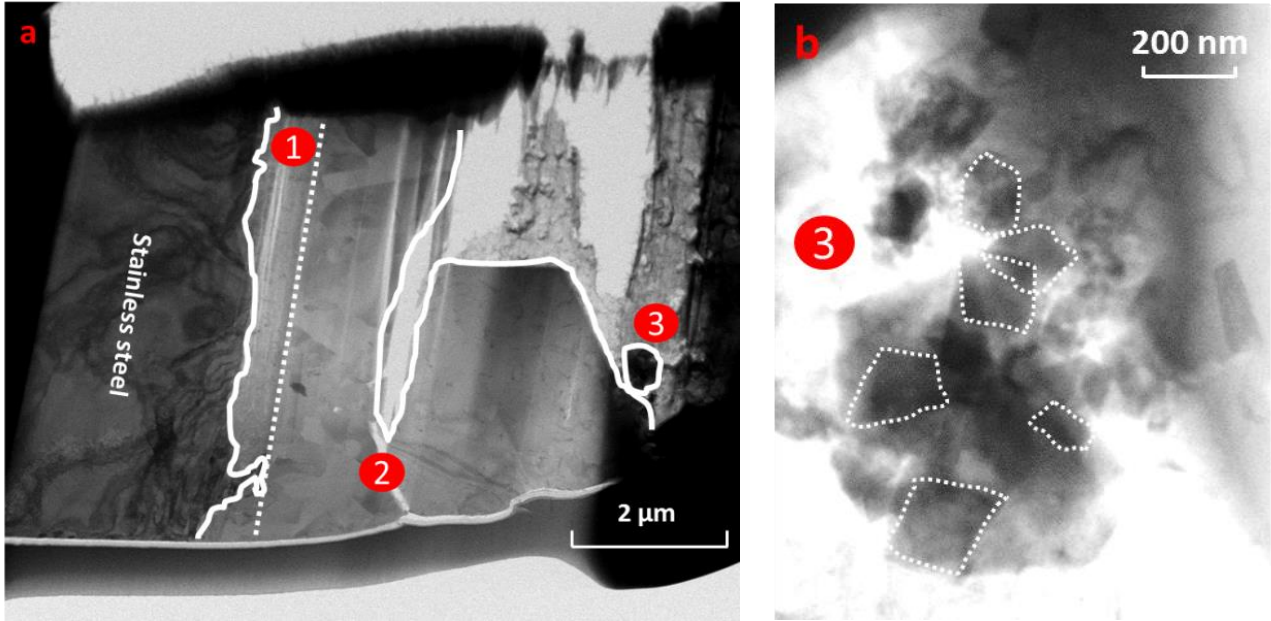


Figure 2.18: Pictures by TEM in the bright field (BF) mode of the thin section of stainless steel sample obtained during the COLENTEC 2015 test (a). Three different layers are observed: (1) Compact inner corrosion layer delimited by an outer-inner layer interface (white dash line), (2) Compact outer corrosion layer and (3) Particle aggregation; Specific TEM BF observation of particle aggregation (b) (Particles size is of about several hundreds of nm).

The evidence of inner and outer corrosion layers seems consistent with the literature, as presented in paragraph 1.2.6.3.3. Indeed, a well-defined regular line (Figure 2.18a, white dash line) delimits the inner and outer layers, which appears to be the original metal-water interface. The inner layer appears compact (Figure 2.18a, (1)). The outer layer (Figure 2.18a, (2)) also appears compact, which is different from the observations during stainless steel corrosion investigations in the absence of iron in the feed water at the inlet of the SG (1.2.6.3.3). The dense layer may result from the presence of iron in the secondary fluid as particles and/or solubilized species. The iron incorporation into stainless steel corrosion layer may be indirectly confirmed by previous observation on titanium sample. Indeed, iron exists in titanium corrosion layer (2.2.4.2.1) whereas iron has different ionic radius from titanium. It can be expected that the external iron is more largely present in stainless steel corrosion layer, together with iron provided by material, forming corrosion layer majorly on iron and oxygen. It seems that stainless steel corrosion is not responsible for the formation of the particle aggregation onto the outer corrosion layer because the aggregation appears to have a different morphology from the corrosion layers. Moreover, the interface between the aggregation and the outer layer is discontinuous (Figure 2.18b). Therefore, the observed particles are more likely provided by iron species in the secondary fluid rather than stainless steel corrosion. The particle size in the aggregation can be estimated to be several hundreds of nm (Figure 2.18b). EDS characterizations reported in Figure 2.19 and Table 2.7 were performed in order to (i) analyse the chemical composition of different layers and (ii) find indications to confirm the formation of particle aggregation layer provided by secondary fluid.

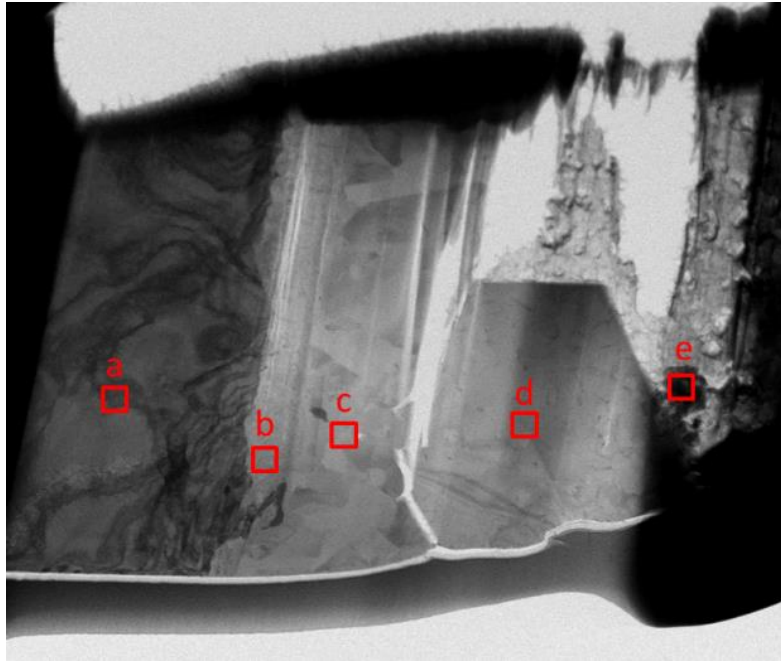


Figure 2.19: Surface TEM and EDS analysis of stainless steel sample obtained during the COLENTEC-2015 test. (a) stainless steel material; (b) inner corrosion layer; (c) and (d) outer corrosion layer; (e) particle aggregation. The EDS analysis was performed under same conditions in the five red areas (see composition in Table 2.7).

Table 2.7: Chemical composition (in at%) obtained by comparative EDS of the different regions defined in Figure 2.19. Percentages of each element are normalized to have a total of 100%. Relative uncertainties are estimated to be 0.5% for iron and oxygen, and 5% for other elements.

		O(K)	Al(K)	S(K)	P(K)	Ca(K)	Cr(K)	Mn(K)	Fe(K)	Ni(K)
Stainless steel	a	7.26					12.43	0.60	79.58	0.13
Inner corrosion layer	b	64.24			0.18		10.82	0.27	24.36	0.13
Outer corrosion layer	c	68.38	0.24		0.27		0.04	0.18	30.49	0.40
	d	65.99			0.02				33.69	0.30
Particle aggregation	e	65.79	0.18	0.05	0.11	0.07	0.11	0.35	33.08	0.26

Iron and oxygen are the two major elements in both inner (b) and outer (c and d) corrosion layers, and particle aggregation (e) layer. Chromium is largely present in the inner (b) corrosion layer (10.82%), whereas its percentage in outer corrosion layer becomes negligible (c and d). This observation is in accordance with the literature statements: Chromium enrichment occurs in the inner corrosion layer of stainless steel and the outer corrosion layer contains only magnetite (see paragraph 1.2.6.3.3). Phosphate is not detected by EDS in the initial material (a), whereas it should be present as indicated in Table 2.2. This may be attributed to its small percentage, which may not be high enough to be detected. The detection of phosphate for all other 4 points highlights potentially another phosphate source than initial material, which can be supposed to be COLENTEC fluid. The presence of calcium, sulfur, aluminium and phosphate is believed to be under inclusion form, surrounded by iron particles, as their atomic radius is largely different from iron. However, no evidence was found experimentally. The proportion of nickel seems higher in the outer layer and particle aggregation layer than in the inner layer. No obvious difference of oxygen and iron percentages can be observed between the outer corrosion layer and the particle aggregation.

Impurity elements like calcium, sulfur and aluminium, which are not present in the original stainless steel material, may be provided by secondary fluid. The presence of all of these impurities is observed in the particle aggregation, indicating that this aggregation may arise more likely from fluid than material corrosion even

though the impurities' quantity remains small. The chemical composition of the particle aggregation of the stainless steel sample obtained during the COLENTec tests (Table 2.7) is similar to EDS analysis of iron particles contained in the titanium porous layer (EDS point *b* in Figure 2.16a (Table 2.6)), with detection of aluminium, sulfur and phosphate impurities and chromium. Moreover, aggregation particles onto stainless steel coupons seem to have the same particle size (several hundreds of nm) as small particles observed in the titanium porous layer (Figure 2.16a). These results may highlight that the particle aggregation on the stainless steel sample is formed by fluid contribution, given that iron deposit onto titanium sample can only be provided by particular or soluble iron species in secondary fluid and iron deposit exhibits the same morphology and composition as those observed onto the stainless steel sample.

The electron diffraction patterns acquired for *b*, *c* and *d* areas and HRTEM image of a particle located in (*e*) area (Figure 2.20a) are shown in Figure 2.20b-e.

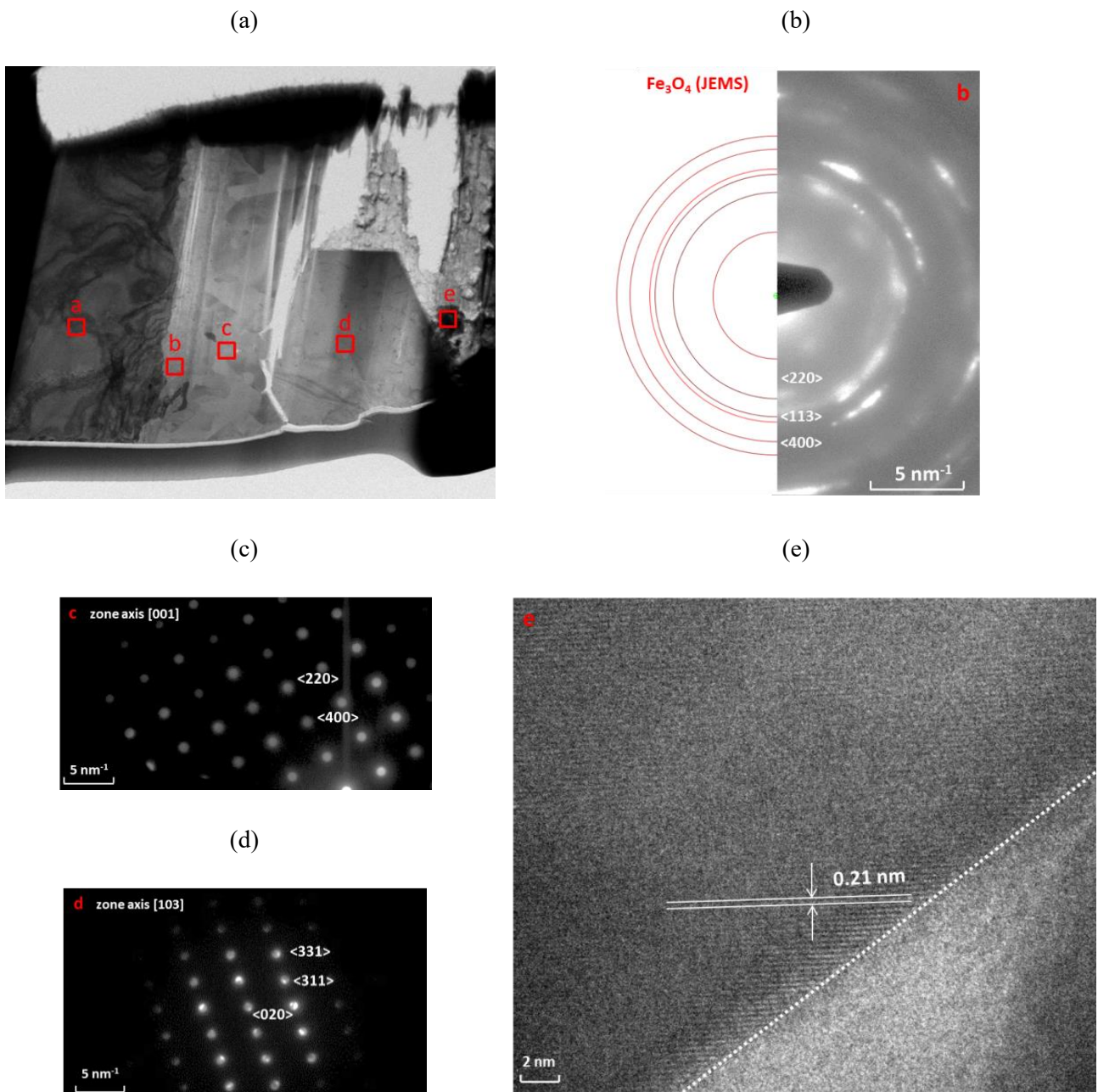


Figure 2.20: Indicator of different regions where analyses are performed (a); Diffraction patterns of *b* area (b); Diffraction patterns of *c* area (c); Diffraction patterns of *d* area (d); High resolution (HR) TEM image of a particle from *e* area (white dash line represents the border of a particle present in this layer) (e).

The observation of ring electron diffraction (Figure 2.20b) highlights that the inner corrosion layer is composed of a mixture of small particles, like previously reported by the literature. The interatomic distances calculated in this diffraction pattern are 2.1, 2.5 and 3.0 Å, corresponding to the $\langle 400 \rangle$, $\langle 113 \rangle$ and $\langle 220 \rangle$ planes of synthesised magnetite particles, respectively (JEMS source). The electron diffraction patterns in Figure 2.20c and d show the presence of large well crystallized particles in the outer corrosion layer, consistent with the literature observation. The $\langle 220 \rangle$ and $\langle 400 \rangle$ planes of magnetite particles have been identified for the c area (Figure 2.20c), and the $\langle 020 \rangle$, $\langle 311 \rangle$ and $\langle 331 \rangle$ planes of magnetite are identified for the d area (Figure 2.20d). Magnetite structure can thus be considered as the major compound of both inner and outer corrosion layer. Detected chromium, manganese and nickel may substitute iron in the magnetite structure and affect poorly the electron diffraction results, as they have similar atomic radius. For example, chromium substituted spinel ferrites, e.g., Fe_2CrO_4 , have very close cubic lattice parameters (a) to magnetite particles. ($a_{(\text{Fe}_2\text{CrO}_4)}$ vs. $a_{(\text{Fe}_3\text{O}_4)} = 8.38 \text{ \AA}$ vs. 8.40 \AA). Composition of the inner corrosion layer varies following chromium variation. Iron and oxygen are the two main composing elements of particles present in (e) area of Figure 2.20a (Table 2.7). The high-resolution transmission electron image (Figure 2.20d) shows an interatomic distance of 2.1 Å, which corresponds to the $\langle 400 \rangle$ plane of the synthesised magnetite particles.

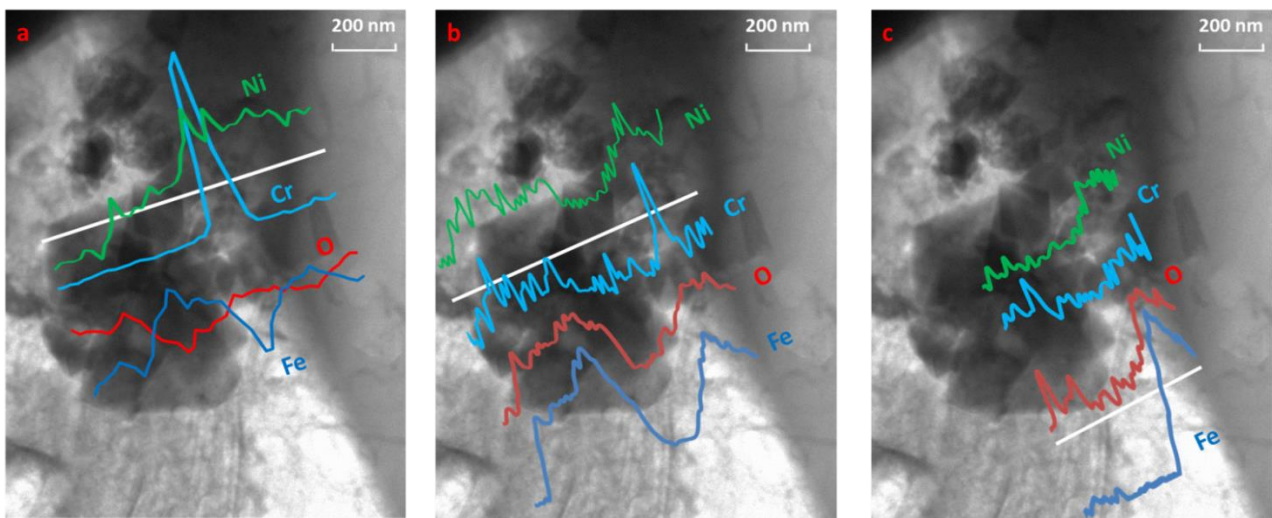


Figure 2.21: EDS analyses performed along the white line in images (a), (b) and (c). Only the evolution of each element is intended to be shown along the white line. Comparisons between different elements are not significant.

Figure 2.21a and b show two EDS linear measurements (white line) across the particle aggregation area and the outer corrosion layer. The presence of the chromium peak at the interface demonstrates that the stainless steel sample may be passivated. EDS mapping of the interface zone between the particle aggregation and outer corrosion layer shows the formation of a continuous Chromium enriched layer at the outermost corrosion layer of about 100 nm thickness (Figure 2.22). Indeed, the passivation of stainless steel occurs when a thin layer enriched by chromium forms at the outermost corrosion layer. This chromium layer will inhibit the oxygen diffusion from the external into the solid material. Further corrosion can thus be prevented. Therefore, the presence of the iron particle layer is more likely induced by another phenomenon than material corrosion, e.g., deposition or precipitation phenomenon by iron species in secondary fluid. Another EDS measurement, which is not performed in the particle aggregation area, shows the absence of the chromium peak at the outermost corrosion layer (Figure 2.21c). The above observations seem to reveal an important impact of stainless steel passivation for the start of a proper formation of a deposition layer: when the stainless steel material is passivated, external iron species can form a deposition layer onto the material corrosion layer. Otherwise, the deposition layer cannot be formed and external iron species may be incorporated into material corrosion layer until passivation.

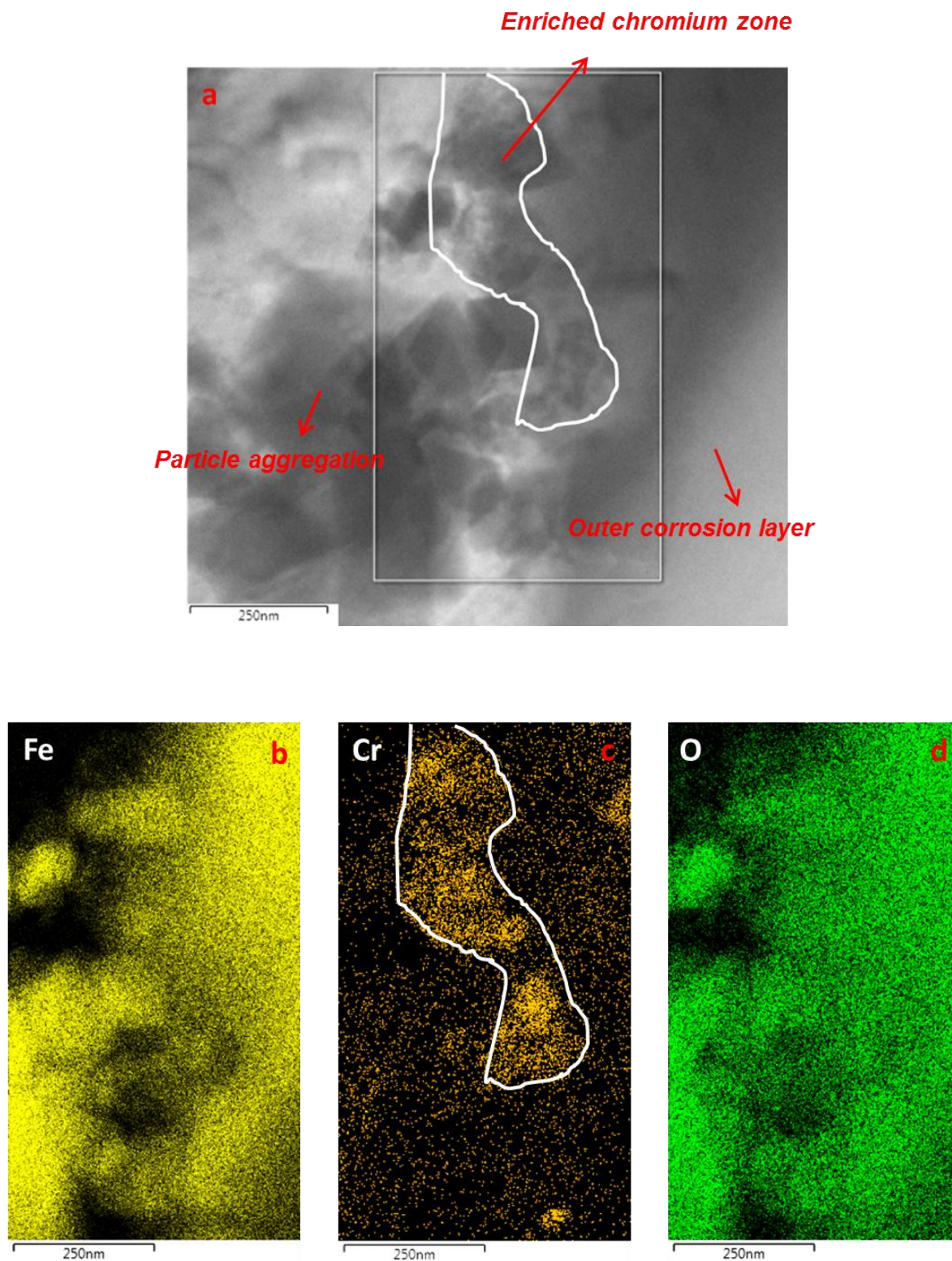


Figure 2.22: EDS mapping of the interface area between particle aggregation layer and outer corrosion layer, showing the TEM image and mapping zone (a); and element distribution of iron (b), chromium (c) and oxygen (d). A thin chromium (around 100 nm) enriched layer is observed at the outermost corrosion layer and delimited by white line in (c).

The above chemical and morphological analyses highlight an influence of the nature of the material on deposit formation: iron oxide deposition is formed more rapidly with a thicker and more compact deposition layer for the titanium sample than for stainless steel sample. The kinetic of deposition formation seems to be conditioned by material corrosion. In the case of stainless steel, corrosion layer containing Fe and O favours likely the incorporation of external iron species provided by secondary fluid. Material is then more difficult to be passivated and the deposition formation is kinetically delayed. In the case of titanium sample, TiO₂ corrosion layer may be formed rapidly and may initiate the iron deposition formation.

Injection of tracer species in secondary fluid may be useful to confirm the external contribution by fluid to stainless steel corrosion.

In the next section, results from autoclave tests will be presented in order to bring complementary information about the possible iron incorporation into stainless steel corrosion layer from an external source. Potential galvanic corrosion effect between Ti and SS will be studied as well.

2.3 Simulated experiments

Simulated tests using autoclaves were performed in monophasic and static solutions. The same experimental conditions regarding the chemistry and temperature as during COLENTEC-2015 test were chosen. Iron precipitation into stainless steel corrosion layer will be investigated by varying iron concentration in the solutions containing stainless steel samples. Ti/SS galvanic corrosion effects will majorly be studied by specifically designed Ti-SS-Ti samples.

2.3.1 Description of autoclave tests

Material corrosion was investigated in parallel with COLENTEC tests by autoclaves. Test conditions are representative of COLENTEC conditions in terms of temperature and water chemistry. However, the autoclave samples can only be immersed in a monophasic and static environment, compared to the representative dynamic two-phase flow tests.

Four individual stainless steel autoclaves were used in the present work (4776 General Purpose Pressure Vessel, 100 ml, Parr Instrument). Temperature and pressure were daily controlled during the test. The maximum of temperature and pressure in these autoclaves was of 300 °C and 100 bars, respectively. Figure 2.23 shows a photo of the autoclaves used in this work.

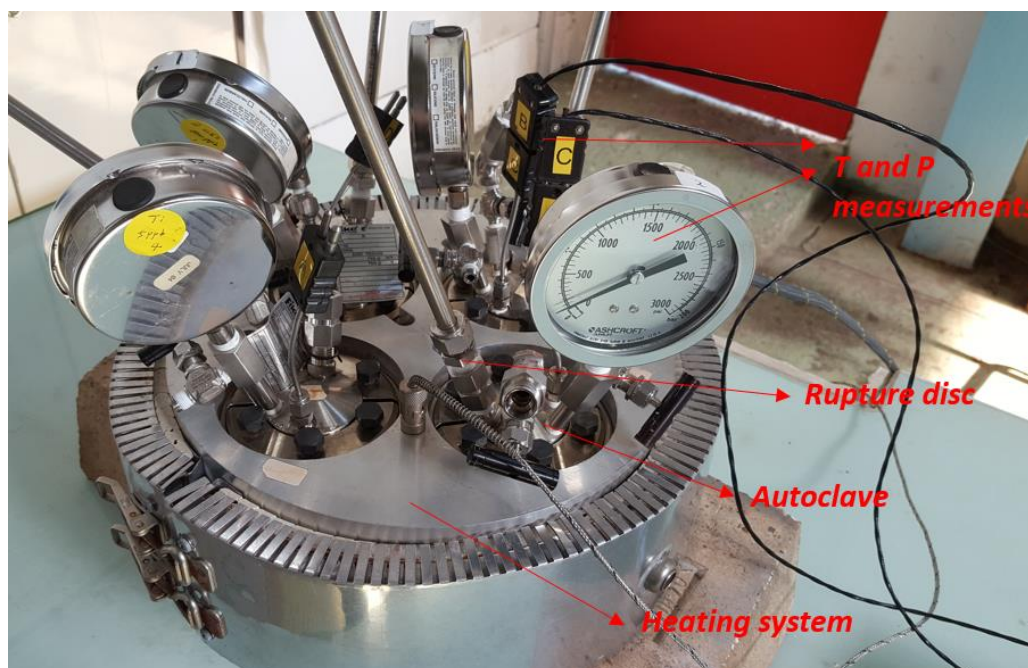


Figure 2.23: Photo of autoclave system.

The same stainless steel (SS) and titanium (Ti) test coupons used in COLENTEC tests were used in the autoclaves. A titanium-stainless steel-titanium (Ti-SS-Ti) coupon was specifically designed by assembling a 10 mm x 7.2 mm x 1.5 mm stainless steel coupon over a pre-machined titanium coupon, as illustrated in Figure 2.24. The sample was designed to simulate the configuration of a stainless steel test coupon inserted into a titanium TSP like in COLENTEC 2015 tests. Such a configuration is particularly interesting for investigating the galvanic corrosion between titanium surface and stainless steel materials.

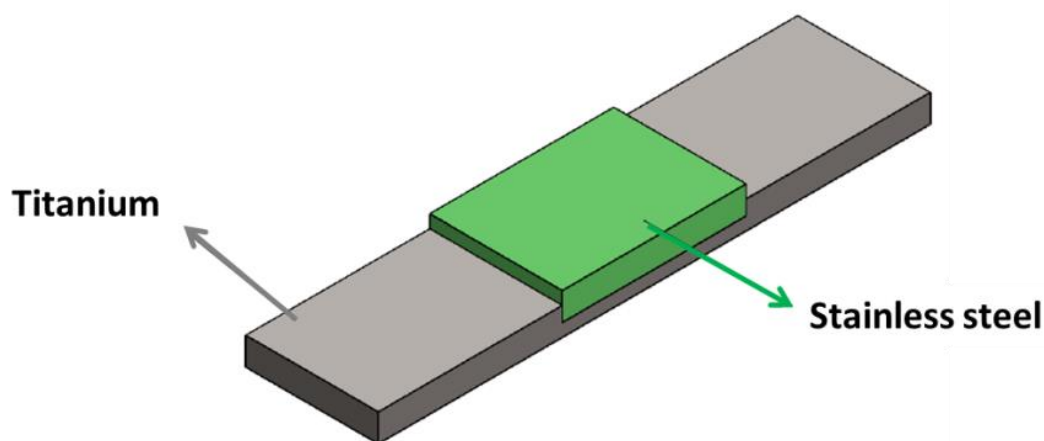


Figure 2.24: Scheme of the test coupon designed especially for autoclave to investigate galvanic corrosion. Green coupon is made of stainless steel inserted into the pre-machined titanium coupon coloured in grey.

Four tests were performed: autoclave-A, autoclave-B, autoclave-C and autoclave-D. In each test, 30 ml of solution containing morpholine (supplied by VWR International SAS) and ammonia (supplied by VWR International SAS) was added into each autoclave to obtain a $\text{pH}_{25\text{ }^\circ\text{C}}$ of 9.2 as during the COLENTEC-2015 tests. The reduced gas atmosphere in autoclaves was achieved by bubbling N_2/H_2 gaz. The test coupons were immersed in solution at 250 °C and 30 bars. Magnetite particles (supplied by Goodfellow, LS402492/4) were dissolved during some specific test. Total iron concentration was measured by UV spectrophotometry. After immersion, the samples were taken out of the autoclaves and characterized by SEM. Experimental conditions for these tests are gathered in Table 2.8:

Table 2.8: Experimental conditions for tests in autoclaves.

	Autoclave-A	Autoclave-B	Autoclave-C	Autoclave-D
Test samples/associated iron concentration in autoclave solution(ppb)	Ti-SS-Ti/0 Ti/0 SS/0	Ti-SS-Ti/5 Ti/5 SS/5 SS/60	Ti-SS-Ti/0 Ti/0 SS/0 SS/60	Ti-SS-Ti/5 Ti/5 Ti/5 SS/5
Duration	60 days		10 days	
Temperature (°C)			250	
Pressure (bars)			30	
pH_{25 °C}			9.2	

2.3.2 Iron incorporation into stainless steel corrosion layer

Autoclave-A and Autoclave-B allow performing comparisons between stainless steel materials (SS samples and SS coupon inside the Ti-SS-Ti samples) in the presence of 0, 5 and 60 ppb of iron in solution after 60 days. The same comparison can be done after 10 days by analysing the samples in Autoclave-C and Autoclave-D (Table 2.8).

Figure 2.25 shows a comparison between the corrosion layer formed onto the surface of the SS coupon from Autoclave-A (Ti-SS-Ti sample) and the Autoclave-B (Ti-SS-Ti sample). Both samples were immersed in solution during one month at 250 °C and 30 bars, in the presence of 0 ppb and 5 ppb of iron respectively. A corrosion layer of about 2 µm containing iron, oxygen, silicon, aluminium and chromium is observed for the sample in the autoclave containing iron. The addition of 5 ppb of iron in autoclave is responsible for the formation of a corrosion layer of 6 µm, which exhibits the same chemical composition as the corrosion layer formed in absence of iron in the autoclave. This result suggests the presence of iron is responsible for an increase of corrosion layer thickness, likely because of the incorporation of iron species into the corrosion layer, as previously mentioned in paragraph 2.2.4.2.2.

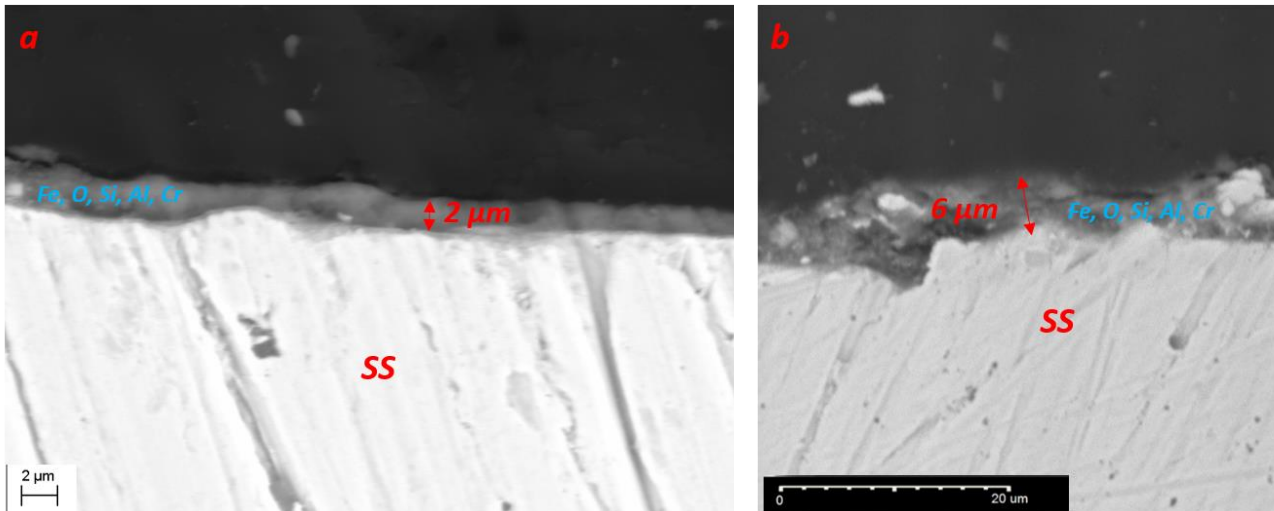


Figure 2.25: SEM observation of the SS coupon in the Autoclave-A (Ti-SS-Ti sample) after an immersion during one month at 250 °C and 30 bars without iron in the autoclave (a). A corrosion layer of 2 µm containing iron, oxygen, silicon, aluminium and chromium is observed; SEM observation of the SS coupon in the Autoclave-B (Ti-SS-Ti sample) after an immersion during one month in an autoclave containing 5 ppb of iron (b). A corrosion layer of 6 µm containing iron, oxygen, silicon, aluminium and chromium is observed.

Another comparison is made between the corrosion layer formed onto the surface of the SS coupon in the Autoclave-C and the Autoclave-D (Ti-SS-Ti samples), as shown in Figure 2.26. The same tendency is observed after ten days of immersion.

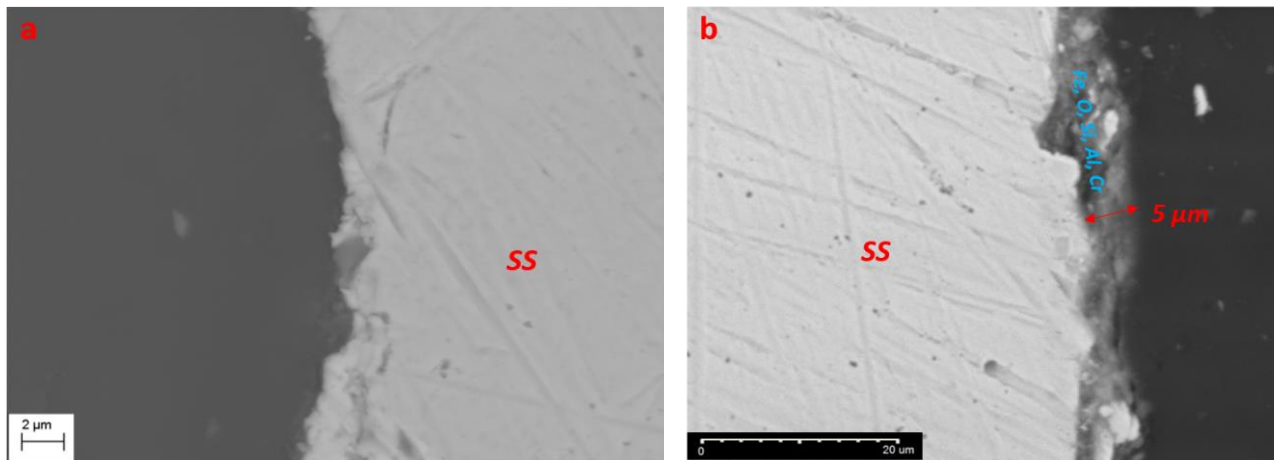


Figure 2.26: SEM observation of the surface of SS coupon in the Autoclave-C (Ti-SS-Ti sample) after ten days of immersion at 250 °C and 30 bars in autoclave without iron (a). No corrosion layer is observed; SEM observation of the surface of SS coupon in the Autoclave-D (Ti-SS-Ti sample) after ten days of immersion in the presence of 5 ppb of iron in the autoclave (b). A corrosion layer of 5 µm containing iron, oxygen, silicon, aluminium and chromium is observed.

The same chemical composition of the corrosion layer of is also observed for the SS samples (presence of iron, oxygen, silicon, aluminium and chromium). Table 2.9 gives the thickness of the corrosion layers formed on Ti-SS-Ti sample deduced from SEM analyses (not shown here).

Table 2.9: Average thicknesses of the corrosion layer on SS samples and SS coupons from the Ti-SS-Ti samples.

Samples	60 days					10 days				
	SS	SS	SS	Ti-SS-Ti	Ti-SS-Ti	SS	SS	SS	Ti-SS-Ti	Ti-SS-Ti
Iron concentration contained in solution (ppb)	0	5	60	0	5	0	5	60	0	5
Average corrosion layer thickness (μm)	1	10	1	2	6	0	0	4	0	5

Increasing iron concentration in solution induces the formation of thicker corrosion layer on SS samples. A surprisingly important corrosion layer thickness (10 μm) is observed after one month of immersion of stainless steel sample in the Autoclave-B in the presence of 5 ppb of iron. More data should be acquired to confirm the general tendency. Corrosion layer formation was observed after ten days, neither on SS sample without iron nor on the SS sample in the presence of 5 ppb of iron in solution. This result may suggest that ten days are not sufficient for observing a detectable corrosion layer on SS samples under the present experimental conditions ($T = 250\text{ }^{\circ}\text{C}$, $\text{pH}_{25\text{ }^{\circ}\text{C}} = 9.2$). In this case, the presence of iron in solution appears to have no observable effects. The presence of iron particles can be supposed in solution when iron concentration reaches 60 ppb. The observation of SS sample with 60 ppb of iron after 10 days highlights a favourable effect of the presence of particle on corrosion formation.

The presence of iron species seems to increase the thickness of stainless steel corrosion layer. This result brings complementary supports to the previous prediction by TEM characterization of COLENTEC samples. More experimental tests should be conducted to confirm the effects of the presence of soluble species and particular species as discrepancies are observed in SS samples' autoclave results. Nevertheless, a general trend supports the hypothesis of iron incorporation into stainless steel corrosion formation.

2.3.3 Ti/SS galvanic corrosion effects

Galvanic corrosion is an electrochemical process in which one metal corrodes preferentially another one when both metals are in electrical contact in the presence of an electrolyte (one metal acts as an anode and the other one plays the role of cathode). The difference of electric potential between the metals is the driving force of anodic dissolution (Serhan et al., 2004). Voltage differences of 0.2 V or more can suggest a galvanic corrosion risk (Finšgar, 2013).

For the specific stainless steel/titanium couple, the potential difference ranges from 0.2 to 0.4 V (titanium is the cathode and stainless steel is the anode). Such a potential difference is theoretically sufficient to lead to galvanic corrosion. Investigations conducted by various groups (El-Dahshan et al., 2002; Reza Moshrefi et al., 2011; Serhan et al., 2004) have confirmed that galvanic corrosion can occur between stainless steel L316 and titanium in low-temperature seawater environment. Conversely, no data is available for describing the stainless steel/titanium galvanic corrosion at high-temperature and high-pressure in two-phase flow conditions as in SG. Moshrefi et al. stated the elevation of galvanic corrosion intensity with decrease of anode/cathode area ratio (Reza Moshrefi et al., 2011). In COLENTEC tests, removable stainless steel test coupons were inserted into a titanium TSP. The galvanic corrosion can thus be supposed to occur during COLENTEC tests.

In autoclave tests, this effect can be studied by comparing the thickness of formed corrosion layer on SS samples and SS coupons inside Ti-SS-Ti samples with the same iron concentration in solution. As predicted above, the corrosion layer formed on the SS coupons inside Ti-SS-Ti samples should be thicker than that formed on SS

samples. Table 2.9 indicates the thickness of corrosion layer of 2 μm on the SS part of the Ti-SS-Ti sample after one month without Fe presence in solution and a corrosion layer of 1 μm on the SS sample under the same conditions. This result is consistent with the theoretical prediction. The same tendency is found by comparing the SS (0 μm) and Ti-SS-Ti (5 μm) samples after ten days with 5 ppb of iron in solution. Ten days seem insufficient for corrosion detection without iron presence in solution even enhanced by galvanic effects.

Galvanic corrosion effects seem to be confirmed, increasing stainless steel corrosion layer formation when stainless steel is in contact with titanium. Corrosion of titanium should be prevented by this effect. However, the corrosion layer of titanium is too small to be detected by SEM. Galvanic effects can be supposed to contribute to the stainless steel corrosion in COLENTEC test (Figure 2.19), enhancing corrosion phenomenon and retarding potentially the material passivation, and thus the initiation of deposit formation. The further COLENTEC tests are planned to conduct with a stainless steel tube support plate to make a comparison.

2.4 Conclusions of Chapter 2

Material corrosion was supposed to impact the initiation of deposition. Material passivation has been found essential and necessary to initiate deposit formation. Incorporation of external iron species into material corrosion layer has been supposed, encouraging corrosion formation and delaying passivation. This was supported by complementary autoclave investigations under similar chemical and temperature conditions. Galvanic corrosion, if existing, also affects corrosion process and deposit initiation. Injection of tracer species seems pertinent to directly investigate the external contribution to material corrosion layer.

Deposits by iron particle deposition were not observed in COLENTEC tests, which may be due to the insufficient concentration of suitable particles in test section. The role of particles remains thus unknown. Dedicated experiments should be conducted to highlight the particle contribution to the deposit by varying the particle size and concentration.

No lipping and ripple form was observed at the inlet of TSP in COLENTEC-2015 investigations as it was observed in the EDF NPP.

In the next chapter, further experimental studies will be introduced to investigate electrokinetic phenomenon. This result will be compared to previous COLENTEC results and NPP feedbacks to estimate the contribution of electrokinetics to the global TSP clogging formation and discuss the effects of different chemical and thermohydraulic parameters on deposit build-up.

Chapter 3 Specific experimental investigation of deposit build-up by electrokinetic phenomenon

3.1 Introduction and basic notions of electrokinetically induced deposit

General introduction

As mentioned previously in paragraph 1.5.3.4, iron oxide deposits can be induced by electrokinetic phenomena in flow acceleration regions. Electrokinetics allows perfectly explaining the formation of clogging deposits under lipping form at the inlet of TSP and periodic annular ripples along the TSP, observed by EDF (Figure 1.14 and Figure 1.15). It has been supposed to contribute considerably to TSP clogging formation.

In the course of the present work, a collaboration with the team of Scenini et al. in *the University of Manchester* has been established in order to estimate the electrokinetic contribution during the deposit build-up in location where the geometry favours fluid acceleration, *e.g.*, flow holes of TSP. The experimental deposit build-up by this phenomenon has never been reported in the literature under simulated PWR secondary water conditions. Therefore, the contribution of electrokinetics in TSP clogging formation remains unknown. From a phenomenological point of view, there are limited experimental data nowadays allowing to indicate the effects of different PWR water thermohydraulic and chemical parameters on electrokinetics. Numerical investigations on this phenomenon are also in the very initial phase.

In this section, preparative investigations of deposit build-up by electrokinetics will be performed, which provide experimental feedbacks for conducting further investigations under simulated COLENTec and nominal EDF conditions. First elements of deposit formation by electrokinetics are obtained. Effects of different water parameters, particularly the flow velocity, will be discussed on deposit formation. A first suggestion of electrokinetic contribution to TSP clogging will be made, by combining electrokinetic results with experimental results obtained during tests (Chapter 2) and EDF NPP feedbacks (Chapter 1).

Basic notions of electrokinetically induced deposit

In the following of this introduction, basic notions of deposits formed by electrokinetics will be given. Discs with drilled micro-orifice through the centre are usually used to create accelerated areas to study the electrokinetic phenomenon. The deposit build-up onto a contraction is quantified by three Build-Up Rates (BUR) (Figure 3.1): radial BUR (B_R), surface BUR (B_S) and inner orifice BUR (B_T).

The radial BUR quantifies the deposit growth perpendicular to flow direction at the inlet of a contraction and is expressed as the ratio between the perpendicular thickness and time. B_R appears to be the critic deposit build-up rate, which allows evaluating the time to completely obstruct a given orifice. The EDF feedback regarding TSP clogging formation at the inlet of TSP shows that deposition rate can reach 386 $\mu\text{m}/\text{year}$ as previously mentioned in paragraph 1.4.2.3, which corresponds to a radial BUR.

Deposits formed on the micro-orifice of disc samples are often asymmetric. The free orifice area after deposit formation is calculated and then converted to an equivalent diameter and a radial BUR (B_R) using the following equations:

$$\text{Equivalent diameter} = \sqrt{\frac{4 \times \text{calculated area}}{\pi}} \quad 3-1$$

$$B_R = \frac{\text{Start diameter} - \text{Equivalent diameter}}{2 \times \text{time}} \quad 3-2$$

The surface BUR (B_S) quantifies the volume of deposits formed onto the front face of the contraction per unit of time. Laser confocal microscopy is generally used to measure the formed deposit volume. The surface BUR is expressed as below:

$$B_S = \frac{\text{Volume of deposits on disc surface}}{\text{time}} \quad 3-3$$

The inner orifice BUR (B_T) quantifies the deposits formed along the inside disc. It can be expressed as the ratio between the average deposit thickness perpendicular to the flow direction and the time ($\mu\text{m}/\text{h}$ for example).

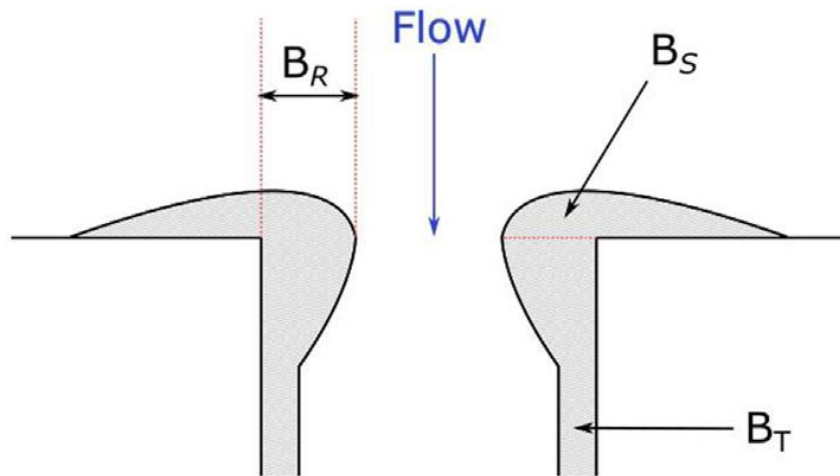


Figure 3.1: Scheme showing the deposits on the disc (gray color) that are quantified and converted to Build-Up Rates (B_R : radial BUR; B_S : surface BUR; B_T : inner orifice BUR) (McGrady et al., 2017).

In the next section, a very recent experimental investigation under simulated PWR coolant water conditions using similar test facility and disc samples will be presented, completing the previous literature study of electrokinetic phenomenon (see paragraph 1.5.3.4). Effects of different parameters, like the flow velocity, were discussed in this work, which may bring supports for further discussion.

3.2 Literature review relative to the effects of water chemistry and thermohydraulics on electrokinetic deposit build-up

McGrady et al. (McGrady et al., 2017) investigated deposit formation in accelerated flow conditions, using the similar experimental system to our study (paragraph 3.3) and stainless steel disc samples. Tests were conducted at 230 °C with a measured oxygen concentration lower than 2 ppb. The effect of iron concentration on deposit formation was studied by adding iron into water for several disc samples. However, the exact values of iron concentration in each test are not provided. Iron exists under both soluble and solid (colloidal particles and precipitate). Flow velocities ranged from 11.9 to 47.5 m/s inside the disc. pH was not conditioned nor measured in this work. Soluble dihydrogen concentration was maintained between 200 to 2500 ppb for the different tests.

The effect of dihydrogen concentration was not discussed in this work. The only significant comparison between two tests under similar flow velocity and iron concentration with respectively 200 and 250 ppb of dissolved dihydrogen shows that the increase of dihydrogen concentration promotes deposit formation on the surface (B_S) and affects slightly the radial BUR (B_R). Dihydrogen decreases the electrochemical potential, encouraging magnetite formation from hematite in iron-water system (Figure 1.4). Magnetite has a considerably higher solubility than hematite, as previously mentioned in paragraph 1.2.6. Eq. 1-10 shows that an increase of dihydrogen concentration promotes the dissolution of the magnetite corrosion layer formed onto stainless steel materials. Iron (II) ions arising from magnetite dissolution are oxidized into iron (III) ions due to electrokinetic phenomenon, which precipitates and forms magnetite deposits again. However, this phenomenon is reversible, as magnetite formed due to electrokinetic phenomenon may be dissolved again due to the presence of dihydrogen.

The effects of flow velocity on deposit build-up appear competing and difficult to conclude. The increasing flow velocity may:

- Increase the mechanical force, promoting removal and reducing BUR;
- Increase the magnitude of streaming current by shearing ions from the diffuse layer of EDL, promoting the oxidation of ferrous ions by providing a driving force for anodic reactions;
- Increase the potential between the bulk and the material surface, increasing particle deposition by electrophoresis;
- Increase the mass transport to the surface, increasing BUR;
- Inhibit potential interaction of iron ions in solution or solid iron with the surface, decreasing BUR.

The effects of flow velocity may thus vary following different water conditions and different regions on the disc.

The increase of iron concentration in solution has been found to decrease the volume of deposits on the front surface (B_S) and increase the volume of deposits within the orifice (B_T), whilst having no effect on the radial BUR (B_R) and deposit morphology. According to the postulated electrokinetic mechanism, it can be expected that an increase of iron concentration in solution may increase the deposit build-up phenomenon since more iron (II) ions are available to be oxidized by the increasing streaming current at the surface. It appears that the deposit is more important within the orifice than onto the disc surface because the mass transport effects in the accelerated region may reduce significantly any potential interaction of iron species with the surface.

Robertson (Robertson, 1986) predicted the decrease of streaming current with the increase of temperature by modelling electrokinetic currents.

Eq. 1-10 shows that an increase of the pH inhibits magnetite corrosion layer dissolution, decreasing iron (II) ions available for electrokinetic oxidation. Furthermore, magnetite particles are less easily deposited onto TSP

surface when pH increases because the charge of the magnetite particles is more negative at high pH (paragraph 1.3.2). High pH can be supposed to inhibit deposit formation.

The contribution of the electrokinetic effect in build-up appears to be highly complex because it is controlled by thermohydraulic, chemical and electrochemical phenomena. More experimental parametric investigations are essential to highlight the effects of the different parameters and to better understand electrokinetic mechanisms. In the following part of the present manuscript, the contribution of the electrokinetic phenomenon in the deposit build-up will be investigated under comparable COLENTEC-2015 secondary water conditions. These tests would provide first information for the electrokinetics and global TSP formation understanding.

3.3 Experimental system

Figure 3.2 shows the scheme of the autoclave loop used in the present study. It is composed of recirculating 13 liters vessel displayed in Figure 3.3a, which can operate up to 360 °C and 200 bars with a flow rate of 35 l/h maximum. The material of the pipework and both 250 liters feed tanks in the autoclave loop are made of 316L stainless steel (Figure 3.3b). Water chemistry was assayed by using an oxygen sensor (Orbisphere 410/A/P1C00000) and a conductivity electrode (ABB AX410/50001). Dissolved oxygen concentration measurements were made at the outlet of the reaction vessel prior to water purification by means of ion exchange resins.

Feed water was stored in feed tanks (13) displayed in Figure 3.2 where the water chemistry can be controlled. The water was pumped by a volumetric pump (15) into the autoclave vessel (1) after being pre-heated to the appropriate temperature. Afterwards, the water flowed through the main return valve (4) and was cooled (5) and depressurised (8) before being flowed through mixed bed ion exchange resins (12) after which it was re-injected into the feed tank. The flow cell (2) placed within the vessel could be activated by closing the main return valve (4) and opening the flow cell valve (3). Pressure transducers were placed upstream and downstream of the reaction vessel to log the pressure drop across the orifice ((6), (7)). As the pressure drop and velocity of the flow were directly related, it was necessary to maintain a constant pressure drop across the orifice to accurately monitor the velocity changes due to deposit build-up. This was done by using a by-pass back-pressure regulator which was set at just above the level of the primary back pressure regulator. This means that any increase in pressure drop due to deposit formation in the micro-orifice would result in part of the water flow being redirected through the by-pass loop, maintaining constant pressure across the flow cell.

Deposit build-up under accelerated flow conditions was investigated by flowing comparable PWR secondary water through a titanium disc with a central micro-orifice (Figure 3.4). The chemical composition of the used titanium discs was the same as the titanium test coupons used in COLENTEC-2015 tests (Table 2.3).

The morphology of the deposit build-up and the diameter of free section, *e.g.*, the radial BUR (B_R), were analysed by SEM and laser confocal microscopy. The latter was used to measure the volume of deposits onto the disc surface. This technique takes multiple optical images of the samples in the z-axis direction to build a 3D picture. The image treatments including surface and volume calculation were performed by using the MultiFileAnalyzer VK-H1XME software.

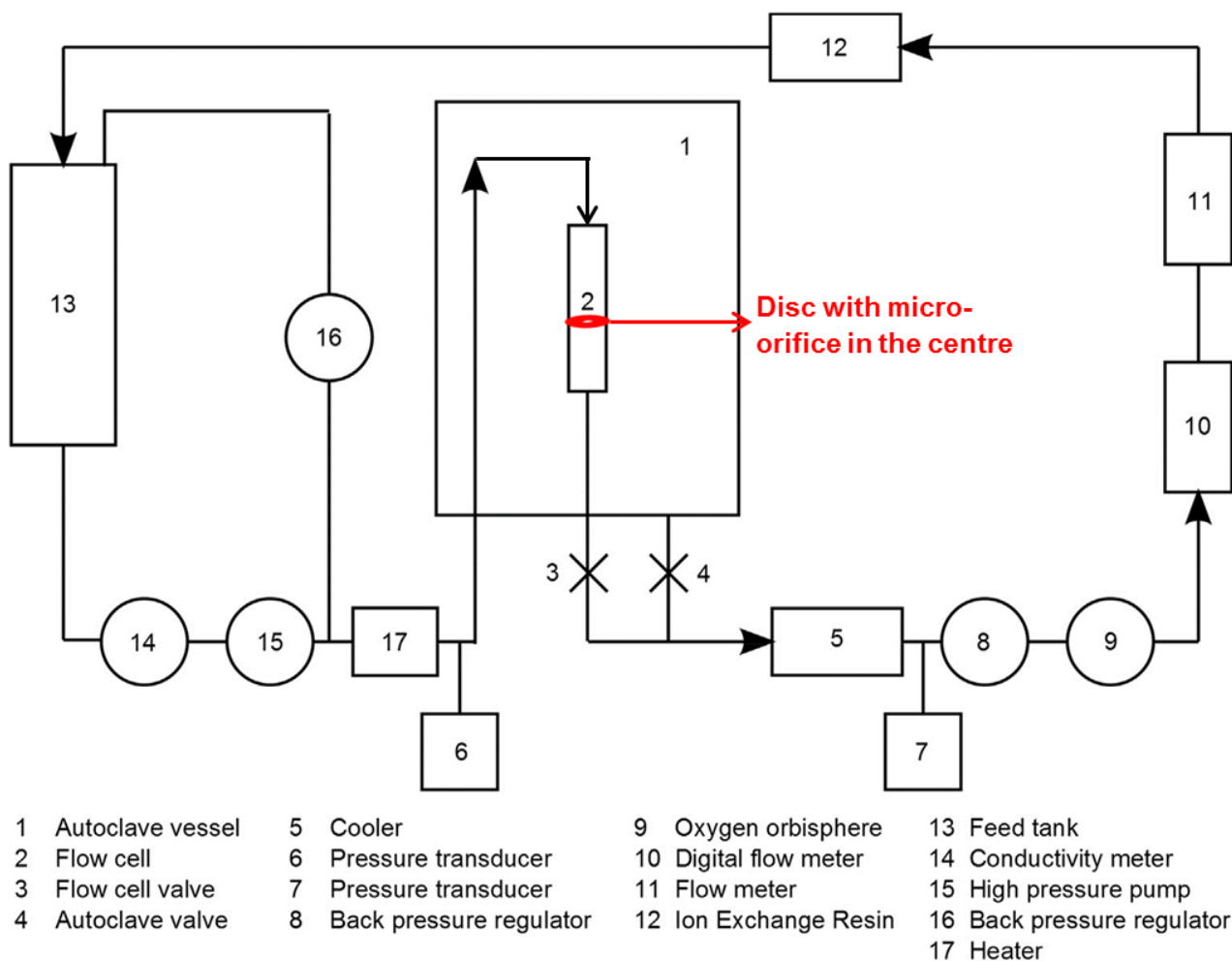


Figure 3.2: Scheme of the recirculating stainless steel autoclave at *the University of Manchester* fitted with a flow cell (2) which could be activated by opening the flow cell valve (3) (McGrady et al., 2017).

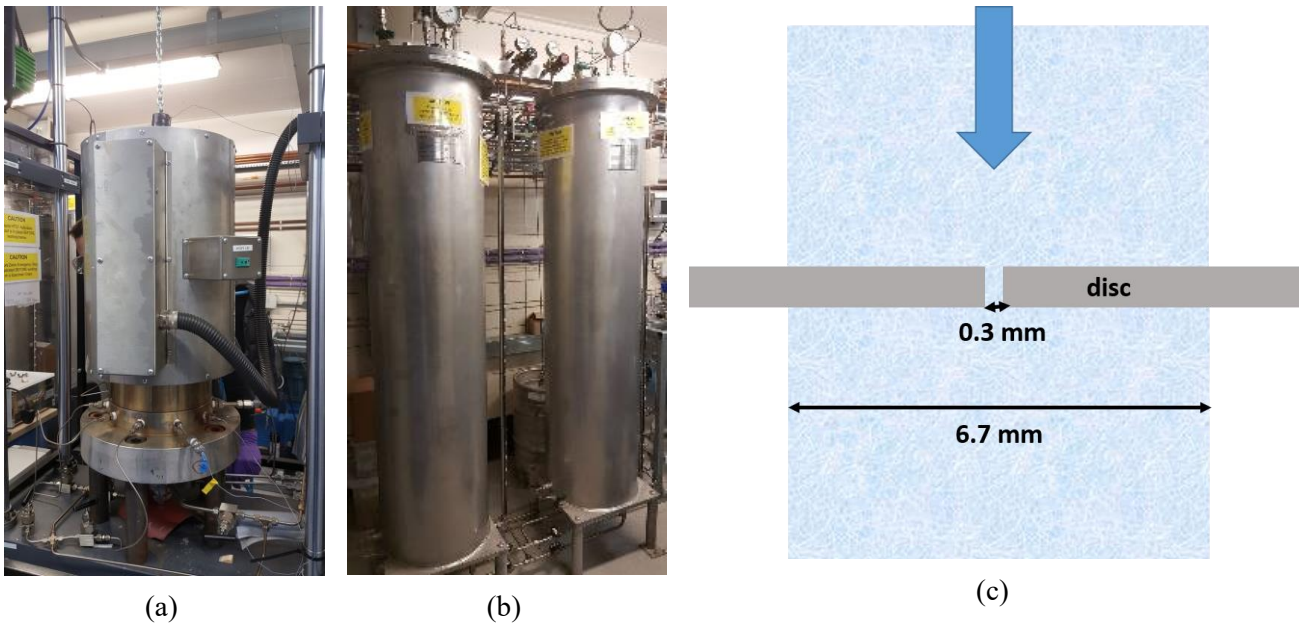


Figure 3.3: Photos of the recirculating autoclave containing the flow cell (a) and feed tanks (b); Geometry of the flow cell inside the autoclave vessel (c).

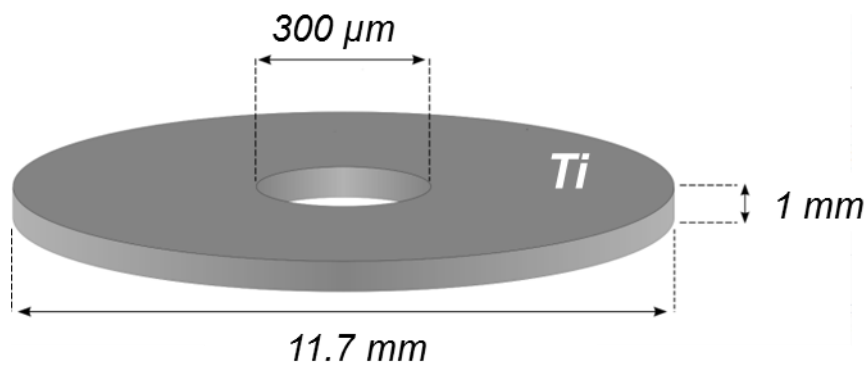


Figure 3.4: Scheme of titanium discs used for studying the deposit build-up during test at *the University of Manchester*.

3.4 Experimental conditions

Test coolant was remained in the liquid phase at 250 °C and 100 bars during all the tests to avoid flashing phenomenon. The tank was filled with N₂ prior to tests in order remove soluble oxygen from the secondary fluid (reductant environment). The soluble oxygen concentration was measured to be less than 5 ppb during the tests. About 5 ppm of morpholine and 0.3 ppm of ammonia were added into the feed tanks before flow circulating and heating. Online pH measurements were not performed in the present experimental system. pH values were therefore estimated by using pH values previously determined under the same conditions at room temperature and by sampling the recirculating flow after cooling. The estimated pH at 25 °C was lower than that of COLENTEC-2015 (pH = 9.2) and was estimated between 8.5 and 8.8. The presence of iron in the experimental

system came from FAC of stainless steel pipes (no more iron was added during the tests). Regular water sampling was conducted and the total iron concentration was measured by ICP-MS after acidification by nitric acid. The total iron concentration was found to be lower than 5 ppb during all the tests (with an average concentration of 3 ppb). Circulating iron species can thus be considered to exist majorly under soluble form, as the magnetite solubility is above 8 ppb at 250 °C when $\text{pH}_{25\text{ }^\circ\text{C}}$ ranges from 8.75 to 9.2 (Figure 1.5). However, particle deposition phenomena cannot be excluded under such conditions as FAC induced particles may deposit onto discs.

Table 3.1 summarizes the general test conditions for all the performed investigations. Five individual tests were conducted under such general conditions using five titanium discs, as previously described. Discs 1 to 3 were investigated with three different flow velocities (4, 8 and 18 m/s, respectively) without dihydrogen injection (Table 3.2). Dihydrogen injection was performed after 40 hours for the disc 5 and after 143 hours for disc 4 (Table 3.2). Three different flow velocities were also tested by using disc 4. Discs 4 and 5 were removed and characterized after the total duration, because characterization was not possible after each test step. The flow velocities inside the disc were not directly measured but it was calculated by using the volumetric flow rate.

Table 3.1: General test conditions during electrokinetic tests. *: Conditioned by ammonia and morpholine.

Total iron concentration (ppb)	<5
Dissolved oxygen (ppb)	<5
Temperature (°C)	250
Pressure (bars)	100
$\text{pH}_{25\text{ }^\circ\text{C}}$	8.5 to 8.8*

Table 3.2: Flow velocity inside the hole of the disc, soluble dihydrogen concentration and duration of each test. Discs 4 and 5 underwent 4 and 3 steps, respectively, with dihydrogen injection or flow velocity change. Characterization was not performed after each step.

Disc	Test sequences	Flow velocity inside the disc (m/s)	Dihydrogen concentration (ppm)	Duration (h)
1	/	4	0	46
2	/	8	0	16
3	/	18	0	90
4 (4 steps)	Step 1	5	0	120
	Step 2	34	0	23
	Step 3	34	2.5	33
	Step 4	43	2.5	41
5 (3 steps)	Step 1	12	0	40
	Step 2	12	0.13	49
	Step 3	12	2.5	23

As mentioned previously that this study consists of a preparative test for further investigations under simulated COLENTEC or EDF conditions. Parameters as flow velocity, test duration and dihydrogen concentration were sometimes simultaneously adjusted for the operation test. Complete parametric studies should be carried out to investigate the effect of each parameter on deposit formation. Online pH measurement system appears also

essential to ensure a representative value. Despite these test limitations, first elements for phenomenon understanding are obtained and are analysed in the next paragraphs.

3.5 Results

The previously mentioned EDF feedback regarding TSP clogging formation after 15 to 20 years corresponds to the deposit quantification by the radial BUR (B_R). No quantitative information concerning the deposits formed onto the front face of TSP inlet (B_S) and the inner surface along TSP (B_T) has been reported in the literature. Visual observation (Figure 1.14) performed by EDF shows obviously that after 15 to 20 years, deposits formed at the inlet of TSP perpendicular to flow are more important than that formed along the inside TSP. The following qualitative relationship can then be obtained between the radial BUR (B_R) and the inner orifice BUR (B_T).

$$B_R > B_T \text{ and } B_R < 386 \mu\text{m/year} \quad 3-4$$

The previous global deposit build-up tests performed with the COLENTEC facility showed a relatively homogeneous deposit formation onto titanium test coupons after 11 (5 μm) and 63 days (30 μm), under COLENTEC-2015 conditions (See paragraph 2.2.4.1). No lipping form was obtained and a depleted-deposit region was observed on most of the titanium test coupons as shown in Figure 2.7. The following relationship between the radial BUR (B_R) and the inner orifice BUR (B_T) can be estimated, which is different from the EDF observation.

$$B_R = 0; B_T = 0.5 \mu\text{m/day} (183 \mu\text{m/year}) \quad 3-5$$

This difference will be discussed based on the electrokinetic results obtained at *the University of Manchester*. Effects of different thermohydraulic and chemical parameters will then be highlighted.

Preferential deposits in regions of accelerated flow under comparable COLENTEC-2015 conditions were recreated on discs 1-5 with a central micro-orifice (start diameter = 300 μm). The front surface and the inner orifice surface of the discs were examined to reveal the effect of different parameters on deposit morphology. The radial and surface Build-Up Rates (BUR) were then estimated. Determination of the inner orifice BUR and its fine characterization were not performed in the present work because of the need further precise FIB (Focused Ion Beam) cross sectioning of the discs.

3.5.1 Morphology and characterization of the deposits

Discs 1 to 3

Figure 3.5 shows the front surface of discs 1-3 performed by SEM and the corresponding 3D images deduced from laser confocal microscopy measurements. Discs 1-3 underwent tests without dihydrogen addition. Three different flow velocities inside the disc were tested: 4 m/s, 8 m/s and 18 m/s for discs 1, 2 and 3, respectively. The morphology of the deposits formed onto the front face of the discs is characterized by concentric circles that radiate outwards from the orifice. Deposits contain exclusively iron and oxygen (EDS analyses). Disc 1 (Figure 3.5a) shows that the deposit is formed very close to the micro-orifice edge when the flow velocity into

the micro-orifice is equal to 4 m/s while an increase of flow velocity increases the distance between the edge of the micro-orifice and the deposit location. For instance, this distance is equal to 20 μm when the flow velocity is increased to 8 m/s (disc 2, Figure 3.5b) and 40 μm when the flow velocity is equal to 18 m/s (disc 3, Figure 3.5c). This result is in agreement with previous observation obtained by McGrady et al. (McGrady et al., 2017).

In the close-orifice region, the surface deposits onto discs 1 (4 m/s) and 2 (8 m/s) appear to follow the flow direction as we can observe converging ridges surrounding the micro-orifice (Figure 3.6). Therefore, the morphology of the deposits may be hydrodynamically controlled. Figure 3.7 shows the surface deposits formed onto the surface of the disc 3 at a flow velocity of 18 m/s. The previously mentioned ridges-like morphology is not observed and the deposit is less porous and no preferred direction is observed for the deposit formation. An increase of velocity from 4 m/s to 18 m/s may activate the electrokinetic streaming current, which may be responsible for ridges-like deposits perpendicular to the flow direction. Both electrokinetic and hydrodynamic phenomena might be responsible for the formation of compact deposits without preferred direction. Flow velocities into the micro-orifice of 4 m/s and 8 m/s seem to be too low for activating electrokinetic phenomenon.

The presence of small oxide germs observed onto discs 1-3 (in Figure 3.6 and Figure 3.7) seems to indicate that precipitation may contribute to the deposit formation on the initial titanium disc surface while no particle deposition is observed.

On the edge of the orifice, there are negligible iron deposits onto discs 1 and 2, as shown in Figure 3.8a and b, respectively. EDS analyses confirm this observation indicating that the disc edge is exclusively composed of titanium. When the velocity is increased to 18 m/s, iron deposits are observed on the disc edge (Figure 3.8c). EDS profile analysis throughout the disc orifice shows two iron peaks on the edge (Figure 3.8d, iron peaks are surrounded by red circles). Deposits on the orifice edge of the disc 3 can also be visualised in Figure 3.10a, showing a bright circle containing iron and oxygen along the entire orifice circumference.

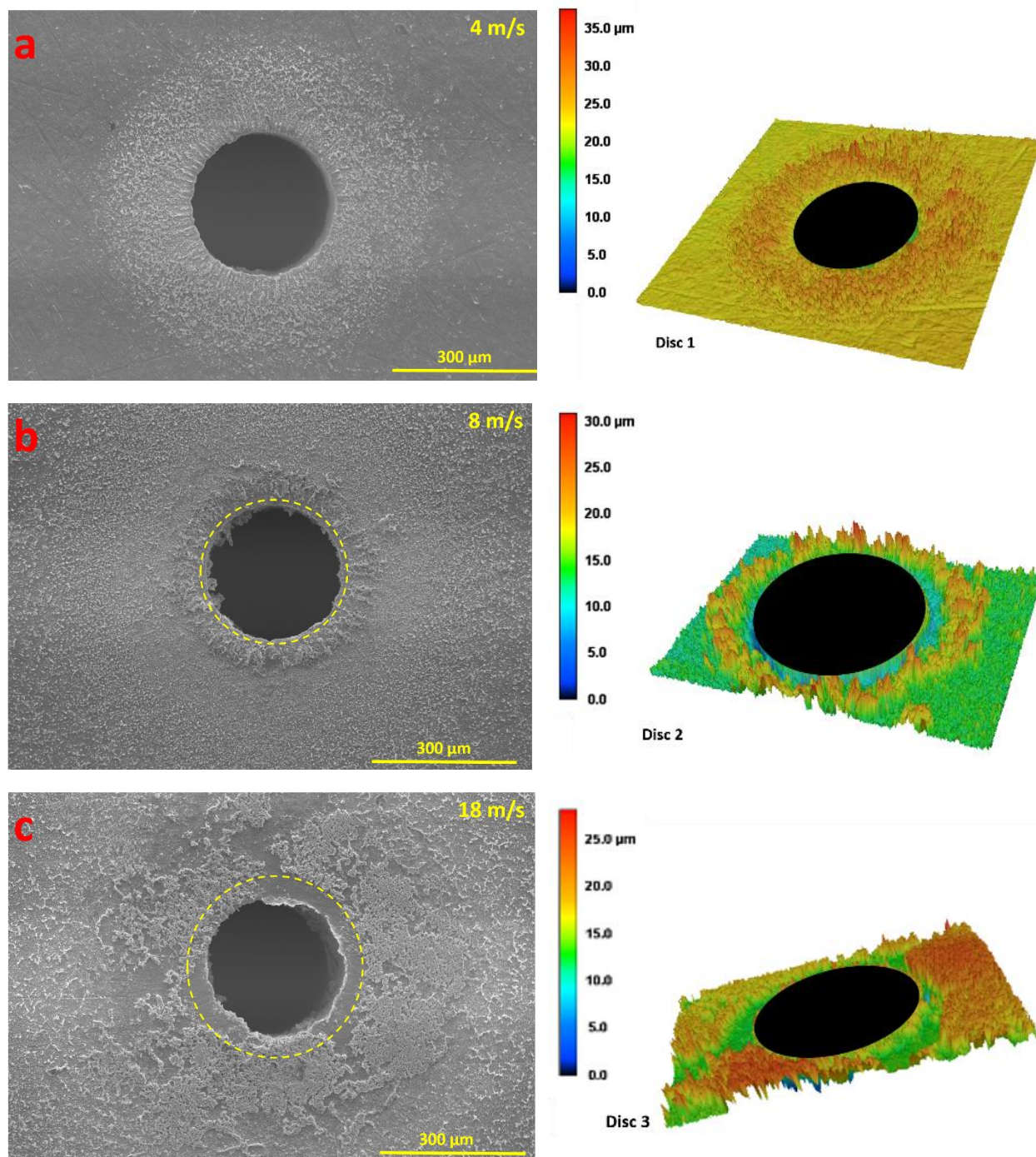


Figure 3.5: Secondary electron mode SEM pictures (left column) and 3D visualisations obtained by laser confocal microscopy measurements (right column) of front face of disc 1 (4 m/s (a)), disc 2 (8 m/s (b)) and disc 3 (18 m/s (c)) after electrokinetic tests. Yellow dash circles show the location where deposit formation starts onto the surface of discs 2 and 3.

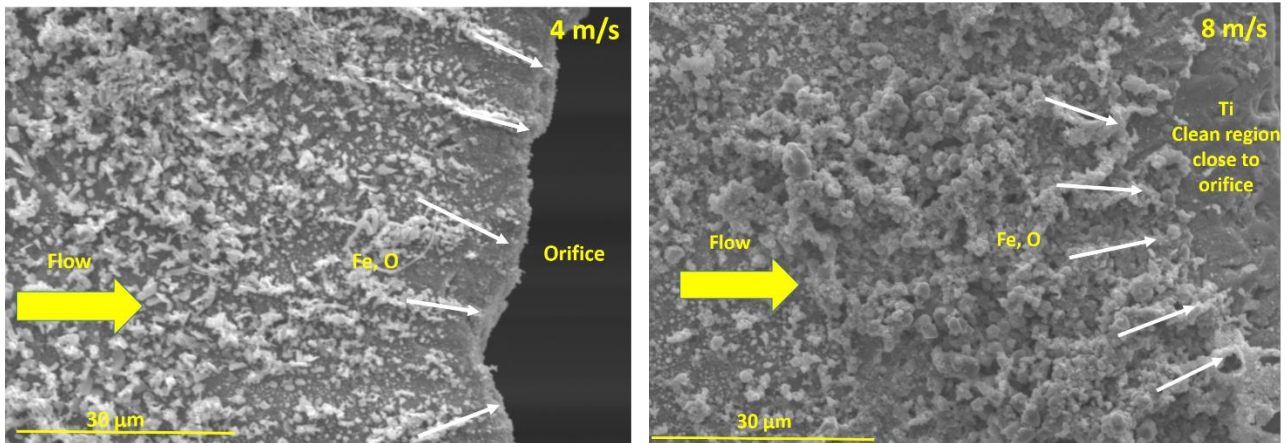


Figure 3.6: Magnified secondary electron mode SEM images of the surface deposits on (left) disc 1 (4 m/s) and (right) disc 2 (8 m/s). Deposits containing iron and oxygen follow the flow direction.

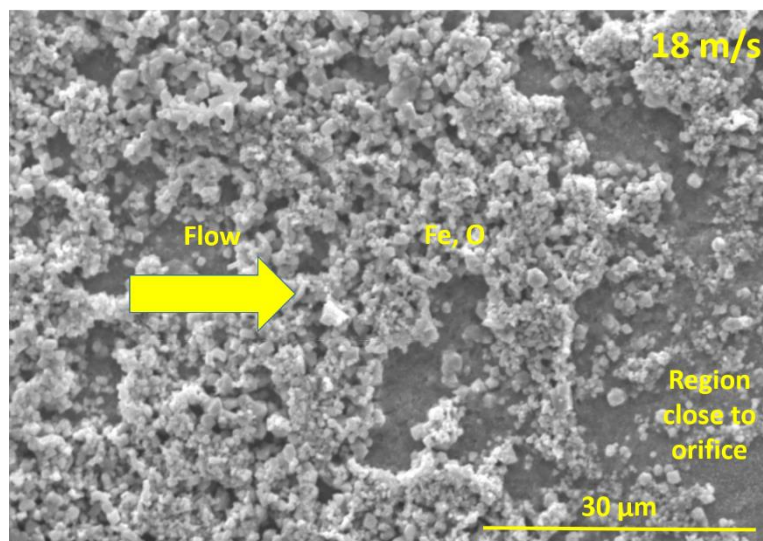


Figure 3.7: Magnified secondary electron mode SEM images of the surface deposits of disc 3 (18 m/s). Deposits containing iron and oxygen seem to be less porous than that formed on discs 1 and 2. No preferred direction is observed for the deposit formation.

Deposits within the orifice throat are then investigated. Figure 3.9a and b show negligible deposits on the orifice inner surface of disc 1 (4 m/s) and 2 (8 m/s) at the entrance. Likely hydrodynamically controlled deposits appear to be formed downstream the depleted region onto the inner surface of disc 1 (Figure 3.9a). Deposits with different morphology are observed onto the inner surface of disc 2 (Figure 3.9b), localised irregularly on the surface from a certain distance to the orifice edge (about 100 μm). Ridges-like deposits or ripples, containing iron and oxygen, are observed on the orifice inner surface of disc 3 (18 m/s), as shown in Figure 3.10. The formation of perpendicular-to-flow ripples agrees with the deposits induced by electrokinetic phenomenon. Indeed, build-up of the “first deposit” causes the formation of a second current loop downstream due to disruption of the solution flow caused by the newly formed deposit. Another anode forms thus downstream where oxide build-up can newly occur, and the process continues forming discrete ridges of oxide on the surface. These electrokinetically induced ripples’ formation is observed both on the front surface (pre-restriction) and on the inner surface (post-restriction) of disc 3 in this study, suggesting the electrokinetic mechanism is active on both pre- and post-restriction with an orifice inner velocity of 18 m/s.

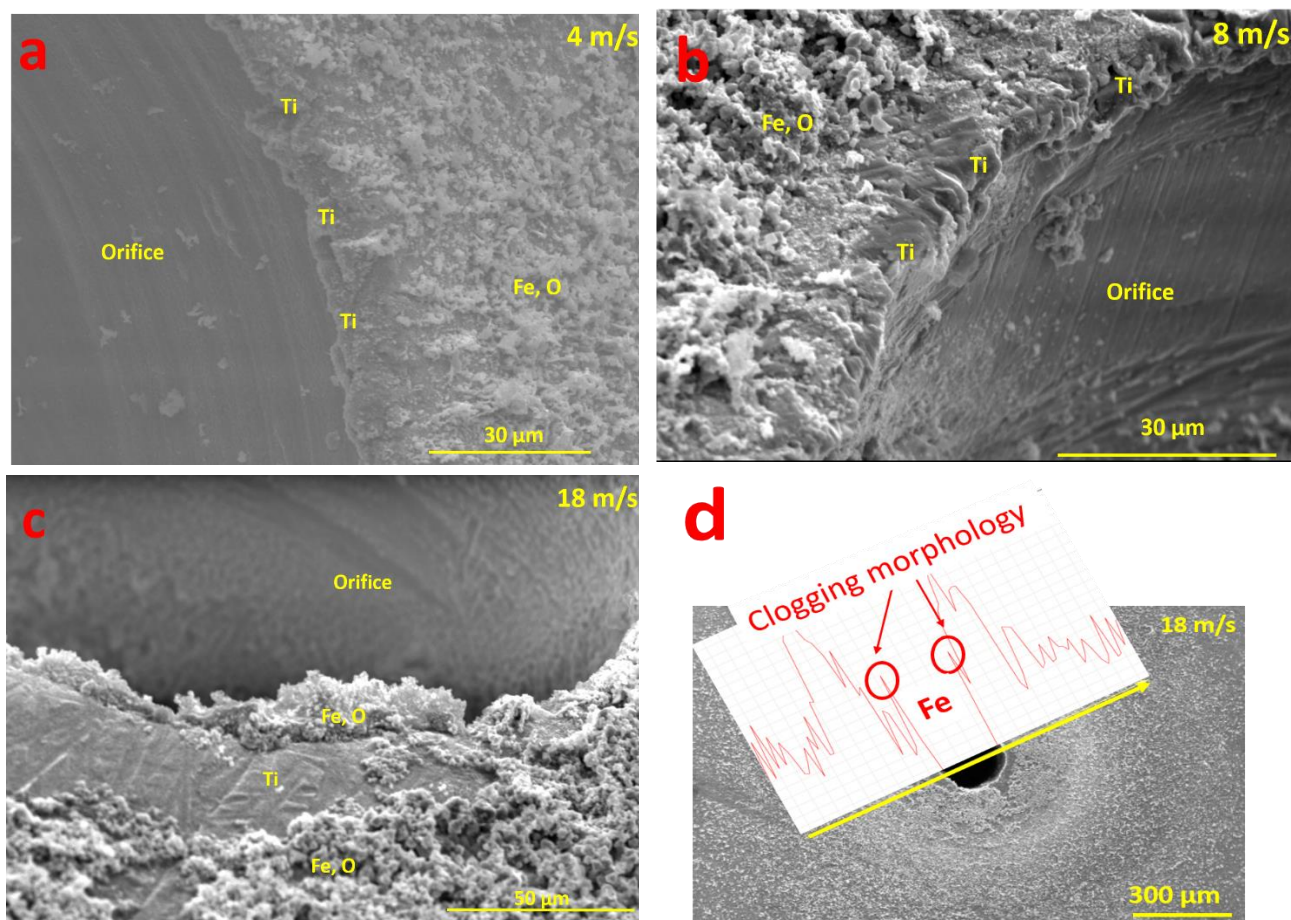


Figure 3.8: Magnified secondary electron mode SEM images of the inlet of disc 1 (4 m/s (a)), disc 2 (8 m/s (b)) and disc 3 (18 m/s (c)); EDS profile analysis of a line crossing the orifice of disc 3, indicating the formation of iron oxide on the edge of the orifice (d).

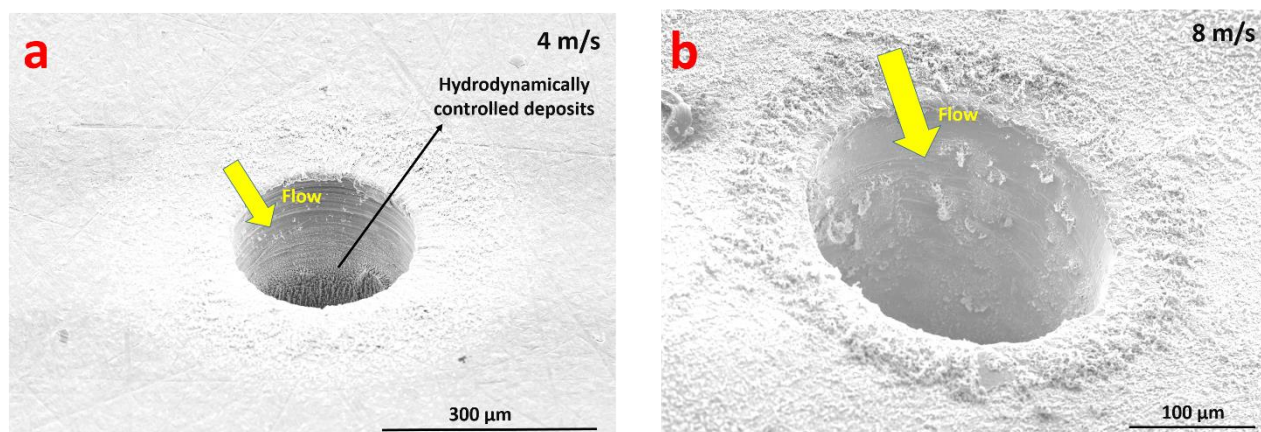


Figure 3.9: SEM images of the inner surface of disc 1 (4 m/s (a)) and disc 2 (8 m/s (b)). Negligible deposits are present onto the inner surface at the entrance region. For disc 1, hydrodynamically controlled deposits appear to be formed on the inner surface at about 150 μm from the orifice edge.

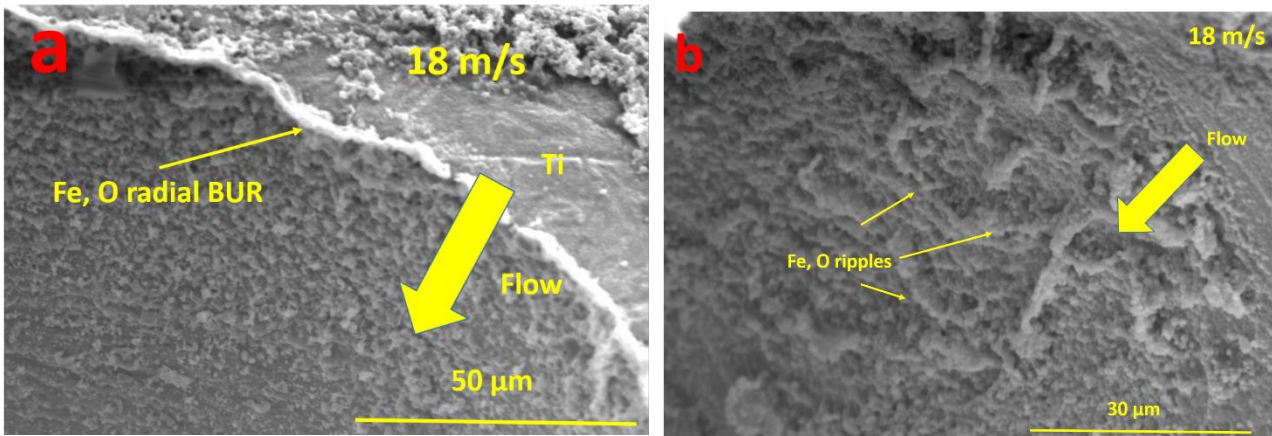


Figure 3.10: Secondary electron mode SEM image of disc 3 (a) showing the formation of deposits on the edge of orifice (radial BUR) and a general view of the inner surface near the orifice inlet; magnified visualisation of the inner surface of disc 3 (b), indicating the formation of ripples containing iron oxide.

Discs 4 and 5

For the disc 4 (Figure 3.11a), dihydrogen was added after 143 h. Dihydrogen concentration was maintained at 2.5 ppm during 74 h afterwards. A flow velocity in the micro-orifice of 5 m/s was tested during the first 120 hr. The velocity was then increased up to 34 and 43 m/s in the last steps of the test. The previously observed concentric deposits from the orifice are equally obtained on the present disc. However, the deposits overlap the orifice reducing largely the orifice free section (Figure 3.11a). The initial orifice edge (Figure 3.11a, red dash circle) cannot be seen. The corresponding 3D observation of the deposits appears to highlight that large amount of deposits are formed near the edge regions of the orifice. SEM image (Figure 3.11a) shows the formation of three different regions with different morphologies:

- i. an outer layer similar to the deposits observed onto the front surface of discs 1 and 2;
- ii. an intermediate layer similar to the deposits observed onto the front surface of disc 3;
- iii. an inner deposit layer that overlaps the edge and clogs the orifice.

Figure 3.12a and b show the outer and the intermediate layers formed onto disc 4, respectively. In the outer layer (Figure 3.12a), deposits follow the flow direction, like previously mentioned for discs 1 and 2. In this region, the formation of deposits is thus considered to be controlled by hydrodynamics while electrokinetic phenomenon does not occur. In the intermediate layer (Figure 3.12b), the deposits seem to be less porous where electrokinetically induced ripples are observed. The deposits like that formed in the outer layer may have been built-up during the first step of the test (120 h) during which a flow velocity of 5 m/s was applied almost like during test performed with discs 1 and 2 (4 and 8 m/s, respectively). It is expected that electrokinetic phenomenon may occur at flow velocity of 34 and 43 m/s given that a flow velocity into the micro-orifice of 18 m/s has been previously found to be sufficient for activating electrokinetics.

Figure 3.13 shows two important circular ripples close to the initial edge of the orifice of disc 4. These ripples correspond to thick deposits in the edge region visualised in Figure 3.11a by the laser confocal 3D technique. Depleted-deposit zones (observed onto discs 2 and 3, but not onto disc 1) are not observed between the intermediate deposit layer and the important ripples formed on the edge. Deposits are directly formed from the edge during the first step of the test (5 m/s, 120 hr), which was conducted at almost the same flow velocity as for disc 1 (4 m/s). The initiating deposits formed during step 1 may then change the initial surface state and promote deposit formation by creating more sites for precipitation and inducing supplementary current loops when electrokinetic phenomenon is activated by velocity increase.

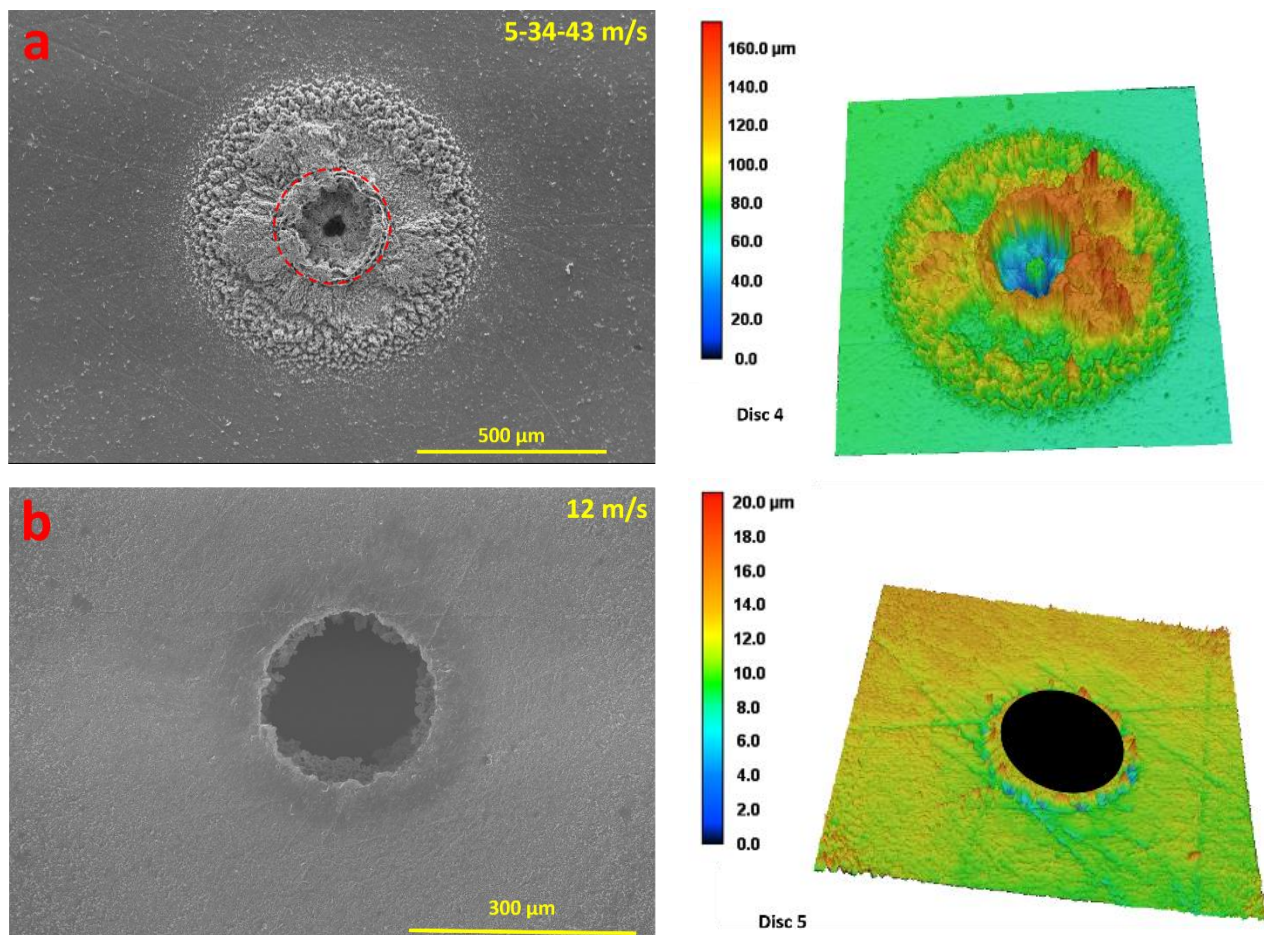


Figure 3.11: Secondary electron mode SEM pictures (left column) and 3D visualisations obtained by laser confocal microscopy measurements (right column) of front face of disc 4 (a) and disc 5 (b) after electrokinetic tests. Red dash circle represents the initial orifice edge, overlapped by deposits for disc 4.

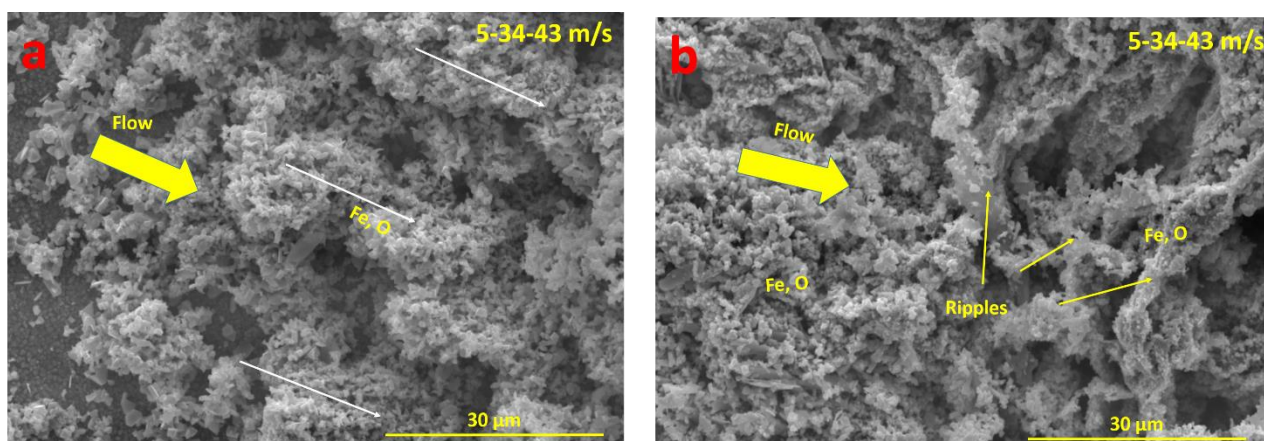


Figure 3.12: SEM image (secondary electron mode) of the outer deposit layer onto disc 4 in which deposits appear to follow the flow (a); SEM image of the intermediate deposit layer which is less porous than the outer layer (flow-perpendicular ripples containing iron and oxygen are observed) (b).

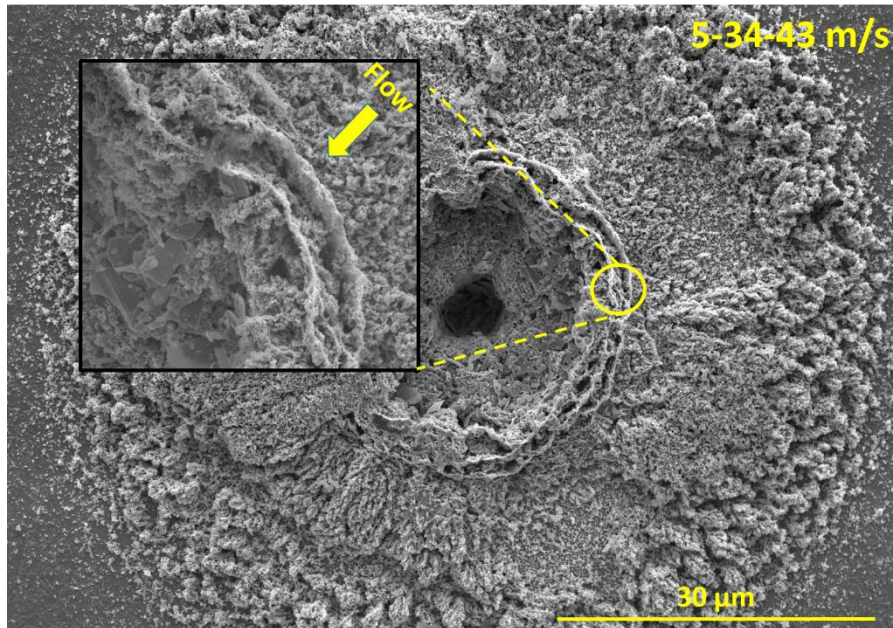


Figure 3.13: Observation of two important circular ripples containing iron and oxygen on the initial edge of the orifice of disc 4.

Figure 3.14a shows the inner deposit layer formed onto disc 4, clogging largely the free section of the orifice. Micrometric faceted particles are largely present within the orifice throat. These particles contain all 10%_{at} of chromium in average and their sizes reach up to 15 μm (Figure 3.14b). However, chromium is not detected in the deposits formed by precipitation. The presence of these particles is thought to be caused by FAC of the stainless steel materials. The disc 4 test was conducted at higher velocities (34 and 43 m/s), which may increase FAC rate and promote particle entrainment from the corrosion layer containing chromium.

EDS mapping (Figure 3.15) of the surface of disc 4 shows that chromium is preferentially located within the orifice at the entrance, indicating preferential particle deposition at the inlet of the orifice. This result is consistent with the particle deposition by *vena contracta* mechanism, as previously discussed in paragraph 1.5.3.1. The particle deposition seems to highly promote the orifice clogging, inducing considerably deposit formation on the inlet surface and in the radial direction at the entrance. According to Prusek (Prusek et al., 2013), particle deposition may initiate TSP clogging formation, which creates nucleation sites for precipitation phenomena by flashing or electrokinetics, encouraging deposit formation.

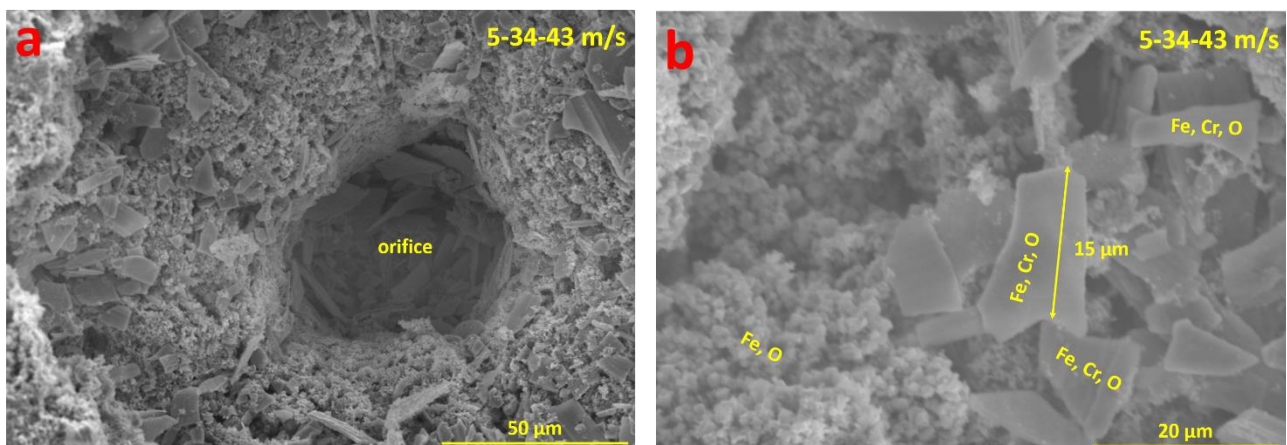


Figure 3.14: SEM image (secondary electron mode) of the inner deposit layer observed within the orifice of the disc 4 where faceted particles can be observed (a); SEM image of particles present in this layer (b), which contain iron, chromium and oxygen (size of these particles can reach 15 μm).

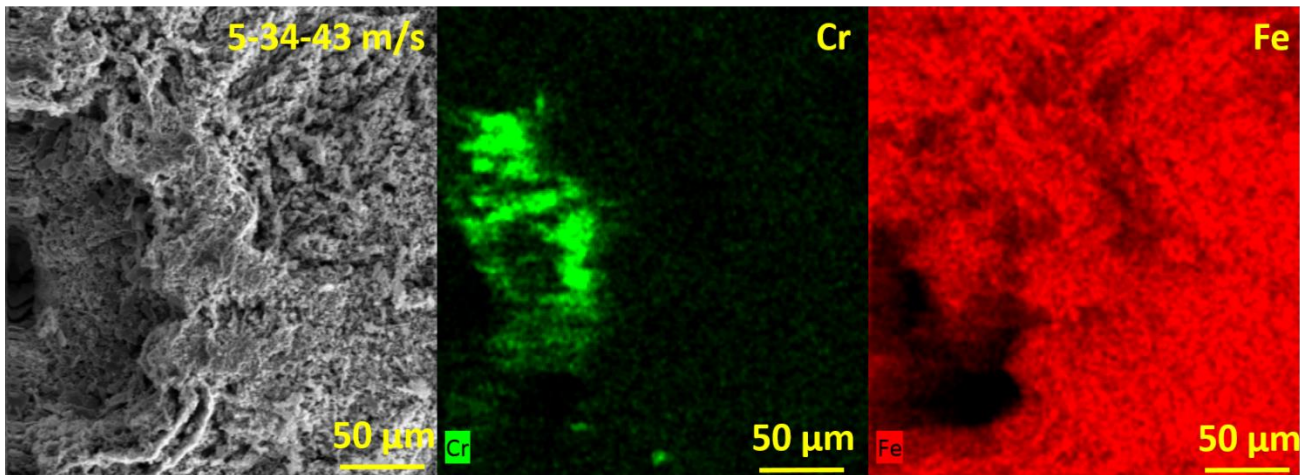


Figure 3.15: EDS mapping of a part of the disc 4 showing chromium and iron distribution throughout the orifice as well as the inner and intermediate deposit layers. Particles containing chromium are preferentially present within the orifice at the inlet.

The flow velocity was maintained constant at 12 m/s during all test steps for disc 5 (Figure 3.11b). Dihydrogen was injected after 40 h, and afterwards maintained at 0.13 ppm and 2.5 ppm during 49 and 23 h, respectively. At several points on the disc edge, deposits are thicker than away from the orifice. This tendency is much less obvious than that previously observed for disc 4. A concentric region of about 80 μm between the edge and the beginning of the outwards deposits is observed. Global deposit quantity formed on disc 5 seems much smaller than that formed on the previous samples. Figure 3.16a shows that iron is locally present along the circumference. The presence of iron appears less important and less continuous in the orifice edge of the disc 5 than in the orifice edge of disc 3 (Figure 3.10a).

Figure 3.16b shows that there is no significant deposit onto the inner surface of disc 5 at the entrance region. Deposits without ripples are located at about 100 μm from to the orifice edge as it was observed previously onto the inner surface of disc 2 for which the flow velocity was equal to 8 m/s (see Figure 3.9b).

SEM observations of disc 5 indicate electrokinetic phenomenon is not activated at an inner orifice velocity of 12 m/s and, therefore, no deposit is induced by electrokinetic onto the disc surface (pre-restriction) and onto the inner surface (post-restriction). The reason of the absence of the hydrodynamically controlled deposits on the front face of disc 5 remains unclear. The soluble iron concentration in the solution for the investigation of disc 5 may be lower than for the other tests.

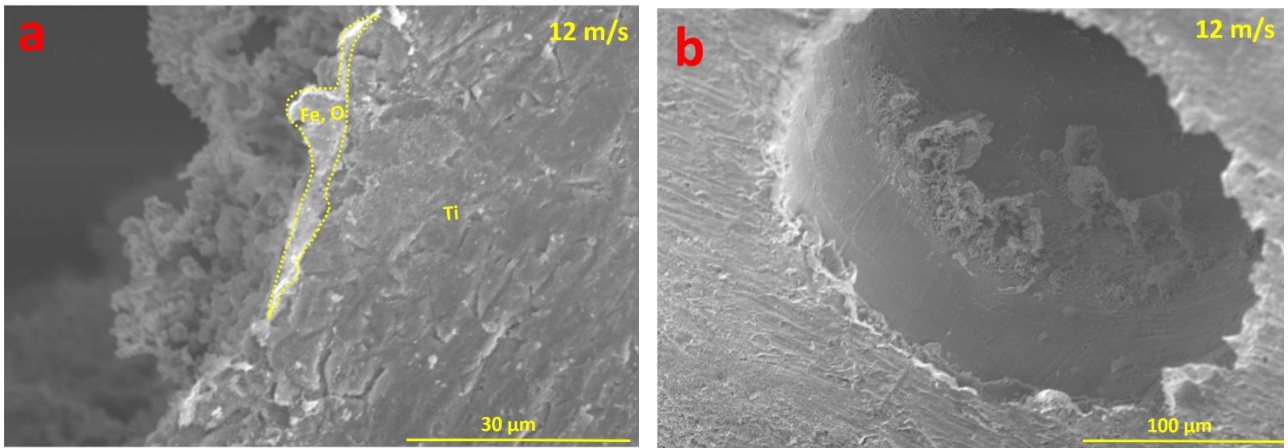


Figure 3.16: SEM image (secondary electron mode) of the front surface of disc 5 showing the presence of iron oxide on the edge (a); SEM image of disc 5 (b), showing a depleted-deposit region within the orifice throat at the entrance. Deposits can be observed on the inner surface at about 100 μm from the orifice.

3.5.2 Deposit build-up rates

The orifice surface after deposit formation and the volume of the deposits can be assayed by numerical treatment of SEM pictures gathered in Figure 3.5 and Figure 3.11. The radial BUR (B_R) and surface BUR (B_S) can be calculated using Eq. 3-1, 3-2 and 3-3 (Table 3.3). The inner orifice BUR (B_T) cannot be estimated because such a calculation requires the measurement of the average deposit thickness along the disc after FIB cross sectioning. The volume of the deposit was calculated by performing the same image processing for each disc.

Table 3.3: Calculated radial BUR deduced from Eq. 3-1 and 3-2) and surface BUR deduced from Eq. 3-3 of deposits formed onto discs 1-5.

Disc	Equivalent diameter post-test (μm)	Volume of deposits on disc surface (μm^3)	Duration (h)	Flow velocity (m/s)	Dihydrogen concentration (ppm)	Detection of particles	Radial BUR (B_R) ($\mu\text{m}/\text{h}$)	Surface BUR (B_S) ($\mu\text{m}^3/\text{h}$)
1	/	395594	46	4	0	No	/	8600
2	/	153532	16	8	0	No	/	9596
3	284	1011240	90	18	0	No	0.09	11236
4	81	12315540	217	Step 1: 5 Steps 2 and 3: 34 Step 4: 43	Steps 1 and 2: 0 Step 3 and 4: 2.5	Yes	0.50	56753
5	291	148413	112	12	Step 1: 0 Step 2: 0.13 Step 3: 2.5	No	0.04	1325

The surface reduction of discs 1 and 2 is not calculated and supposed to be nil as previous SEM observations showed the absence of iron oxides on the edge of the orifice (Figure 3.8). Increasing flow velocity promotes the

surface BUR (except for disc 5) and also the radial BUR whether the influence of dihydrogen is not taken into account. The high radial BUR value calculated for disc 4 (0.5 $\mu\text{m/h}$) may be attributed to the high velocities (34 and 43 m/s) in the last steps.

A thorough discussion will be given in the next paragraph based on the above results in order to highlight the potential effects of the flow velocity on the deposit formation. Comparisons of the results from EDF observation, COLENTEC tests and electrokinetic tests will bring essential information on the potential involvement of electrokinetic phenomenon to TSP clogging formation.

3.6 Discussions

Dihydrogen was added during the investigations of discs 4 and 5. The presence of dihydrogen has been supposed previously to affect the soluble iron concentration and deposit composition (See paragraph 3.2). Nevertheless, it is difficult to conclude its effects from the present work as no significant comparison exists under different dihydrogen concentrations and same flow velocity. Performed qualitative EDS analyses show no difference on Fe/O atomic report between the deposits formed in the presence of dihydrogen (discs 4 and 5) and without dihydrogen (discs 1-3). Therefore, in the following discussions, the effect of dihydrogen concentration will not be considered.

Electrokinetics seems to be considerably velocity-dependent. The effects of flow velocity on deposit formation will be carefully discussed in paragraph 3.6.1. Deposits built-up under nominal EDF conditions and certain electrokinetics investigations' conditions (discs 3 and 4) exhibit lipping and ripple forms. However, these forms were not observed on COLENTEC-2015 samples. Explanations will be suggested in paragraph 3.6.2 based on the differences of the major operation parameters. This comparison, combined with the suggested velocity effects, will allow proposing how electrokinetics is involved in TSP clogging formation.

3.6.1 Effect of flow velocity

From the above results in paragraph 3.5 about the electrokinetic phenomenon, it can be assumed that an increase of the flow velocity is responsible for:

- i. more deposit formation onto the orifice edge (see values of the radial BUR in Table 3.3).
- ii. an increase of the volume of deposits onto the front surface of the disc (see values of the surface BUR in Table 3.3).
- iii. an increase of the distance from the orifice edge and the location of the deposit onto the front surface of the disc.
- iv. the formation of micrometric particles containing Fe, Cr and O, which deposit preferentially at the inlet of the restriction. The presence of particles in this region appears to highly enhance the formation of deposits and clogging considerably the restriction (disc 4).

Effect (i) may be the result of high flow velocity in the close restriction region of the disc. Such a high flow velocity can indeed be responsible for a mechanical detachment of the deposit located close to the orifice edge. Figure 3.17 and Figure 3.18 show a modelling by COMSOL 5.2 CFD software of the flow streamlines of the fluid through the orifice of discs 1-3. The investigation domain is set at 20 mm upstream the disc and 30 mm downstream. Upstream flow velocities are considered to be well established with a distance of 20 mm before

the restriction and estimated by constant volumetric flux inside and outside the restriction. They are estimated to be 0.008, 0.016 and 0.036 m/s for disc 1 (4 m/s), disc 2 (8 m/s) and disc 3 (18 m/s), respectively, as the modelling initial conditions. The outlet is a constant pressure boundary condition. The number of mesh elements was equal to 31221 for all the three velocities.

Figure 3.17 and Figure 3.18 show that dramatic increase of velocity occurs at the inlet of the restriction. A recirculation flow takes place downstream the disc. In the cases of disc 2 (8 m/s) and disc 3 (18 m/s), a second recirculation flow occurs in the right corner. It can be figured out higher is the velocity in the recirculation, bigger is this second circulation flow. The flow is found to converge towards the disc orifice by a top view of modelling streamlines as shown in Figure 3.19, which agrees with the previous observed deposits onto the discs 1-2 (Figure 3.6). This modelling result confirms the formation of deposits by hydrodynamic effects.

Dramatic flow acceleration occurs at the inlet region of restriction, up to 6 (disc 1), 12 (disc 2) and 25 m/s (disc 3) at the edge of the orifice. Zooms of the restriction inlet region are displayed in Figure 3.20 for each disc. A flow velocity of 6 m/s is observed at the edge of disc 1 where deposits begin to form (Figure 3.6). A flow velocity of 6 m/s is found onto the disk surface at about 20 and 40 μm from the orifice edge for discs 2 and 3, respectively (Figure 3.20). These distances match perfectly with the dimension of depleted deposit regions, previously measured by SEM for discs 2 and 3 (See Figure 3.5). This result could confirm that a local flow velocity of 6 m/s may inhibit the presence of deposit. The increase of the flow velocity leads to an increase of the distance between the beginning of the deposits and the orifice edge. The distribution of the flow velocity vector is the same for all these three discs but the magnitude of these vectors is different depending on the disc.

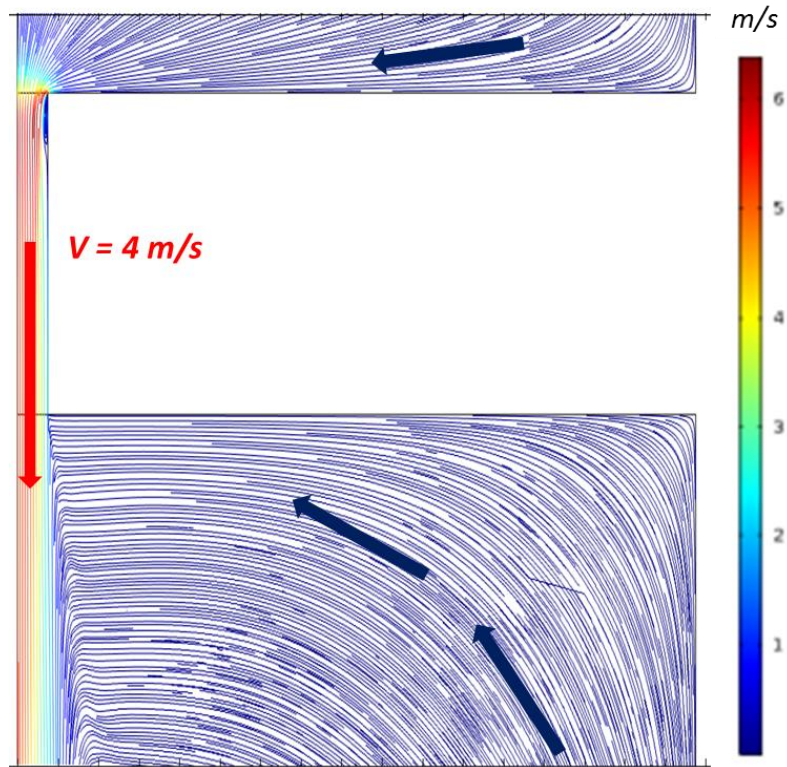


Figure 3.17: 2D CFD modelling streamlines of pure water flow crossing through the orifice of disc 1 (flow velocity of 4 m/s at the inner orifice). Modelling was performed by taking half of the flow cell (shown in Figure 3.3c) with a restriction radius of 0.15 mm and a pre-restriction radius of 3.35 mm.

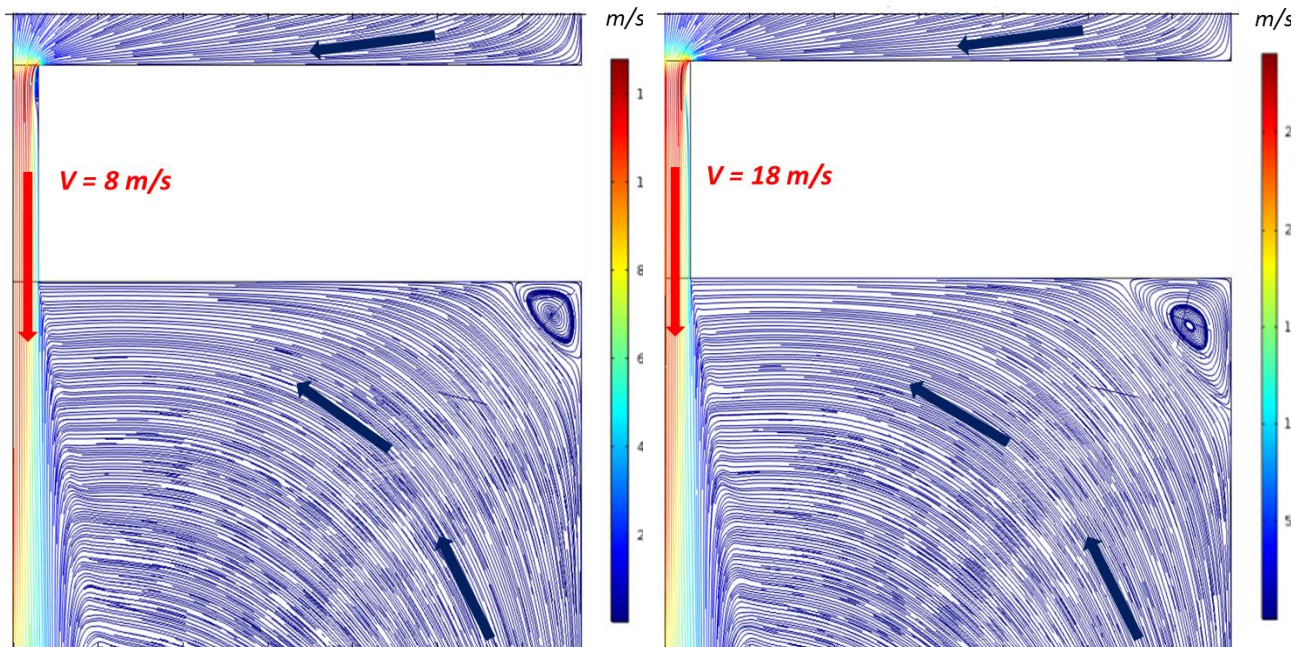


Figure 3.18: 2D CFD modelling streamlines of pure water flow crossing through the orifice of disc 2 (left) and disc 3 (right).

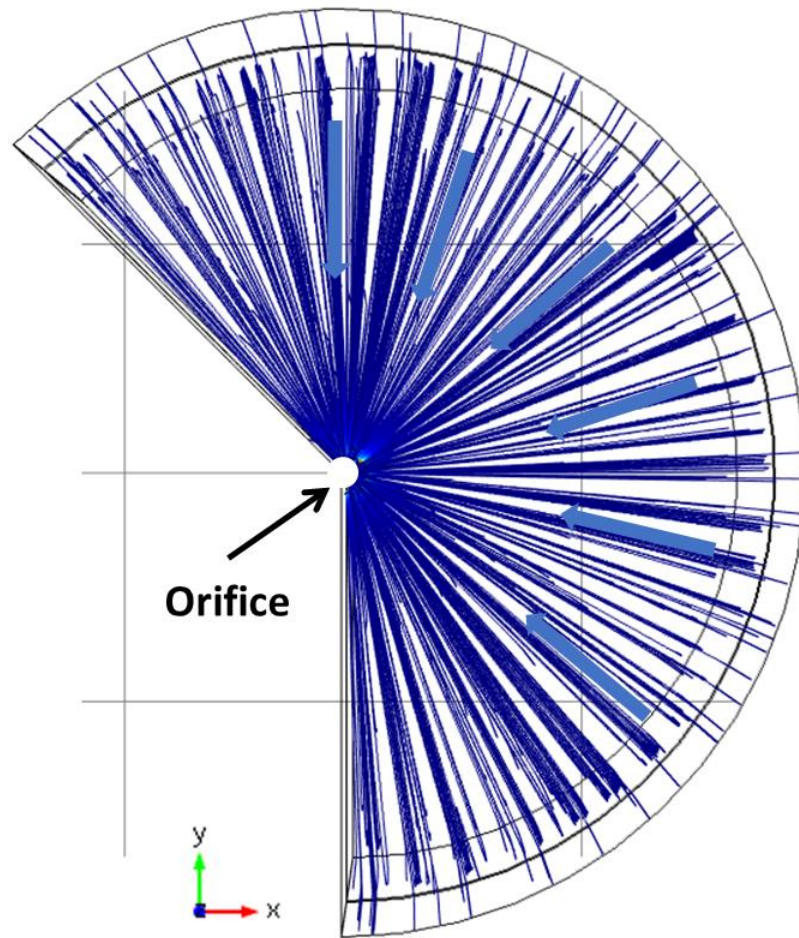


Figure 3.19: Top view of CFD modelling streamlines of disc 1-3, showing that the flow converges towards the disc orifice on the front surface.

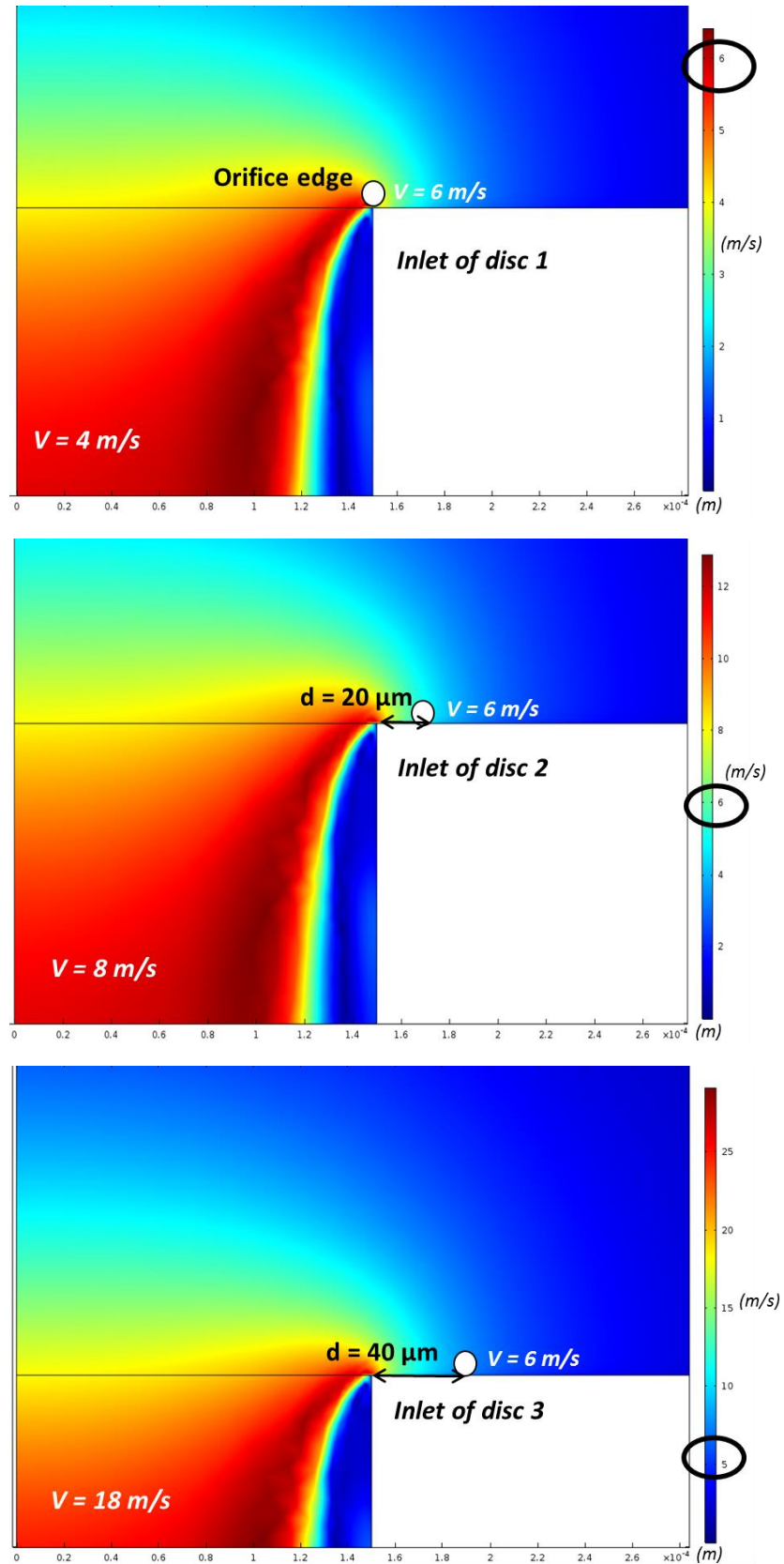


Figure 3.20: Magnitude of flow velocity at the inlet region of the disc 1 (4 m/s, top), disc 2 (8 m/s, middle) and disc 3 (18 m/s, bottom). 6 m/s corresponds to the magnitude of flow velocity at a certain distance from the orifice edge, respectively 0, 20 and 40 μm for the disc1, disc 2 and disc 3.

Radial BUR for discs 1 and 2 are close to zero as previously observed in Figure 3.8. The maximum value of the flow acceleration at the edge of the restriction may be responsible for two opposite phenomena: (i) more deposit detachment due to an increase of drag forces onto the surface or (ii) more deposit formation due to an increase of the magnitude of the streaming current resulting from shearing ions from the diffuse layer of the EDL. In the case of the discs 1 (4 m/s) and 2 (8/s), there is no electrokinetic phenomenon because the flow velocities are too low at the inlet of restriction. On the opposite, disk 3 undergoes electrokinetic phenomena since flow viscosity is higher at the inlet of restriction, which leads to deposit formation onto the front surface at the restriction edge and onto the orifice inner surface (Figure 3.10a). Finally, magnitude of electrokinetic phenomenon responsible for deposit formation seems to be more important than deposit detachment due to mechanical forces. Therefore, a threshold value of the flow velocity is essential for achieving electrokinetic phenomenon. Under the present investigation conditions, this threshold value can be estimated to be between 8 and 18 m/s.

An increase of the flow velocity may promote mass transport of soluble iron species onto disc surface, which may induce higher surface BUR. When electrokinetic phenomenon occurs in the pre-restriction zone, like it is the case for disc 3, velocity may promote deposit formation onto the surface.

An increase of the flow velocity promotes FAC of materials, as previously mentioned in paragraph 1.2.6.2, inducing more particles and soluble iron species in solution. *Vena contracta* mechanism can then be dramatically accelerated by increasing flow velocity (paragraph 1.5.3.1). Important particle deposition can thus be present preferentially at the inlet of restriction. The particle deposition at the inlet induces the contraction more restricted, enhancing flow acceleration and electrokinetic phenomenon. Particle deposition may also provide nucleation sites for precipitation phenomena, encouraging global deposit formation (paragraph 1.5.2). Therefore, increasing flow velocity may also indirectly promote electrokinetic phenomenon by increasing particle concentration in solution and deposition.

In the next paragraph, electrokinetically induced deposits will be compared to the deposits observed by EDF and the deposits obtained during COLENTEC test campaigns in 2015. The effect of various parameters including the presence of particles and flow velocity will be discussed. Involvement of electrokinetic phenomenon will be suggested.

3.6.2 Comparisons with COLENTEC results and EDF observations

Typical electrokinetically induced deposits were obtained onto disc 3 surface. This deposit exhibits lipping forms at the inlet of orifice and ridges within the orifice as previously shown in Figure 3.10. This disc sample has been chosen for a sake of comparison with EDF observation and COLENTEC-2015 results to reveal the potential involvement of electrokinetic phenomena in TSP clogging formation. A comparison of major parameters is shown in Table 3.4 between different conditions.

Table 3.4: Comparison of operating conditions used during COLENTEC-2015 campaign test, electrokinetic investigation for disc 3 and EDF feedback under nominal conditions. *: The flow velocity within TSP flow holes under EDF or COLENTEC two-phase flow conditions is estimated by mass flow rate, supposing that liquid phase velocity is equal to that of the vapour phase.

	EDF nominal operation	COLENTEC-2015 operation	Electrokinetics investigation of disc 3
pH at 25 °C, conditioned by morpholine and ammonia	9.2	9.2	8.5 to 8.8
Flow	Two-phase (void fraction = 85%)	Two-phase (void fraction = 90%)	Liquid
Temperature (°C)	277.2	250	250
Dissolved dihydrogen concentration	0.2 to 2 ppb without considering the formation by corrosion and by hydrazine decomposition	0.38 ppm	0
Flow velocity within TSP flow holes (m/s)	7*	7*	18
Presence of particles	20 ppb	No	No

Deposits observed by EDF suggest important implication of electrokinetics to TSP clogging formation (Figure 1.14b and Figure 1.15). Electrokinetic phenomenon is not expected to occur under COLENTEC-2015 operating conditions as neither lipping form at the inlet of restriction nor ripples along the titanium test coupons has been observed (Figure 2.7). Figure 3.21 shows iron deposits onto titanium coupons of COLENTEC-2015 tests governed by the hydrodynamics. Deposits follow the flow and are similar to that formed onto the front surface of discs 1 and 2 (Figure 3.6). Electrokinetic phenomenon may be inhibited by higher pH in COLENTEC tests as high pH reduces iron concentration in solution. However, electrokinetic phenomenon seems to occur in EDF reactors while the latter operate at the same pH of COLENTEC tests. The difference on dihydrogen concentration and temperature between COLENTEC and EDF nominal operation does not explain the absence of electrokinetic phenomenon under COLENTEC conditions as increasing dihydrogen concentration and decreasing temperature are both supposed to favour electrokinetic phenomenon (paragraph 3.2). The presence of particles and high flow velocity can thus be found to have a potentially important effect on electrokinetics activation. Indeed, around 20 ppb of iron particles are supposed to be present in secondary fluid under normal EDF operation conditions (paragraph 1.2.6.3.4) and particles were not observed on almost all COLENTEC-2015 samples (paragraph 2.2.4). This result is consistent with the previous observation on the disc 4, which indicates a potential initiating effect of particle deposition, inducing higher flow velocity and more nucleation sites (paragraph 3.5.1). The flow velocity in COLENTEC tests is estimated to be around 7 m/s, which is close to the inner flow velocity of disc 2 (8 m/s). A flow velocity of 8 m/s has been found insufficient to activate electrokinetic phenomenon. This result agrees with the observed deposit by COLENTEC test. Therefore, the insufficient presence of suitable particles or the insufficient flow velocity may explain the absence of lipping and ripple forms under COLENTEC conditions.

The presence of particles can favour electrokinetic activation without being indispensable given that electrokinetics was activated on disc 3 in the absence of particles and high inner orifice velocity, *e.g.*, 18 m/s. Therefore, electrokinetics may be important when particles are present or flow velocity is sufficiently high. High velocity situation can be achieved, for example, when TSP is already clogged. Electrokinetics may be important after certain time of NPP functioning or after cleaning of steam generator, which may be more or less efficient, exhibiting already formed deposits.

Based on the above discussions, it can be suggested the following involvement of electrokinetic phenomenon on TSP clogging: at the beginning step of NPP functioning (when flow holes are “clean” on a novel TSP), the flow velocity inside the clean flow holes is relatively low (about 7 m/s). Electrokinetics is more likely activated by particle deposition following *vena contracta* mechanism. It becomes then more and more important as the

flow hole is more and more restricted. Electrokinetics may predominate other phenomena implicated in TSP clogging formation from a certain flow velocity, imposing its typical ripples continuously propagating along the TSP.

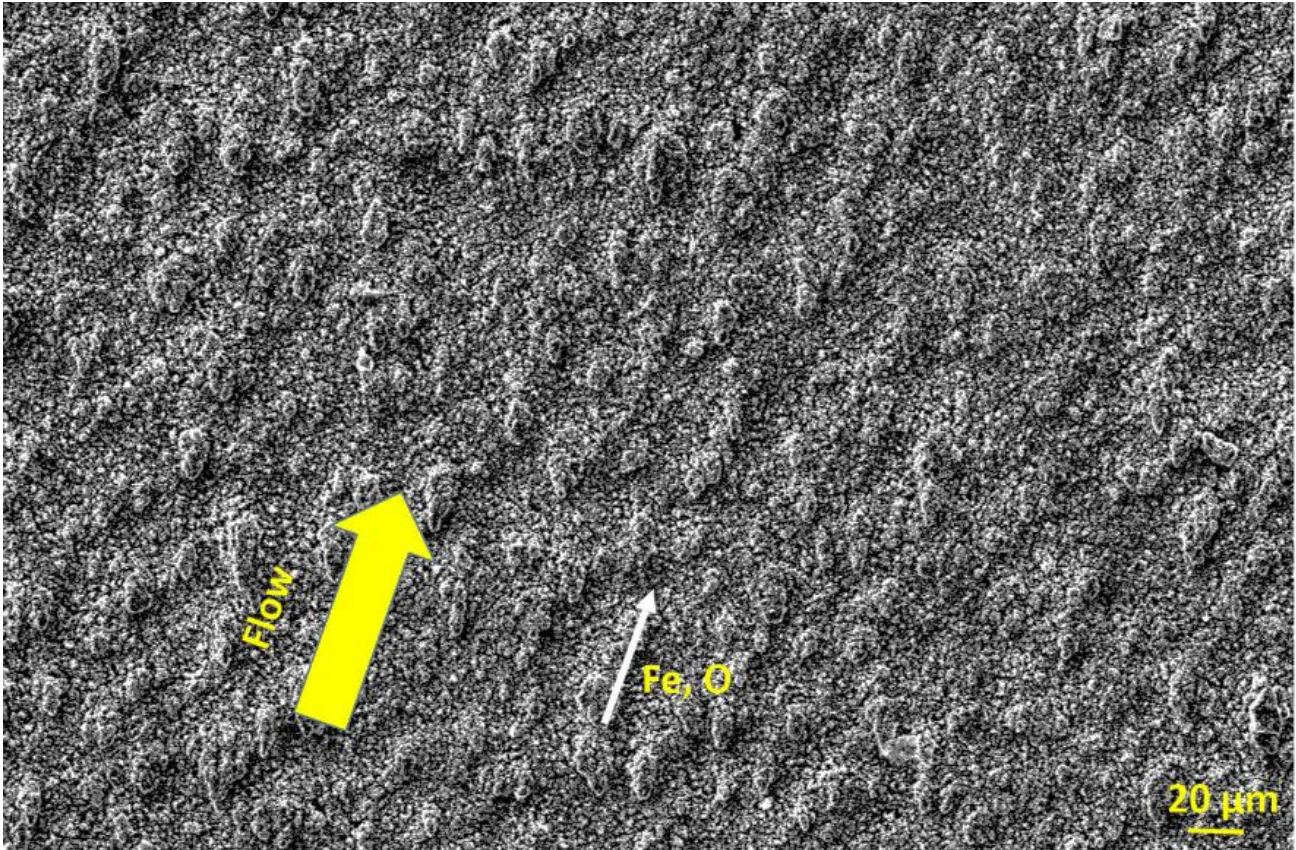


Figure 3.21: An example of the iron oxide deposits formed onto titanium test coupons after COLENTEC-2015 test, showing that the deposits are hydrodynamically affected by flow.

3.7 Conclusions of Chapter 3

Electrokinetic experiments under comparable secondary water conditions were performed in order to study the impact on representative deposits. These deposits exhibit typical lipping and ripple forms. Electrokinetics has been supposed to be favoured by high-velocity and/or the presence of particles. In the context of TSP clogging, electrokinetic phenomenon may be prevailed and activated at initial state by particle deposition. When flow becomes sufficiently fast, electrokinetics may become predominant and drives the global form of TSP clogging deposits observed by EDF.

Experiments carried out at the *University of Manchester* are a first step for thorough electrokinetic investigation under secondary conditions and have shown encouraging results. Both comparative studies with COLENTEC tests and parametric investigations of different operating parameters are valuable for phenomenological understanding. Collaboration should be continued to deeply understand the effect of different parameters, *e.g.*, flow velocity, pH, the presence of particles, etc., by varying one sole parameter each time and to estimate the contribution of electrokinetics to global TSP clogging.

In the next chapter, all expected phenomena involved in TSP clogging formation will be investigated by means of a numerical approach, which will allow quantifying the contribution of each mechanism.

Chapter 4 Numerical investigation of TSP clogging phenomenon

4.1 Introduction

Lipping form is observed by EDF for the clogging deposits at the inlet of TSP. The deposit formation rate can reach 386 $\mu\text{m}/\text{year}$ in this region in EDF NPPs, as previously mentioned in paragraph 1.4.2.3. Three specific mechanisms have been supposed to contribute to the deposit formation at the inlet of TSP: particle deposition by *vena contracta*, flashing and electrokinetics (paragraph 1.5.3). Prusek (Prusek et al., 2013) attributed an initiation role to particle deposition phenomenon, which was suggested essential for flashing and electrokinetics at the inlet of TSP. The experimental results of global deposit build-up investigations using COLENTEC facility were in agreement with this proposal as no lipping form was observed on COLENTEC test samples and no particle was present in the test section (Chapter 2). Specific electrokinetics investigations at *the University of Manchester* also suggested an initiation role of particle deposition, which may facilitate the activation of electrokinetic phenomenon (Chapter 3).

Therefore, particle deposition may initiate TSP clogging formation process. Afterward, cementation of the deposits formed by particle deposition may occur because of flashing and electrokinetic phenomena. From a quantitative point of view, the contribution percentage of these three mechanisms remains poorly studied and unknown. Electrokinetics may have a major contribution as it can explain the ripple form along the TSP afterwards the inlet.

The present chapter aims at prioritizing these three mechanisms by performing a numerical estimation of the contribution percentage of each phenomenon towards global TSP clogging.

Particle deposition phenomenon is described by *vena contracta* mechanism and is described using Eq. 1-32, 1-33 and 1-34 (See paragraph 1.5.3.1 for details):

$$K_{v,p}(t) = a_v k_v (\rho_p - \rho_l) C_g d_p^2 U_z^2 / \mu_l \quad 1-32$$

$$k_v(t) = \frac{L - [R(1 - \tau_c)]}{S} \quad 1-33$$

$$e_d(t) = \frac{\rho_l C_p K_{v,p} t}{\rho_d} \quad 1-34$$

Flashing (See paragraph 1.5.3.2 for details) will be quantified by Eq. 1-35 and 1-36, which allow calculating the mass flux of soluble species precipitation ϕ , per unit area ($\text{kg}/\text{s}/\text{m}^2$):

$$\phi_s = \frac{\phi_1 \Delta H_1 S_s}{H_{1g}} \quad 1-35$$

$$\Delta H_1 = \lambda(\tau_c) U_{z,1}^2 \quad 1-36$$

with ϕ_1 (kg/s/m²) = $\rho_1 U_{z,1}$

Nowadays, there is no numerical model capable to describe deposit formation by electrokinetic phenomenon. Its contribution cannot be directly calculated and will be estimated by means of the hypotheses reported below in paragraph 4.2.1.

Particle size (d_p) and particle concentration (C_p) are particularly important among the parameters useful for quantifying the different phenomena involved in TSP clogging. Particle size equal to 1 μm is considered to be in agreement with the size distribution observed in SG. However, particles sizing from 100 nm to 100 μm have been reported by previous feedbacks (See paragraph 1.2.6.3.4). Total iron concentration is maintained at 30 ppb in EDF SG feedwater and COLENTEC test solution. The real local iron concentration in restricted regions, *e.g.*, TSP flow holes, remains undetermined and is susceptible to be dramatically higher than in feedwater (See paragraph 1.2.5). Calculations will be performed by varying values of particle size and particle concentration in order to reveal the phenomenon prioritization in different situations.

Calculations will be performed under nominal EDF operation conditions in order to estimate the relative contribution of each phenomenon by using the observed global TSP clogging formation data (up to 386 $\mu\text{m}/\text{year}$ at the inlet of TSP). No deposit was observed during COLENTEC-2015 tests at the inlet of TSP. Therefore, the global deposit formation data in this region is unknown, which is probably due to the unintended upstream particle trapping by components before test section. The phenomenon prioritization is thus impossible under COLENTEC-2015 conditions. Nevertheless, the same calculations will be performed under COLENTEC conditions for particle deposition and flashing, which will bring valuable information to explain the effects of the differences between EDF and COLENTEC operation conditions on each phenomenon.

4.2 Hypotheses and input data

Hypotheses will be made for different parameters to facilitate the quantification (paragraph 4.2.1). All input data used for calculation are listed in paragraph 4.2.2, under nominal EDF and COLENTEC-2015 conditions.

4.2.1 Hypotheses

In the present work, clogging at the inlet of TSP is supposed to be exclusively formed by particle deposition by *vena contracta*, flashing and electrokinetics. Erosion of formed deposits is not taken into account. Electrokinetics is estimated by simply subtracting particle deposition and flashing from global TSP clogging formation. The author would like to emphasize that the calculated contribution percentage of electrokinetic phenomenon may vary following different parameters as the particle size and total iron concentration due to the changes on particle deposition or flashing terms. Nevertheless, this variation may not reproduce the real contribution from these parameters to electrokinetic phenomenon from a phenomenological point of view.

Magnetite (Fe_3O_4) has been identified as the major component in TSP clogging from EDF and COLENTEC feedbacks. In the following calculations, TSP clogging deposits and deposited particles will be supposed to be pure magnetite with a density of 5180 kg/m^3 (Table 1.4), which is considered to be independent of temperature. To facilitate the deposit thickness (e_d) calculations, the deposit porosity will not be taken into account. Therefore, the particle and deposit densities (ρ_d and ρ_p , respectively) are supposed to be the same and equal to 5180 kg/m^3 .

Particle deposition will be modelled with three different magnetite particle sizes (d_p) (100 nm, 1 μm and 10 μm), which are believed to fairly represent real particle size dispersion in PWR steam generators as previously mentioned (paragraph 1.2.6.3.4).

Different total iron concentrations (soluble iron concentration (S_s) and particle concentration (C_p)) will be used (magnetite solubility, 30 ppb, 100 ppb, 1 ppm and 3 ppm) for calculations in order to reveal the effect of the previously mentioned super-concentration phenomenon in SG (paragraph 1.2.5) on mechanism prioritization.

Regarding the vertical secondary fluid velocity at the inlet of TSP, the mixture velocity U_z (m/s) is supposed to be equal to liquid phase velocity $U_{z,l}$ (m/s).

Addition of chemical agents, *e.g.*, morpholine and ammonia, is considered to have no effects on water density (ρ_l), dynamic viscosity (μ_l) and heat of vaporisation (H_{lg}), for which characteristics of pure water will be used at a given temperature.

A maximal global TSP clogging formation rate will be considered at the inlet of TSP: 386 $\mu\text{m}/\text{year}$, which corresponds to a totally clogged TSP ($e_d = 5.8 \text{ mm}$) after 15 years.

The dimensionless TSP clogging rate (τ_c), representing the ratio between the flow blockage section to the total hole section, is considered to be 0 and 1 at $t=0$ and $t=15$ years, respectively. In the following calculations, the deposit is supposed to be formed onto a totally-clogged TSP with a constant rate during 15 years, *e.g.*, $\tau_c = 1$, in order to maximize the particle deposition phenomenon (Eq. 1-33). Indeed, the flow contraction becomes more and more important as the deposit grows, *e.g.*, τ_c increases, and consequently, the particle deposition is more and more favoured.

The modelling dimensionless parameter λ in Eq. 1-36 for flashing quantification depends on TSP clogging rate (τ_c). Three values were proposed in the literature (Prusek et al., 2013): 7.97, 18 and 76 corresponding to TSP clogging rates equal to 0, 0.44 and 0.72, respectively. λ equal to 76 will be used in the present work to simulate deposit formation onto a well-clogged TSP induced by flashing for maximization.

Based on the above hypotheses, all used input data will be listed in the next paragraph, under both nominal EDF operating and COLENTEC conditions.

4.2.2 Input data

The secondary water properties, *e.g.*, dynamic viscosity (μ_l), water density (ρ_l) and heat of vaporisation (H_{lg}) were calculated by using the *SteamTab* software (*SteamTab*, 2010). Magnetite solubility at different temperatures of EDF and COLENTEC operating was obtained by using Figure 1.5. The vertical mixture velocity at the inlet of TSP (U_z) under nominal conditions equal to 2.7 m/s was proposed previously by EDF and used in the EDF modelling tool (Prusek, 2012). This velocity was calculated under COLENTEC-2015 conditions from the mass flow rate and was found to be 3.2 m/s. Particle concentration (C_p) was calculated by subtracting the magnetite solubility (S_s) from the total iron concentration. Mass fraction of vapour phase (C_g) was calculated using the void fraction and density values. Values of the half distance between two consecutive tubes (L), the equivalent radius of a TSP flow hole (R) and its section (S) were provided by the TSP design in COLENTEC facility, which is representative of the real TSP geometry in EDF NPPs. Values of the above parameters are listed in Table 4.1 under both nominal and COLENTEC-2015 conditions.

Table 4.1: Values of input parameters for quantification of particle deposition and flashing, under nominal EDF operating and COLENETC-2015 conditions.

	Nominal EDF operating conditions (277.2 °C, void fraction = 85%, pH _{25 °C} = 9.2)	COLENTEC-2015 operating conditions (250 °C, void fraction = 90%, pH _{25 °C} = 9.2)
S_s (kg/kg)	6x10 ⁻⁹	8x10 ⁻⁹
μ_l (kg/m/s)	9.5x10 ⁻⁵	1.1x10 ⁻⁴
ρ_l (kg/m³)	755.2	799.9
C_g (kg/kg)	0.19	0.20
H_{lg} (J/kg)	1.6x10 ⁶	1.7x10 ⁶
C_p (kg/kg)	Total iron concentration-6x10 ⁻⁹	Total iron concentration-8x10 ⁻⁹
U_{z/z,1} (m/s)	2.7	3.2
d_p (m)	1x10 ⁻⁷ - 1x10 ⁻⁶ - 1x10 ⁻⁵	
L (m)	3.254x10 ⁻²	
R (m)	2.895x10 ⁻³	
S (m²)	7.214x10 ⁻⁵	
ρ_{p/d} (kg/m³)	5180	
τ_c	1	
a_v	0.00087	
λ	76	

4.3 Results

Two types of phenomenon prioritization are performed, by varying (i) magnetite particle size (paragraph 4.3.1) and (ii) total iron concentration (paragraph 4.3.2). A total iron concentration equal to 30 ppb is used for calculation (i), and the particle size is fixed to 1 μm when iron concentration is varied (ii).

4.3.1 Phenomenon prioritization with different particle sizes

The calculations of deposit thickness formed after 15 years due to different phenomena are presented in Table 4.2 following different particle sizes. These calculated thicknesses allow then estimating the contribution percentage of each phenomenon to global deposit formation, as shown in Figure 4.1, under nominal EDF operating conditions. Deposit thickness induced by flashing is found to be independent of magnetite particle size (534.3 μm after 15 years), representing 9.21% of the global deposit. In the contrast, particle size appears to dramatically affect the particle deposition phenomenon. When particle size is lower than 1 μm, the contribution of particle deposition is minor (< 1%) and electrokinetics predominates in the global deposit formation with a contribution percentage of about 90% (Figure 4.1a and b). When particle size reaches 10 μm, this trend changes

as shown in Figure 4.1c. Deposition of large particles (72.24%) prevails electrokinetics (18.53%) and flashing (9.21%)

The same calculations were also performed under COLENTEC-2015 conditions to quantify deposit formation induced by particle deposition and flashing (Table 4.2). Electrokinetics cannot be estimated as no global deposit was formed at the inlet of TSP under COLENTEC conditions. COLENTEC conditions seem to promote particle deposition and flashing compared to nominal conditions, which may arise from the difference in secondary fluid velocity at the inlet of TSP (3.2 m/s under COLENTEC conditions vs. 2.7 m/s under nominal conditions), as both flashing and vena contracta mechanisms are highly dependent on fluid velocity (Eq. 1-32, 1-35 and 1-36).

Table 4.2: Quantification of particle deposition, flashing and electrokinetics phenomena under nominal EDF operating conditions and COLENTEC-2015 operating conditions after 15 years (Particle size is equal to 0.1, 1 and 10 μm ; total iron concentration is equal to 30 ppb).

	Nominal EDF operating conditions (277.2 °C, void fraction = 85%, pH _{25 °C} = 9.2)			COLENTEC-2015 operation conditions (250 °C, void fraction = 90%, pH _{25 °C} = 9.2)		
Global deposit thickness at the inlet of TSP after 15 years (μm)	5800			/		
Particle size (μm)	0.1	1	10	0.1	1	10
Deposit thickness due to vena contracta after 15 years (μm)	0.419	41.9	4190	0.514	51.4	5140
Deposit thickness due to flashing after 15 years (μm)	534.3	534.3	534.3	1182	1182	1182
Deposit thickness due to electrokinetics after 15 years (μm)	5265	5224	1075	/		

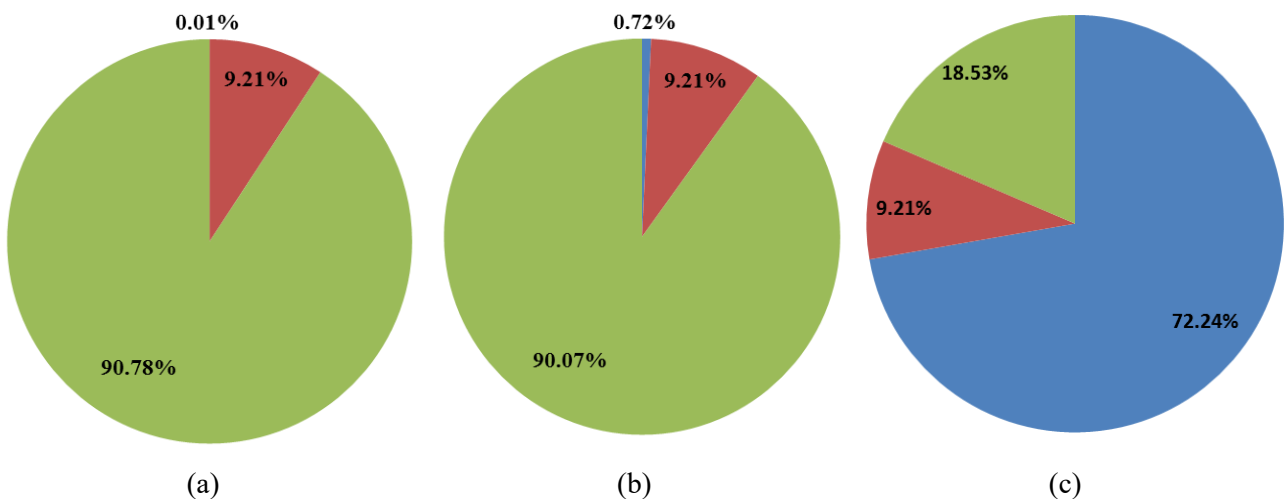


Figure 4.1: Schematic representation of the calculated contribution percentage of particle deposition by *vena contracta* (blue), flashing (red) and electrokinetics (green) to global deposit formation under nominal EDF conditions, with particle size equal to 100 nm (a), 1 μm (b) and 10 μm (c).

4.3.2 Phenomenon prioritization with different total iron concentrations

The calculations of deposit thickness formed after 15 years due to different phenomena are presented in Table 4.3 following different total iron concentrations. These calculated thicknesses allow then estimating the contribution percentage of each phenomenon to global deposit formation, as shown in Figure 4.2, under nominal EDF operating conditions. Deposit thickness induced by flashing is found to be independent of total iron concentration. Nevertheless, particle deposition phenomenon is affected by the change of iron concentration. When the total iron concentration is inferior to 1 ppm, the contribution of particle deposition is secondary and electrokinetic phenomenon predominates the global deposit formation (Figure 4.2a-d). This trend changes as shown in Figure 4.2e, when iron species is concentrated to 3 ppm in solution. Deposition of particles (90.12%) prevails electrokinetics (0.67%) and flashing (9.21%).

The same promoting effect on particle deposition and flashing by COLENTEC conditions is obtained as previously mentioned in paragraph 4.3.1.

Table 4.3: Quantification of particle deposition, flashing and electrokinetics phenomena under nominal EDF operating conditions and COLENTEC-2015 operating conditions after 15 years (Particle size is equal to 1 μm ; total iron concentration is equal to magnetite solubility, 30 ppb, 100 ppb, 1 ppm and 3 ppm).

Nominal EDF operating conditions (277.2 °C, void fraction = 85%, $\text{pH}_{25\text{ }^\circ\text{C}} = 9.2$)						COLENTEC-2015 operation conditions (250 °C, void fraction = 90%, $\text{pH}_{25\text{ }^\circ\text{C}} = 9.2$)				
Global deposit thickness at the inlet of TSP after 15 years (μm)	5800					/				
Total iron concentration (ppb)	6	30	100	1000	3000	8	30	100	1000	3000
Deposit thickness due to <i>vena contracta</i> after 15 years (μm)	0	41.9	164.1	1736	5227	0	51.4	215.1	2319	6994
Deposit thickness due to flashing after 15 years (μm)	534.3	534.3	534.3	534.3	534.3	1182	1182	1182	1182	1182
Deposit thickness due to electrokinetics after 15 years (μm)	5266	5224	5102	3530	38.25	/				

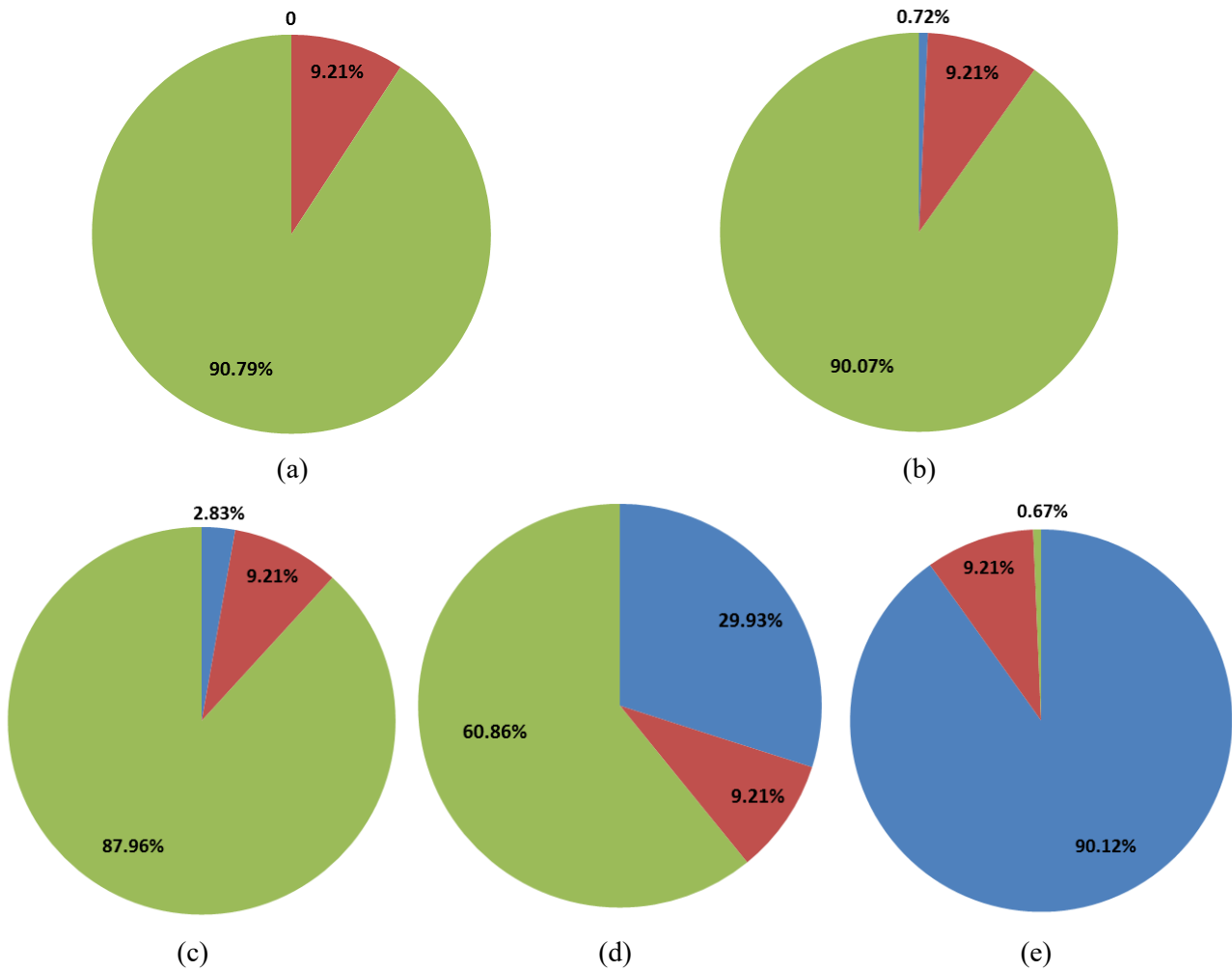


Figure 4.2: Schematic representation of the calculated contribution percentage of particle deposition by *vena contracta* (blue), flashing (red) and electrokinetics (green) to global deposit formation under nominal EDF conditions, with total iron concentration of 6 ppb (a), 30 ppb (b), 100 ppb (c), 1 ppm (d) and 3 ppm (e).

4.4 Discussions

The presence of lipping and ripple forms in the deposits observed during previous EDF NPP feedbacks suggested the importance of the electrokinetic phenomenon in global TSP clogging formation. In a previous modelling study, Prusek (Prusek et al., 2013) proposed a sequence of TSP clogging formation: deposit is initiated by particle deposition throughout a *vena contracta* mechanism, then flashing and electrokinetics occur to cement the formed deposits. Global deposit build-up investigations using COLENTEC facility showed the absence of clogging at the inlet of TSP under similar nominal EDF conditions, without occurring of particle deposition. Specific electrokinetic investigations suggested consistently the initiation role of particle deposition for electrokinetic activation.

The present numerical phenomenon prioritization highlights, from a quantitative point of view, the predominance of electrokinetic phenomenon in TSP clogging formation compared to particle deposition and flashing, when the total iron concentration and magnetite particle size are below to 3 ppm and 10 μm ,

respectively. Specific electrokinetic investigation suggested a radial deposit build-up rate of $0.09 \mu\text{m/h}$ when electrokinetics was activated by an inner orifice flow velocity equal to 18 m/s (Table 3.3). This rate corresponds to a deposit thickness, exclusively due to electrokinetics, of 11.8 mm after 15 years, which is about two times of the maximal clogging thickness at the inlet of TSP (5.8 mm). It is premature to extrapolate this radial BUR in quantification of the electrokinetic contribution to TSP clogging, as the contraction geometry, flow chemistry and thermohydraulics are not representative in the specific experimental electrokinetics studies at the *University of Manchester*. However, this experimental result seems to indicate that electrokinetically induced deposits grow and clog the TSP flow holes with a considerably high rate, in agreement with the predominant role of electrokinetics highlighted by calculations.

Contribution of particle deposition by *vena contracta* appears negligible when particle size is lower than $1 \mu\text{m}$ and the total iron concentration is below 1 ppm (Figure 4.1 and Figure 4.2). The absence or insufficient concentration of particles onto COLENTEC test coupons may be due to the upstream trapping of large particles ($> 1 \mu\text{m}$) before entering test section. Indeed, many geometric singularities are present inside the secondary boiler upstream the test section (Figure 2.1), favouring unintended particle trapping. The low concentration of total iron of about 30 ppb in COLENTEC solution may also explain the absence of particle deposition phenomenon in COLENTEC tests as shown by calculation. When particle size reaches $10 \mu\text{m}$, the contribution of particle deposition becomes important. This result agrees with the deposits formed onto the disc 4 during electrokinetic investigation in which large particles ($> 10 \mu\text{m}$) were observed in deposits (Figure 3.14). It can be figured out that particle deposition phenomenon is more important under COLENTEC-2015 conditions than under nominal EDF operation conditions. The slightly higher flow velocity in COLENTEC tests may explain this trend.

Flashing is found to be independent of the total iron concentration and the particle size. It contributes about 10% of global deposits. Flow velocity at the inlet of TSP has a major effect on this phenomenon, as shown in Eq. 1-36. Water temperature and pH, inducing changes in magnetite solubility (S_s), also affect flashing. Therefore, the higher deposit thickness calculated under COLENTEC-2015 conditions can be explained by the higher flow velocity and the higher magnetite solubility.

4.5 Conclusions of Chapter 4

Numerical calculations under EDF nominal operating conditions have been performed to describe particle deposition and flashing phenomena. Electrokinetic contribution was estimated by subtracting particle deposition and flashing from the global deposit formation. Electrokinetics has been found to play a predominant role in TSP clogging formation whereas no significant contribution of magnetite particle deposition occurs, if the size of particles is below to $1 \mu\text{m}$ and the total iron concentration is less than 1 ppm .

Calculations performed under COLENTEC-2015 conditions allowed attributing an enhancing effect of flow velocity to particle deposition and flashing phenomena. Flashing would also be strengthened by the lower temperature under COLENTEC conditions ($250 \text{ }^\circ\text{C}$ vs. $277.2 \text{ }^\circ\text{C}$), which increases the magnetite solubility.

Previous COLENTEC-2015 tests and specific electrokinetic investigations suggested an essential role of particle deposition, which initiates flashing and electrokinetics occurring. Experimental validation by COLENTEC facility should be conducted, avoiding the upstream particle trapping. Direct particle injection into the test section appears pertinent. The above quantification results of particle deposition phenomenon, following different total iron concentration and particle sizes, are useful for the further test design of particle injection.

Chapter 5 Overall conclusions and perspectives

Optimal functioning of steam generators is essential for PWR production and safety. Corrosion phenomena, particularly flow accelerated corrosion, induce the formation of soluble and particle iron species in PWR secondary fluid. These particles are then conveyed into SG and are responsible for various degradation deposit phenomena, *e.g.*, tube fouling and tube support plate clogging. TSP clogging phenomenon refers to the deposits, majorly composed of magnetite (Fe_3O_4), obstructing the secondary flow holes between SG tubes and TSP. This phenomenon decreases the secondary flow section and induces high velocity zones and transverse velocities, which can imply SG tube cracks and leaks in the worse cases. Currently used diagnosis methods and countermeasures face to TSP clogging have been identified. Chemical cleaning can be efficient but remains extremely costly and difficult to perform. Therefore, finding alternative solutions to avoid TSP clogging is necessary. Current main remedies, without understanding the phenomenology of deposit formation, are applied for decreasing the soluble and particle iron species concentration, *e.g.*, the source of TSP clogging, in PWR secondary solution by minimizing magnetite solubility. High pH has been found to have a primary role to reduce magnetite solubility. The present work aimed at thoroughly understanding the phenomena responsible for TSP clogging by a mechanistic approach in order to identify the preponderant formation processes and reveal their contributions to global deposit formation.

Magnetite particle deposition and soluble iron precipitation are the two main formation processes of SG degradation phenomena. Previous experimental and numerical studies have been thoroughly reviewed, bringing essential information to generally understand these two mechanisms. A schematic illustration of TSP clogging formation is shown in Figure 5.1, governing particle deposition and soluble iron precipitation phenomena.

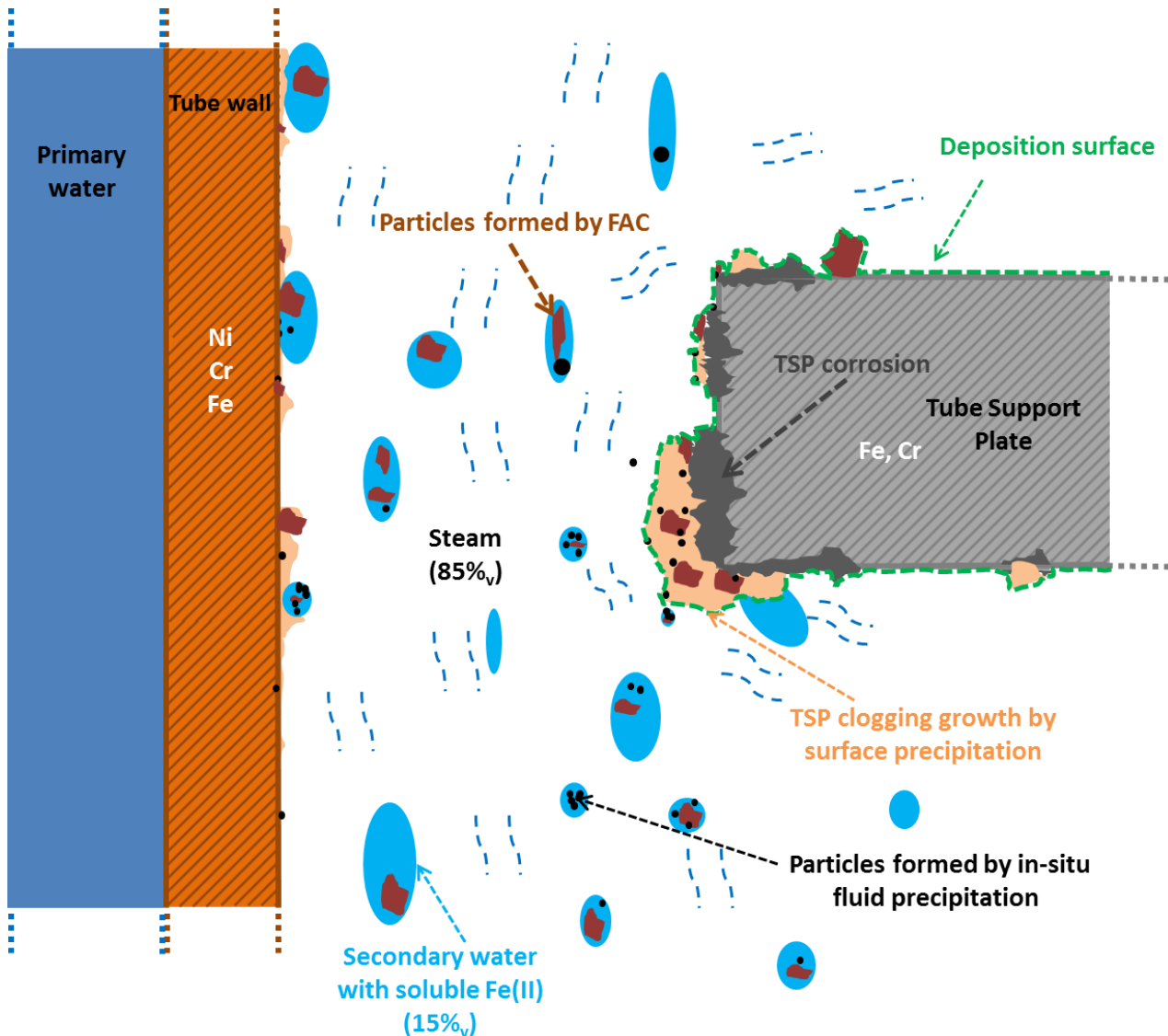


Figure 5.1: Schematic illustration of TSP clogging formation by particle deposition and precipitation phenomena.

TSP clogging deposits in nuclear power plant feedbacks are characterized by lipping and ripple forms. Maximal TSP clogging formation rate was estimated to be 386 $\mu\text{m}/\text{year}$ at the inlet of TSP. TSP clogging may occur onto two steps: (i) initiation by particle deposition and (ii) propagation by flashing and electrokinetic phenomena. Laboratory-scale deposit build-up tests were performed by means of the two-phase flow COLENTEC facility under close representative conditions of the 8th TSP in SG. COLENTEC is a unique tool of great interest to carry out parametric studies for improving the comprehension of TSP clogging phenomenon. The performed tests clearly indicated the effect of surface roughness and the deposit formation by soluble iron precipitation. Fine TEM characterizations were performed onto titanium and stainless steel test coupons from COLENTEC tests. They confirmed the effect of the nature of the material on deposit formation. Incorporation of external iron species into material corrosion layer has been supposed, following the different chemical and crystallographic affinities between material and external iron. The incorporation may encourage corrosion and delay material passivation, which has been proposed to be essential for initiating deposit formation. Monophasic autoclave tests under COLENTEC temperature and chemistry were developed in parallel. These tests provided results in accordance with the previously suggested material effects. Particle deposition was not highlighted in the deposits reformed by COLENTEC facility, which is due to the non-favouring experimental conditions. Specific TSP clogging lipping and ripple forms were not observed on COLENTEC samples, which was considered to be related to the insufficient concentration of particles in the test section or the insufficient flow velocity in quaterfoils.

Electrokinetic phenomenon, induced by charge rearrangement in flow acceleration regions, allows forming deposits and perfectly explaining the formation of clogging deposits under lipping form at the inlet of TSP and periodic ripples along the TSP. This mechanism may contribute considerably to clogging formation. The specific experimental investigations allowed reforming deposits under representative lipping and ripple forms with a high inner orifice velocity of 18 m/s, using a world unique dedicated recirculating autoclave system at *the University of Manchester*. Electrokinetic indications were not shown with two lower velocities (4 and 8 m/s), suggesting that electrokinetic phenomenon depends largely on flow velocity and may only be activated from a certain velocity. Electrokinetic activation by particle deposition was equally suggested by thorough comparisons based on the differences between nominal EDF operation, COLENTEC and specific electrokinetic investigation conditions. Strong involvement of electrokinetics in TSP clogging formation was suggested, needing likely initiation by particle deposition.

Mechanistic prioritization between particle deposition, flashing and electrokinetics was performed by numerical calculations under EDF nominal operating conditions. Electrokinetic contribution was estimated by subtracting particle deposition and flashing from the global deposit formation, and has been found to play a predominant role in TSP clogging formation. Nevertheless, contribution of magnetite particle deposition has been estimated to be minor and flashing contributes in about 10% of clogging deposits if the particle size remains below to 1 μm and the total iron concentration is less than 1 ppm.

The present work has allowed a thorough comprehension of TSP clogging formation processes (Figure 5.2). In a novel steam generator, the flow velocity in the quatrefoils is about 7 m/s, which is insufficient to activate the electrokinetics. Particle deposition may initiate deposits once material passivated with an average particle size of 1 μm and a total iron concentration likely much higher than 30 ppb in SG. Flashing and electrokinetics occur afterward, with more nucleation sites and higher flow velocity induced by particle deposition, to enhance the previously formed deposits. Electrokinetic phenomenon has been estimated to have a predominant contribution in TSP clogging formation.

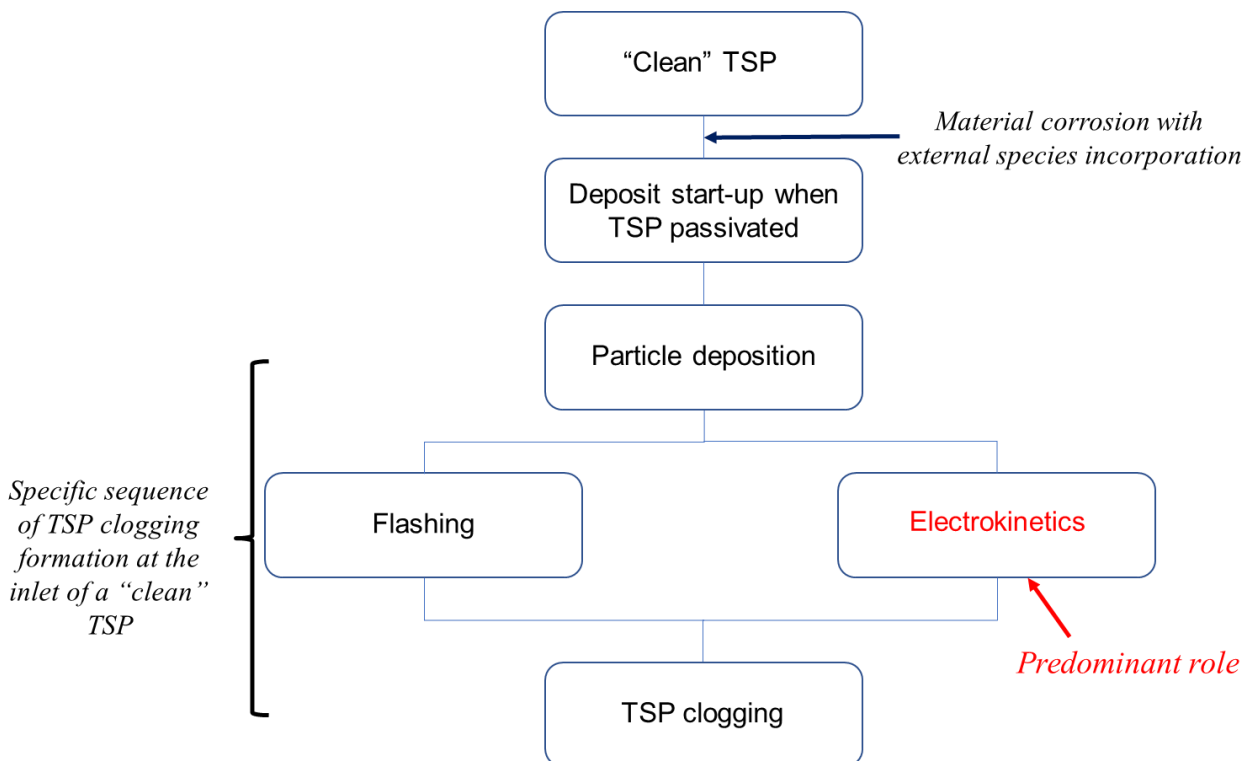


Figure 5.2: Suggested formation processes of TSP clogging phenomenon.

From the above results, TSP material passivation is found to be essential for deposit occurring onto the material surface. Microscopic characterizations of COLENTEC and autoclave tests suggested incorporation of external iron into material corrosion layer. Supplementary autoclave tests are necessary in order to better establish the trend of formed corrosion layer thickness following different iron concentrations. Adding isotopic species as tracer, *e.g.*, ^{57}Fe and ^{18}O , into COLENTEC and autoclave solution may be pertinent to directly reveal the contribution of external iron in material corrosion. Secondary ion mass spectrometry (SIMS) appears particularly useful to evidence the presence of isotopic elements in corrosion layer as post-characterization tool.

Particle deposition may initiate TSP clogging formation, encouraging afterward flashing and electrokinetic occurring. Deepening the understanding of this phenomenon is necessary. COLENTEC-2015 tests provided deposits without particle contribution, an interesting comparison with these deposits can be expected by conducting future COLENTEC tests with the presence of particles in order to reveal experimentally their role in deposit formation. For this purpose, following recommendations are proposed:

- Particles should be directly injected in the COLENTEC test section, without passing through the secondary boiler in order to avoid trapping. The implementation of injection system and necessary modifications to COLENTEC facility are ongoing. The injected quantity has been determined using vena contracta model, by supposing a formed deposit thickness characterisable by SEM. If specific lipping and ripple forms of TSP clogging are observed by particle injection, the initiating role of particle deposition would be confirmed.
- Adding of particles containing isotopic tracers in the secondary circuit of COLENTEC test loop are useful, which may aid to identify the preferred localisations of particle deposition and facilitate the distinction between the deposits formed by particle deposition and by precipitation. Effects of particle concentration and particle size may also be experimentally studied, which were found to influence the mechanistic prioritization. Effects of external contribution to material corrosion may equally be confirmed by injection of tracer species. Nevertheless, particles with isotopic tracers are extremely costly. Using core-shell particles as tracer may be an alternative solution, with the shell composed of magnetite to ensure the representability and the core composed of tracer element. The main challenge in the synthesis of core-shell particles consists of the simultaneousness between the formation of the core-shell configuration and the synthesis of the core and shell components. A dedicated research program should be established for synthesising size-controlled core-shell particles, if this approach is chosen. A tentative investigation of the synthesis of $\text{CeO}_2\text{-Fe}_3\text{O}_4$ core-shell particles has been conducted in the course of the present work and is briefly presented in Appendix C.
- Injection of radioactive magnetite particles, *e.g.*, ^{59}Fe , may bring data on particle deposition kinetics by monitoring formed deposits by on line γ -ray detector. The first campaign with radioactive injection is planned in 2018 using modified COLENTEC facility.

Inhibiting particle deposition phenomenon may be an interesting solution to avoid TSP clogging. Implementation of particle trapping components can be suggested upstream SG, as the role played by the secondary boiler in COLENTEC-2015 tests. For this purpose, a configuration of inside trapping system with large numbers of geometric singularities may be useful, encouraging particle trapping by coating and sedimentation phenomena. Particle trapping by magnetic effect may also be efficient as magnetite has the strongest magnetism of all the natural minerals.

Electrokinetic phenomenon has been predicted to be predominant by the present work. A guideline for the future research works on TSP clogging phenomenon can thus be strongly proposed, which consists of the thorough understanding of this relatively poorly-known mechanism. Performed preparative experimental investigations in *the University of Manchester* provided first and unique results of electrokinetically induced deposit formation under simulated PWR secondary solution. Supplementary parametric studies should be carried out in order to reveal the effects of different secondary thermohydraulic and chemical parameters on electrokinetic phenomenon. Comparative investigations with COLENTEC tests appear useful for the experimental validation of the numerically suggested predominance electrokinetics. Several recommendations are listed below, based on the previously conducted investigations presented in Chapter 3:

- On-line pH measurement sensor should be implemented in the test loop in order to control precisely the pH, which may strongly affect the deposit formation.
- Specific investigation on the inner flow velocity appears of great interest as electrokinetics may be high-velocity activated. Supplementary velocities should be tested under the same conditions with that of the investigations of discs 1-3 (See paragraph 3.4). Velocities ranging from 8 to 18 m/s should be finely studied, in order to determine the threshold velocity for electrokinetic activation.
- Injection of iron particles is useful to highlight the role of particle deposition, which was supposed to initiate electrokinetics. Particle injection to the tests with velocities lower than threshold velocity of electrokinetic activation appears particularly pertinent.
- One-step tests should be preferentially performed, with only one studied parameter for each disc, for facilitating interpretations.
- Other parameters, *e.g.*, fluid temperature, pH, conductivity, dissolved oxygen and dihydrogen concentration, disc material, etc., should be all investigated, in order to thoroughly understand electrokinetics.
- The presence of particles may not be indispensable for electrokinetic activation, suggested by the results obtained on disc 3 ($v = 18$ m/s). Deposit formation with high inner TSP velocities, *e.g.*, 18 m/s, should be conducted using current COLENTEC test loop (without particles in the test section) and compared to deposits formed in COLENTEC-2015 tests and disc 3 investigations. The activation mode of electrokinetics would be better understood.
- Comparative studies should be performed between the future COLENTEC and specific electrokinetic investigations, if lipping and ripple forms are both observed, allowing experimentally to estimate the electrokinetic contribution to global deposit formation.

A model can finally be proposed based on the above complete experimental investigations, which describes the electrokinetically induced deposits under PWR secondary conditions. This model would practically be the model of TSP clogging phenomenon if the predominance of electrokinetics is confirmed. Novel geometric design of TSP allowing to decrease velocity change at the inlet, *e.g.*, larger secondary flow hole section between TSP and SG tubes and more smoothing TSP inlet, may then be proposed as alternative solution for delaying TSP clogging.

References

- Altarawneh, M. and Dlugogorski, B.Z. (2012), “A Mechanistic and Kinetic Study on the Decomposition of Morpholine”, *The Journal of Physical Chemistry A*, Vol. 116 No. 29, pp. 7703–7711.
- Arioka, K., Yamada, T., Terachi, T. and Staehle, R.W. (2006), “Intergranular stress corrosion cracking behavior of austenitic stainless steels in hydrogenated high-temperature water”, *Corrosion*, Vol. 62 No. 1, pp. 74–83.
- Balakrishnan, P., Mcsweeney, P., Forst, C. and Walmsley, P. (1981), “A Chemical Cleaning Process for Nuclear Steam-Generators”, *Nuclear Technology*, Vol. 55 No. 2, pp. 349–361.
- Bansal, B., Chen, X.D. and Mueller-Steinhagen, H. (2008), “Analysis of ‘classical’ deposition rate law for crystallisation fouling”, *Chemical Engineering and Processing*, Vol. 47 No. 8, pp. 1201–1210.
- Barale, M., Guillodo, M., Foucault, M., Ryckelynck, N., Clinard, M.-H., Chahma, F., Brun, C., et al. (n.d.). “Secondary side TSP deposit buildup: lab test investigation focused on electrokinetic considerations”, available at: http://inis.iaea.org/Search/search.aspx?orig_q=RN:46102410 (accessed 11 October 2016).
- Barale, M., Mansour, C., Carrette, F., Pavageau, E.M., Catalette, H., Lefevre, G., Fedoroff, M., et al. (2008), “Characterization of the surface charge of oxide particles of PWR primary water circuits from 5 to 320 degrees C”, *Journal of Nuclear Materials*, Vol. 381 No. 3, pp. 302–308.
- Barnes, M.C., Addai-Mensah, J. and Gerson, A.R. (1999), “The kinetics of desilication of synthetic spent Bayer liquor seeded with cancrinite and cancrinite/sodalite mixed-phase crystals”, *Journal of Crystal Growth*, Vol. 200, pp. 251–264.
- Basset, M., Mcinerney, J., Arbeau, N. and Lister, D.H. (2000), “The fouling of alloy-800 heat exchange surfaces by magnetite particles”, *The Canadian Journal of Chemical Engineering*, Vol. 78 No. 1, pp. 40–52.
- Beal, S. and Chen, J.. (1986), *A Model of Sludge Behavior in Nuclear Plant Steam Generators*, No. NP-4620, EPRI.

- Bignold, G.J., Garbett, K., Garnsey, R. and Woolsey, I.S. (1980), “Water chemistry of Nuclear Reactor System 2”, presented at the BNES, London, UK, pp. 5–18.
- Bischoff, J., Motta, A.T., Eichfeld, C., Comstock, R.J., Cao, G. and R.Allen, T. (2012), “corrosion of ferritic-martensitic steels in steam and supercritical water”, *J. Nucl. Mater.*
- Blaney, L. (2007), “Magnetite (Fe₃O₄): Properties, Synthesis, and Applications”, *The Lehigh Review*, available at: <http://preserve.lehigh.edu/cas-lehighreview-vol-15/5> (accessed 7 May 2017).
- Bock, T., Mahaffey, D. and Olsea, J. (1969), *Corrosion of Servo Valves by an Electrokinetic Streaming Current*.
- Bockris, J. and Reddy, A. (1973), *Modern Electrochemistry 2*, Springer, New York.
- Bodineau, H. and Sollier, T. (2013), “Tube support plate clogging up of French PWR steam generators”, available at: http://inis.iaea.org/Search/search.aspx?orig_q=RN:44067716 (accessed 4 January 2016).
- Bonavigo, L. and Salve, M.D. (2011), “Issues for Nuclear Power Plants Steam Generators”, available at: <https://doi.org/10.5772/14853>.
- Bott, T.R. (1997), “Aspects of crystallization fouling”, *Experimental Thermal and Fluid Science*, Vol. 14 No. 4, pp. 356–360.
- Broglioli, D. and Vailati, A. (2000), “Diffusive mass transfer by non equilibrium fluctuations: Fick’s law revisited”, *Physical Review E*, Vol. 63 No. 1, available at: <https://doi.org/10.1103/PhysRevE.63.012105>.
- Burrill, K.A. (1977), “The deposition of magnetic particles from high velocity water onto isothermal tubes”, *The Deposition of Magnetic Particles from High Velocity Water onto Isothermal Tubes*, p. 27 pp.
- Burrill, K.A., Cheluget, E.L. and Chocron, M. (1996), “Precipitation fouling of heat transfer surfaces in CANDU nuclear power stations”, *Water Chemistry of Nuclear Reactor Systems 7. Proceedings of the Conference*, pp. 615–24 vol.2.
- Carrette, F. (2015), “Décontamination et Nettoyage chimique en centrales à réacteur à eau sous pression”, presented at the Corrosion dans les centrales nucléaires, INSTN, Saclay, 27 November.

- Charlesworth, D.. (1970), “The deposition of corrosion products in boiling water systems”, *Chem Eng Prog Symp Ser*, pp. 21–30.
- Chen, Q. and Ahmadi, G. (1997), “Deposition of particles in a turbulent pipe flow”, *Journal of Aerosol Science*, Vol. 28 No. 5, pp. 789–796.
- Chen, Y., Sridharan, K., Allen, T.R. and Ukai, S. (2006), “Microstructural examination of oxide layers formed on an oxide dispersion strengthened ferritic steel exposed to supercritical water”, *Journal of Nuclear Materials*, Vol. 359 No. 1–2, pp. 50–58.
- Cheng, L., Ribatski, G. and Thome, J.R. (2008), “Two-Phase Flow Patterns and Flow-Pattern Maps: Fundamentals and Applications”, *Applied Mechanics Reviews*, Vol. 61 No. 5, pp. 050802-050802-28.
- Chexal, B., Horowitz, J., Dooley, B., Millet, P., Wood, C., Jones, R., Bouchacourt, M., et al. (1998), *Flow Accelerated Corrosion in Power Plants*.
- Chivot, J. (2004), *Fonctions Thermodynamiques, Diagrammes de Solubilité, Diagrammes E-pH Des Systèmes Fe-H₂O, Fe-CO-H₂O, Fe-S-H₂O, Cr-H₂O et Ni-H₂O En Focntion de La Température*, Andra.
- Cong, T., Tian, W., Qiu, S. and Su, G. (2013), “Study on secondary side flow of steam generator with coupled heat transfer from primary to secondary side”, *Applied Thermal Engineering*, Vol. 61 No. 2, pp. 519–530.
- Cong, T., Zhang, R., Tian, W., Qiu, S. and Su, G. (2015), “Effects of power level on thermal-hydraulic characteristics of steam generator”, *Progress in Nuclear Energy*, Vol. 81, pp. 245–253.
- Corredera, G., Alves-Vieira, M. and De Bouvier, O. (2008), *Fouling and TSP Blockage of Steam Generators on EDF Fleet: Identified Correlations with Secondary Water Chemistry and Planned Remedies*.
- D., T. and Grigull, U. (1974), “Experimental investigation of the deposition of suspended magnetite from the fluid flow in steam generating tubes”, -*Warme-Kraft*, p. 109.
- De Bouvier, O. (2015a), “Corrosion-érosion des aciers dans le circuit scondaire”, presented at the Corrosion dans les centrales nucléaires à eau sous pression, INSTN, Saclay, November.

- De Bouvier, O. (2015b), “Dégradation par corrosion dans les générateurs de vapeur”, presented at the Corrosion dans les centrales nucléaires à eau sous pression, INSTN, Saclay, November.
- Delaunay, S. (2010), *Réactivité de La Magnétite Dans Les Conditions Représentatives Du Circuit Secondaire Des Réacteurs À Eau Sous Pression*, Université Pierre et Marie Curie, October.
- “Detachment of Spherical Microparticles Adhering on Flat Surfaces by Hydrodynamic Forces”. (n.d.). , available at: http://www.academia.edu/8417664/Detachment_of_Spherical_Microparticles_Adhering_on_Flat_Surfaces_by_Hydrodynamic_Forces (accessed 19 February 2016).
- Devouard, B., Pósfai, M., Hua, X., Bazylnski, D.A., Frankel, R.B. and Buseck, P.R. (1998), “Magnetite from magnetotactic bacteria: Size distributions and twinning”, *American Mineralogist*, Vol. 83 No. 11–12 PART 2, pp. 1387–1398.
- Dinov, K., Ishigure, K., Matsuura, C. and Hiroishi, D. (1993), “Solubility of Magnetite in High-Temperature Water and an Approach to Generalized Solubility Computations”, *Journal of Nuclear Materials*, Vol. 207, pp. 266–273.
- Duffy, G.G., Kazi, S.N. and Chen, X.D. (2011), “Heat transfer and pressure drop characteristics of suspensions of synthetic and wood pulp fibres in annular flow”, *Applied Thermal Engineering*, Vol. 31 No. 14–15, pp. 2971–2980.
- Dupré, A., Ricciardi, G., Bourennae, S. and Mylvaganam, S. (2016), “Identification of flow regimes using raw EIT measurements”, presented at the WCIPT8, Brazil.
- El-Adawy, M., Paillat, T., Touchard, G. and Martin Cabaleiro, J. (2011), “Numerical Simulation of the Electrical Double Layer Development: Physicochemical Model at the Solid and Dielectric Liquid Interface for Laminar Flow Electrification Phenomenon”, *Ieee Transactions on Dielectrics and Electrical Insulation*, Vol. 18 No. 5, pp. 1463–1475.
- El-Dahshan, M.E., Shams El Din, A.M. and Haggag, H.H. (2002), “Galvanic corrosion in the systems titanium/316 L stainless steel/Al brass in Arabian Gulf water”, *Desalination*, Vol. 142 No. 2, pp. 161–169.

- EPRI. (1984), *Investigation of Steam Generator Corrosion Products Under Typical PWR Operating Conditions*, No. EPRI NP-3068.
- Erdemoglu, M. and Sarikaya, M. (2006), “Effects of heavy metals and oxalate on the zeta potential of magnetite”, *J Colloid Interface Sci*, pp. 795–804.
- Feron, D. (2012), *Nuclear Corrosion Science and Engineering*, Elsevier.
- Feron, D. (2015), “Différents types de corrosion dans les réacteurs à eau sous pression”, presented at the Corrosion dans les centrales nucléaires à eau sous pression, November.
- Féron, D. and Richet, C. (2010), *Corrosion and Alteration of Nuclear Materials*, CEA.
- Finšgar, M. (2013), “Galvanic series of different stainless steels and copper- and aluminium-based materials in acid solutions”, *Corrosion Science*, Vol. 68, pp. 51–56.
- Friedlander, S. and Johnstone, H. (1951), “Deposition of suspended particles from turbulent gas streams”, *Ind. Eng. Chem.*, p. 1151.
- Fu, C. (2012), *Magnetite Iron Oxide Nanoparticles: Synthesis, Characteristics, Magnetic Behavior, and Biomedical Applications*, Faculty of New Jersey Institute of Technology, May.
- Fujiwara, K., Domae, M., Ohira, T., Hisamune, K., Takiguch, H., Uchida, S. and Lister, D. (2008), , presented at the 16th Pacific Basin Nuclear Conference, AES, Tokyo, Japan.
- Fujiwara, K., Domae, M., Yoneda, K. and Inada, F. (2011), “Model of physico-chemical effect on flow accelerated corrosion in power plant”, *Corrosion Science*, Vol. 53 No. 11, pp. 3526–3533.
- Gainey, R.J. and Thorp, C.A. (1963), “CaSO₄ SEEDING PREVENTS CaSO₄ SCALE”, *Industrial & Engineering Chemistry*, Vol. 55 No. 3, pp. 39–43.
- Gerischer, H. (1973), “M. J. Sparnaay: The Electrical Double Layer; Vol. 4 of Properties of Interfaces; Topic 14 of The International Encyclopedia of Physical Chemistry and Chemical Physics. Pergamon Press, Oxford 1972. 415 Seiten. Preis: £ 6,50.”, *Berichte Der Bunsengesellschaft Für Physikalische Chemie*, Vol. 77 No. 8, pp. 658–658.

- Girard, S. (2012), *Diagnostic du colmatage des générateurs de vapeur à l'aide de modèles physiques et statistiques*, phdthesis, Ecole Nationale Supérieure des Mines de Paris, 17 December, available at: <https://pastel.archives-ouvertes.fr/pastel-00798355/document> (accessed 16 December 2015).
- Girard, S. (2014), “State of the Art of Clogging Diagnosis”, *Physical and Statistical Models for Steam Generator Clogging Diagnosis*, Springer International Publishing, pp. 15–24.
- Girard, S., Romary, T., Favennec, J.-M., Stabat, P. and Wackernagel, H. (2013), “Sensitivity analysis and dimension reduction of a steam generator model for clogging diagnosis”, *Reliability Engineering & System Safety*, Vol. 113, pp. 143–153.
- Grahame, D.. (1947), “The Electrical Double Layer and the Theory of Electrocapillarity”, *Chem. Rev.*, pp. 441–501.
- Guillodo, M. (2004), “A parametric study of hematite reduction in steam generator secondary side chemistry conditions”, San Francisco.
- Guillodo, M., Foucault, M., Ryckelynck, N., Chahma, F., Guingo, M., Mansour, C., Alos-Ramos, O., et al. (2012), “Experimental and numerical study of deposit formation in secondary side SG TSP by electrokinetic approach”, available at: http://inis.iaea.org/Search/search.aspx?orig_q=RN:46071752 (accessed 11 October 2016).
- Handbook of Water Chemistry of Nuclear Reactor System.* (2000), , Atomic Energy Society of Japon, Tokyo, Japon.
- Hasson, D. and Zahavi, J. (1970), “Mechanism of Calcium Sulfate Scale Deposition on Heat Transfer Surfaces”, *Industrial & Engineering Chemistry Fundamentals*, Vol. 9 No. 1, pp. 1–10.
- Heitmann, V.H.G. and Katsner, W. (1974), *VGB Kraftwerkstechnik (German Edition)*, pp. 211–219.
- Heitmann, V.H.G. and Schub, P. (1994), “Water chemistry of Nuclear Reactor System 3”, Vol. 1, presented at the BNES, London, UK, pp. 243–252.
- Helmholtz, H. (1879), “Studien über elektrische”, *Ann Phys*, pp. 337–82.

- Hill, R.J., Craig, J.R. and Gibbs, G.V. (1979), “Systematics of the spinel structure type”, *Physics and Chemistry of Minerals*, Vol. 4 No. 4, pp. 317–339.
- Hirano, H., Domae, M., Miyajima, K. and Yoned, K. (2010), “Study on the mechanism of flow-hole blockage of steam generator tube support plates under PWR secondary conditions”, presented at the NPC.
- Hogsett, S. and Ishii, M. (1997), “Local two-phase flow measurements using sensor techniques”, *Nuclear Engineering and Design*, Vol. 175 No. 1–2, pp. 15–24.
- Ida, N., Hoshikawa, H. and Lord, W. (1985), “Finite element prediction of differential eddy current probe signals from Fe₃O₄ deposits in PWR steam generators”, *NDT International*, Vol. 18 No. 6, pp. 331–338.
- Izumiya, M., Mizuniwa, F., Osumi, K., Kanbayashi, T., Matsushima, Y. and Tanno, K. (1976), *Karyoku Genshiryoku Hatsuden*, pp. 292–295.
- J. Morrison, J. (2014), *Corrosion, Transport, and Deposition in Pressurised Water Nuclear Reactor Primary Coolant Systems*, University of Birmingham, 25 September.
- K. Popov, N. (2015), *The Essential CANDU-Thermal-Hydraulic Design*, available at: <http://www.nuceng.ca/candu/pdf/6%20-%20Thermalhydraulic%20Design.pdf>.
- Keller, V.. (1974), *VGB Kraftwerkstechnik (German Edition)*, pp. 292–295.
- Le Calvar, M. and De Curières, I. (2012), “15 - Corrosion issues in pressurized water reactor (PWR) systems”, in Féron, D. (Ed.), *Nuclear Corrosion Science and Engineering*, Woodhead Publishing, pp. 473–547.
- Lei, C., Peng, Z., Day, T., Yan, X., Bai, X. and Yuan, C. (2011), “Experimental observation of surface morphology effect on crystallization fouling in plate heat exchangers”, *International Communications in Heat and Mass Transfer*, Vol. 38 No. 1, pp. 25–30.
- Liu, Z., Gao, X., Du, L., Li, J., Kuang, Y. and Wu, B. (2015), “Corrosion behavior of low-alloy steel with martensite/ferrite microstructure at vapor-saturated CO₂ and CO₂-saturated brine conditions”, *Applied Surface Science*, Vol. 351, pp. 610–623.

- “llnl.dat: The llnl.dat database. in phreeqc: R Interface to Geochemical Modeling Software”. (n.d.). , available at: <https://rdr.io/cran/phreeqc/man/llnl.dat.html> (accessed 19 July 2017).
- Lu, D., Yuan, B., Wu, L., Ma, Z. and Chen, Y. (2015), “Research on the deposition model of particle-like corrosion product in”, *Annals of Nuclear Energy*, Vol. 81, pp. 98–105.
- Lyklema, J. (1995), *Fundamentals of Interface and Colloid Science: Solid-Liquid Interfaces*, Academic Press.
- Machiels, A. and Munson, D. (2005), *Pressurized Water Reactors: Hydrazine and Oxygen Investigations*, EPRI.
- Mankina, N.. (1960), “Investigation of conditions of formation of iron oxide deposits”, *Teploenergetika*, pp. 8–12.
- Mansour, C. (2009), *Spéciation Des Espèces Souffrées Dans Les Générateurs de Vapeur Des Centrales Nucléaires À Réacteur À Eau Sous Pression*.
- McGrady, J., Scenini, F., Duff, J., Stevens, N., Cassineri, S., Curioni, M. and Banks, A. (2017), “Investigation into the effect of water chemistry on corrosion product formation in areas of accelerated flow”, *Journal of Nuclear Materials*, Vol. 493, pp. 271–279.
- McNab, G.S. and Meisen, A. (1973), “Thermophoresis in liquids”, *Journal of Colloid and Interface Science*, Vol. 44 No. 2, pp. 339–346.
- Moreau, O., Beddek, K., Clenet, S. and Le Menach, Y. (2013), “Stochastic Nondestructive Testing Simulation: Sensitivity Analysis Applied to Material Properties in Clogging of Nuclear Powerplant Steam Generators”, *IEEE Transactions on Magnetics*, Vol. 49 No. 5, pp. 1873–1876.
- Morrison, J., Cooper, C., Ponton, C., Connolly, B. and Banks, A. (2012), “Effect of water chemistry on corrosion of stainless steel and deposition of corrosion products in high temperature pressurised water”, available at: http://inis.iaea.org/Search/search.aspx?orig_q=RN:46071844 (accessed 11 October 2016).
- Morrison, J., Hewett, J., Cooper, C., Ponton, C. and Connolly, B. (2013), “Effects of Water Chemistry on Corrosion of Stainless Steel and Diposition of Corrosion Products in Hign Temperature Pressurised Water”.

- Mwaba, M.G., Golriz, M.R. and Gu, J. (2006), “A semi-empirical correlation for crystallization fouling on heat exchange surfaces”, *Applied Thermal Engineering*, Vol. 26 No. 4, pp. 440–447.
- Nordmann, F. and Fiquet, J.-M. (1996), “Selection criteria for the best secondary water chemistry”, *Nuclear Engineering and Design*, Vol. 160 No. 1, pp. 193–201.
- Paillard, S., Skarlatos, A., Pichenot, G., Cattiaux, G. and Sollier, T. (2010), *Simulation of Eddy Current Testing of Steam Generator Tubes in the Proximity of Support Plates Quadrefoil-Shaped Holes with an Hybrid Finite FE-VIM Model*.
- Parkins, W.. (1961), *Surface Film Formation in Reactor Systems*, No. 1265, AECL.
- Pointeau, V. (2015), *Boucle D’essais COLENTEC : Bilan de La Campagne D’essais 2015*, No. DO 154, CEA.
- Pourbaix, M. (1963), “Atlas d’équilibres électrochimiques”, presented at the Gautiers-Villars & Cie, Paris.
- Pressurized Water Reactor Systems*, No. 0603. (n.d.). , USNRC Technical Training Center, available at: <https://www.nrc.gov/reading-rm/basic-ref/students/for-educators/04.pdf>.
- Prigogine, I. and Rice, S.A. (2009), *Advances in Chemical Physics*, John Wiley & Sons.
- Prusek, T. (2012), *Modélisation et Simulation Numérique Du Colmatage À L’échelle Du Sous-Canal Dans Les Générateurs de Vapeur*, Aix-Marseille, 11 December, available at: <http://www.theses.fr/2012AIXM4333> (accessed 7 January 2016).
- Prusek, T., Moleiro, E., Oukacine, F., Adobes, A., Jaeger, M. and Grandotto, M. (2013), “Deposit models for tube support plate flow blockage in Steam Generators”, *Nuclear Engineering and Design*, Vol. 262, pp. 418–428.
- Pujet, S. (2002), *Encrassement Secondaire Des GV: Analyse Du REX et Des Essais En Laboratoire Sur Le Laboatoire et Le Dépôt de Produits de Corrosion*.
- Pujet, S. and Dijoux, M. (n.d.). *Modeling of the Combined Effects of Particle Deposition and Soluble Iron Precipitation on PWR Steam Generator Fouling*, EDF.

- Puzzuoli, F.V., Leinonen, P.J., Lowe, G.A. and Murchie, B. (1997), "Steam generator cleaning campaigns at Bruce A: 1993-1996", *Proceedings. Fourth International Conference on CANDU Maintenance*, pp. 355–85.
- Rautenbach, R. and Habbe, R. (1991), "Seeding Technique for Zero Discharge Processes, Adaption to Electrodialysis", *Desalination*, Vol. 84 No. 1–3, pp. 153–161.
- Reitzer, B.J. (1964), "Rate of Scale Formation in Tubular Heat Exchangers. Mathematical Analysis of Factors Influencing Rate of Decline of Over-all Heat Transfer Coefficients", *Industrial & Engineering Chemistry Process Design and Development*, Vol. 3 No. 4, pp. 345–348.
- Reza Moshrefi, Mohammad Ghassem Mahjani, Ali Ehsani and Majid Jafarian. (2011), "A study of the galvanic corrosion of titanium/L 316 stainless steel in artificial seawater using electrochemical noise (EN) measurements and electrochemical impedance spectroscopy (EIS)", *Anti-Corrosion Methods and Materials*, Vol. 58 No. 5, pp. 250–257.
- Robertson, J. (1986), *Corrosion and Deposition due to Electrokinetic Currents*, No. TPRD/L/3030/R86, CEGB.
- Rocchini, G. (1994), "Magnetite stability in aqueous solutions as a function of temperature", *Corrosion Science*, pp. 2043–2061.
- Royer, E. (2015), "Connaissances fondamentales et phénoménologie", presented at the Thermohydraulique diphasique dans les réacteurs nucléaires, Saclay, France.
- Ruchenstein, E. and Prieve, D.. (1973), "Rate of deposition of Brownian Particles under the Action of London and Double-Layer Forces", *J. Chem. Soc. Faraday Trans*, p. 1522.
- Rufus, A.L., Sathyaseelan, V.S., Srinivasan, M.P., Kumar, P.S., Veena, S.N., Velmurugan, S. and Narasimhan, S.V. (2001), "Chemistry aspects pertaining to the application of steam generator chemical cleaning formulation based on ethylene diamine tetra acetic acid", *Progress in Nuclear Energy*, Vol. 39 No. 3–4, pp. 285–303.
- Rummens, H.E.. (1999), *The Thermalhydraulics of Tube-Support Fouling in Nuclear Steam Generators*, Carleton University, September.

- Rummens, H.E.C., Rogers, J.T. and Turner, C.W. (2004), “The Thermal Hydraulics of Tube Support Fouling in Nuclear Steam Generators”, *Nuclear Technology*, Vol. 148 No. 3, pp. 268–286.
- Scenini, F., Palumbo, G., Stevens, N., Cook, A. and Banks, A. (2014), “Investigation of the role of electrokinetic effects in corrosion deposit formation”, *Corrosion Science*, Vol. 87, pp. 71–79.
- Schindler, P. (2010), *COLENTEC: Vérification Du Dimensionnement de L’installation*, No. DEN/CAD/DTN/STRI/DIR/NT/2010/02, CEA.
- Schindler, P. (2016), *COLENTEC: Améliorations Pour Le Passage Aux Conditions Nominales D’un GV REP*, No. CEA/DEN/CAD/DTN/STCP/NT 2016-014-INDICE A, CEA.
- Schindler, P., Tevissen, E., Pointeau, V. and Ungar, A. (2012), “COLENTEC: A new approach to investigate tube support plate clogging of Steam Generators”, presented at the NPC, Paris, France, pp. 2–10.
- Schoonen, M.A.A. (1994), “Calculation of the point of zero charge of metal oxides between 1 and 350°C”, *Geochimica et Cosmochimica Acta*, pp. 2845–2851.
- Serhan, H., Slivka, M., Albert, T. and Kwak, S.D. (2004), “Is galvanic corrosion between titanium alloy and stainless steel spinal implants a clinical concern?”, *The Spine Journal: Official Journal of the North American Spine Society*, Vol. 4 No. 4, pp. 379–387.
- Silbert, M. (2002), “Flow-Accelerated Corrosion”, *The Analyst*.
- Sinha, P.K., Kumar, M.K. and Kain, V. (2015), “Effect of microstructure of carbon steel on magnetite formation in simulated Hot Conditioning environment of nuclear reactors”, *Journal of Nuclear Materials*, Vol. 464, pp. 20–27.
- Skarlatos, A., Gilles-Pascaud, C., Pichenot, G., Cattiaux, G. and Sollier, T. (2010), “A hybrid volume integral-finite elements approach for the simulation of eddy current inspection of steam generator tubes in the region of quadrifoiled support plate”, *American Institute of Physics*.
- Smith, B.R. and Sweett, F. (1971), “The crystallization of calcium sulfate dihydrate”, *Journal of Colloid and Interface Science*, Vol. 37 No. 3, pp. 612–618.

SteamTab. (2010), , ChemicaLogic Corporation, available at:
http://www.chemicalogic.com/Documents/steamtab_manual.pdf.

Stinchcombe, R.. (1966), *Solids Deposition in Boiling Water Systems*, AERE.

Suat, O. and Francis, N. (n.d.). “Chimie du circuit secondaire des PWR et VVER”.

Surface Chemistry and Ion Exchange. (n.d.), , available at:
<http://www.geo.utexas.edu/courses/376m/LectureNotes/Surface.pdf>.

Takamatsu, H., Matsunaga, T., Wilson, R.M. and Kusakabe, T. (2000), “Sludge collector performance in steam generators of pressurized water reactor”, *Nuclear Engineering and Design*, Vol. 200 No. 1–2, pp. 295–302.

Tan, L., Machut, M.T., Sridharan, K. and Allen, T.R. (2007), “corrosion behavior of a ferritic/martensitic steel HCM12A exposed to harsh environments”, *J. Nucl. Mater.*, pp. 161–170.

Tan, L., Yang, Y. and Allen, T.R. (2006), “Porosity prediction in supercritical water exposed ferritic/martensitic steel HCM12A”, *Corrosion Science*, Vol. 48 No. 12, pp. 4234–4242.

Terachi, T., Yamada, T., Miyajima, T., Arioka, K. and Fukuya, K. (2008), “Corrosion Behavior of Stainless Steels in Simulated PWR Primary Water—Effect of Chromium Content in Alloys and Dissolved Hydrogen—”, *Journal of Nuclear Science and Technology*, Vol. 45 No. 10, pp. 975–984.

Tewari, P.H. and Mclean, A.W. (1972), “Temperature dependance of point of zero charge of alumina and magnetite”, *J. of Colloid and Interface Sci*, p. 167.

Tian, W.X., Zhang, K., Hou, Y.D., Zhang, Y.P., Qiu, S.Z. and Su, G.H. (2016), “Hydrodynamics of two-phase flow in a rod bundle under cross-flow condition”, *Annals of Nuclear Energy*, Vol. 91, pp. 206–214.

Tsubakizaki, S., Ando, H., Takei, Y., Naganuma, T., Sakamoto, Y. and Nishi, T. (2013), “Improved Reliability of High-AVT (High-pH Water Treatment) Application to Combined Cycle Plants”, *Mitsubishi Heavy Industries Technical Review*, March.

- Tsuruta, T., Murata, K., Shoda, Y. and Yamamoto, K. (2006), “Contribution of materials investigations to improve the safety and performance of LWRs”, Vol. 1, presented at the SFEN, Paris, France, pp. 181–190.
- Turner, C.. (1997), *Physical and Chemical Factors Affecting Sludge Consolidation*, No. 11674, AECL.
- Turner, C.. and Godin, M. (1994), *Mechanisms of Magnetite Deposition in Pressurized Boiling and Non-Boiling Water*, No. 11046, AECL.
- Turner, C., Klimas, S. and Brideau, M.. (1997), *The Effect of Alternative Amines on the Rate of Boiler Tube Fouling*, No. AECL-11848.
- Turner, C., Liner, Y. and Carver, M.. (1994), *Modelling Magnetite Particle Deposition in Nuclear Steam Generators and Comparisons with Plant Data*, No. 11128, AECL.
- Turner, C. w. (2013), “Fouling Of Nuclear Steam Generators: Fundamental Studies, Operating Experience and Remedial Measures Using Chemical Additives”, *CNL Nuclear Review*, Vol. 2 No. 1, pp. 61–88.
- Turner, C.W., Guzonas, D.. and Klimas, S.. (2000), *Surface Chemistry Interventions to Control Boiler Tube Fouling*, No. 12036, AECL.
- Vaessen, R.J.C., Himawan, C. and Witkamp, G.J. (2002), “Scale formation of ice from electrolyte solutions on a scraped surface heat exchanger plate”, *Journal of Crystal Growth*, Vol. 237–239, Part 3, pp. 2172–2177.
- Vergnault, A., Dorel, R. and Goux, F. (2008), “Steam Generator Blockage: A Thermal-Hydraulic Approach Based on CATHARE 2”, pp. 381–387.
- Weisbrod, N., Dahan, O. and Adar, E.M. (2002), “Particle transport in unsaturated fractured chalk under arid conditions”, *Journal of Contaminant Hydrology*, Vol. 56 No. 1–2, pp. 117–136.
- “World Energy Outlook 2016”. (2016), available at: <http://www.ica.org/newsroom/news/2016/november/world-energy-outlook-2016.html> (accessed 18 April 2017).

- Wu, X., Qin, S. and Dubrovinsky, L. (2010), “Structural characterization of the FeTiO₃–MnTiO₃ solid solution”, *Journal of Solid State Chemistry*, Vol. 183 No. 10, pp. 2483–2489.
- Yang, G., Pointeau, V., Tevissen, E. and Chagnes, A. (2017a), “A review on clogging of recirculating steam generators in Pressurized-Water Reactors”, *Progress in Nuclear Energy*, Vol. 97, pp. 182–196.
- Yang, G., Pointeau, V., Tevissen, E. and Chagnes, A. (2017b), “Experimental and numerical investigation of PWR Tube Support Plate (TSP) clogging formation mechanisms”, Vol. draft, presented at the NURETH, Xi’an, China.
- Zaitsev, V.S., Filimonov, D.S., Presnyakov, I.A., Gambino, R.J. and Chu, B. (1999), “Physical and Chemical Properties of Magnetite and Magnetite-Polymer Nanoparticles and Their Colloidal Dispersions”, *Journal of Colloid and Interface Science*, Vol. 212 No. 1, pp. 49–57.
- Zarembo, V., Kritskii, V., Slobodov, A. and Puchkov, L. (1988), “Solubility of Magnetite in the Coolant of an Atomic Power-Station Equipped with a Boiling-Water Reactor”, *Soviet Atomic Energy*, Vol. 65 No. 1, pp. 587–593.
- Zhang, K., Hou, Y.D., Tian, W.X., Fan, Y.Q., Su, G.H. and Qiu, S.Z. (2017), “Experimental investigations on single-phase convection and steam-water two-phase flow boiling in a vertical rod bundle”, *Experimental Thermal and Fluid Science*, Vol. 80, pp. 147–154.
- Zohuri, B. and Fathi, N. (2015), *Thermal-Hydraulic Analysis of Nuclear Reactors*, Springer.

Appendix A Scanning Electronic Microscope

In scanning electronic microscope (SEM), the sample surface is raster-scanned in high vacuum with a focused beam of electrons. Secondary or backscattered electrons are detected to provide an image of the sample surface with up to nanometre-scale resolution. In addition to structural imaging, the elemental composition of the surface can be assessed from characteristic X-rays that are emitted (Figure A.1).

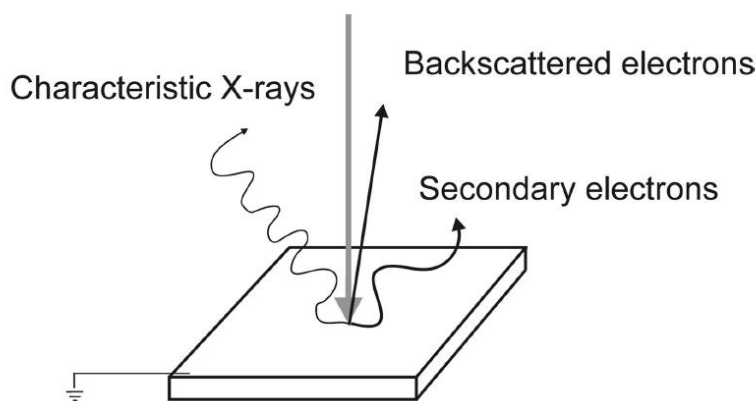


Figure A.1: Rudimentary processes that occur upon impingement of an electron beam onto a sample surface in SEM.

In general, sample surfaces for SEM analysis require pre-treatment to render them clean and conductive to prevent the accumulation of charges in the specimens. This pre-treatment may consist of a thin coating of metals, such as gold or platinum, or of graphite.

Due to its surface sensitivity, the secondary electron imaging mode is widely used. In this mode, low-energy secondary electrons (< 50 eV) are detected that were ejected from specimen atoms by inelastic scattering interactions with primary electrons. The low energy leads to a limited escape depth of only a few nanometres.

Backscattered electrons possess much higher energy compared to secondary electrons and allow one to image with atomic number contrast. High atomic number elements backscatter the primary electrons more effectively compared to lighter elements.

Characteristic X-rays are emitted from atoms at depths of up to a micrometre upon interaction with the incident electrons. The ejection of photoelectrons is followed by subsequent rearrangements of the electronic shells of the energetically excited atoms. One pathway for deactivation of the excited state is the emission of a characteristic X-ray photon. To analyze the X-rays the SEM must be equipped with an energy dispersive X-ray detector (EDX). Since the escaping photon is not charged, like for instance the mentioned secondary electrons, the escape depth is considerable.

A ZEISS EVO HD15MA SEM (LaB₆ source) and a HIROX SH 4000M mini-SEM equipped with an OXFORD SDD X-Max 50 EDS detector for chemical analysis was used for SEM observations in the present work.

Appendix B Transmission Electronic Microscope

Transmission electronic microscope is a microscopy technique where a beam of electrons is transmitted through an ultra-thin specimen and a unique tool in characterization of materials' crystal structure simultaneously by diffraction and imaging techniques. TEM has three essential systems (Figure B.1):

- i. An electron gun, which produces the electron beam, and the condenser system, which focuses the beam onto the object. The source of electrons is heated V-shaped tungsten filament or, in high performance instruments, a sharply pointed rod of a material such as lanthanum hexaboride.
- ii. The image producing system, consisting of the objective lens, movable specimen stage, and intermediate and projector lenses which focus the electrons passing through the specimen to form a real and highly magnified image. The quality of the final image in the electron microscope depends highly on the accuracy of the various mechanical and electrical adjustments with which the various lenses are aligned to one another and to the illuminating system.
- iii. The image recording system, which converts the electron image into some form perceptible to the human eye. The image recording system usually consists of a fluorescent screen for viewing focusing the image and a digital camera for permanent records.

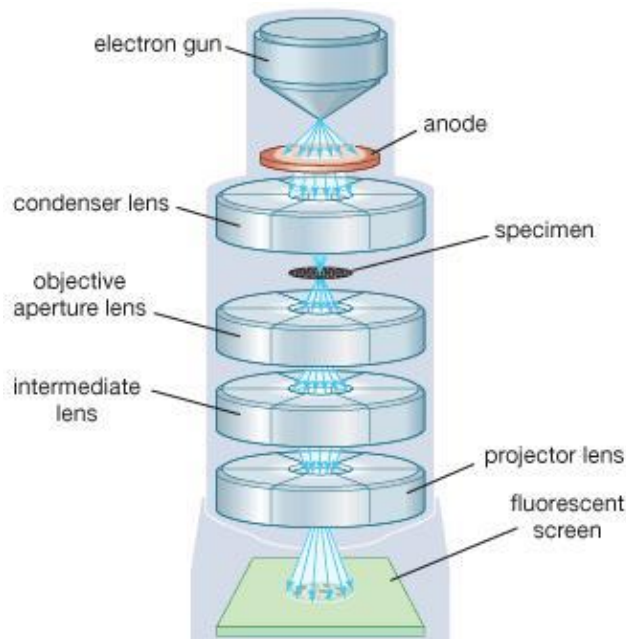


Figure B.1: Schematic diagram of TEM

Three major imaging modes are generally used: High Angle Annular Dark Field (HAADF), Annular Dark Field (ADF) and Bright Field (BF), as schematized in Figure B.2.

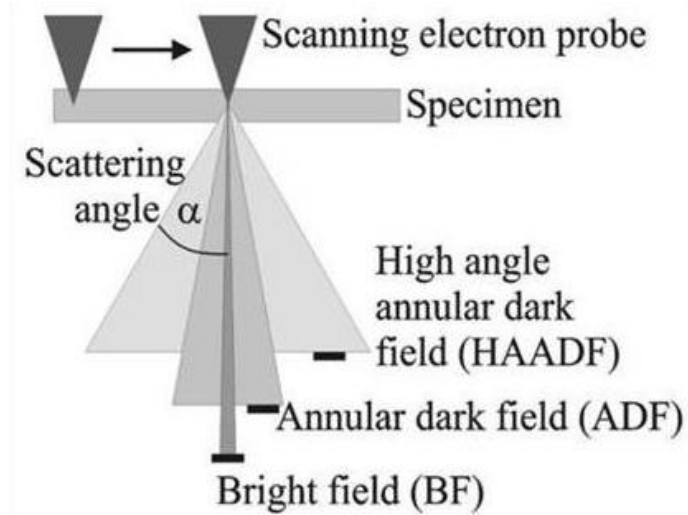


Figure B.2: Schematic representation of TEM imaging modes

Crystallographic information, *e.g.*, crystal orientation and lattice parameters, can be obtained by electron diffraction patterns (Figure B.3).

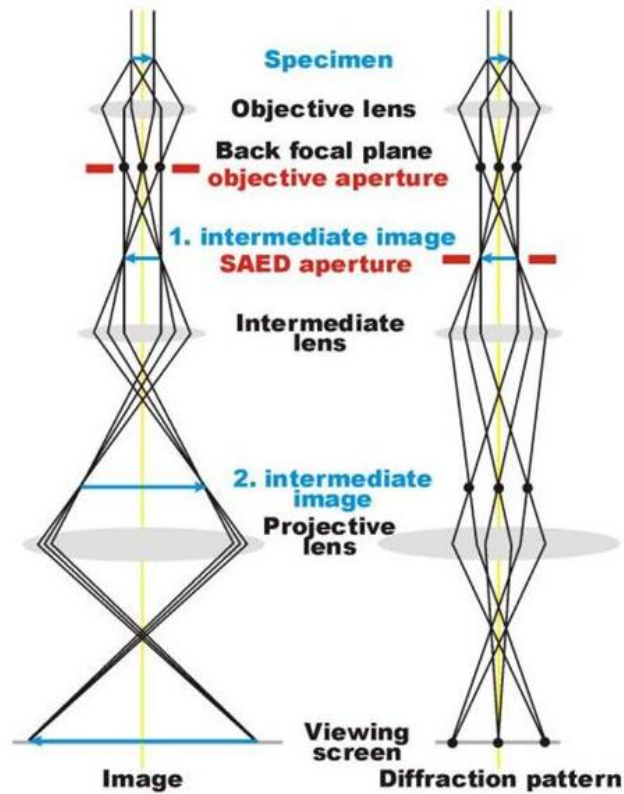


Figure B.3: Schematic comparison between TEM imaging mode and diffraction mode. SAED represents Selected Area Electron Diffraction.

TEM observations in the present work were performed on a FEI Tecnai G2 transmission electron microscope equipped with a LaB₆ source, operating at 200 kV. Samples for TEM observations were cut with the FEI FIB-Helios 600 Nanolab Dual Beam.

Appendix C Synthesis of $\text{CeO}_2\text{-Fe}_3\text{O}_4$ core-shell particles

• Synthesis of CeO_2

- Reagents:
 - ✓ 50 ml of $\text{Ce}(\text{NO}_3)_3 \cdot 6\text{H}_2\text{O}$ solution (CAS: 10294-41-4)
 - ✓ Adding of 25 ml of ammonia (CAS: 1336-21-6)
- Synthesis conditions:

Temperature	Atmosphere	Stirring rate	Duration
50 °C	Air	500 rpm	2 hours

- Results:

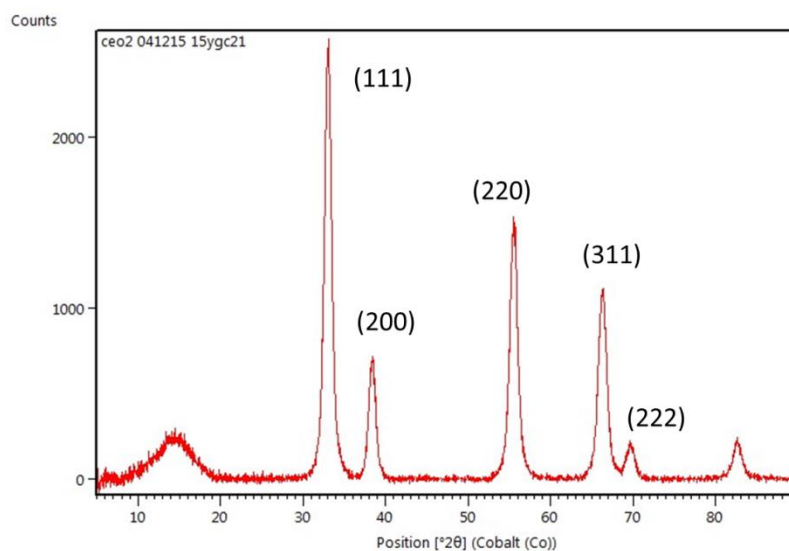


Figure C.1: Synthesized CeO_2 particles in suspension (left); XRD diagram of synthesized particles showing the chemical composition of CeO_2 (right).

• Synthesis of core-shell $\text{CeO}_2\text{-Fe}_3\text{O}_4$ particles

- Reagents:
 - ✓ 24 g of urea (CAS: 57-13-6) in 500 ml of H_2O in Teflon container.
 - ✓ Adding of 13.5 g of $\text{FeCl}_3 \cdot 6\text{H}_2\text{O}$ (CAS: 10025-77-1) and 5.3 g of $\text{FeCl}_2 \cdot 4\text{H}_2\text{O}$ (CAS: 13478-10-9).
 - ✓ Adding of 0.7 g of synthesized CeO_2 particles.
- Synthesis conditions:

Temperature	Atmosphere	Stirring rate	Duration
85 °C	Air	0	48 hours

- Results: formation of mixture of Fe_3O_4 and CeO_2 , without achieving the core-shell configuration.

- **Perspectives:**

- Implementation of automatic CeO_2 particles adding system, allowing progressive and slow addition and implementation of stirring system without using magnetic effects.

